

High-resolution large-eddy simulation studies of the turbulent structure of the convective boundary layer over homogeneous and heterogeneous terrain and implications for the interpretation of scintillometer data

Von der Fakultät für Mathematik und Physik
der Gottfried Wilhelm Leibniz Universität Hannover
zur Erlangung des Grades

Doktor der Naturwissenschaften

Dr. rer. nat.

genehmigte Dissertation

von

Dipl.-Met. Björn Maronga

geboren am 6. März 1984 in Bad Segeberg

Referent: Prof. Dr. Siegfried Raasch
Korreferent: Prof. Dr. Dieter Etling
Korreferent: Dr. Arnold Moene
Tag der Promotion: 4. November 2013

Abstract

The atmospheric boundary layer is the lower part of the atmosphere that is directly affected by the Earth's surface and characterized by turbulent transport of momentum, heat and moisture. Numerical weather prediction models (NWP) do not allow for resolving turbulent motions at scales smaller than current grid resolutions in the order of several kilometers. Turbulence must thus be parametrized within such models. Moreover, NWP models strongly rely on the quality of micro-meteorological measurement data such as the surface fluxes of sensible and latent heat. Scintillometry offers a promising technique to obtain these fluxes at a regional scale that might be representative for an area of size of current NWP grid boxes. It is possible to derive the structure parameters of temperature C_T^2 and humidity C_q^2 from large-aperture scintillometer (LAS) and microwave scintillometer data. These structure parameters in turn can be linked to the surface fluxes of sensible and latent heat, respectively, using Monin-Obukhov similarity theory (MOST). However, several aspects of the scintillometer principle are still unclear, particularly in natural landscapes where the Earth's surface is often very heterogeneous and the surface fluxes vary in space and time. Large-eddy simulation (LES) offers a unique technique for studying the atmospheric boundary layer. In the present thesis LES is used to study C_T^2 and C_q^2 and their similarity relationships in homogeneously- and heterogeneously-heated convective boundary layers (CBL). Moreover, the general effect of surface heterogeneity on the boundary-layer turbulence is investigated. Boundary conditions for the simulations are derived from measurements during the RECAB campaign at Cabauw (The Netherlands) and during the LITFASS-2003 experiment at Lindenberg (Germany).

Three different methods to obtain C_T^2 and C_q^2 from LES are investigated over homogeneous terrain and validated against in situ aircraft and LAS observations at Cabauw. Virtual path measurements in the LES are used to study the representativeness of such measurements. The LES results suggest that sufficient temporal averaging and an adequate ratio of the path length to height above ground are required for LAS systems in order to approach the domain average of C_T^2 in free convection. Moreover, the applicability of MOST and local free convection similarity (LFC) scaling is studied. The LES data suggest that the MOST function for C_T^2 is usually universal and that the derived similarity functions are within the range of the functions proposed from measurement data. C_q^2 is found to follow MOST if entrainment of dry air from the free atmosphere is sufficiently small. In this case the similarity functions for C_T^2 and C_q^2 are identical. Otherwise, dissimilarity between the transport of heat and moisture is observed and C_q^2 no longer follows MOST. In the free convection limit the universal functions should collapse to universal constants. For C_T^2 the LES data suggest values around 2.7, in agreement with the value proposed in literature. Like for MOST, the LFC similarity constant for C_q^2 no longer follows MOST if entrainment of dry air is affecting the surface layer structure.

The effect of surface heterogeneity on the CBL flow and the structure parameters is studied using an irregularly distributed surface heterogeneity, observed during LITFASS-2003. Secondary circulations (SC) develop that are superimposed on the turbulent field and that partly take over the vertical transport of heat and moisture. The SC vary between local and roll-like structures depending on the background wind conditions. For higher background wind speeds, the flow feels an effective surface heat-flux pattern that derived from the original pattern by streamwise-averaging. However, it is found that these SC are usually weak in the surface layer where scintillometers are operated.

The LES data from a high-resolution case study for the LITFASS-2003 experiment shows that signals of the surface heterogeneity are present in the structure parameters in the entire surface layer and thus above typical height levels where scintillometers are operated. The prerequisite for MOST of horizontal homogeneity of turbulence is thus not valid for the studied case and no blending height for structure parameters is found below the scintillometer systems installed during the LITFASS-2003 experiment. Nevertheless, it is found that the application of MOST and LFC scaling for C_T^2 still give reliable estimates of the surface flux of sensible heat. It is found, however, that this flux, derived from LAS data, will be rather representative for the local footprint area of the scintillometer than for an area at regional scale and thus of size of current NWP models. Furthermore, the previous finding from the simulations over homogeneous terrain that C_q^2 does not follow MOST is confirmed.

Key words: Atmospheric boundary layer, Large-eddy simulation, Structure parameter

Kurzzusammenfassung

Die atmosphärische Grenzschicht ist der untere Teil der Atmosphäre, der direkt durch die Erdoberfläche beeinflusst wird und der sich durch turbulenten Transport von Impuls, Wärme und Feuchte auszeichnet. Numerische Wettervorhersagemodelle (NWP Modelle) können Turbulenz auf Skalen, die kleiner sind als die derzeitige Gitterweite, nicht auflösen (im Bereich einiger Kilometer). Die Turbulenz muss daher in solchen Modellen parametrisiert werden. Weiterhin sind NWP Modelle stark auf die Qualität mikrometeorologischer Messdaten angewiesen, wie z.B. die bodennahen turbulenten Flüsse fühlbarer und latenter Wärme. Scintillometrie ist eine vielversprechende Technik um diese Flüsse auf regionaler Skala zu bestimmen, die für ein Gebiet von Größe eines NWP Gittervolumens repräsentativ sein könnten. *Large-aperture scintillometer*- (LAS) und Mikrowellen-scintillometer erlauben die Bestimmung der turbulenten Strukturparameter der Temperatur C_T^2 und Feuchte C_q^2 . Aus diesen können mittels Monin-Obukhov-Ähnlichkeitstheorie (MOST) die bodennahen Flüsse abgeleitet werden. Dennoch sind einige Aspekte des Scintillometerprinzips nicht hinreichend untersucht worden. Dies gilt speziell für Naturlandschaften, in denen der Erdboden oft sehr heterogen ist und die bodennahen Flüsse sowohl räumlich und zeitlich variieren. Grobstruktursimulationen (LES) bieten eine besondere Technik für die Untersuchung der atmosphärischen Grenzschicht. In der vorliegenden Studie werden solche LES verwendet um C_T^2 und C_q^2 und deren Ähnlichkeitsbeziehungen sowohl in homogen als auch in der heterogen geheizten konvektiven Grenzschichten (CBL) zu untersuchen. Zudem wird der generelle Effekt von Bodenheterogenitäten auf die Grenzschichtturbulenz untersucht. Randbedingungen für die Simulationen werden dabei aus Messungen während der RECAB Kampagne in Cabauw (Niederlande) und während des LITFASS-2003 Experimentes in Lindenberg (Deutschland) bestimmt.

Es werden drei Methoden über homogenem Gelände untersucht mit denen C_T^2 und C_q^2 aus LES Daten bestimmt werden können. Diese werden mittels Flugzeug- und LAS Messungen in Cabauw validiert. Virtuelle Pfadmessungen werden in den LES verwendet um die Repräsentativität solcher Messungen zu bestimmen. Die LES zeigen, dass ausreichende zeitliche Mittelung und ein adäquates Verhältnis von Pfadlänge zu Messhöhe nötig sind um sich dem horizontalen Mittel von C_T^2 in freier Konvektion zu nähern. Weiterhin wird die Anwendbarkeit von MOST und *local free convection* (LFC) Skalierung untersucht. Die LES Daten zeigen dabei, dass die MOST Beziehungen für C_T^2 universell zu sein scheinen und dass die bestimmten Ähnlichkeitsfunktionen im Bereich der in der Literatur vorgeschlagenen Funktionen aus Messdaten liegen. Es wird gezeigt, dass MOST nur dann für C_q^2 gültig ist, wenn das Einmischen von trockener Luft aus der freien Atmosphäre hinreichend klein ist. In diesem Falle sind die MOST Beziehungen für C_T^2 und C_q^2 identisch. Andernfalls kann Unähnlichkeit zwischen dem Transport von Wärme und Feuchte beobachtet werden, so dass MOST für C_q^2 nicht gültig ist. Im Bereich der LFC sollten die MOST Beziehungen universelle Konstanten ergeben. Hier deuten die LES Daten für C_T^2 auf einen Wert von 2.7 hin, was mit dem vorgeschlagenen Wert aus der Literatur übereinstimmt. Wie bei MOST ergibt sich für die LFC Skalierung, dass die Konstante für C_q^2 nicht mehr universell ist, wenn das Einmischen von trockener Luft die bodennahe Schicht beeinflusst.

Der Effekt von Bodenheterogenitäten auf die CBL und die Strukturparameter wird mittels einer irregulär verteilten Heterogenität untersucht, die während des LITFASS-2003 Experimentes beobachtet wurde. Sich entwickelnde Sekundärzirkulationen (SC) überlagern die Turbulenz und übernehmen teilweise den vertikalen Transport von Wärme und Feuchte. Die SC Muster variieren in Abhängigkeit vom mittleren Wind zwischen lokalen und rollenartigen Strukturen. Bei stärkerem Wind "sieht" die Strömung ein effektives Muster des bodennahen fühlbaren Wärmestroms, welches aus dem ursprünglichen Muster entsteht indem man es entlang des mittleren Windes mittelt. Dennoch zeigt sich, dass SC in der bodennahen Schicht, also dort wo Scintillometer verwendet werden, gewöhnlich sehr schwach sind.

Die LES Daten einer hochaufgelösten Fallstudie für LITFASS-2003 zeigen, dass Signale der Bodenheterogenität in der gesamten bodennahen Schicht sichtbar sind und damit über Höhenbereiche hinausgehen in denen Scintillometer verwendet werden. Horizontale Homogenität der Turbulenz, wie sie MOST voraussetzt, ist deshalb für den untersuchten Fall nicht gültig und eine Mischungshöhe für Strukturparameter unterhalb der Scintillometer, die während LITFASS-2003 verwendet wurden, existiert nicht. Gleichwohl wird gezeigt, dass MOST und LFC Skalierung für C_T^2 anwendbar sind und verlässliche Schätzwerte des bodennahen fühlbaren Wärmestroms liefern. Dieser, durch ein LAS bestimmte, Fluss ist jedoch nur repräsentativ für sein lokales Einzugsgebiet und nicht für ein Gebiet auf regionaler Skala der Größe von NWP Modellgittervolumen. Weiterhin wird das vorangegangene Ergebnis aus den Simulationen über homogenem Gelände, dass MOST nicht für C_q^2 gültig ist, in der Fallstudie bestätigt.

Schlagwörter: Atmosphärische Grenzschicht, Grobstruktursimulation, Strukturparameter

Contents

Abstract	I
Kurzzusammenfassung	II
1 Introduction	1
1.1 The atmospheric boundary layer	2
1.2 The effect of surface heterogeneity on the convective boundary layer	3
1.3 The LITFASS experiments	3
1.4 Current state of research	4
1.4.1 Structure parameters and the scintillometer technique	4
1.4.2 Monin-Obukhov similarity relationships for structure parameters	6
1.4.3 Effects of surface heterogeneity on the convective boundary layer and structure parameters	7
1.5 Aim and scope of this thesis	9
2 Methods	11
2.1 Large-eddy simulation model description	11
2.1.1 Governing equations	12
2.1.2 Subgrid-scale model	12
2.1.3 Discretization	13
2.1.4 Initial and boundary conditions	14
2.2 Analysis methods	16
2.2.1 Calculation of structure parameters from turbulence spectra	16
2.2.2 Calculation of structure parameters from wavelet analysis	17
2.2.3 Calculation of structure parameters from local dissipation rates	18
2.2.4 Determination of secondary circulations from large-eddy simulation data	18
3 Cumulative part of the thesis	19
3.1 Research article A: Derivation of structure parameters of temperature and humidity in the convective boundary layer from large-eddy simulations and implications for scintillometer observation	20
3.1.1 Declaration of my contribution	20
3.1.2 Published article	20
3.2 Research article B: Monin-Obukhov Similarity relationships for structure parameters of temperature and humidity in the unstable surface layer: results from high-resolution large-eddy simulations	51
3.2.1 Declaration of my contribution	51
3.2.2 Accepted manuscript	51
3.3 Research article C: Large-eddy simulations of surface heterogeneity effects on the convective boundary layer during the LITFASS-2003 Experiment	102
3.3.1 Declaration of my contribution	102
3.3.2 Published article	102

3.4	Research article D: The effect of surface heterogeneity on the structure parameters of temperature and humidity - An LES case study for the LITFASS-2003 experiment	131
3.4.1	Declaration of my contribution	131
3.4.2	Draft manuscript	131
4	Summary and outlook	159
	Acknowledgments	165
	Appendices	166
	A: NCL script spectral_method.ncl	167
	B: NCL script wavelet_method1.ncl	171
	C: NCL script wavelet_method2.ncl	176
	D: Extract from FORTRAN source code user_actions.f90	179
	E: FORTRAN source code avg.f90	181
	Bibliography	193
	Curriculum Vitae	200

1 Introduction

The turbulent exchange of momentum, energy and water vapor in the atmospheric boundary layer (ABL) is an important element of the land-surface-atmosphere interaction (Beyrich et al., 2012). The ABL is the lower part of the troposphere that is directly influenced by the Earth's surface. Surface effects include frictional drag, heating, cooling, evaporation and transpiration. These effects result in significant fluxes of sensible and latent heat as well as momentum that are usually of turbulent nature (Stull, 1988; Garratt, 1992) and that have large impact on the processes in the ABL such as ABL growth, warming, moistening, cloud formation and subsequently precipitation patterns (Beyrich et al., 2012).

Current weather prediction and climate models are not able to explicitly resolve turbulence. These models operate at horizontal grid resolutions in the order of 1 – 100 km (Beyrich et al., 2012), but such coarse resolutions do not allow for resolving the energy-containing turbulent eddies whose size range from kilometer scale down to the meter and millimeter scale. Hence, the turbulent processes must be parametrized in these models. Originally, these parameterizations were derived from measurements over locally homogeneous terrain, e.g. during the Kansas Experiment (grassland prairie, see Businger et al., 1971). In reality, however, the Earth's surface is often very heterogeneous and different heterogeneities of kilometer to meter scale superimpose each other. A grid cell of a few kilometers can thus contain different surface patches, including forest, lakes, farmland or settlements. The surface fluxes of sensible and latent heat over different land-use types may differ significantly and induce effects that are not captured by current turbulence parameterizations.

Measuring the area-averaged turbulent fluxes of sensible and latent heat is thus not only required for the validation of both numerical weather prediction and climate model results, and of algorithms based on satellite data for estimating the fluxes, but it is also essential for a better understanding of the effects of surface heterogeneity on the ABL. A technique that might provide reliable estimates of the area-averaged fluxes of sensible and latent heat is scintillometry. Scintillometers measure the intensity fluctuations of electromagnetic radiation in the lower atmosphere (see Section 1.4.1). A measure for these intensity fluctuations in the atmosphere are the turbulent structure parameters of temperature C_T^2 and humidity C_q^2 that can be obtained from scintillometer data. Monin-Obukhov similarity theory (Obukhov, 1946) provides a framework that relates C_T^2 and C_q^2 to the surface fluxes of sensible and latent heat, respectively (see Section 1.4.2). However, the validation of scintillometer observations (and the subsequent estimates of the surface fluxes), particularly over complex heterogeneous terrain, is challenging because no independent measurements of the path-averaged fluxes can be obtained. Furthermore, only point measurements using eddy covariance technique can be used for comparison that can be only considered representative under horizontally homogeneous conditions (Andreas, 1991). It was also previously shown that the turbulence intensity and hence the structure parameters can vary in space in time (e.g. Cheinet and Siebesma, 2009). Moreover, the turbulence structure in the ABL can be modified by heterogeneity-induced secondary circulations that might also affect scintillometer and other micro-meteorological measurements (see Section 1.4.3).

In the present study turbulence-resolving large-eddy simulation (LES) technique is used to treat some of the open problems in the field of scintillometry and the general effect of surface

heterogeneity on the ABL. The advantage of the LES is that heterogeneous surface fluxes of sensible and latent heat (as well as roughness) can be explicitly prescribed in the model. Furthermore, the four-dimensional character of the LES data allows for investigating several aspects of the ABL that would not be feasible with in situ measurements.

Chapter 1 is organized as follows: Section 1.1 deals with the general structure of the ABL, whereas possible effects of surface heterogeneity on the ABL are discussed in Section 1.2. Within the scope of the present thesis, data from the LITFASS-2003 experiment was used. A short description of the experiment is thus given in Section 1.3. The current state of research is discussed in Section 1.4, followed by details on the aim and scope of this thesis (Section 1.5).

1.1 The atmospheric boundary layer

The ABL structure can be divided into three different idealized flow regimes: the convective boundary layer (CBL), the neutral or shear-driven boundary layer, and the stable boundary layer. The latter develops when the surface is cooler than the air, e.g. at night over land, where it is known as nocturnal boundary layer (Stull, 1988). It is characterized by damping of turbulence by stability and the only source of production being wind shear. Neutral boundary layers are observed when the surface heating is negligible, e.g. in overcast conditions and under high background winds (Garratt, 1992). Under such conditions turbulence is generated by wind shear. Over land CBLs develop when solar radiation is heating the surface and buoyancy becomes a relevant mechanism, triggering convection. Such CBLs are the subject of this thesis.

During daytime the (cloudless) CBL can be divided into idealized vertical layers that occur over land surfaces in high pressure regions: *microlayer*, *surface layer*, *mixed layer* and *entrainment layer*. In the lowest few centimeters of the CBL, the microlayer, molecular transport dominates and turbulence is absent (Stull, 1988). Turbulence production by wind-shear and buoyancy mainly happens in the lowest 10 % of the CBL, where temperature and velocity gradients are large. In this surface layer the flow “feels” the influence of the surface the most and organized turbulent structures (such as cellular patterns) can develop. Here one can also usually observe unstable stratification and a logarithmic profile of the horizontal wind velocity. The mixed layer above is characterized by rising thermals that are organized in narrow updrafts (warm) and broader weaker downdrafts (cold). This *primary circulation* is responsible for mixing heat, moisture and momentum vertically. In the presence of background winds, the thermals can be stretched and skewed so that roll-like patterns develop. Because this process is very effective, meteorological variables tend to be vertically well-mixed and stratification is near-neutral. The mixed layer is limited in the vertical direction by a capping temperature inversion and the stably-stratified free atmosphere aloft. The capping inversion marks the *entrainment layer* (also often referred to as entrainment zone). Entrainment is the turbulent mixing between relatively cold air from the mixed layer and warmer air of the free atmosphere aloft. Entrainment processes can be triggered by rising thermals that penetrate into the capping inversion and wind shear at the interface between mixed layer and free atmosphere.

In the course of the day the CBL depth z_i increases mainly by *encroachment*, which is the warming of the mixed layer due to upward directed surface heat flux and thus transport of sensible heat, but also by entrainment of warm air from the free atmosphere (downward directed heat flux). Consequently the CBL warms up in the course of the day. It is commonly found that about 80 % of the boundary-layer growth can be explained by encroachment, whereas entrainment makes up the remaining 20 % (Stull, 1988). In the late afternoon, when solar heating of the surface stops and the surface fluxes vanish, the convective forcing for the mixed-layer turbulence ceases. A residual slightly stable layer remains that can persist throughout the night. During night outgoing long-wave

radiation cools the surface, and subsequently the near-surface air. Consequently, a near-surface temperature inversion can often develop during nighttime and the boundary-layer regime becomes stable.

1.2 The effect of surface heterogeneity on the convective boundary layer

Land-surface heterogeneities (topographical and land use) are widely spread over the Earth's surface. Differences in land use represent heterogeneities with a high variability in vegetation, soil texture and wetness. They lead to spatial differences in surface properties such as temperature, humidity and roughness and thus to different surface fluxes of sensible and latent heat as well as momentum. These fluxes can trigger local anisotropy of turbulence and mesoscale secondary circulations (that are generally not resolved by weather prediction models). Many studies have shown that secondary circulations can also develop in the CBL over smaller heterogeneities (see Section 1.4.3). The strength and type of such circulations strongly depends on the synoptic conditions (such as background wind, CBL depth, incoming radiation and so forth) and the scale of the heterogeneity.

In the surface layer, effects of surface heterogeneity can be more prominent than in the mixed layer above because the turbulent eddies are small and depend on the local surface properties. Realistic land-use heterogeneities typically consist of water, forest and different agricultural fields. Moreover, urban or other built-up areas can affect the surface-layer flow. Patterns of heterogeneous temperature, humidity and roughness might thus be seen at least in the lowest decameters of the atmosphere. The concept of the *blending height* suggests that at a specific height above ground, surface heterogeneity is no longer visible (Mahrt, 2000). This is important for micro-meteorological measurements, such as scintillometer observations, as will be discussed in the following sections.

1.3 The LITFASS experiments

Within the scope of the present thesis, simulations of the CBL over an irregular surface heterogeneity were performed. The setup for these simulations was based on measurement data observed during the LITFASS-2003¹ experiment within the framework of the EVA-GRIPS² project. EVA-GRIPS was launched in 2002 to investigate the influence of surface heterogeneities on the ABL. Several groups in the area of experimental and numerical meteorology participated to benefit from synergy effects of this large-scale project. In 2003, the LITFASS-2003 experiment was taking place in the surrounding of the meteorological super-site of the German Weather Service (DWD) in Lindenberg in the southeast of Berlin (Germany).

The experiment was conducted from 05/19/2003 to 06/17/2003 in a 20 km × 20 km area in the surroundings of the Lindenberg Meteorological Observatory (MOL) of DWD. The area was dominated by forest and water areas as well as several agricultural patches (43% forest, 32% agriculture, 13% grassland, 7% water and 5% settlements). Orography was rather flat, varying between 40 and 160 m above mean sea level, thus shadowing effects could be neglected. The instrumentation consisted of several energy balance stations and soil sensors placed over each land-use type (except settlements). For the forest and water patches, permanently installed systems by DWD were used. Radiosondes were released daily in Lindenberg at 5, 11, 17 and 23 UTC. For

¹Lindenberg Inhomogeneous Terrain Fluxes between Atmosphere and Surface: a long-term Study

²Regional Evaporation at Grid/Pixel Scale over Heterogeneous Land Surfaces

selected days, the soundings were complemented by releases at 8 UTC and 14 UTC. Furthermore, a SODAR³/RASS⁴, a lower atmospheric profiler and a tropospheric wind profiler provided vertical profiles of temperature and wind. A microwave radiometer profiler measured temperature and water vapor content. Additionally, LIDAR⁵ systems were used. The measurements were complemented by scintillometer observations and measurements from the helicopter-borne probe Helipod (Bange et al., 2006). For a complete and more detailed description of the LITFASS-2003 experiment, see Beyrich and Mengelkamp (2006) and Beyrich et al. (2006a).

A follow-up experiment was launched in 2009: the LITFASS-2009⁶ experiment (Beyrich et al., 2012). The experiment was designed to validate scintillometer measurements and to answer some of the open questions in scintillometry. To achieve this, the experiment combined tower-based turbulence measurements, field-scale laser scintillometers, large-aperture scintillometers (LAS, sensitive to temperature fluctuations, designed for long-range measurements), microwave scintillometers (sensitive to humidity fluctuations) and airborne turbulence measurements using small unmanned aircraft.

Unfortunately, the synoptic conditions during the LITFASS-2009 experiment did not allow for deriving a data set that was required to carry out comparative LES as originally intended within the scope of this thesis. All LES with heterogeneous surface forcing were thus based on the well-documented LITFASS-2003 data. However, as scintillometer observations were made during LITFASS-2003, particular attention will be given to the research questions formulated in Beyrich et al. (2012) within the framework of this thesis (see Section 1.5).

1.4 Current state of research

1.4.1 Structure parameters and the scintillometer technique

Several measuring instruments have been used to observe the turbulence structure of the ABL, such as RADARs⁷, SODARs, lifted kites and aircraft (Petenko and Shurygin, 1999; Muschinski, 2004; Muschinski et al., 2004; Martin et al., 2010, among others). Recently, scintillometers have been increasingly employed to measure the optical interference along a horizontal path (e.g. Ochs and Wang, 1978; Kohsiek, 1982; Beyrich et al., 2002; among others). Scintillometers are operated in the atmospheric surface layer and consist of a wave transmitter and a receiver at both ends of a path, which can cover several kilometers. The transmitted waves that are propagating through the atmosphere are affected by turbulent density fluctuations, so-called *scintillations* (Peltier and Wyngaard, 1995). This scattering of the transmitted radiation is related to spatial fluctuations in the refractive index of air n . Tatarskii (1961) described this scattering theoretically using the refractive index structure function

$$D_n(\mathbf{x}, \mathbf{r}, t) \equiv \{ [n(\mathbf{x}, t) - n(\mathbf{x} + \mathbf{r}, t)]^2 \}, \quad (1.1)$$

where \mathbf{x} and $\mathbf{x} + \mathbf{r}$ are two points in the three-dimensional space with displacement $r = |\mathbf{r}|$ at time t . The curly brackets denote the ensemble average. Both n and D_n are dimensionless. If the displacement is in the inertial subrange of turbulence, the structure function can be expressed as

$$D_n = C_n^2 r^{2/3}, \quad (1.2)$$

³Sonic Detection And Ranging

⁴Radio Acoustic Sounding System

⁵Light Detection And Ranging

⁶Lindenberg-To-Falkenberg Aircraft Scintillometer Study experiment

⁷Radio Detection And Ranging

where C_n^2 (units: $\text{m}^{-2/3}$) is called the *refractive index structure parameter*. Under suitable conditions, scintillometer measurements may be traced back to the path mean C_n^2 . Hill (1978) and Andreas (1988), among others, showed that C_n^2 is determined by the structure parameters of temperature, humidity and a joint structure parameter C_{Tq} , because variations in n are dominantly caused by fluctuations of temperature T and specific humidity q . Hill (1978) derived an expression for writing C_n^2 in terms of the structure parameters of meteorological variables, which reads

$$C_n^2 = \frac{A_T^2}{\{T\}^2} C_T^2 + 2 \frac{A_T}{\{T\}} \frac{A_q}{\{q\}} C_{Tq} + \frac{A_q^2}{\{q\}^2} C_q^2. \quad (1.3)$$

The dimensionless coefficients A_T and A_q are functions of the wavelength of the transmitted beam by the scintillometer, atmospheric pressure, temperature and humidity (e.g. Hill et al., 1980).

Scintillometer observations have been frequently used to obtain horizontal path-averages of C_n^2 , and to deduce C_T^2 and C_q^2 from it, over typical distances of 5 – 10 km (e.g. Kohsiek et al., 2002; Meijninger et al., 2002a,b, 2006; Evans et al., 2012). So far, scintillometers are the only operational instruments that allow for estimating C_T^2 and C_q^2 at a spatial scale which might be representative for an area of several square kilometers. Surface heterogeneity such as soil moisture, vegetation and elevation, however, might affect the scintillometer measurements significantly. Footprint models for the scintillometer path can provide an estimate of its (heterogeneous) footprint. Nevertheless, it is difficult to validate these observations, particularly because usually only point measurements by sonic anemometer-thermometer/hygrometer can be used for validation.

Several studies have revealed that the mean vertical profiles of C_T^2 and C_q^2 in the CBL strongly depend on the entrainment of dry warm air at the top of the mixed layer. (e.g. Wyngaard and LeMone, 1980; Druilhet et al., 1983; Fairall, 1984, 1987, 1991). In particular, it is found that C_q^2 is often dominated by entrained air from the free atmosphere. Wyngaard and LeMone (1980) showed that deviations from the mixing-layer scaling laws are caused by entrainment effects that lead to a peak of the structure parameters near the capping inversion in free convection. Fairall (1984) studied the effect of wind shear on this peak and found that the wind shear enhancement of entrainment leads to an increase of the peak values. The data of Druilhet et al. (1983) showed two peaks for C_T^2 , one near the surface and a secondary peak in the entrainment layer. For C_q^2 the entrainment peak was dominant, whereas the near-surface peak was only weak. They concluded that if the entrainment characterizes the changes in humidity in the CBL, a new mixing-layer humidity scale should be defined that incorporates the entrainment humidity flux instead of the surface flux. Based on these findings, Fairall (1987) and Fairall (1991) used LES data and the top-down (entrainment) and bottom-up (surface fluxes) approach in order to derive semi-empirical profiles of C_T^2 and C_q^2 for the entire CBL. These profiles take into account the entrainment flux ratio and z_i and include also an extension for the surface layer, as proposed by Wyngaard et al. (1971). However, these semi-empirical profiles all assume that the surface fluxes are dominantly determining the surface layer part of the structure parameter profiles. Moreover, these profiles can be only used when information about the inversion layer is available. This is often challenging and hence Monin-Obukhov Similarity Theory (MOST) is usually applied instead to relate scintillometer observations to the surface fluxes (see Section 1.4.2).

There are few other studies that investigated structure parameters using LES. Peltier and Wyngaard (1995) showed that LES can be employed to study the vertical distribution of the structure parameters in the CBL. They derived vertical profiles of C_T^2 , C_q^2 and C_{Tq} and showed that their LES data agree well with experimental results. Cheinet and Siebesma (2009) investigated the spatial variability of C_T^2 in the dry CBL with LES and showed the relation of the spatial variability of C_T^2 to the presence of ascending plumes. These updraft structures show a hexagonal cellular pattern near the surface, where the horizontal size of the cells scales with z_i (Stull, 1988). The vertical profiles of C_T^2 showed the decrease with height proposed by Kaimal et al. (1976), but Cheinet and Siebesma

(2009) observed a gap of a factor two in the magnitude. Furthermore they found a bimodal distribution of C_T^2 near the surface, which was previously found in the SODAR measurements of Pertenko and Shurygin (1999). Cheinet and Cumin (2011) supplemented the previous LES studies by studying the variability of C_q^2 . They showed that the spatial distribution of C_q^2 in the mixed layer is dominated by air that is entrained at the top of the mixed layer, in agreement with previous studies (e.g. Druilhet et al., 1983; Fairall, 1987, see above). Cheinet and Siebesma (2007) used a wave propagation modeling framework to derive the scintillation rate and coherence length from virtual path measurements in their LES. They found that the variability of their virtual measurements of C_n^2 increased with height, while the path mean decreased. They stated that for their virtual paths (2 km length) it was not possible to provide representative estimates of C_n^2 with time-averaging of 500 s. However, the coarse spatial resolution of 39 m in the horizontal and 32 m in the vertical direction did not allow to study the wave propagation at realistic scintillometer heights and no in situ scintillometer or aircraft measurements were used for comparison. Recently, Wilson and Fedorovich (2012) used LES to evaluate C_n^2 directly by calculating the refractive index structure functions. They calculated the refractive index at each grid point and used Eq. 1.2, but they also employed Eq. 1.3 and calculated C_T^2 , C_q^2 and C_{Tq} from the fields of temperature and humidity. They could show that (for visible radiation) temperature is dominantly contributing to C_n^2 in the lower half of the CBL, but that C_{Tq} becomes important near the entrainment zone.

Despite the fact that different methods have been proposed in literature to derive the structure parameters from LES data (Peltier and Wyngaard, 1995; Moene and Gioli, 2008; Cheinet and Siebesma, 2009), a direct comparison or an evaluation of these methods against in situ measurement data, particularly LAS observations, is still lacking. The methods described by Cheinet and Siebesma (2009) and Moene and Gioli (2008) might be suitable for estimating the representativeness of scintillometer measurements, as both provide the spatial and temporal variability of C_T^2 and C_q^2 . For this purpose, however, the LES must be designed in such a way that the turbulence in the surface layer, where scintillometers are operated, can be resolved. The previous LES studies of Peltier and Wyngaard (1995), Cheinet and Siebesma (2007), Cheinet and Siebesma (2009) and Cheinet and Cumin (2011) did not provide sufficiently high grid resolutions in order to achieve this.

1.4.2 Monin-Obukhov similarity relationships for structure parameters

MOST provides a framework that relates the estimates of C_T^2 and C_q^2 to the surface fluxes of sensible and latent heat, respectively. In this way, scintillometers offer a technique for estimating the surface fluxes at spatial scales that might be representative for an area of several square kilometers and thus in the order of current numerical weather prediction models. Nevertheless, a validation of such scintillometer observations is challenging. A first attempt was made by using low-level aircraft flights along a scintillometer path during the LITFASS-2009 experiment (Beyrich et al., 2012; van den Kroonenberg et al., 2012).

In order to estimate the surface fluxes from measurements of C_T^2 and C_q^2 , universal similarity functions are needed that are not given by theory and must be determined experimentally. Several similarity functions have been proposed in the literature (Wesely, 1976; Wyngaard et al., 1971; Andreas, 1988; Hill et al., 1992; Thiermann and Grassl, 1992; De Bruin et al., 1993; Li et al., 2012), but there is no consensus on an explicit form so far. One reason might be that there are differences in the definition of the relevant scaling parameters, namely the Obukhov length L . While some studies take into account the effect of moisture on the buoyancy flux and thus L , other rather use the Obukhov length for dry air (e.g. Wyngaard et al., 1971; Wesely, 1976; Thiermann and Grassl, 1992). It is also usually assumed that the similarity functions are identical for temperature and humidity. Li et al. (2012) discussed possible reasons for dissimilarity between the turbulent transport of heat and

moisture that can lead to differences in the similarity relationships of C_T^2 and C_q^2 . They found such dissimilarity in their data under weakly unstable conditions and ascribed this to non-local effects like non-stationarity of the flow, advection and entrainment.

In the free convection limit, the MOST relationships become more simple and yield universal constants. There is consensus on the constant for C_T^2 to be around 2.7, but it is still an open question whether the constant for C_q^2 is equal to that for C_T^2 . Theoretically, local free convection (LFC) can only be considered in the absence of a mean wind, but in practice it is often applied also in case of weak winds (e.g. De Bruin et al., 1995; Kohsiek, 1982; Kohsiek et al., 2002).

While most previous studies used experimental data, there are only few studies that investigated the surface layer similarity by means of LES. Mason and Thomson (2002) showed that Smagorinski-style subgrid-scale (SGS) closures that are commonly used in LES models fail to predict MOST relationships in the near-surface layer correctly (see also Section 2.1.2). They found a systematic peak (“overshoot”) in the dimensionless wind shear. Khanna and Brasseur (1997) used LES to study the effect of grid resolution and the used SGS model on the MOST functions for mean fields, variances, budgets of temperature and turbulent kinetic energy under near-neutral to moderately convective conditions. In order to resolve the surface layer they nested a high-resolution mesh in the lower part of their model domain. They stated that the lowest few grid levels are always affected by the SGS model in such a way that the turbulent flow cannot be resolved, which is a known feature of LES models. Furthermore they found an overshoot in the normalized vertical profiles for mean shear and mean temperature gradient. With increasing grid resolution this overshoot was moved to lower levels, but it did not vanish. Khanna and Brasseur (1997) showed that this overshoot can be ascribed to the SGS model. Recently, Brasseur and Wei (2010) focused on the mentioned overshoot in the mean gradient of the dimensionless horizontal velocity and developed criteria to design LES that reduce this overshoot. However, they also stated that MOST scaling was not reached in the first couple of grid levels. Khanna and Brasseur (1997) also found that temperature variance satisfied LFC scaling even for conditions with considerable wind shear. Moreover, they suggested that not only the common parameter z/L (where z is the height above ground), but also z_i/L might be a proper scaling parameter in the surface layer. The latter was supported by field measurement data by Johansson et al. (2001), who stated that the normalized temperature variance might have a slight dependence on z_i/L (see also discussion in Johansson et al., 2002).

Peltier and Wyngaard (1995) derived C_T^2 and C_q^2 from LES data of a CBL and derived LFC scaling constants. They particularly found that entrainment effects decrease C_T^2 and increase C_q^2 in the lower mixed layer. This led to a higher LFC constant for humidity than for temperature. Generally, the derived constants from the LES were smaller than the suggestions from measurement data.

To the author’s knowledge, the MOST and LFC scaling relationships for structure parameters have not been studied by means of LES so far. First LFC predictions have been made by Peltier and Wyngaard (1995), but they could not resolve the surface layer sufficiently.

1.4.3 Effects of surface heterogeneity on the convective boundary layer and structure parameters

In operational weather forecast models, the orography of the land surface is already considered, being a crucial factor for the quality of the forecast. Despite the known effects of large-scale heterogeneities such as land and sea (e.g. the land-sea breeze), it is still uncertain whether the heterogeneous land use on the mesoscale and microscale produces significant effects on the ABL and on the local weather.

In several experimental studies, e.g. LITFASS-98 (Beyrich et al. 2002a, 2002b), LITFASS-2003 (Beyrich and Mengelkamp, 2006), IHOP-2002 (Weckwerth et al., 2004) and SMACEX (Kustas et al., 2005), the CBL characteristics over a heterogeneous land surface have been investigated. However, a heterogeneous effect could hardly be captured.

Over the past two decades, LES have been used increasingly for the investigation of the interaction between surface heterogeneities and the CBL by resolving the bulk of the energy-containing eddies (e.g. Hechtel et al. 1990; Hadfield et al. 1991, 1992; Shen and Leclerc 1995; Avissar and Schmidt 1998; Gopalakrishnan and Avissar 2000; Raasch and Harbusch 2001; Letzel and Raasch 2003; Patton et al. 2005; Courault et al. 2007; Huang and Margulis 2009).

The earlier studies investigated small-scale heterogeneities in the order of a few hundreds of meters with no background wind (Hechtel et al. 1990; Hadfield et al. 1991) or with background wind (Hadfield et al., 1992), but found no significant effect on the boundary-layer structure. The later studies of Shen and Leclerc (1995) as well as Raasch and Harbusch (2001) used checkerboard-like two-dimensional heterogeneities and reported that the surface heterogeneities in fact must be at least of the size of z_i to influence the boundary-layer characteristics. The simulations of sinusoidal stripe-like one-dimensional heterogeneity by Avissar and Schmidt (1998) showed the development of secondary circulations, but that a background wind speed of 5 m s^{-1} suffices to eliminate the effect of the surface heterogeneity. Raasch and Harbusch (2001) found the secondary circulations to persist even for background wind speeds up to 7.5 m s^{-1} depending on the mean flow orientation relative to their checkerboard inhomogeneity. Letzel and Raasch (2003) observed temporal oscillations in the turbulent kinetic energy (TKE) for larger heterogeneity scales that led to an oscillation of the secondary circulation magnitude. Kang (2009) also investigated these temporal oscillations and suggested that the onset of the oscillations might be the start of a break-up process of fluctuations at the scale of the mesoscale heterogeneity to small-scale fluctuations. Gopalakrishnan and Avissar (2000) showed that surface heterogeneities with a characteristic length scale of 5 km decrease the vertical mixing of particles, but increase the horizontal mixing.

Patton et al. (2005) used one-dimensional soil-moisture heterogeneities in their LES coupled to a soil-vegetation-atmosphere-transfer (SVAT) model, which incorporates the feedback between secondary circulations and surface fluxes, while most other studies used prescribed surface fluxes. They reported a dependency of the secondary circulations on the scale of the heterogeneity (wavelength λ), z_i and the initial state of moisture. Particularly, they found that the strongest CBL response to the heterogeneity occurs for λ/z_i between 4 and 9, owing to the interaction of the secondary circulations and the induced surface fluxes in the SVAT model. Furthermore, Patton et al. (2005) showed that the secondary circulations contribute up to 70 % (height-dependent) to vertical fluxes. The coupled LES-SVAT study of Courault et al. (2007) investigated the feedback of surface heat fluxes to secondary circulations, and suggested that small-scale heterogeneities (here $\lambda = 5 \text{ km}$) are able to induce secondary circulations that lead to the horizontal transport of moisture from wet to dry areas. Courault et al. (2007) reported a decrease in the surface sensible heat flux over the dry patch, leading to a modification of the area-averaged surface fluxes. Liu et al. (2011) used checkerboard surface heat-flux patterns in their LES and showed that their heterogeneity-induced circulations break-up after a certain time, when λ/z_i is small enough due to the increasing z_i . This can be traced back to the results of Shen and Leclerc (1995) and Raasch and Harbusch (2001). Liu et al. (2011) also reported no significant impact on the profiles of temperature and the sensible heat flux. Kang and Davis (2008) used a spatial filtering method and showed that the vertical mesoscale transport in the presence of large-scale heterogeneities ($\lambda = 16 \text{ km}$ and $\lambda = 32 \text{ km}$) is negligible compared to the turbulent transport.

Until now these dependencies of secondary circulations on the background flow as well as on the heterogeneity scale have been investigated by means of idealized one- or two-dimensional

periodic heterogeneities only. The question whether the findings mentioned above are also valid over complex terrain, where heterogeneities of a whole range of scales are superimposed upon each other, or whether secondary circulations develop at all, has not been studied to date. Furthermore the question arises, how secondary circulations vary when simulating a full diurnal cycle, in which the surface forcing as well as z_i changes in time.

Some studies reported modifications of the CBL depth in such a way that the mixing layer is deeper over warmer surface patches and thinner over colder patches (e.g. van Heerwaarden and Vilà-Guerau de Arellano, 2008; Fesquet et al. 2009). The reason for the spatial variation of z_i in the study of van Heerwaarden and Vilà-Guerau de Arellano (2008) was associated with rising secondary circulation updrafts that increase the entrainment above the warm patches. Furthermore they reported changes in the entrainment rate, but attributed this finding to differences in their model spin-up or as an effect of horizontal averaging (Lilly, 2002). Moreover, van Heerwaarden and Vilà-Guerau de Arellano (2008) found the specific humidity variance in the entrainment zone to be larger than under homogeneous conditions and thus suggested that cloud formation might be enhanced over heterogeneous surfaces.

Contrary to most previous studies, Huang and Margulis (2009) recently used observed surface fluxes from SMACEX in their LES to investigate the CBL development over irregular surface heterogeneities. They found increasing entrainment rates for increasing surface heterogeneity scales. Nevertheless their results displayed untypical large entrainment fluxes, whose origin was not discussed. The question of whether area-averaged vertical fluxes are modified due to the effects of observed heterogeneous surfaces has thus not been sufficiently clarified so far.

In order to derive representative structure parameters from LAS observations it is required that the beam height is above a blending height for structure parameters, above which signals of a present surface heterogeneity are absent (Wieringa, 1976; Mahrt, 2000; Meijninger et al., 2002b). Furthermore, MOST requires horizontal isotropy of turbulence, which is questionable in the presence of horizontally heterogeneous surface fluxes and roughness. So far it has not been possible to show even the existence of a blending height and surface heterogeneity thus might affect scintillometer measurements, which has not been justified so far. Sühring and Raasch (2013) studied the CBL over the LITFASS area by means of LES and showed that no blending height exists for turbulent fluxes. Recently, van den Kroonenberg et al. (2012) employed small unmanned aircraft to study the variability of C_T^2 along an LAS path during LITFASS-2009. They found a considerable variability of C_T^2 along the path and ascribed this to both temporal variations as well as the underlying surface heterogeneity. However, as Sühring and Raasch (2013) pointed out, sufficient independent flight measurements are required to obtain a significant estimate of a heterogeneity-induced effect. This appears to be hardly feasible with in situ airborne measurements.

1.5 Aim and scope of this thesis

Different methods have been proposed in literature to derive the structure parameters from LES data (Peltier and Wyngaard, 1995; Moene and Gioli, 2008; Cheinet and Siebesma, 2009). It was thus plausible to perform first LES of the homogeneously-heated CBL in order to compare and evaluate these methods. The super-site at Cabauw (The Netherlands) provides a flat and fairly homogenous area that mainly consists of grassland. The data from the RECAB-2002⁸ measurement campaign at Cabauw provide an ideal data set for validation of the LES with in situ LAS and aircraft measurements of the structure parameters in the CBL. Hence, high-resolution (grid spacing

⁸Regional assessment and modeling of the CARbon Balance in Europe, European Commission research project EVK2-CT-1999-00034

of 2 – 4 m) LES setups for comparison with the Cabauw data were developed. The spatial and temporal variability of the structure parameters are studied based on this Cabauw setup (research article A, see Section 3.1).

A prerequisite for the application of MOST in order to derive the surface fluxes of sensible and latent heat from scintillometer observations is horizontal homogeneity of the flow. The MOST relationships for structure parameters in the surface layer were thus calculated and studied based on the Cabauw setup for different atmospheric stability, ranging from free convective to nearly-neutral conditions (research article B, see Section 3.2).

In order to capture the effect of surface heterogeneity on the CBL, four selected days of the LITFASS-2003 experiment were simulated with a horizontal analysis domain of 20 km \times 20 km and a grid resolution of 50 – 100 m (research article C, see Section 3.3). In order to investigate the effect of surface heterogeneity on scintillometer observations (blending height, similarity functions, see above), it was required to use a grid resolution that allows for explicitly resolving the turbulence in the lowest few decameters of the CBL (the surface layer). Consequently, due to limited computational resources, the model domain had to be shrunk to 5 km \times 5 km, and a case study using a single day of the LITFASS-2003 experiment and a grid resolution of < 4 m was conducted (research article D, see Section 3.4).

The following open issues (see also Beyrich et al., 2012) are addressed within the research articles in the framework of this thesis:

- Structure parameters in the homogeneously-heated CBL
 - What is the variability of structure parameters along a scintillometer path?
 - Under which conditions can LAS measurements give representative estimates of the structure parameters for an area of several square kilometers?
 - Do universal similarity functions exist, linking the area-averaged structure parameters to the surface fluxes of sensible and latent heat over homogeneous terrain? Are they the same for temperature and humidity?
- The effect of surface heterogeneity on the CBL and scintillometer observations
 - What is the effect of surface heterogeneity on the CBL? Do secondary circulations develop over complex terrain and do they affect turbulent fluxes and micro-meteorological measurements?
 - Does a blending height exist for the structure parameters, above which the signal of surface heterogeneity vanishes? Is it equal for C_T^2 and C_q^2 ?
 - Do area-averaged similarity functions exist for heterogeneous terrain, linking area-averaged fluxes to area-averaged structure parameters? Do they differ from the similarity functions for homogeneous conditions?

The present thesis is organized as follows: Chapter 2 describes the used LES model and general analysis methods. Results are presented within the cumulative part of this thesis in Chapter 3, which consists of four research articles. A summary is given in Chapter 4.

2 Methods

2.1 Large-eddy simulation model description

Three basic types of models are commonly employed for simulating the ABL. The most intuitive way to study turbulence is to solve the Navier-Stokes equations directly (direct numerical simulation, DNS). Such models are very precise and only numerical errors due to discretization in space and time have to be considered. DNS models resolve all scales of turbulence, from the largest eddies of size of z_i with a lifetime of several minutes down to the Kolmogorov dissipation length (millimeter scales), and a lifetime of a split second. This, in turn, restricts the choice of the model resolution in both space and time. On the one hand, the grid spacing must be small enough to capture the smallest eddies. Consequently, a sufficiently small time step is required. On the other hand, the model domain has to be large enough to cover even largest eddies that can be of size of kilometers. A number of grid points in the order of 10^{18} would thus be required to use DNS for the simulation of realistic boundary layers, which is far beyond the capability of today's supercomputers. As a consequence of this, DNS is a pure research tool and usually applied for unrealistic low Reynolds numbers¹ and maximum domain sizes in the order of $(1 \text{ m})^3$.

Another widely spread model type is based on the Reynolds-averaged Navier-Stokes (RANS) equations. In so-called RANS models the full spectrum of turbulence is parametrized. RANS models are computational cost-efficient and find their application e.g. in mesoscale models. Their disadvantage, however, is that the quality of the model output depends on the parametrization of turbulent motions. Furthermore, only mean quantities can be predicted and the turbulent field is not simulated explicitly. RANS models are thus inappropriate for studying the boundary-layer turbulence.

LES has been increasingly used over the last decades as a compromise between the two extremes (RANS and DNS) for simulating the ABL. Unlike RANS models, the (energy containing) large eddies are directly resolved, whereas the smallest eddies (isotropic and most computational expensive due to the small time step, see above) are parametrized in a SGS model. In this way flows with large Reynolds numbers can be simulated at relative low grid resolutions in the order of meters. The idea of LES goes back to Smagorinsky (1963) and first key features of LES have been studied by Deardorff (1970).

In the present study, the parallelized LES model PALM was used for simulating the turbulent flow in the CBL (Raasch and Schröter, 2001; Riechelmann et al., 2012). PALM is the parallelized version of an LES model which has been used at the Institute of Meteorology and Climatology (IMUK) at Leibniz Universität Hannover (Germany) (Raasch and Etling, 1991, 1998). It has been continuously developed by the PALM work group at IMUK since 1989. In the following the most relevant parts of the model that play a major role for the present study will be discussed. For a more detailed description of PALM see Raasch and Etling (1998) and Raasch and Schröter (2001). Furthermore, PALM offers some optional features, e.g. an option for using surface-mounted topography (e.g. Letzel et al., 2008), an ocean version with an additional prognostic equation for the state of sea-water (see Noh et al., 2011), a cloud physics parametrization and an embedded

¹For a definition of the Reynolds number see relevant literature, e.g. Stull (1988).

Lagrangian particle model (see Steinfeld et al., 2008; Riechelmann et al., 2012). The following formulation of the model is thus valid for the present study, but might differ for other setups, e.g. when condensation is allowed (cloud physics module).

2.1.1 Governing equations

PALM is based on the non-hydrostatic, filtered, incompressible Navier-Stokes equations in Boussinesq-approximated form. The equations for the conversation of mass, energy and moisture that are filtered over the grid size read (Riechelmann et al., 2012):

$$\frac{\partial u_i}{\partial t} + u_j \frac{\partial u_i}{\partial x_j} = -\varepsilon_{ijk} f_j u_k + \varepsilon_{i3k} f_3 u_{g,k} - \frac{1}{\rho_0} \frac{\partial p^*}{\partial x_i} + g \frac{\theta_v - \langle \theta_v \rangle}{\langle \theta_v \rangle} \delta_{i3} - \frac{\partial}{\partial x_j} \left(\overline{u_i'' u_j''} \right), \quad (2.1)$$

$$\frac{\partial u_j}{\partial x_j} = 0, \quad (2.2)$$

$$\frac{\partial \theta}{\partial t} + u_j \frac{\partial \theta}{\partial x_j} = -\frac{\partial}{\partial x_j} \left(\overline{u_j'' \theta''} \right), \quad (2.3)$$

$$\frac{\partial q}{\partial t} + u_j \frac{\partial q}{\partial x_j} = -\frac{\partial}{\partial x_j} \left(\overline{u_j'' q''} \right). \quad (2.4)$$

Here, $i, j, k = 1, 2, 3$, u_i are the velocity components (u, v, w) on a Cartesian grid with location x_i ($x_1 = x, x_2 = y, x_3 = z$), t is time, f is the Coriolis parameter, u_g is the geostrophic wind speed, ρ_0 is the density of dry air, p^* is the so-called perturbation pressure and g is the gravitational acceleration. Angular brackets denote a horizontal average. A subscript 0 indicates a value at the surface. $\theta_v = \theta (1 + 0.608q)$ is the virtual potential temperature. Please note that variables in the equations are implicitly filtered by averaging over discrete grid volumes (Schumann, 1975). Nevertheless, the continuous form of the equations is used here for convenience. A double prime indicates SGS variables. The overbar indicating filtered quantities is omitted for readability, except for the SGS flux terms.

In order to ensure a divergence-free wind field, a predictor–corrector method is used where the Poisson equation for the perturbation pressure is solved after every time step (e.g. Patrinos and Kistler, 1977).

2.1.2 Subgrid-scale model

One of the main challenges in LES modeling is the turbulence closure. The filtering process yields three SGS covariance terms (see Eqs. 2.1-2.4) that cannot be explicitly calculated. These SGS terms are thus parametrized using a $1\frac{1}{2}$ order closure after Deardorff (1980). The closure is based on the assumption that the energy transport by SGS eddies is proportional to the local gradients of the mean quantities and reads

$$\overline{u_i'' u_j''} = -K_m \left(\frac{\partial u_i}{\partial x_j} + \frac{\partial u_j}{\partial x_i} \right), \quad (2.5)$$

$$\overline{u_i'' \theta''} = -K_h \frac{\partial \theta}{\partial x_i}, \quad (2.6)$$

$$\overline{u_i'' q''} = -K_h \frac{\partial q}{\partial x_i}, \quad (2.7)$$

$$(2.8)$$

where K_m and K_h are the local SGS eddy diffusivities of momentum and heat, respectively. They are related to the SGS turbulent kinetic energy (SGS-TKE) $e = \frac{1}{2} \overline{u_i'' u_i''}$ as follows

$$K_m = c_m l \sqrt{e} , \quad (2.9)$$

$$K_h = \left(1 + \frac{2l}{\Delta} \right) K_m . \quad (2.10)$$

Here, $c_m = 0.1$ is a model constant and $\Delta = \sqrt[3]{\Delta_x \Delta_y \Delta_z}$ with $\Delta_x, \Delta_y, \Delta_z$ being the grid resolutions in the indexed direction. The SGS mixing length l depends on height and stratification and is calculated by

$$l = \min \left(0.7z, \Delta, 0.76 \sqrt{e} \left(\frac{g}{\theta_{v,0}} \frac{\partial \theta_v}{\partial z} \right)^{-\frac{1}{2}} \right) \quad \text{for } \frac{\partial \theta_v}{\partial z} > 0 \quad \text{and} \quad (2.11)$$

$$l = \min(0.7z, \Delta) \quad \text{for } \frac{\partial \theta_v}{\partial z} \leq 0 , \quad (2.12)$$

where z is the height above ground. Moreover, the closure includes a prognostic equation for the SGS-TKE:

$$\frac{\partial e}{\partial t} + u_j \frac{\partial e}{\partial x_j} = - \left(\overline{u_i'' u_j''} \right) \frac{\partial u_i}{\partial x_j} + \frac{g}{\theta_{v,0}} \overline{u_3'' \theta_v''} - \frac{\partial}{\partial x_j} \left[\overline{u_j'' \left(e'' + \frac{p''}{\rho_0} \right)} \right] - \varepsilon . \quad (2.13)$$

The pressure term in Eq. 2.13 is parametrized as

$$- \frac{\partial}{\partial x_j} \left[\overline{u_j'' \left(e'' + \frac{p''}{\rho_0} \right)} \right] = -2K_m \frac{\partial \bar{e}}{\partial x_j} \quad (2.14)$$

and ε is the SGS dissipation rate within a grid volume, given by

$$\varepsilon = \left(0.19 + 0.74 \frac{l}{\Delta} \right) \frac{e^{3/2}}{l} . \quad (2.15)$$

2.1.3 Discretization

The model domain in PALM is discretized in space using finite differences and equidistant horizontal grid spacings Δ_x, Δ_y . The grid can be stretched in the vertical direction well above the ABL to save computational time in the free atmosphere. The Arakawa Staggered C-grid (Arakawa and Lamb, 1977) is used, where scalar quantities are defined at the center of each grid volume, whereas velocity components are shifted by half a grid width in their respective direction so that they are defined at the edges of the grid boxes (see Fig. 2.1). It is thus possible to calculate the centered derivatives of the velocity components at the center of the volumes (same location as the scalars). By the same token derivatives of scalar quantities can be calculated at the edges of the volumes. In this way it is possible calculate second-order approximations of spatial derivatives over only one grid length and the effective spatial model resolution can be increased by a factor of two in comparison with non-staggered grids.

The advection terms in Eqs. 2.1-2.3 are discretized using the 5th-order scheme after Wicker and Skamarock (2002) (hereafter WS-5). Alternatively the 2nd-order scheme after Piacsek and Williams (1970) (hereafter PW-2) is used for comparative simulations. The WS-5 scheme consists of a centered non-dissipative 6th-order flux with an artificially added numerical dissipation term. The latter is required in order to guarantee a stable numerical solution. On the

one hand, the WS-5 scheme thus suffers from significant numerical dissipation that can affect small turbulence scales up to 8Δ , but turbulent structures are generally well-preserved and dispersion errors are small. The PW-2 scheme, on the other hand displays immense numerical dispersion, leading to unrealistic turbulence structures, phase shifts, and oscillations near large gradients (generating so-called wiggles), but it does not suffer from numerical dissipation.

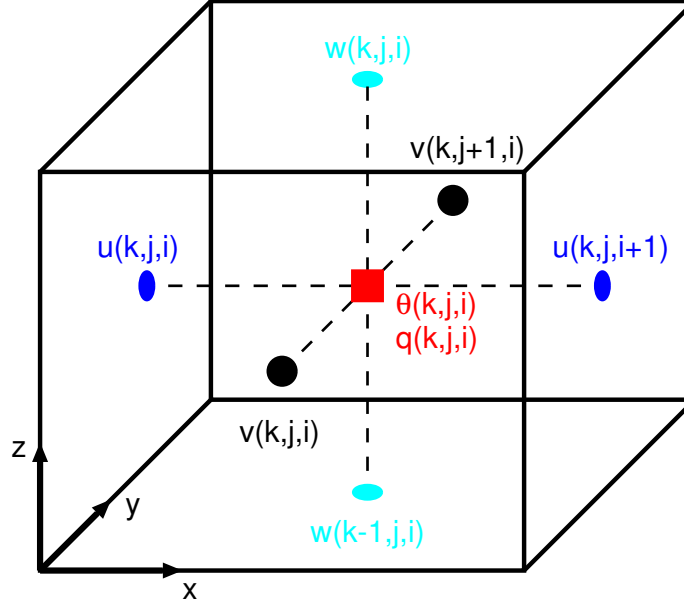


Figure 2.1: The Arakawa Staggered C-grid. The indices i , j , k refer to grid points in x , y and z direction, respectively.

Discretization in time is achieved using a 3rd-order Runge-Kutta time-stepping scheme (Williamson, 1980). The time step Δ_t is usually dynamically calculated and varies, depending on atmospheric conditions. It is restricted by two criteria. The CFL² criterion (Courant et al., 1928) reads as

$$\Delta_{t,\text{CFL}} \leq \min \left(\frac{\Delta_{x_i}}{u_{i,\text{max}}} \right). \quad (2.16)$$

Δ_t is also restricted by the diffusion criterion (Roache, 1985):

$$\Delta_{t,\text{Diff}} \leq 0.125 \cdot \min \left(\frac{\Delta_{x_i}^2}{\max(K_h, K_m)} \right). \quad (2.17)$$

Both criteria secure the numerical stability of the Runge-Kutta scheme. In PALM the time step is calculated by

$$\Delta_t = 0.9 \cdot \min(\Delta_{t,\text{CFL}}, \Delta_{t,\text{Diff}}), \quad (2.18)$$

including a safety reduction of the time step of 10 %. It should be noted that the Runge-Kutta scheme displays both dispersion and dissipation errors and interacts with the advection schemes.

2.1.4 Initial and boundary conditions

In the present study cyclic lateral boundary conditions are used. That implies a horizontally repeating model domain, and outflowing eddies at the one lateral boundary match the inflowing

²Courant-Friedrichs-Lewy

eddies on the opposite boundary. Dirichlet boundary conditions were chosen at the top of the model domain (z_{\max}) for the horizontal velocity components ($u(z = z_{\max}) = u_g, v(z = z_{\max}) = v_g$) and perturbation pressure ($p^*(z = z_{\max}) = 0$). Neumann conditions are used for SGS-TKE ($e(z = z_{\max}) = e(z = z_{\max} - \Delta_z)$) and the scalar quantities. For the latter the vertical gradient is constant in time and calculated from the initial values:

$$\left. \frac{\partial \theta}{\partial z} \right|_{z_{\max}} = \left. \frac{\partial \theta}{\partial z} \right|_{z_{\max}, t=0}, \quad \left. \frac{\partial q}{\partial z} \right|_{z_{\max}} = \left. \frac{\partial q}{\partial z} \right|_{z_{\max}, t=0}. \quad (2.19)$$

The vertical grid spacing in the lowest grid volume is halved to $0.5\Delta_z$ for all quantities except w , so that all variables are defined at the bottom surface. At this bottom boundary of the model (Earth's surface), Dirichlet conditions are used for velocity ($u(z = 0) = v(z = 0) = w(z = 0) = 0$). Moreover, Neumann boundary conditions are used for the scalars ($\theta(z = 0) = \theta(z = 0.5\Delta_z), q(z = 0) = q(z = 0.5\Delta_z)$) as well as for perturbation pressure ($p^*(z = 0) = p^*(z = 0.5\Delta_z)$) and SGS-TKE ($e(z = 0) = e(z = 0.5\Delta_z)$).

MOST is assumed as boundary condition between the surface and the first grid level where scalars and horizontal velocities are defined ($z_p = 0.5\Delta_z$). Momentum fluxes are calculated at the surface as well as the horizontal velocity components at z_p . The surface fluxes of sensible and latent heat are explicitly prescribed by the user. The friction velocity u_* is calculated from integrating

$$u_* = \left(\left(\overline{u'' w''}_0 \right)^2 + \left(\overline{v'' w''}_0 \right)^2 \right)^{1/4}. \quad (2.20)$$

From this definition one can deduce the momentum fluxes:

$$\overline{u'' w''}_0 = -u_*^2 \cos(\alpha), \quad \overline{v'' w''}_0 = -u_*^2 \sin(\alpha), \quad (2.21)$$

where α is the angle between the x -direction and the wind direction:

$$\alpha = \arctan \left(\frac{v(z_p)}{u(z_p)} \right). \quad (2.22)$$

Note that the minus signs in Eq. 2.21 account for the fact that the surface acts as a sink for momentum. The transport of momentum is thus directed downward. The horizontal wind $u_h = (u(z_p)^2 + v(z_p)^2)^{1/2}$ is defined as

$$\frac{\partial u_h}{\partial z} = \frac{u_*}{\kappa z_p} \phi_m \left(\frac{z_p}{L} \right), \quad (2.23)$$

where $\kappa = 0.4$ is the Von Kármán constant and ϕ_m are functions that depend on the Obukhov length L . Using the formulation of Businger-Dyer (see e.g. Panofsky and Dutton, 1984), the friction velocity can then be calculated as

$$u_* = \begin{cases} \frac{\kappa u_h}{\ln \left(\frac{z_p}{z_0} \right) + 5 \cdot \text{Rif} \frac{z_p - z_0}{z_p}} & \text{for Rif} \geq 0 \\ \frac{\kappa u_h}{\ln \left(\frac{(1+b)(1-a)}{(1-b)(1+a)} \right) + 2 \cdot (\arctan(b) - \arctan(a))} & \text{for Rif} < 0, \end{cases} \quad (2.24)$$

where z_0 is the roughness length which is given by the user. a and b are given by

$$a = (1 - 16 \cdot \text{Rif})^{1/4}, \quad b = \left(1 - 16 \cdot \text{Rif} \frac{z_0}{z_p} \right)^{1/4}. \quad (2.25)$$

Rif is the flux Richardson number that is calculated as

$$\text{Rif} = \frac{z_p \kappa g}{\theta_v(z_p)} \frac{\theta_* + 0.61 \theta(z_p) q_*}{u_*^2}. \quad (2.26)$$

Note that u_* from the previous time step is used for the calculation of Rif. The scaling parameters θ_* , q_* are given by MOST:

$$\theta_* = -\frac{\overline{w''\theta''}_0}{u_*}, \quad q_* = -\frac{\overline{w''q''}_0}{u_*} \quad (2.27)$$

The horizontal wind components are calculated using Eq. 2.22 and Eq. 2.23:

$$\frac{\partial u}{\partial z} = \frac{-\overline{u''w''}_0}{u_* \kappa z} \phi_m\left(\frac{z}{L}\right), \quad (2.28)$$

and

$$\frac{\partial v}{\partial z} = \frac{-\overline{v''w''}_0}{u_* \kappa z} \phi_m\left(\frac{z}{L}\right), \quad (2.29)$$

and integrating vertically. With this framework it is possible to derive the friction velocity as well as $\overline{u''w''}_0$, $\overline{v''w''}_0$, and the horizontal velocity components locally at $z = z_p$.

As already stated, initial values for the fluxes of sensible and latent heat as well as roughness length are prescribed at the surface. Furthermore, initial profiles of potential temperature and specific humidity are explicitly defined. In case of a prescribed geostrophic wind, a one-dimensional version of the model with fully-parametrized turbulence, using a mixing-length approach after Blackadar (1997) and the given initial profiles of the scalars, is used for precursor simulations to generate steady-state wind profiles as initialization for the three-dimensional LES model.

2.2 Analysis methods

In the framework of this thesis some analysis tools were developed in order to derive the structure parameters from LES data. These methods are described in detail in research article A. As these methods are the crucial factor regarding reliability and repeatability of the results in this thesis they should be outlined at this point and complemented by the NCL³ post-processing routines to determine structure parameters and the user code in FORTRAN that is used in PALM to calculate structure parameters online during the simulation. Furthermore, a flexible post-processing FORTRAN-program is outlined that was developed to derive secondary circulations from an ensemble of LES runs.

2.2.1 Calculation of structure parameters from turbulence spectra

The structure parameters C_T^2 and C_q^2 are directly proportional to the spectra of temperature and humidity in the inertial subrange, respectively. Wyngaard et al. (1971) related the structure parameter of the scalar S (temperature or humidity) at a given height to the power spectral density Φ_S by

$$C_S^2 = \frac{1}{0.2489} \Phi_S(k) k^{5/3}, \quad (2.30)$$

where k is a wave number in the inertial subrange (slope $\Phi_S \sim k^{-5/3}$) and $0.2489 = 2/3\Gamma(1/3)$ after Muschinski et al. (2004). Since this method directly derives the structure parameters from the turbulence spectra, it will hereafter be referred to as *spectral method*.

³The NCAR Command Language (Version 5.2.1) [Software]. (2010). Boulder, Colorado: UCAR/NCAR/CISL/VETS. <http://dx.doi.org/10.5065/D6WD3XH5>

Domain-averaged vertical profiles of the structure parameters were calculated according to Eq. 2.30. The turbulence spectra were calculated from three-dimensional LES data of temperature and humidity. First all one-dimensional spectra in x - and y -direction for each horizontal plane were calculated. These spectra were subsequently averaged. Second, a quality check following Hartogensis and De Bruin (2005) was performed to determine whether an inertial subrange was present in the spectrum. This check is basically testing small block intervals of the spectrum whether they follow the $-5/3$ power law and if the variance in these intervals is sufficiently small. If less than 30% of the wave numbers k in the spectrum were found to be the inertial subrange, a missing value was output. Third, the structure parameters were calculated at the height of each plane for all wave numbers in the inertial subrange and subsequent spectral averaging. The largest wave number in the inertial subrange usually depends on the grid resolution and is typically found to be at $k \approx 2\pi/6\Delta_{x,y}$ (equivalent to scales of $6\Delta_{x,y}$) throughout the surface layer and boundary layer. A commented routine of this spectral method can be found in appendix A. Please note that for large model domains, e.g. with 1600×1600 grid points in the horizontal directions, this routine can take several hours on a single processor to calculate a single vertical profile of a structure parameter.

2.2.2 Calculation of structure parameters from wavelet analysis

As stated above the scalar structure parameter can be derived from the inertial subrange in the scalar Fourier spectrum. A drawback of this method is that the Fourier spectrum is a global quantity, yielding a global estimate of the structure parameter. However, using a wavelet spectrum (derived from the continuous wavelet transform at a given location in space) one can determine the *local* spectrum from which a local estimate of the structure parameter can be derived (see Moene and Gioli, 2008). As long as an identifiable inertial subrange is present in the local wavelet spectrum, the relationship between the Fourier spectrum and the structure parameter should be locally retained.

The local structure parameters can be calculated from Eq. 2.30 by substituting Φ_S with its local estimate:

$$C_{S,\Delta k}^2(x_m) = \frac{1}{0.2489} \Phi_S(x_m, k) k^{5/3}, \quad (2.31)$$

where Δk indicates the spectral range over which is averaged (see below). x_m is the discrete series in space at the location m (see also Torrence and Compo, 1998). As wavelet function the Morlet wavelet was used with non-dimensional frequency 6 as it reproduces - when integrated over the entire series - a Fourier spectrum best. Furthermore it provides a good balance between locality in space and time (Grinsted et al., 2004). The Fourier-equivalent wavelength for this wavelet is 1.03 times the scale of the wavelet (see Torrence and Compo, 1998).

For the *wavelet method* first the local Fourier spectrum were obtained from one-dimensional wavelet transforms, using the smallest resolved scale in the LES ($2\Delta_{x,y}$) as smallest scale of the wavelet. All one-dimensional local spectra in x - and y -direction were calculated for each horizontal plane. These local spectra were subsequently averaged. Second, the structure parameters as a function of k for each one-dimensional series were calculated in each horizontal plane (first in one direction, then in the orthogonal direction). Due to high variability in the local Fourier spectra it was not possible to determine a local inertial subrange. Third, all local Fourier spectra were thus spatially averaged. In this way an inertial subrange could be determined. Fourth, this calculated wave number range was used to apply a spectral averaging on the structure parameter values from the local spectra. Note that, due to the nature of the wavelet spectrum, the large-scale end of the inertial subrange takes into account larger spatial scales than the small-scale end. The local structure parameters are thus to some extent artificially smoothed, but this does not affect their global mean values. In order to determine vertical mean profiles steps one and three were performed first. Then

the structure parameter was calculated as a function of k from the averaged spectrum followed by spectral averaging. The commented routines for the derivation of global and local structure parameters from wavelet analysis can be found in appendix B and C, respectively.

2.2.3 Calculation of structure parameters from local dissipation rates

Research article A describes a method to derive local structure parameters from LES data using the local dissipation rates of scalar quantities and TKE. This *dissipation method* can be written in terms of the SGS parametrization used in PALM as (cf. Cheinet and Siebesma, 2009, Eq. 8)

$$C_S^2 = \frac{0.2 \beta}{0.2489} l^{4/3} \left(1 + \frac{2l}{\Delta}\right) \left(0.19 + 0.74 \frac{l}{\Delta}\right)^{-1/3} \left(\frac{\partial S}{\partial x_i}\right)^2 \quad (2.32)$$

where $\beta = 0.4$ is the Obukhov-Corrsin constant (Sreenivasan, 1996). PALM provides a user interface that allows for extending the default code by own source code. This user interface was used to implement the dissipation method and to calculate the structure parameters online during the simulation. A snippet of the source code used in the user routine `user_actions.f90` can be found in appendix D.

2.2.4 Determination of secondary circulations from large-eddy simulation data

In research article C secondary circulations and heterogeneity-induced quantities are derived from LES data. The research article gives a detailed derivation of the method. According to this method the 1 h-averaged heterogeneity-induced part $\overline{\varphi}_{\text{hi}}$ of a quantity φ can be calculated by

$$\overline{\varphi}_{\text{hi}}(x, y, z, t) = \widetilde{\overline{\varphi}}(x, y, z, t) - \langle \overline{\varphi} \rangle(z, t) \quad (2.33)$$

where the overbar denotes a temporal average (here over 1 h of simulation time) and the tilde denotes the ensemble average. A FORTRAN program was written and parallelized with OpenMP in order to calculate $\overline{\varphi}_{\text{hi}}$ from an ensemble of LES runs. The program loads NetCDF data and stores the processed data again in NetCDF format. Its source code can be found in appendix E. The program also includes a user interface that allows for extending the included procedures by own post-processing code.

3 Cumulative part of the thesis

Preface to the research articles

This cumulative part of this thesis consists of four research articles (A, B, C and D), that have already been partly published in peer-reviewed journals. **Research article A** deals with the derivation of the structure parameters C_T^2 and C_q^2 from LES data using different methods. Besides a comparison of these methods, the LES data is compared with in situ measurements of aircraft and an LAS system operated at Cabauw. The Cabauw area is flat and fairly homogeneous and thus provided suitable conditions for a first LES-LAS intercomparison. Moreover, the systematic error in LAS measurements due to randomly distributed turbulent convection is estimated using virtual LAS (VLAS) measurements in the LES model.

Research article B deals with the derivation of MOST relationships for C_T^2 and C_q^2 in the unstable surface layer from LES. The setup was based on the Cabauw simulations, covering different stability conditions ranging from near-neutral to free convective boundary layers. The LES results are compared with the proposed similarity functions in literature that relate the structure parameters to the surface fluxes of sensible and latent heat. Sensitivity analyses are carried out, considering the effect of entrainment, atmospheric stability as well as the effect of humidity on the MOST relationships. Moreover, the similarity formulations in the free convection limit are studied.

Research article C focuses on some general features of the CBL over complex heterogeneous terrain, particularly the development and importance of secondary circulations on the CBL dynamics. The LITFASS area was of size of 400 km² and consisted of forest and lake areas as well as several agricultural fields of different size. These different land-use types were in turn characterized by different surface fluxes of sensible and latent heat as well as roughness that are all considered in the LES. Four LES cases for the LITFASS-2003 experiment are studied and compared with reference simulations with homogeneously distributed surface heat fluxes.

In **research article D** a high-resolution case study for LITFASS-2003 is conducted in order to investigate the effect of complex surface heterogeneity on the structure parameters in the unstable surface layer. In order to resolve this surface layer sufficiently, a grid resolution of 2 – 3.2 m was required. The model domain was thus limited to an area of 25 km², located around the LAS system that was operated during the experiment phase. The MOST relationships that have been derived in the scope of article B are evaluated over the heterogeneous terrain and the concept of a blending height, above which signals from a surface heterogeneity vanish, is studied. Moreover a direct comparison of an LAS over the LITFASS area is compared to the VLAS system that was used in the LES runs.

3.1 Research article A: Derivation of structure parameters of temperature and humidity in the convective boundary layer from large-eddy simulations and implications for scintillometer observations

3.1.1 Declaration of my contribution

I carried out all LES-related simulations and analyses included in this paper. The raw scintillometer and tower data from the measurement site at Cabauw were provided by the coauthor Dr. Fred C. Bosveld from the Royal Netherlands Meteorological Institute in De Bilt (The Netherlands). The processing and analysis of this data set was done by myself. The aircraft data from the RECAP measurement campaign were made available by coauthor Dr. Beniamino Gioli from the National Research Council in Florence (Italy). Coauthor Dr. Arnold Moene from Wageningen University (The Netherlands) provided the structure parameters from the aircraft data. He also contributed the concept of the wavelet method that is described in the paper. The study was inspired by an internship report from coauthor Daniëlle van Dinther (Wageningen University). I wrote the manuscript of the article. The manuscript benefits from discussions with the coauthors. Additionally the manuscript has been improved during the review process.

3.1.2 Published article

This article is published with open access in *Boundary-Layer Meteorology*.
Submitted: 27 August 2012. Published online: 12 February 2013, as print: Volume 148, 1 Issue, 1-30, July 2013.

Maronga, B., A. F. Moene, D. van Dinther, S. Raasch, F. Bosveld and B. Gioli, 2013: Derivation of structure parameters in the convective boundary layer from large-eddy simulations and implications for the interpretation of scintillometer observations. *Boundary-Layer Meteorol.*, **148**, 1-30, doi: 10.1007/s10546-013-9801-6.

Boundary-Layer Meteorol (2013) 148:1–30
DOI 10.1007/s10546-013-9801-6

ARTICLE

Derivation of Structure Parameters of Temperature and Humidity in the Convective Boundary Layer from Large-Eddy Simulations and Implications for the Interpretation of Scintillometer Observations

Björn Maronga · Arnold F. Moene ·
Daniëlle van Dinter · Siegfried Raasch ·
Fred C. Bosveld · Beniamino Gioli

Received: 27 August 2012 / Accepted: 22 January 2013 / Published online: 12 February 2013
© The Author(s) 2013. This article is published with open access at Springerlink.com

Abstract We derive the turbulent structure parameters of temperature C_T^2 and humidity C_q^2 from high-resolution large-eddy simulations (LES) of a homogeneously-heated convective boundary layer. Boundary conditions and model forcing were derived from measurements at Cabauw in The Netherlands. Three different methods to obtain the structure-parameters from LES are investigated. The shape of the vertical structure-parameter profiles from all three methods compare well with former experimental and LES results. Depending on the method, deviations in the magnitude up to a factor of two are found and traced back to the effects of discretization and numerical dissipation of the advection scheme. Furthermore, we validate the LES data with airborne and large-aperture scintillometer (LAS) measurements at Cabauw. Virtual path measurements are used to study the variability of C_T^2 in the mixed layer and surface layer and its implications for airborne and LAS measurements. A high variability of C_T^2 along a given horizontal path in the LES data is associated with plumes (high values) and downdrafts (low values). The path average of C_T^2 varies rapidly in time due to the limited path length. The LES results suggest that measured path averages require sufficient temporal averaging and an adequate ratio of path length to height above the ground for the LAS in order to approach the domain average of C_T^2 .

B. Maronga (✉) · S. Raasch
Institut für Meteorologie und Klimatologie,
Leibniz Universität Hannover, Herrenhäuser Str. 2, 30419 Hannover, Germany
e-mail: maronga@muk.uni-hannover.de

A. F. Moene · D. van Dinter
Meteorology and Air Quality Section, Wageningen University, Wageningen, The Netherlands

F. C. Bosveld
Regional Climate Division,
Royal Netherlands Meteorological Institute, De Bilt, The Netherlands

B. Gioli
Institute of Biometeorology, National Research Council, Florence, Italy

Keywords Convective boundary layer · Large-eddy simulation · Turbulent structure parameter · Virtual scintillometer

1 Introduction

A number of measurement systems have been used to observe the turbulence structure of the atmospheric boundary layer, including radars, sodars, lifted kites and aircraft (Petenko and Shurygin 1999; Muschinski 2004; Muschinski et al. 2004; Martin et al. 2010, among others). Recently, scintillometers have been increasingly employed to measure the optical interference along a horizontal path (e.g. Ochs and Wang 1978; Kohsiek 1982; Beyrich et al. 2002; among others). Scintillometers are operated in the atmospheric surface layer and consist of a wave transmitter and a receiver at both ends of a path that can cover several km. The transmitted waves that propagate through the atmosphere are affected by turbulent density fluctuations, so-called *scintillations* (Peltier and Wyngaard 1995). This scattering of the transmitted radiation is related to spatial fluctuations in the refractive index of air n . Tatarskii (1971) described this scattering theoretically using the refractive index structure function,

$$D_n(\mathbf{x}, \mathbf{r}, t) \equiv \{[n(\mathbf{x}, t) - n(\mathbf{x} + \mathbf{r}, t)]^2\}, \quad (1)$$

where \mathbf{x} and $\mathbf{x} + \mathbf{r}$ are two points in space with displacement $r = |\mathbf{r}|$ at time t , and the curly brackets denote the ensemble average. If the displacement is in the inertial subrange of turbulence, the structure function can be expressed as

$$D_n = C_n^2 r^{2/3}, \quad (2)$$

where C_n^2 is called the refractive index structure parameter. Under suitable conditions, scintillometer measurements may be traced back to the path mean C_n^2 . Hill (1978) and Andreas (1988), among others, showed that C_n^2 is determined by the structure parameters of temperature, humidity and a joint structure parameter C_{Tq} , because variations in n are dominantly caused by fluctuations in temperature T and specific humidity q . Hill (1978) derived an expression for C_n^2 in terms of the structure parameters of meteorological variables, viz.

$$C_n^2 = \frac{A_T^2}{\{T\}^2} C_T^2 + 2 \frac{A_T A_q}{\{T\} \{q\}} C_{Tq} + \frac{A_q^2}{\{q\}^2} C_q^2, \quad (3)$$

where the dimensionless coefficients A_T and A_q are functions of the wavelength λ of the transmitted beam by the scintillometer, atmospheric pressure p , temperature and humidity (e.g. Hill et al. 1980).

Scintillometer observations have been frequently used to obtain horizontal path averages of C_n^2 , and to deduce C_T^2 and C_q^2 from it, over typical distances of 5–10 km (e.g. Kohsiek et al. 2002; Meijninger et al. 2002a,b, 2006). So far, scintillometers are the only operational instruments that allow for estimating C_T^2 and C_q^2 at a spatial scale that might be representative for an area of several square km. Surface heterogeneity due to horizontal variations in soil moisture, vegetation and elevation, however, might affect the scintillometer measurements significantly. Footprint models for the scintillometer path can provide an estimate of its (heterogeneous) footprint. Nevertheless, it is difficult to validate these observations, particularly because usually only point measurements by, e.g. a sonic anemometer-thermometer/hygrometer system can be used for validation.

The surface fluxes of sensible and latent heat can be derived from the scintillometer measurements by means of Monin–Obukhov similarity theory (MOST). Some attempts have thus

been made to validate scintillometer-derived fluxes by means of aggregated eddy-covariance measurements (Meijninger et al. 2002a,b, 2006), and Beyrich et al. (2006a) compared the structure parameters derived from scintillometer data to tower-based measurements. However, these studies have two major weaknesses: they compared path-averaged measurements with point measurements, and the effect of the surface heterogeneity could not be quantified. A few studies used airborne measurements that are generally representative of a larger area to validate scintillometer observations (Beyrich et al. 2006b; Moene et al. 2006). A first attempt has been made to use low-level aircraft flights along a scintillometer path during the LITFASS-2009 experiment (van den Kroonenberg et al. 2012, see also Beyrich et al. 2012). To the authors' knowledge (also stated by Beyrich et al. 2012), it has not been possible so far to validate scintillometer-derived structure parameters against independent data representative of the same area.

There are few studies that have investigated structure parameters using large-eddy simulations (LES). Peltier and Wyngaard (1995) showed that LES can be employed to study the vertical distribution of the structure parameters in the convective boundary layer (CBL), and derived vertical profiles of C_T^2 , C_q^2 and C_{Tq} , and showed that their LES data agree well with experimental results. Cheinet and Siebesma (2009) investigated the spatial variability of C_T^2 in the dry CBL with LES and showed the relation of the spatial variability of C_T^2 to the presence of ascending plumes. These updraft structures show a hexagonal cellular pattern near the surface, where the horizontal size of the cells scales with the boundary-layer depth z_i (Stull 1988). The vertical profiles of C_T^2 showed the decrease with height proposed by Kaimal et al. (1976), but Cheinet and Siebesma (2009) observed a gap of a factor two in the magnitude. Furthermore they found a bimodal distribution of C_T^2 near the surface, which was previously found in the sodar measurements of Petenko and Shurygin (1999). Cheinet and Cumin (2011) supplemented the previous LES studies by studying the variability of C_q^2 . Cheinet and Siebesma (2007) used a wave propagation modeling framework to derive the scintillation rate and coherence length from virtual path measurements in their LES, and found that the variability of their virtual measurements of C_n^2 increased with height, while the path mean decreased. They stated that for their virtual paths (2 km length) it was not possible to provide representative estimates of C_n^2 with time averaging of 500 s. However, the coarse spatial resolution of 39 m in the horizontal and 32 m in the vertical direction did not allow the study of the wave propagation at realistic scintillometer heights, and no in situ scintillometer or aircraft measurements were used for comparison. Recently, Wilson and Fedorovich (2012) used LES to evaluate C_n^2 directly by calculating the refractive-index structure functions. They calculated the refractive index at each grid point and used Eq. 2, but they also employed Eq. 3 and calculated C_T^2 , C_q^2 and C_{Tq} from the fields of temperature and humidity. They could show that (for visible radiation) temperature contributes dominantly to C_n^2 in the lower half of the CBL, but that C_{Tq} becomes important near the entrainment zone.

In the present paper we wish to gain more insight into the scintillometer technique by using the advantages of high-resolution LES that actually resolve the surface layer. The simulations are initialized by temperature and humidity profiles and driven by surface fluxes, derived from measurements during the RECAP¹ campaign at Cabauw in The Netherlands (de Arellano et al. 2004). Mean profiles of the structure parameters are derived from the LES data using different approaches, and validated for the first time directly with airborne and large-aperture scintillometer (LAS) measurements. Furthermore we extend the previous results of the LES study of Cheinet and Siebesma (2009) by calculating local structure parameters in order to

¹ "Regional Assessment and Modeling of the Carbon Balance in Europe", European Commission research project EVK2-CT-1999-00034.

investigate the effect of the temporal and spatial variability of C_T^2 in the CBL on aircraft and particularly LAS measurements. Virtual path measurements of the local C_T^2 are then used for studying the representativeness of in situ measurements.

The paper is organized as follows: Sect. 2 deals with different methods to derive structure parameters, while Sect. 3 gives a case description, including synoptic conditions, the LES set-up and data processing. Results are presented in Sect. 4, and in Sect. 5 we discuss and summarize our results.

2 Derivation of Structure Parameters from LES

Different approaches to determining structure parameters from turbulence data have been proposed in the literature. In this section we outline three different methods that can be applied to LES data in order to obtain vertical profiles of C_T^2 (here for potential temperature) and C_q^2 (for specific humidity). As estimates of the surface fluxes of sensible and latent heat can be calculated from C_T^2 and C_q^2 by means of MOST, these two structure parameters are of most practical interest. All of these methods are based on Kolmogorov's similarity hypotheses for the turbulence spectra.

2.1 Structure Parameters from Turbulence Spectra

The structure parameters C_T^2 , C_q^2 and C_{Tq} are directly proportional to the spectra of temperature, humidity and their cospectrum in the inertial subrange, respectively. [Wyngaard et al. \(1971b\)](#) related the structure parameter of the scalar S (temperature or humidity) at a given height to the power spectral density Φ_S by

$$C_{S,G}^2 = \frac{1}{0.2489} \Phi_S(k) k^{5/3}, \quad (4)$$

where k is a wavenumber in the inertial subrange (slope $\Phi_S \sim k^{-5/3}$) and $0.2489 = 2/3\Gamma(1/3)$ after [Muschinski et al. \(2004\)](#). The subscript G indicates that this method derives global values of C_S^2 (i.e. horizontally-averaged values). Since this method directly derives the structure parameters from the turbulence spectra, we hereafter refer to this method as the *spectral method*.

2.2 Structure Parameters from (Local) Dissipation Rates

In the inertial subrange the power spectral density is proportional to the 2/3 power of the dissipation rate ε of turbulent kinetic energy (TKE) and can be calculated after [Tennekes and Lumley \(1973\)](#) by

$$\Phi_{u,v}(k) = \alpha \varepsilon_{\text{TKE,G}}^{2/3} k^{-5/3}, \quad (5)$$

$$\Phi_w(k) = \frac{4}{3} \alpha \varepsilon_{\text{TKE,G}}^{2/3} k^{-5/3}, \quad (6)$$

where $\alpha \approx 0.52$ is the Kolmogorov constant and u , v and w are the velocity components on a Cartesian coordinate system. [Corrsin \(1951\)](#) showed that the power spectral density of temperature is related to the dissipation of temperature variance ε_T and TKE ε_{TKE} . Generalized for any scalar quantity, this relation reads

$$\Phi_S(k) = \beta \varepsilon_{\text{TKE,G}}^{-1/3} \varepsilon_{S,G} k^{-5/3}, \quad (7)$$

where $\beta \approx 0.4$ is the Obukhov–Corrsin constant (Sreenivasan 1996). A derivation of $\varepsilon_{S,G}$ from the turbulence spectra follows from substitution of $\varepsilon_{\text{TKE},G}$ into Eq. 7 with Eqs. 5–6. Substituting Φ_S in Eq. 4 with Eq. 7 yields an expression that relates the structure parameters of a scalar quantity to the dissipation rates of TKE and scalar fluctuations (Wyngaard and LeMone 1980; Peltier and Wyngaard 1995),

$$C_{S,G}^2 = \frac{\beta}{0.2489} \varepsilon_{\text{TKE},G}^{-1/3} \varepsilon_{S,G}. \quad (8)$$

The structure parameter can be regarded as a local and instantaneous quantity. It can be defined through the average over a small volume in the inertial subrange and it is thus possible to rewrite Eq. 8 after Cheinet and Siebesma (2009) in terms of local dissipation rates,

$$C_{S,\Delta\mathbf{x}}^2(\mathbf{x}, t) = \frac{\beta}{0.2489} \varepsilon_{\text{TKE},\Delta\mathbf{x}}^{-1/3}(\mathbf{x}, t) \varepsilon_{S,\Delta\mathbf{x}}(\mathbf{x}, t), \quad (9)$$

where $\Delta\mathbf{x}$ denotes the size of the volume. Since the above equation allows the calculation of $C_{S,\Delta\mathbf{x}}^2$ by means of the dissipation rates only, this method is hereafter referred to as the *dissipation method*. Cheinet and Siebesma (2009) discussed that the empirical constant β might not be well-determined, but we follow their choice and use the widespread value of $\beta = 0.4$.

In LES the turbulent eddies are directly resolved down to the truncation size Δ , which is assumed to be located in the inertial subrange, whereas eddies smaller than Δ are parametrized within the subgrid-scale (SGS) model. The used LES model employs implicit filtering so that the nominal truncation size is determined by the grid resolution (see below). In practice, however, the SGS model affects to some extent also eddies that are larger than Δ . The actual truncation size is thus not sharp and located at larger scales than Δ . We follow Cheinet and Siebesma (2009) and relate the local dissipation rate of TKE to the SGS parametrization in the LES model. In the LES model PALM (Raasch and Schröter 2001), $\varepsilon_{\text{TKE},\Delta\mathbf{x}}$ for a grid volume is calculated very similarly to the DALES model (Heus et al. 2010), used by Cheinet and Siebesma (2009) and going back to Deardorff (1980), as

$$\varepsilon_{\text{TKE},\Delta\mathbf{x}} = \left(0.19 + 0.74 \frac{l}{\Delta}\right) \frac{e^{3/2}}{l}, \quad (10)$$

where $\Delta = \sqrt[3]{\Delta_x \Delta_y \Delta_z} = \sqrt[3]{\Delta\mathbf{x}}$ with Δ_x , Δ_y and Δ_z being the grid resolutions of the Cartesian coordinate system (x, y, z) , e is the subgrid-scale TKE (also referred to as SGS-TKE). The subgrid-scale mixing length l depends on height and stratification; in unstable stratification l usually equals Δ , whereas l becomes smaller in stably stratified regions (Deardorff 1980). The local dissipation of scalar fluctuations can be modelled using the local budget, equating dissipation and mean-gradient production (Cheinet and Siebesma 2009; see also Peltier and Wyngaard 1995), viz.

$$\varepsilon_{S,\Delta\mathbf{x}} = 2K_S \left(\frac{\partial S}{\partial x_i}\right)^2, \quad (11)$$

where K_S is the local SGS eddy diffusivity of the scalar, which is related to the SGS-TKE in the used SGS model as follows (see also Sect. 3.3):

$$K_S = K_m \left(1 + \frac{2l}{\Delta}\right) = c_m l \left(1 + \frac{2l}{\Delta}\right) \sqrt{e}, \quad (12)$$

where $K_m = c_m l \sqrt{e}$ is the SGS eddy diffusivity of momentum and $c_m = 0.1$ is a model constant. Equation 9 can thus be written in terms of the SGS model parametrization above as

$$C_{S,\Delta x}^2 = \frac{0.2 \beta}{0.2489} l^{4/3} \left(1 + \frac{2l}{\Delta}\right) \left(0.19 + 0.74 \frac{l}{\Delta}\right)^{-1/3} \left(\frac{\partial S}{\partial x_i}\right)^2, \quad (13)$$

where the SGS-TKE has cancelled out (cf. [Cheinet and Siebesma 2009](#), Eq. 8).

2.3 Structure Parameters from Wavelet Analysis

As shown in Sect. 2.1 the scalar structure parameter can be derived from the inertial subrange in the scalar Fourier spectrum. A drawback of this method is that the Fourier spectrum is a global quantity, yielding a global estimate of the structure parameter. However, using a wavelet spectrum (derived from the continuous wavelet transform at a given location in space) one can determine the *local* spectrum from which a local estimate of the structure parameter can be derived (see [Moene and Gioli 2008](#)). As long as an identifiable inertial subrange is present in the local wavelet spectrum, the relationship between the Fourier spectrum and the structure parameter should be locally retained.

The local structure parameters can be calculated from Eq. 4 by substituting Φ_S with its local estimate,

$$C_{S,\Delta k}^2(x_m) = \frac{1}{0.2489} \Phi_S(x_m, k) k^{5/3}, \quad (14)$$

where Δk indicates the spectral range over which Φ_S is averaged (see below); x_m is the discrete series in space at the location m (see also [Torrence and Compo 1998](#)). For the wavelet function we use the Morlet wavelet with non-dimensional frequency six as it reproduces, when integrated over the entire series, an optimum Fourier spectrum. Furthermore it provides a good balance between locality in space and time ([Grinsted et al. 2004](#)). The Fourier equivalent wavelength for this wavelet is 1.03 times the scale of the wavelet (see [Torrence and Compo 1998](#)).

The smallest scales in a wavelet transform contain the most localized information, whereas increasingly larger scales of the wavelet transform use information from increasingly larger sections of the data. Hence it would be tempting to apply Eq. 14 to the smallest scale of the spectrum. However, then one needs to be sure that this scale is within the inertial subrange. Furthermore, the variance in the wavelet spectrum is usually high. Therefore, spectral and spatial averaging is applied to Eq. 14 between the smallest scales located inside the inertial subrange and some larger scale that is chosen such that the required spatial information is still retained. This spectral averaging implies also additional implicit spatial averaging. The larger the used spectral scales, the larger is the spatial average. e.g. if spectral scales around 100 m are averaged, this would imply a spatial averaging in the order of 100 m. The index Δk refers to this spectral/spatial averaging.

3 Case Description and LES Model

3.1 Case Description

We use measurements from the RECAP data, observed on 27 July 2002 at Cabauw. The Cabauw area is flat and fairly homogeneous, with terrain being mainly open pasture, crossed by ditches, windbreaks, small built-up areas and the river Lek. The prominent feature of the site is a 213-m high tower constructed for meteorological research. Low geostrophic wind speeds and a cloudless sky were observed at least until 1400 UTC, proving suitable conditions

for the simulation of a free-convective boundary layer. After 1400 UTC, scattered cumulus clouds were observed. Due to intense precipitation on the previous day, the near-surface Bowen ratio B_0 was 0.3–0.4, with B_0 defined as

$$B_0 = \frac{c_p \overline{w'\theta'_0}}{L_v \overline{w'q'_0}}, \quad (15)$$

and where c_p is the specific heat at constant pressure and L_v is the latent heat of vaporization; $\overline{w'\theta'_0}$ and $\overline{w'q'_0}$ are the kinematic surface fluxes of sensible and latent heat, respectively. The boundary-layer depth increased from 353 m at 0816 UTC to 955 m at 1249 UTC. For a detailed description of the conditions during the experiment see [de Arellano et al. \(2004\)](#).

3.2 Observations at Cabauw

Surface fluxes of sensible and latent heat were measured next to the Cabauw tower at 5.37 m by means of the eddy-covariance technique. These fluxes were used as lower boundary conditions for the large-eddy simulations. Additionally, airborne observations of the Sky Arrow ERA aircraft platform ([Gioli et al. 2006](#)) were available; the aircraft had a cruise flight speed of 49 m s^{-1} and recorded temperature and humidity at 50 Hz. Moreover, [de Arellano et al. \(2004\)](#) computed the high frequency attenuation for these specific temperature and humidity sensors and found that signals were not attenuated below 10 and 15 Hz respectively. From a spectral analysis we found that spatial fluctuations at a scale of 10 and 5 m could be resolved for temperature and humidity, respectively. There were two measurement periods: in the morning between 0745 and 0911 UTC and in the afternoon between 1230 and 1355 UTC. During spiral flights, vertical profiles of temperature and humidity were measured, and were used for the initialization and validation of the respective LES profiles. Horizontal flight legs of about 10 km were flown repeatedly at different heights over short grassland, with 3–7 (typically four) repetitions flown at three different height levels. In the morning these height levels were at 79, 167 and 257 m, while in the afternoon flights were performed at 79, 261 and 625 m above the ground. The flight legs were designed to coincide with the path of an LAS, which measured C_n^2 at an average path height of 41 m. Since the LAS uses a radiation source in the near-infrared wavelength range, it is mainly sensitive to C_T^2 ([Kohsiek et al. 2002](#)).

The database was supplemented by a UHF wind profiler, for estimating z_i , and the Cabauw tower with measurement equipment mounted at different heights. A more detailed description of the measurements and Cabauw site characteristics is given in [de Arellano et al. \(2004\)](#) and [Kohsiek et al. \(2002\)](#).

3.3 LES Model and Simulation Set-Up

The **PAR**allelized **LES** Model (PALM, [Raasch and Schröter 2001](#)) was used for the present study, and has been widely applied to study different flow regimes in the convective boundary layer (e.g. [Raasch and Franke 2011](#); [Maronga and Raasch 2013](#)). All simulations were carried out using cyclic lateral boundaries. A staggered grid is used, where scalar quantities are defined at the centre of the grid volumes, whereas velocities are defined on the lateral faces of the volumes. The grid was stretched in the vertical direction well above the top of the boundary layer to minimize computational time in the free atmosphere. MOST was applied locally between the surface and the first computational grid level, including the calculation of the local friction velocity u_* . A 1.5-order flux-gradient subgrid closure scheme, after [Deardorff](#)

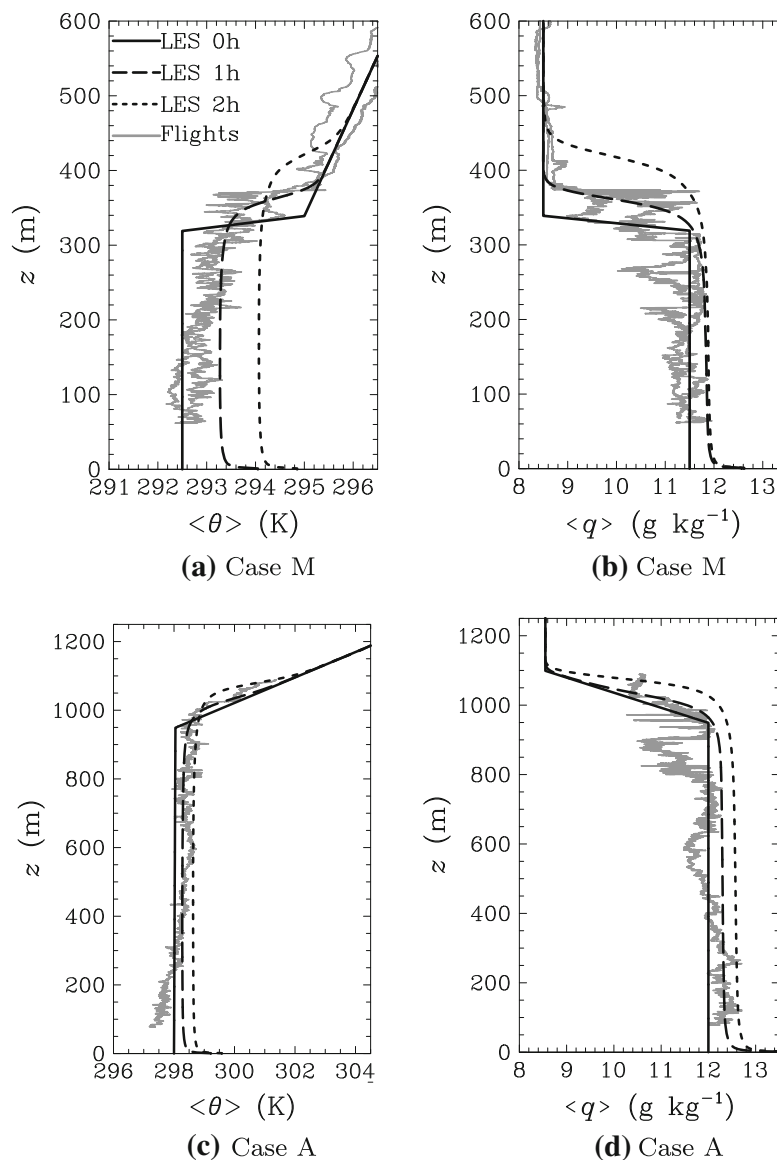


Fig. 1 Domain-averaged profiles of potential temperature (*left*) and specific humidity (*right*) for cases M (**a**, **b**) and A (**c**, **d**). Spiral aircraft flights (*grey*) started at 0812 UTC and 0816 UTC (case M) as well as at 1245 UTC (case A)

(1980), was applied, which requires the solution of an additional prognostic equation for the SGS-TKE. The SGS model contains a diagnostic relation for the SGS-TKE dissipation rate (see Eq. 10). A fifth-order advection scheme of Wicker and Skamarock (2002, hereafter WS-5) was used in this study. Moreover, the second-order scheme after Piacsek and Williams (1970, hereafter PW-2) was chosen for comparative simulations.

Based on the Sky Arrow measurement periods we carried out both a morning and an afternoon simulation (cases M and A, respectively), where each simulation was driven by constant surface fluxes of sensible and latent heat, derived from the eddy-covariance measurements at Cabauw. Despite the fact that the observed surface fluxes displayed a diurnal cycle (see de Arellano et al. 2004), we decided to use constant fluxes, because in this way we could reach a quasi-stationary state in both simulations in short time. Neutrally-stratified initial profiles of temperature (θ_0) and humidity (q_0) with a capping inversion above were prescribed in

Table 1 LES grid set-up and initial parameters

Case	Domain (km × km)	θ_0 (K)	q_0 (g kg ⁻¹)	$\overline{w'\theta'_0}$ (K m s ⁻¹)	$\overline{w'q'_0}$ (g kg ⁻¹ m s ⁻¹)	z_i (m)	$(\Delta z)_i$ (m)	$(\Delta\theta)_i$ (K)	$(\Delta q)_i$ (g kg ⁻¹)
M	2.046 × 2.046	292.5	11.5	0.06	0.055	320	20	2.50	-0.30
ME	10.240 × 2.046	292.5	11.5	0.06	0.055	320	20	2.50	-0.30
A	4.096 × 4.096	298.0	12.0	0.075	0.110	950	250	6.75	-3.45
AE	11.520 × 4.096	298.0	12.0	0.075	0.110	950	150	6.75	-3.45

The vertical grid was stretched starting from 1,000 and 1,500 m above the ground for case M and A, respectively. The lapse rate in the free atmosphere was 7 K km⁻¹ for temperature and zero for humidity. $(\Delta\theta)_i$ and $(\Delta q)_i$ are the temperature and humidity jumps at the inversion interface (with depth $(\Delta z)_i$), respectively

such a way that the mean LES profiles after 1 h of simulation time matched the spiral vertical aircraft flights and tower measurements around 0816 UTC and 1249 UTC, respectively (see also Fig. 1). Additionally an aerodynamic roughness length of 0.1 m was prescribed at the surface. Since only wind speeds < 3 m s⁻¹ were observed, no mean flow was prescribed in the simulation (free convective conditions). The initial settings are listed in Table 1.

The model was discretized in space with 1,024 grid points in each horizontal direction; the grid resolution in case M was 2 m in all spatial directions ($\Delta_x = \Delta_y = \Delta_z = 2$ m) and 448 grid points were used in the vertical direction. In case A, owing to the considerably larger boundary-layer depth, a sufficiently large horizontal domain was necessary in order to capture all relevant turbulent scales (see Sect. 3.1). Hence we used a horizontal grid resolution of 4 m. In the vertical direction 832 grid points were used with $\Delta_z = 2$ m, and both simulations lasted 2 h with a constant timestep of 0.25 s. For studying the representativeness of LAS measurements (see Sect. 4.6) two additional simulations (cases ME and AE) with an extended model domain in the x -direction were carried out. The domain sizes for all four simulations are given in Table 1.

3.4 Derivation of Structure Parameters from the Different Data Sources

3.4.1 LES Data

In Sect. 2 we introduced different methods for obtaining C_T^2 and C_q^2 . In order to compare the different methods we calculated domain-averaged vertical profiles of the structure parameters by means of the spectral, dissipation and wavelet methods.

The turbulence spectra were calculated from three-dimensional LES data of temperature and humidity. First we calculated all one-dimensional spectra in the x - and y -directions for each horizontal plane, and these spectra were subsequently averaged. Second, we performed a quality check following [Hartogensis and De Bruin \(2005\)](#) to determine whether an inertial subrange was present in the spectrum. This check basically tests small block intervals of the spectrum to determine whether they follow the $-5/3$ power law and whether the variance in these intervals is sufficiently small. If less than 30 % of the wavenumbers in the spectrum are found to be the inertial subrange, a missing value was inserted. This occurred only sporadically well above the capping inversion and hence did not affect our results. Thirdly, we calculated the structure parameters at the height of each plane by calculating $C_{S,G}^2(k)$ by means of Eq. 4 for all k in the inertial subrange and subsequent spectral averaging. The largest wavenumber in the inertial subrange usually depends on the grid resolution and was typically found

to be at $k \approx 2\pi/6\Delta_{x,y}$ (equivalent to scales of $6\Delta_{x,y}$) throughout the surface layer and boundary layer. The largest scales (smallest wavenumbers) were typically in the order of several hundreds of metres.

The local structure parameters $C_{S,\Delta\mathbf{x}}^2$ were calculated on-the-fly during the simulation according to the described dissipation method (see Eq. 13) using the three-dimensional fields of temperature and humidity. The gradients in Eq. 13 are approximated using central finite differences on the LES grid. The global values $C_{S,G}^2$ were calculated by the horizontal averaging of $C_{S,\Delta\mathbf{x}}^2$.

For the wavelet method we first obtained the local Fourier spectrum from one-dimensional wavelet transforms, using the smallest resolved scale in the LES ($2\Delta_{x,y}$) as the smallest scale of the wavelet. We calculated all one-dimensional local spectra in the x - and y -directions for each horizontal plane, and these local spectra were subsequently averaged. Second, we determined C_S^2 as a function of k (Eq. 14) for each one-dimensional series in each horizontal plane (first in one direction, then in the orthogonal direction). Due to high variability in the local Fourier spectra it was not possible to determine a local inertial subrange. Third, we thus spatially averaged all local Fourier spectra. In this way we could determine an inertial subrange, which we found to usually cover wavenumbers from $k \approx 2\pi/6\Delta_{x,y}$ to an upper limit $k \approx 0.06\text{ m}^{-1}$. Fourth, we used this calculated wavenumber range to apply a spectral averaging on the C_S^2 values from the local spectra (yields $C_{S,\Delta k}^2$). Note that, due to the nature of the wavelet spectrum, the large-scale end of the inertial subrange takes into account larger spatial scales than the small-scale end (see Sect. 2.3). The local structure parameters are thus to some extent artificially smoothed, but this does not affect their global mean values. In order to determine vertical mean profiles ($C_{S,G}^2$) we first performed steps one and three. Then we calculated C_S^2 as a function of k from the averaged spectrum followed by spectral averaging.

For convenience we will hereafter omit the subscript indices (G, $\Delta\mathbf{x}$, Δk).

3.4.2 Aircraft Data

The wavelet method was used to obtain C_T^2 and C_q^2 from the horizontal flight legs of the Sky Arrow aircraft. The time series of temperature and humidity along the flight legs were first converted to an equidistant space series using the geo-location of the points (linear interpolation was used). The spatial resolution was equal to the mean spatial resolution of the original time series (approximately 1 m). Next the wavelet spectrum was calculated for each point in the spatial series, and the local estimates of $C_S^2(x_m, k)$ were derived from Eq. 14. The smallest scale to be used for the spectral averaging was determined by verifying that the leg-averaged structure parameter was independent of the choice of the smallest scale (this turned out to be 50 m), and the largest scale was selected to be 208 m. The spectral filtering implies as well a spatial filtering. By choosing larger spectral ranges, the variability along the flight legs is thus significantly decreased. The structure parameter was spatially averaged over a running window of 20 m and stored at a spatial interval of 5 m for every 5 m in the flight leg. For validation of the LES profiles, the local C_S^2 estimates were averaged over their full flight legs.

3.4.3 LAS Data

Temporally-averaged values (10 min) of C_n^2 were obtained from the LAS at Cabauw. The relationship between C_n^2 and C_T^2 , C_q^2 , and C_{Tq} was already given in Eq. 3. The importance of T and q on C_n^2 , however, depends on the wavelength of the radiation used. An optical LAS

is mainly sensitive to temperature fluctuations, and if no second scintillometer, operating at a wavelength sensitive to humidity, is available, only little information can be obtained on C_{Tq} and C_q^2 (Moene 2003). It is common to eliminate C_{Tq} and C_q^2 by using the available information about the relationship between temperature and humidity, namely by applying a correction involving the Bowen ratio B . We use the approximation discussed in Moene (2003) to relate C_n^2 to C_T^2 with a Bowen ratio correction term,

$$C_n^2 \approx \frac{A_T^2}{\bar{T}^2} C_T^2 \left(1 + \frac{A_q}{\bar{q}} \frac{\bar{T}}{A_T} \frac{c_p}{L_v} B^{-1} \right)^2. \quad (16)$$

The temporally-averaged temperature \bar{T} and humidity \bar{q} were determined from observations at the Cabauw mast at a height of 40 m and thus close to the level of the LAS; A_T , A_q are functions of T and q and the transmitted wavelength of the LAS ($\lambda = 940$ nm) (Hill et al. 1980). The Bowen ratio at the height of the LAS was not available. As the flux divergence may be significant and different for sensible and latent heat, particularly in morning conditions, we derived B at a height of 41 m from the LES data instead. Since the measured surface fluxes (and thus B_0) were prescribed, we expect that the LES will provide a realistic estimate of the Bowen ratio at the scintillometer height.

3.4.4 Virtual Path Measurements in LES—An Embedded Virtual LAS

In order to study the variability along a measurement path and the variability of the path average, we employ the dissipation method and use virtual measurements along horizontal paths within our LES domain. By doing so, we capture the turbulent fluctuations, represented by the local structure parameter of temperature, as they would be seen from LAS and aircraft. However, on the one hand, the scintillations seen by the LAS are mainly determined by fluctuations at the scale of the beam diameter (0.31 m), while smaller scales are averaged out. Larger scales result in variability of the scintillations. On the other hand, the nominal truncation size is 2–4 m (the actual truncation happens at even larger scales up to $6\Delta_{x,y}$) and hence there is a part of the variability in the structure parameters that is missed by the LES (see Cheinet and Siebesma 2009, Fig. 8).

In contrast to previous studies, the present LES allow for studying the structure parameters in the surface layer, where LAS are typically operated. Path averaging of C_T^2 can be done in two ways. In order to simulate LAS data, the path-weighted average after Wang et al. (1978) is used (see Fig. 9 and Appendix). These virtual LAS (hereafter VLAS) measurements are denoted by $\langle C_T^2 \rangle_p$. In order to simulate aircraft data, a simple arithmetic average is used (denoted by $\langle C_T^2 \rangle_p$).

VLAS measurements are used at typical height levels of LAS measurements between 30 and 70 m above the ground. Additionally we carried out virtual measurements without a weighting function at heights close to the aircraft flights at Cabauw (79, 167, 257, 261 and 625 m, depending on time of the day). In order to study long paths, we carried out the additional simulation cases ME and AE with extended horizontal domains in the x -direction (see Table 1). The virtual measurements were carried out in this extended x -direction. The maximum possible path length was 10.24 and 11.52 km for case ME and AE, respectively, and thus covered the LAS path at Cabauw as well as the aircraft flight legs. Overall we had at least 1,024 paths available for each virtual measurement height. The mean over all VLAS paths in one plane differs slightly from the horizontal mean due to the path weighting. We analyzed the data after 2 h of simulation time and used one-sided causal time averaging based only on past timesteps during the period from 1 to 2 h.

Table 2 Synopsis of basic averaging types that have been applied and for which figures the methods have been used

Average	Data							
	Aircraft		LAS	LES		LES	LES	
	Wavelet m.			Dissipation m.		Spectral m.	Wavelet m.	
	Path ($\langle \rangle_p$)	Local (Δk)	Path ($\langle \tilde{\cdot} \rangle_p$)	Global (G)	Local ($\Delta \mathbf{x}$)	Global (G)	Global (G)	Local (Δk)
Spatial (local)		×						×
Spatial (total)	×			×		×	×	
Spectral	×	×				×		×
Temporal	×	×	×					
Figures	2	5	2	2	3, 8, 10	2, 5, 4	2, 8	3

A local spatial average represents averaging in space over a limited distance, whereas the total spatial average represents the average over the entire data series (path or domain). The lower line in the table header gives the notation or subscript used to denote the given variable

3.4.5 Synopsis of the Data Processing

In order to derive the structure parameters from the different methods, several averaging procedures are applied; this includes spatial, spectral and temporal averages. In Sect. 4 we use all three methods in order to compare the mean profiles of C_S^2 . Two methods for the LES data provide local estimates of C_S^2 that will be mutually compared (dissipation and wavelet method). One method will be used to compare the variability of C_S^2 with measurement data (dissipation method). The used averaging types are summarized in Table 2, and the respective averaging scales and ranges are given in Sects. 3.4.1–3.4.4.

4 Results

4.1 Temperature and Humidity Profiles

The horizontally-averaged (denoted by $\langle \cdot \rangle$) profiles of temperature and humidity from the LES and aircraft observations are shown in Fig. 1. The LES profiles reveal classical CBL profiles with unstable stratification near the surface, a well-mixed layer, a stably-stratified layer in the entrainment zone and in the free atmosphere aloft. As shown in Fig. 1a, the simulated mixed-layer temperature is slightly higher (on average 0.3 K) after 1 h than the observed aircraft profile. Specific humidity is slightly overestimated by the LES as well. The boundary-layer depth in case M is 364 m, which is close to that observed by the aircraft; Fig. 1c, d (case A) reveals a boundary-layer depth of about 1,000 m and negligible deviations between LES and aircraft measurements, except for the humidity in the entrainment zone. Here the aircraft data suggest a smaller humidity jump and an entrainment ratio around zero (see de Arellano et al. 2004, Fig. 4b). We checked the humidity flux profile in the LES and found an entrainment ratio around 0.2, which is at least close to zero. Additionally, de Arellano et al. (2004) gave the mixed-layer velocity scale $w_* = \left[(g/\bar{\theta}) \overline{w'\theta'_0} z_i \right]^{1/3}$ (with g being the gravitational acceleration), which was 0.94 and 1.44 m s^{-1} between 0816–0905 UTC and 1249–1342 UTC, respectively. Due to the similar boundary-layer depth in the observations

Table 3 Scaling parameters for cases M and A

Case	z_i (m)	w_* (m s ⁻¹)	θ_* (10 ⁻² K)	q_* (10 ⁻⁵ kg kg ⁻¹)	$C_{T,*}^2$ (10 ⁻⁵ K ² m ^{-2/3})	$C_{q,*}^2$ (10 ⁻¹¹ kg ² kg ⁻² m ^{-2/3})
M	364	0.89	6.96	6.40	9.50	8.03
A	1038	1.33	5.83	8.54	3.31	7.11

and LES, w_* from the LES was also similar to the observational value, with 0.89 m s⁻¹ in case M and 1.33 m s⁻¹ in case A after 1 h of simulation (see Table 3). We can thus essentially assume that the LES generated a CBL similar to that observed at Cabauw. The measurements of C_T^2 and C_q^2 by aircraft and LAS should thus be comparable to the derived structure parameters from the LES data.

4.2 Structure Parameter Profiles

Figure 2 shows the mean vertical profiles of C_T^2 and C_q^2 for cases M and A after 1 h of simulation calculated by the different methods; aircraft and LAS data were added. Normalization has been applied according to Burk (1981) using z_i and the mixed-layer temperature and humidity scales after Deardorff (1974): $\theta_* = w'\theta'_0/w_*$ and $q_* = w'q'_0/w_*$ (see also Table 3),

$$C_{T,*}^2 = \frac{\theta_*^2}{z_i^{2/3}}, \quad (17a)$$

$$C_{q,*}^2 = \frac{q_*^2}{z_i^{2/3}}. \quad (17b)$$

4.2.1 LES Profiles

The profiles of C_T^2 (Fig. 2a,c) are characterized by high values of C_T^2 close to the surface that are caused by large temperature gradients that lead to a large production of temperature variance and hence to an increase in the energy level in the inertial subrange. C_T^2 decreases in the mixed layer according to $F_T(z/z_i)^{-4/3}$ up to a height of $z/z_i = 0.6$ as proposed in theory (Wyngaard and LeMone 1980); here, F_T is a proportionality constant. Above, entrainment processes dominate and a secondary peak is present in the entrainment zone, where sharp local temperature gradients between the free atmosphere and the boundary layer lead to a high production of temperature variance.

When entrainment effects are negligible, C_q^2 should follow $F_q(z/z_i)^{-4/3}$, at least in the lower boundary layer (Fairall 1987). As shown in Fig. 2b,d, a minimum is located at $z/z_i = 0.3$ and increasing values with height are found, which are caused by high humidity fluctuations in the upper boundary layer due to the entrainment of dry air from the free atmosphere (Peltier and Wyngaard 1995). It is evident that all three calculation methods show these general shapes, which are in agreement with theory (Wyngaard et al. 1971a,b), the semi-empirical profiles after Kaimal et al. (1976) and Fairall (1987), observations (e.g. Wyngaard and LeMone 1980; Kohsiek 1988) and the recent LES of Cheinet and Siebesma (2009) and Cheinet and Cumin (2011).

The magnitude of C_T^2 in the mixed layer from the spectral method is 20 % lower than the semi-empirical profile of Kaimal et al. (1976). Since C_T^2 depends only on the power spectral density, the LES obviously renders proper energy levels in the inertial subrange of

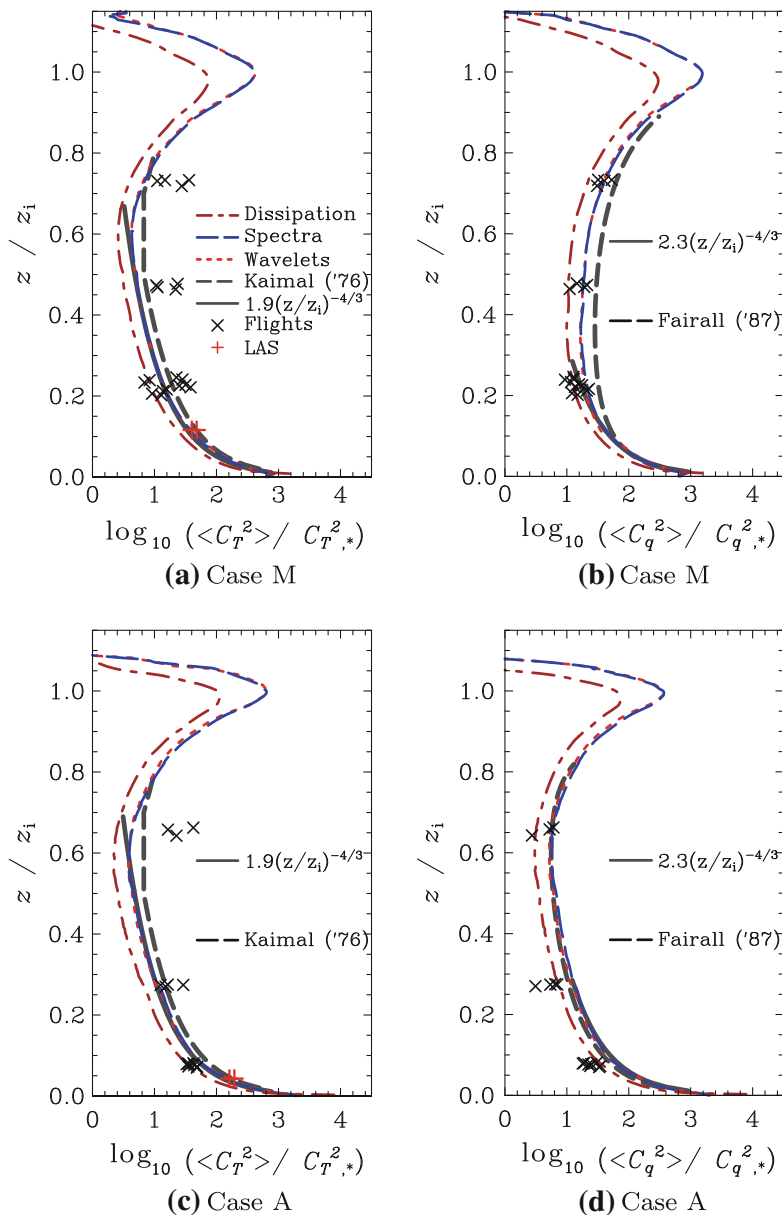


Fig. 2 Normalized profiles of C_T^2 and C_q^2 after 1h of simulation time, derived from different methods, and on a logarithmic scale. Aircraft (\times symbols) and LAS (+ symbols, red) measurements as well as the semi-empirical profile after [Kaimal et al. \(1976\)](#) (dashed black line) are included. Similarity relationships are given for the spectral method (solid black lines)

CBL spectra (respective spectra will be shown and discussed in Sect. 4.5). Therefore, we will hereafter use the spectral method as a reference for the other two methods. The proportionality constant F_T , however, is ≈ 1.9 and thus lower than the value of 2.7 proposed by [Wyngaard and LeMone \(1980\)](#). The dissipation method shows lower values in C_T^2 compared to the spectral method by a factor of 1.7. [Cheinet and Siebesma \(2009\)](#) found a gap of a factor 2 between the dissipation method and the profile of [Kaimal et al. \(1976\)](#). Our results support their finding and we will address this underestimation of the structure parameters by the

dissipation method in Sect. 4.5. The wavelet method shows values similar to the spectral method.

In case M, C_q^2 shows lower values than suggested by the semi-empirical profile after Fairall (1987), whereas in case A, C_q^2 (spectral method) is in remarkable agreement with Fairall (1987). In the lower boundary layer, C_q^2 (Fig. 2b,d) follows the expected decrease with $F_q \approx 2.3$, which is higher than suggested by Wyngaard and LeMone (1980). They also state that differences between F_T and F_q can be ascribed to differing surface transfer processes of the active scalar temperature and the more or less passive scalar humidity. In case M, the peak of C_q^2 at the top of the mixed layer is greater than that of C_T^2 , whereas the peak values are similar for case A. This seems consistent with the fact that the entrainment ratio for q is around 1.3 for case M and around 0.2 for case A (cf. de Arellano et al. 2004, Fig. 4). This implies that the profile of the humidity variance differs significantly from the profile of temperature variance (see Moene et al. 2006 and Sect. 4.3.1) and hence also the dissipation rates. For C_q^2 we observe a gap of 1.8 between the spectral and dissipation methods, whereas the spectral and wavelet methods give very similar profiles.

4.2.2 Validation of the LES Profiles with Cabauw Observations

C_T^2 shows very good agreement between the LES and LAS in case M (Fig. 2a, c). The spectral method compares well to the low-level flights, but the aircraft data do not show the decrease with height as proposed by Kaimal et al. (1976), leading to a significant underestimation of C_T^2 in the LES at heights above $z/z_i = 0.4$. In case A, the LES slightly overestimates C_T^2 from the low-level flights, while the LES compares well to three of the four medium-level flights at $z/z_i = 0.27$. The higher-level flights again suggest an underestimation in C_T^2 by the LES. It appears that C_T^2 compares well with the aircraft data between $z/z_i = 0.2$ and $z/z_i = 0.3$, and below these heights C_T^2 is overestimated. Above, the LES data show an underestimation of C_T^2 . A possible reason for this discrepancy might be the fact that we assumed free convective conditions, whereas the observations are made in light winds. Thus in reality there may be wind shear across the entrainment zone that leads to extra scalar variance and hence higher C_T^2 . In addition, mesoscale fluctuations in advected scalars (here temperature) may yield an extra production of variance as shown by Kimmel et al. (2002). Such effects of shear and advection might generally also apply to C_q^2 . As will be discussed in Sect. 4.6.3, the aircraft measurements suffer from a statistical uncertainty of about 10–20% (shown for C_T^2), which has to be considered as well.

The structure parameter for humidity in the LES data is in much better agreement with the aircraft observations (see Fig. 2b, d). Despite a tendency for a higher C_q^2 , the LES profile agrees well with the aircraft data, particularly for case M. The decrease with height is reproduced well by the LES. For case A, the LES (spectral method) values agree with two of the three high-level flights at $z/z_i = 0.65$, while at the other levels the aircraft data are below the LES values. The statistical uncertainty for aircraft measurements (see Sect. 4.6.3) are shown for C_T^2 , but an uncertainty of 10–20% was obtained for C_q as well.

4.3 Spatial Variability of Structure Parameters

4.3.1 LES Results

Cheinet and Siebesma (2009) investigated the spatial variability of C_T^2 from the dissipation method. Our analysis reproduces their findings and we found similar characteristics for C_T^2

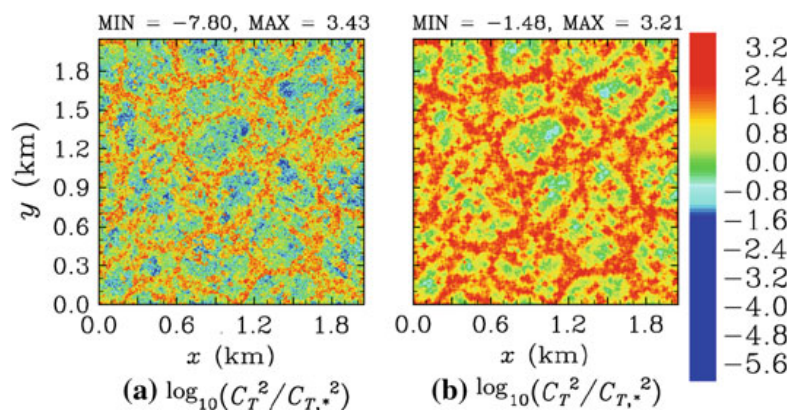


Fig. 3 Cross-sections of $\log_{10}(C_T^2/C_{T,*}^2)$ in the surface layer at $z = 41$ m (LAS height), derived from the dissipation (a) and wavelet methods (b). Results are shown for case M after 1 h of simulation time. Maximum and minimum values are given above the frames

and C_q^2 , which is the reason we limit ourselves to a discussion of C_T^2 in detail. For example, in Fig. 3a a horizontal cross-section of C_T^2 at 41 m (LAS height) is shown for case M, derived with the dissipation method. The flow circulation generates a cellular pattern of C_T^2 with high values at the edges of the cells. Figure 3b shows the respective pattern, derived from the wavelet method. Generally, the dissipation and wavelet methods generate the same structure-parameter pattern. The fact that even the smallest structures are reproduced in both patterns is a remarkable feature and emphasizes that both methods correlate well. However, one might prefer the wavelet method simply because it neither depends directly on the SGS model nor on the parameter β . Both methods also show significant differences: due to generally too low values produced by the dissipation method, the maximum values coincide (3.21 and 3.43 for wavelet and dissipation methods, respectively), whereas minimum values differ significantly (-1.84 and -7.80). Note that the range of values for the wavelet method strongly depends on the spectral averaging range, which was 13–106 m in this case; this applies also to spatial averaging. A direct comparison with the dissipation method is thus challenging.

Unfortunately we found that the wavelet method required a very large computing time in order to calculate a single horizontal cross-section. Furthermore, it is to some extent sensitive to changes of parameters, such as wavelet scale and the chosen averaging window. It was thus not feasible to apply this method for an extended model domain or for several points in time. Hence we limited the application of this method to the derivation of vertical profiles (Fig. 2) and a horizontal cross-section (Fig. 3b). We instead employed the dissipation method in Sect. 4.6 to investigate the variability of C_T^2 along horizontal paths in the lower boundary layer as well as for validation with local structure parameters from aircraft data.

Figure 4 shows the profiles of the variance σ^2 of C_T^2 and C_q^2 (dissipation method). The shape of the profiles coincides with the structure-parameter profiles with a maximum located close to the surface and a secondary maximum at the top of the boundary layer (cf. Fig. 2). The surface peak is similar for cases M and A, whereas the upper maximum is more affected by different entrainment regimes as was pointed out in Sect. 4.2 (see also Moene et al. 2006). The variances rapidly decrease with height in the surface layer and slightly decrease above in the mixed layer until entrainment processes become important. For C_q^2 this difference is noticeable since humidity structures in the CBL are dominated by the entrainment of

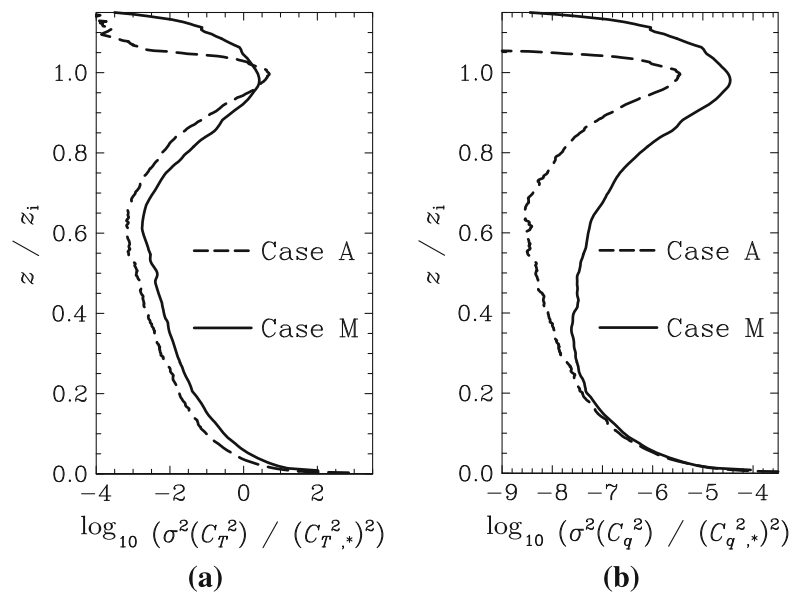


Fig. 4 Normalized profiles of the variances of C_T^2 (a) and C_q^2 (b) after 1 h from cases M and A, derived from the dissipation method

dry air from the free atmosphere. From Figs. 2 and 4 we can infer that $\log_{10}(\sigma^2(C_T^2))$ and $\log_{10}(\sigma^2(C_q^2))$ are linearly correlated to $\log_{10}(C_T^2)$ and $\log_{10}(C_q^2)$, respectively, even though the proportionality is not exact.

4.3.2 Comparison with Aircraft Data

By means of the wavelet method we calculated local structure parameters from the aircraft data (see Sect. 3.4.2). In order to compare the local C_T^2 and C_q^2 from aircraft with the LES data, a running average was applied to the local structure parameters from the dissipation method over a range of 208 m. This is identical to the upper limit of the spectral range over which the wavelet estimates were averaged. In Fig. 5 statistics of the aircraft measurements of the local C_T^2 , C_q^2 and virtual measurements in the LES are shown at the three different flight levels.

From Fig. 5a, c it can be seen that the mean C_T^2 derived from the aircraft is greater than that from the LES data. This is consistent with the underrepresentation of small-scale variations in the LES, although the difference is not constant for different heights. This was already shown and discussed in Sect. 4.2.2 (cf. Fig. 2a, c). The variability of C_T^2 along the path is generally less for the aircraft data than for the LES. Since the spatial variability in the LES data is directly related to the length of the running average, the higher variability than observed for the aircraft data might be ascribed to the fact that the running average cannot exactly mimic the spatial averaging that is involved in the wavelet method procedure (see Sect. 3.4.1). The largest differences in the standard deviation are found at the lowest flight level, where large amplitude variations at small scales dominate. Here, averaging has a larger effect than at higher levels.

The spatial statistics for C_q^2 from LES are in remarkable agreement with the aircraft observations (see Fig. 5b,d). Both show a similar range of values as well as standard deviation at all flight levels and in both simulations. The mean values differ only slightly. In case ME the aircraft data provide higher spatial means than the LES-derived C_q^2 , while in case AE the

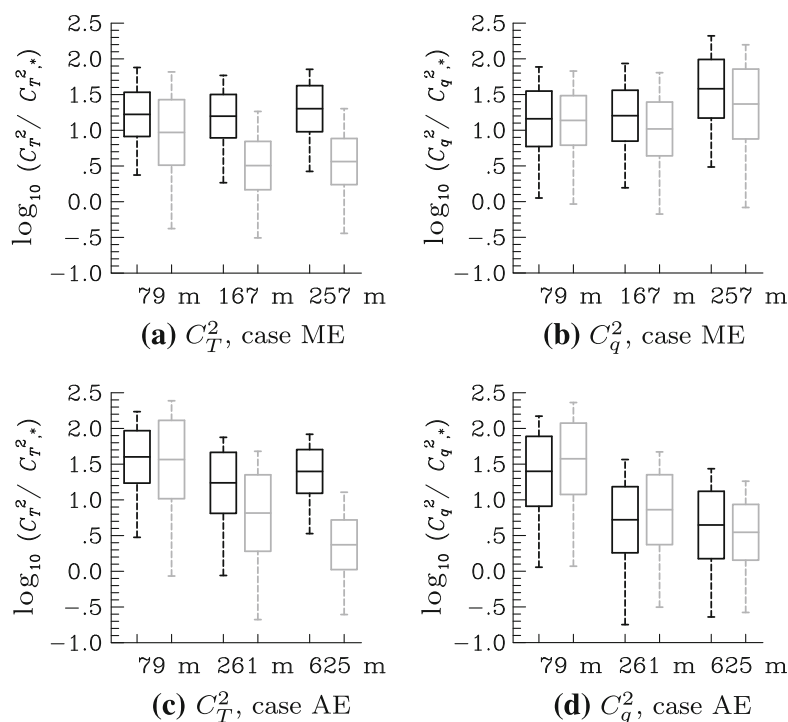


Fig. 5 Statistics of C_S^2 along the aircraft flight legs (black, wavelet method) and virtual measurements along horizontal paths in the LES (grey, dissipation method) for case ME (a, b) and case AE (c, d) at three different heights. For the wavelet method, the spectral window 50–208 m was chosen. A running average over 208 m has been performed on the virtual paths in the LES to make them comparable to the aircraft data. The end of the whiskers represent the maximum/minimum values; the middle of the box is the average over all path-means, and the top and bottom of the boxes show one standard deviation of $\log_{10}(C_S^2/C_{S,*}^2)$ above and below this mean, respectively. The number of flights varied for each height and case between 3 and 11, whereas 1,024 virtual measurements were available from the LES data

aircraft estimates tend to be lower. This is in agreement with the discussed mean profiles (see Fig. 2b, d).

4.4 Modelling ε_S and ε_{TKE} : Validation

In Sect. 4.2.1 we showed that the profiles of C_S^2 , derived from the spectral and dissipation methods, differ in magnitude by a rather constant factor. We also showed that the shape of these profiles is very similar. However, one might claim that modelling the dissipation rates by means of Eqs. 10 and 11 is questionable. Cheinet and Siebesma (2009) compared their modelled dissipation profiles against the profiles from Sorbjan (1988) and found fairly good agreement. We now try to show that Eqs. 10–11 can be used for the derivation of C_S^2 by additionally calculating the dissipation rates directly from the turbulence spectra (Eqs. 5–7). The data processing was done analogous to the derivation of C_S^2 as described in Sect. 3.4.1.

Figure 6 shows the calculated profiles of ε_T , ε_q , and ε_{TKE} for case M. It is obvious that the modelled profiles show the same shape as the profiles that have been derived from the spectra, but with a significant gap between them. The modelled profiles agree with the profiles shown by Cheinet and Siebesma (2009), while the dissipation rates from the spectral method are in much better agreement with Sorbjan (1988). While ε_{TKE} shows a slight linear decrease with height, the shape of the profiles of ε_S is similar to that of C_S^2 (cf. Fig. 2a, b). As both methods (modelled and spectral) give profiles with the same shape, we can thus conclude that Eq. 10

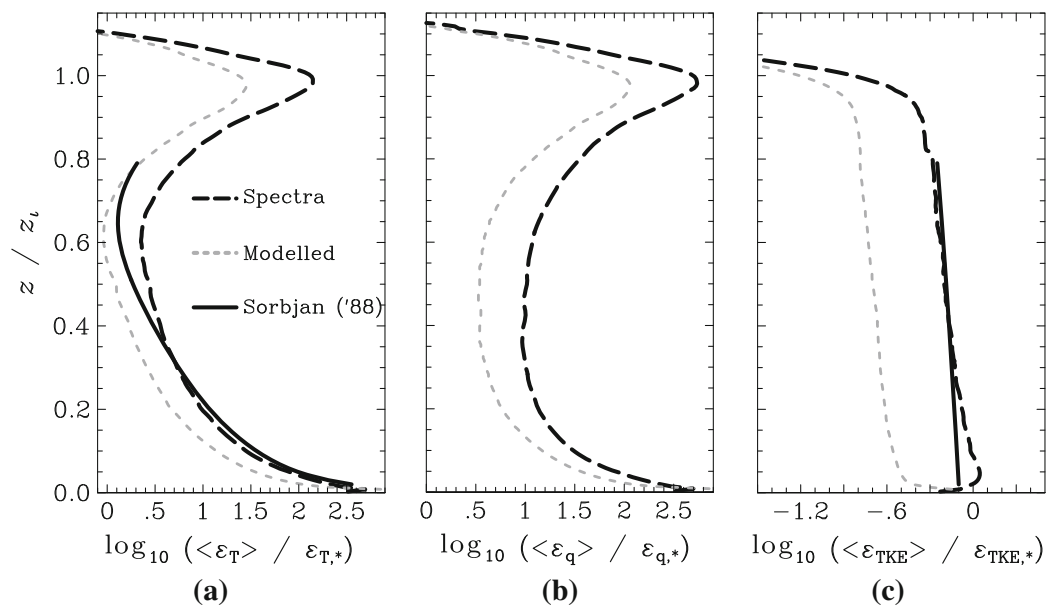


Fig. 6 Profiles of the modelled dissipation rate of temperature fluctuations (a), humidity fluctuations (b), and TKE (c) for case M (short dashed lines) and from the turbulence spectra (dashed lines). The profiles are on a logarithmic scale and have been normalized with $\varepsilon_{S,*} = \frac{S_*^2 w_*}{z_i}$ (a, b) or $\varepsilon_{TKE,*} = \frac{w_*^3}{z_i}$ (c). The profiles after Sorbjan (1988) are given by solid lines

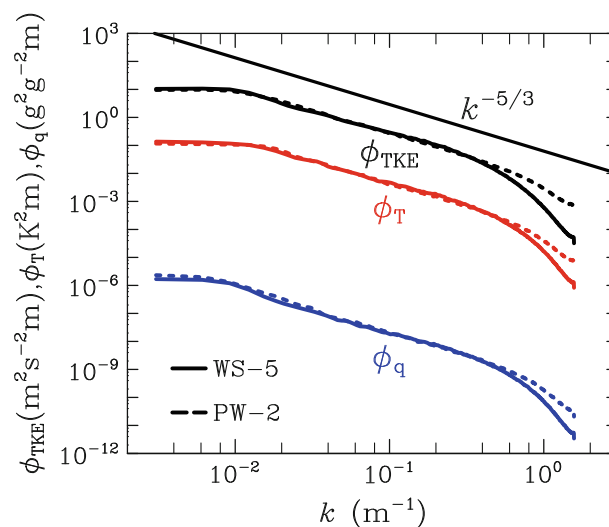
and Eq. 11 are suitable for modelling the dissipation rates (at least for mean profiles). In Eq. 9 the underestimation in ε_{TKE} leads to an overestimation, but the underestimation in ε_S dominates and yields an underestimation in C_S^2 . The resulting profiles of C_S^2 from the spectral and dissipation methods hence differ by a constant factor. This gap between the two methods is explored below.

4.5 Modelling C_S^2 : Exploring the Gap Between the Spectral and Dissipation Methods

In the previous section we showed that a discrepancy between the modelled dissipation rates and those derived directly from the turbulence spectra lead to the gap in the vertical profiles of C_S^2 . Cheinet and Siebesma (2009) supposed that the gap in C_S^2 might be ascribed to uncertainties in α , β , the low Prandtl number in their LES, and a decrease in the spectral density at the highest resolved wavenumbers. The latter will be the starting hypothesis for the analysis in this section.

Figure 7 shows the power spectral density of TKE, temperature and humidity (ϕ_{TKE} , ϕ_T and ϕ_q , respectively), where it is obvious that the spectra capture the inertial subrange very well. At high wavenumbers (small eddies), the power spectral density decreases significantly. This fall-off is a well-known effect of the SGS model, which dissipates energy at the smallest resolved scales (Moeng and Wyngaard 1988). For many higher-order advection schemes, such as WS-5, this fall-off is intensified by numerical dissipation (Glendening and Haack 2001). The spectral method derives C_S^2 directly from the power spectral density in the inertial subrange, while the dissipation method relates C_S^2 to the local gradients of S (see Eq. 13). These gradients mainly capture small-scale variations of the turbulent flow and might thus be directly affected by the spectral fall-off at highest resolved wavenumbers. Furthermore, the discretization of the local gradients in space might play an important role as interpolation is necessary to determine the gradients at a specific location in the LES grid volume. In order

Fig. 7 Area-averaged spectra of TKE, temperature and humidity at a height of $z/z_i = 0.5$, derived from case M with the fifth-order advection scheme of Wicker and Skamarock (2002) (solid lines) and second-order advection scheme of Piacsek and Williams (1970) (dashed lines)



to investigate these possible causes we replaced the central differences approximation of the gradients (see Sect. 3.4.1) with forward differences. We also carried out two comparative simulations with the PW-2 scheme, which does not suffer from numerical dissipation. Again, we present only the results of case M and restrict the analysis to C_T^2 .

4.5.1 Effects of Interpolation

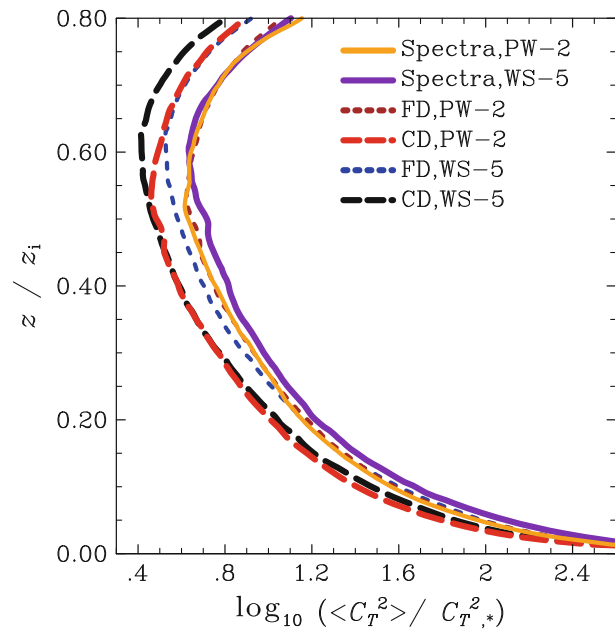
The scalar quantities are defined in PALM at the centre of the grid volumes, and in order to calculate the local gradients of temperature or humidity in all spatial directions at the same location, central finite differences are used. This is equivalent to calculating the local gradients using one-sided differencing and subsequent interpolation to the centre of the grid volume. Owing to the central differencing, scalar fluctuations at the scale of the LES grid $\Delta_{x,y,z}$ are filtered out and cannot be captured. This approximation will consequently underestimate the turbulent fluctuations and hence also underestimate the structure parameters. For comparison we replaced the central differencing with simple forward differencing and omitted the interpolation to the same location. In this way the local gradients were calculated at different positions in the grid volume. This yields also incorrect local estimates of the structure parameters since the gradients implicit in Eq. 11 cannot be calculated at the same location. Although the local estimates will be slightly inaccurate, the horizontal average of the structure parameters, however, will be less affected by this inaccuracy (especially for the horizontal derivatives).

Figure 8 (black lines) shows C_T^2 , derived from the dissipation method using either central or forward differences, and in comparison with the spectral method. It is obvious that the gap between the spectral and dissipation methods is halved when using one-sided differences. This shows that at least 50% of the gap might already be explained by the fact that the approximation of the gradient misses fluctuations at the scale of the LES grid spacing.

4.5.2 Effects of Numerical Dissipation of the Advection Scheme

Based on the finding from the previous section we carried out comparative simulations with the lower-order PW-2 advection scheme that does not suffer from numerical dissipation. The PW-2 scheme has some disadvantages, amongst which is that it suffers from

Fig. 8 Normalized profiles of C_T^2 from spectral (solid lines) and dissipation method after 1 h for case M, simulated with the advection schemes WS-5 and PW-2. For the dissipation method the temperature gradients have been approximated using central differencing (CD, dashed lines) and forward differencing (FD, short-dashed lines)



immense numerical dispersion that leads to unrealistic small-scale structures. This advection scheme is thus not an appropriate choice for deriving realistic local estimates of the structure parameters.

Turbulence spectra from the simulations with PW-2 are additionally given in Fig. 7. A gap in the power spectral density is visible between simulations with PW-2 and WS-5 at the highest wavenumbers, caused by the additional numerical dissipation of the WS-5 scheme. This spectral fall-off leads to too little energy in the smallest resolved scales. It can also be seen that this effect is more prominent for TKE than for the scalar quantities. Furthermore, though less visible, the resolved energy level in the inertial subrange is slightly higher for WS-5 than for PW-2. Consequently, as shown in Fig. 8, C_T^2 , derived from the spectral method, is slightly lower for PW-2 than for WS-5. C_T^2 derived from the dissipation method (central differences), however, does not show a significant response to a change in the advection scheme; at least up to heights where entrainment processes become important. This is counterintuitive as one would expect that the additional numerical dissipation should increase the destruction of fluctuations at the smallest resolved scales and hence decrease C_T^2 .

4.5.3 Combined Effects of Interpolation and Numerical Dissipation

Figure 8 also shows the results for the combination of PW-2 with the one-sided approximation of the scalar gradients. This profile is in remarkable agreement with the respective profile from the spectral method for PW-2. Moreover, a small gap between PW-2 and WS-5 is shown that was not found for central differences. The additional dissipation thus seems to mainly influence the smallest scale, but does not significantly affect larger scales, which are captured by central differences as mentioned above. The good agreement between the spectral and dissipation methods for PW-2 is surprising, since we see from the turbulence spectra in Fig. 7 that the local gradient should suffer from the energy fall-off at high wavenumbers, even for PW-2. The reasons for this good agreement remain unclear and might possibly be ascribed to the fact that the local scalar gradients also carry information from smaller wavenumbers that are reasonably well resolved. Furthermore an overestimation of the signal due to the

one-sided approximation is conceivable. However, we can assume that the remaining gap between the dissipation method (one-sided differences) and the spectral method with WS-5 is caused by the numerical dissipation of the advection scheme.

4.5.4 Summary

In summary we found that the observed gap between the spectral and dissipation methods can be traced back, to a great extent, to the numerical dissipation of the WS-5 advection scheme and the interpolation in space that was necessary to calculate the local scalar gradients. Since the gap between the spectral and dissipation methods is found to be a constant factor, and using one-sided differences give incorrect local estimates, we will use the most straightforward formulation, i.e. the dissipation method with centred differences and the more sophisticated WS-5 scheme for the rest of the article. This decision is also based on the fact that the spectral method does not allow the derivation of local estimates of the structure parameters and that the wavelet method was found to require enormous computational resources (see Sect. 4.3.1).

4.6 Application of LES Results to Estimate the Statistical Uncertainty in LAS Measurements

We now address one important source of errors in LAS measurements, the statistical uncertainty due to the temporal and spatial variability of C_T^2 . Since C_T^2 depends on the randomly distributed turbulent fluctuations, the question arises whether the path-averaged C_T^2 is representative for the horizontal mean under horizontal homogeneous surface conditions. Since LES allows for deriving C_T^2 as a four-dimensional quantity, it presents itself as a unique instrument with which to study the variability of LAS path measurements.

4.6.1 Spatial Variability of C_T^2 Along a Virtual LAS Path

Figure 9 shows the variability of C_T^2 along an arbitrarily chosen virtual path for cases ME and AE at a height of 41 m (height of the LAS at Cabauw). The probability density functions of the shown spatial series suggest a log-normal distribution of C_T^2 along the path, a distribution that can be classified into two different turbulence regimes. Low turbulence intensity with low C_T^2 outside the plumes alternates with high turbulence regions and high C_T^2 values inside the plumes. The probability density functions support the two-regime model, which suggests a superposition of two log-normal distributed convective regimes (light background turbulence and strong turbulence within plumes). [Petenko and Shurygin \(1999\)](#) introduced this two-regime concept based on sodar measurements and it was also found in the LES data of [Cheinet and Siebesma \(2009\)](#). Local maxima occur frequently at the edges of plumes, where the largest gradients in temperature reside (cf. Fig. 3). Case ME exhibits less variance in the scaled and logarithmic C_T^2 along the path ($\sigma^2 = 1.12$) than case AE ($\sigma^2 = 1.43$). The VLAS measurement in case ME gives $\log_{10}(\langle \widetilde{C}_T^2 \rangle_p / C_{T,*}^2) = 1.4$, which is lower than in case AE ($\log_{10}(\langle \widetilde{C}_T^2 \rangle_p / C_{T,*}^2) = 2.0$).

These findings are closely related to the normalized height of the VLAS and the stability parameter $-z/L$, with

$$L = \frac{-\langle \theta_v \rangle \langle u_* \rangle^3}{\kappa g \overline{w' \theta'_{v0}}} \quad (18)$$

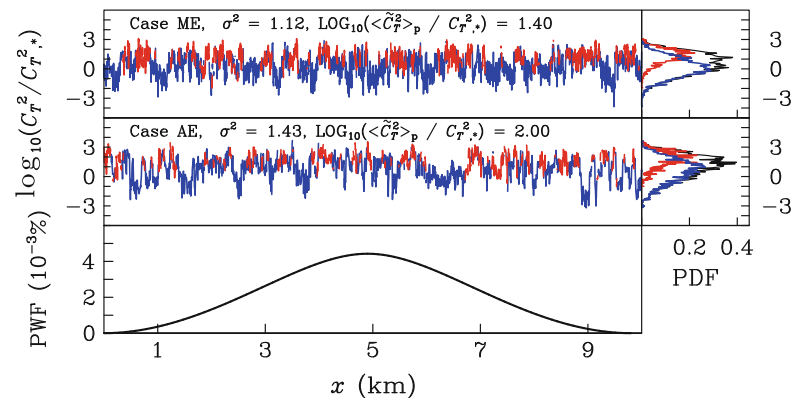


Fig. 9 C_T^2 along an arbitrarily chosen VLAS path of 9.8 km length at a height of 41 m for case ME (*top left*) and case AE (*middle left*) after 1 h simulation time. *Red colours* refer to updrafts (vertical velocity $w > 0.3 \text{ ms}^{-1}$), *blue colours* for background turbulence ($w \leq 0.3 \text{ ms}^{-1}$). The normalized VLAS measurements ($\log_{10}(\langle C_T^2 \rangle_p / C_{T,*}^2)$) and the variance of $\log_{10}(C_T^2 / C_{T,*}^2)$ are listed in the graphs. The probability density functions of updraft regions, background turbulence and the sum of both (*black*) of the shown spatial series of $\log_{10}(C_T^2 / C_{T,*}^2)$ are given on the *right side*. The *bottom graph* displays the path-weighting function (PWF) along the path for the VLAS measurements

being the Obukhov length, where θ_v is the virtual potential temperature and $\kappa = 0.4$ is the von Kármán constant. Since u_* is calculated locally in the LES (see Sect. 3.3), the horizontal average deviates from zero, even in the local free convection limit. In the surface layer, which we simply assume to be the lowest 10% of the boundary layer ($z/z_i \leq 0.1$), there is greater variance than in the mixed layer above (see Fig. 4). Since the nominal height of the VLAS is constant, it is evident that in the shallow CBL, which develops in the morning, the normalized height of the VLAS is $z/z_i \approx 0.1$. The VLAS is thus located at the top of the surface layer. Braam et al. (2012) showed that the LAS at Cabauw can be above the surface layer frequently in the early morning hours. In the afternoon z_i increases in such a way that the VLAS is well within the surface layer (here $z/z_i = 0.04$). At the same time $-z/L$ increases, leading to more unstable conditions at the VLAS height. It is not possible to separate both effects. The virtual measurement $\langle \widetilde{C_T^2} \rangle_p$ and the variance along the path, however, are consequently higher in the afternoon than in the morning.

4.6.2 Temporal Variability of the Path-Averaged C_T^2

The temporal variability of a single VLAS measurement at 41 m for a path length of 9.8 km is shown in Fig. 10, along with the temporal mean over the analysis period of 1 h. The path mean of C_T^2 varies rapidly in time, due to the turbulent motions along the path. These fluctuations result in relative standard deviations (defined as the standard deviation divided by the mean; *RSD*) of about 11%. We found values around 11% to be representative for all VLAS in the LES, but to be strongly dependent on the path length. This result is in agreement with the LAS data that showed an *RSD* between 13 and 15% during the measurement period (not shown). For a shorter path in the LES of only 2 km, *RSD* increases up to 22%. A temporal average over an appropriate period (see below) is thus required in order to ensure a low statistical uncertainty. Furthermore, $\langle \widetilde{C_T^2} \rangle_p$ (and $\langle C_T^2 \rangle_p$ in the mixed layer), on-the-one hand, was found to decrease with height, while on the other hand, its *RSD* increased with height. This is in agreement with Cheinet and Siebesma (2007).

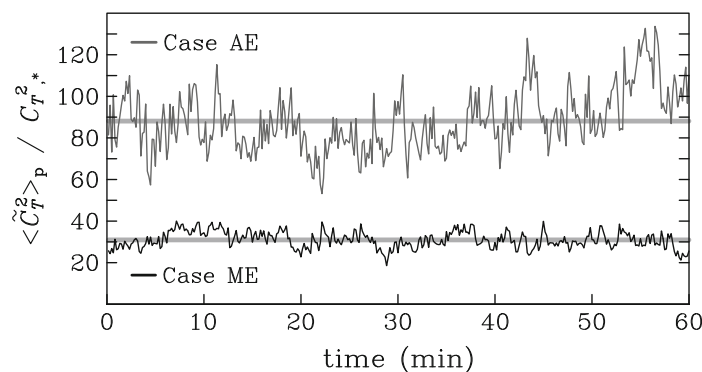


Fig. 10 Time series of the normalized $\langle \widetilde{C}_T^2 \rangle_p$ from the VLAS (path length of 9.8 km) at a height of 41 m for case AE (top) and case ME (bottom). The time averages $\overline{\langle \widetilde{C}_T^2 \rangle_p}$ of the LES series are plotted as grey lines

4.6.3 Representativeness of the Path Average

From the previous Sect. 4.6.1 and Sect. 4.6.2 it is evident that the spatial variability of C_T^2 along the VLAS path, as well as the temporal variability of the path mean, can lead to significant fluctuations in C_T^2 and thus to variations in the VLAS measurements $\langle \widetilde{C}_T^2 \rangle_p$. In order to evaluate the statistical uncertainty of a single virtual measurement due to insufficient temporal/spatial averaging of the randomly distributed convective motions, we determined the *RSD* of C_T^2 from the available virtual path measurements (at least 1,024, depending on the path length). By calculating the *RSD*, it is possible to estimate the representativeness of path measurements of C_T^2 for a homogeneous area, i.e. the model domain.

The uncertainty in LAS measurements can be reduced by adding temporal averaging to the path averaging. We thus calculated *RSD* as a function of the VLAS path length and the temporal averaging period at different height levels (every 4 m). The maximum path length was restricted by the model domain size. The longer the path distance, the more convective updrafts and downdrafts can be captured and consequently averaged by a single path measurement. Since the VLAS measurements during daytime are usually within the surface layer, the ground might have more influence on the turbulence than the capping inversion and z_i should not be a relevant parameter (Wyngaard et al. 1971a). Hence, local free convection scaling was applied. For in situ measurements z_i and the surface fluxes might change rapidly. Time-averaging intervals of 1 h are thus usually not exceeded, and we limit ourselves to practically relevant cases and limit the temporal average to at most 1 h.

We found *RSD* to depend on the height of the VLAS, and in order to achieve results that are valid for any LAS set-up in the local free convection layer, we scaled the path length with its height above the ground. The results showed that *RSD* now mainly depended on the ratio of the VLAS path length to height above the ground, at least for VLAS measurements at $z/z_i \leq 0.1$ (we analyzed data every 4 m in the z -direction). Here *RSD* differed only by 2–3 % between different heights. Figure 11 shows that *RSD* decreases with increasing averaging time and path length. For a VLAS of 9.8-km length at a height of 41 m (equivalent to a ratio of 239), *RSD* is about 15 % in both cases, if no time average is applied. Additional averaging over a period of 15 min (case ME) and 10 min (case AE) is able to reduce *RSD* to below 10 %, which we regard as a target value below. For shorter VLAS paths (lower ratio of length to height), a longer averaging period is necessary to obtain the same *RSD* values. Figure 11 shows that the path in any case requires a length of at least $80z$ in order

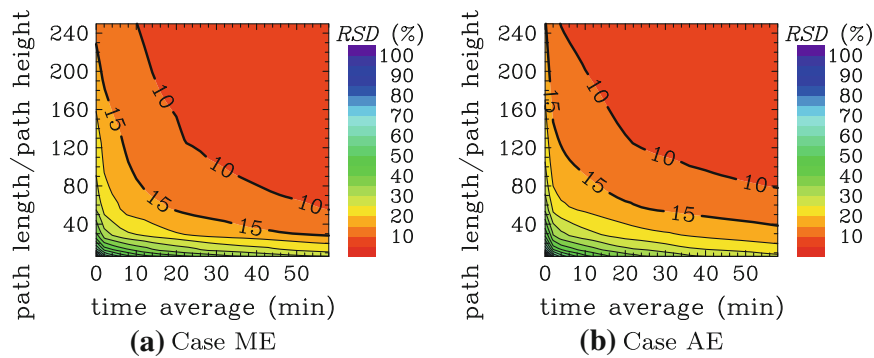


Fig. 11 RSD of $\overline{\langle C_T^2 \rangle_p}$ (in %) against the time-averaging interval and the ratio of path length to the path height (here 41 m above ground)

Table 4 RSD (in %) of $\overline{\langle C_T^2 \rangle_p}$ (flights) and $\overline{\langle C_T^2 \rangle_p}$ (LAS) at different heights for the Cabauw measurements derived from LES

Case	LAS	Low flight	Medium flight	High flight
Height (m)	41	79	167/261	257/625
Path length (km)	9.8	10	10	10
Averaging time (min)	10	–	–	–
ME	9.7	15.6	13.6	10.2
AE	8.7	15.9	23.2	19.2

to obtain $RSD \leq 10\%$. This also supports the result of [Cheinet and Siebesma \(2007\)](#) that a measurement height of 80 m and a path distance of 2 km (equivalent to $25z$) is not sufficient to obtain representative path-averaged values. Unfortunately we did not find a suitable time scale to make the temporal-averaging interval dimensionless so that Fig. 11a, b become more similar. We tried to apply the surface-layer time scale (free convection, see [Stull 1988](#) as well as the convective time scale (z_i/w_*), but the results suggested that a suitable scale would be somewhere in between, at least for the two studied cases. Anyhow, Fig. 11 suggests a rough independence of our results from the boundary-layer depth, and might be used to estimate the statistical uncertainty for a given LAS system in the surface layer. We are aware of the fact that this conclusion is based on the results from only two different simulations and that a more detailed sensitivity study would be required to evaluate whether our findings are case-sensitive or if they are valid for an arbitrary LAS set-up.

From these findings we return to the uncertainties of the measurements at Cabauw. Table 4 shows RSD for both LAS and aircraft, derived from the VLAS and virtual aircraft measurements of the structure parameters. The VLAS data were averaged over a time interval of 10 min, which was the same averaging interval that was applied to the LAS data. The aircraft measured instantaneously over a path length of about 10 km. The RSD for the LAS at Cabauw is below 10%, owing to the extremely long LAS path with a combined time average. In contrast to the LAS, no explicit time averaging was feasible for aircraft data. Table 4 suggests that a higher RSD up to 23% has to be considered for a single flight. When more repetitions are flown, RSD will decrease (four repetitions would reduce RSD by a factor of 2). Our analysis suggests that a typical uncertainty in the order of 10–20% has to be taken into account. It is also shown that RSD increases with height in the lower half of the mixed layer as suggested by [Cheinet and Siebesma \(2007\)](#).

5 Summary and Conclusions

The turbulent structure parameters for temperature and humidity were investigated by means of LES of the CBL. Two high-resolution simulations of the morning and afternoon CBL, driven by airborne and surface measurements at Cabauw in The Netherlands, were performed. Three different methods, based on the Fourier spectrum of turbulence, a method based on local dissipation rates and a new method based on the local estimate of the Fourier spectrum using wavelet analysis were used to obtain vertical profiles of the structure parameters from LES data. We found that the methods based on the power spectral density in the inertial subrange from Fourier spectra and wavelet analysis compare very well with the proposed profiles after [Kaimal et al. \(1976\)](#) and [Fairall \(1987\)](#). The derivation of local estimates of the structure parameters by means of the method based on wavelets, however, turned out to be rather problematic as it required enormous computing time. Moreover we derived C_T^2 and C_q^2 from aircraft observations and LAS measurements at Cabauw, and found that LES estimates of C_T^2 were in very good agreement with the LAS observations. The LES data did compare well for C_q^2 with the aircraft observations, but C_T^2 from the aircraft data did not show the proposed decrease with height, for which we do not have a satisfying explanation. It can possibly be ascribed to wind shear or variance production by a mesoscale gradient in advected scalar fields ([Kimmel et al. 2002](#)), which was not considered in the LES.

Local structure parameters were derived by means of a method based on local dissipation from the LES data. The characteristics of these local structure parameters were in agreement with the recent LES of [Cheinet and Siebesma \(2009\)](#) and [Cheinet and Cumin \(2011\)](#) and reflect the structure of turbulence well. This was shown by means of probability density functions that supported the two-regime model developed by [Petenko and Shurygin \(1999\)](#) based on sodar measurements. Moreover, both dissipation and wavelet methods displayed the same cellular pattern of high intensity and low intensity turbulence in the surface layer. However, a gap in the magnitude between the structure parameters from the spectral and dissipation methods was observed. It can be ascribed to a combined effect of the approximation of the local gradients of temperature and humidity by means of central differencing and additional numerical dissipation of the fifth-order scheme after [Wicker and Skamarock \(2002\)](#). We could show that central differencing implies an underestimation in the local scalar gradients that makes up 50% of the observed gap in the structure parameters. A comparison of the vertical profiles from simulations with the fifth-order advection scheme and a second-order scheme of [Piacsek and Williams \(1970\)](#), which does not suffer from numerical dissipation, showed that the remaining underestimation of the structure parameter vanished in the absence of numerical dissipation.

Horizontal virtual path measurements of C_T^2 at different heights were used in order to explore the spatial and temporal variability along a single line or LAS path. The representativeness of path measurements for a horizontal area was studied using the statistical uncertainty due to the randomly distributed convection. We focussed on the implications for LAS in the surface layer and airborne measurements. We found that fluctuations of C_T^2 in time and space along a given path lead to a high variability of the path-averaged virtual measurements, which can affect LAS and aircraft observations. This estimated uncertainty increased with height up to the middle of the mixed layer.

The statistical uncertainty that results from this variability was found to strongly depend on the path length, the height above the ground and the temporal averaging interval. For the LAS that is installed at Cabauw at a height of 41 m above the ground ([Kohsiek et al. 2002](#))

it is found that the path length of 9.8 km is sufficient to obtain representative measurements for the fairly homogeneous area with a statistical uncertainty $\leq 10\%$. For other LAS, which cover a shorter path (e.g. at Lindenberg, Germany, see [Meijninger et al. 2006](#)), a longer time-averaging interval might be required to reduce the statistical uncertainty down to 10%. The required spatial averaging in the surface layer was found to depend on the ratio of path length to height above the ground. For LAS this ratio is a constant and the time averaging must thus be chosen in an appropriate way. Our results point out that, for a daytime CBL, an averaging interval of up to 1 h might be necessary for LAS measurements, depending on the LAS beam height and path length. Such long averaging intervals are strictly limited to changes in the surface fluxes and the diurnal cycle. Consequently, a higher statistical uncertainty has to be considered, if sufficient averaging is not possible.

In order to derive the surface sensible heat flux from C_T^2 and Monin–Obukhov similarity theory, the height of the LAS must be within the surface layer. It is evident that for a shallow CBL (e.g. in the early morning), the LAS might not be within the surface layer. For aircraft measurements, where a temporal averaging is not feasible, we found that the statistical uncertainty is higher than for LAS and can reach the order of 25% for a path length of 10 km, depending on the height above the ground.

In a follow-up study we will further address the uncertainty of the flux estimates by the LAS and aircraft measurements in the idealized homogeneously-heated CBL, but especially under more realistic heterogeneous conditions.

Acknowledgments This study was supported by the German Research Foundation (DFG) under grant RA 617/20-1. All simulations were performed on the SGI Altix ICE at The North-German Supercomputing Alliance (HLRN), Hannover/Berlin. Aircraft data were obtained within the European Commission research project RECAP (EVK2-CT-1999-00034). We appreciate the two anonymous reviewers for their numerous valuable comments that helped to improve the manuscript. The first author would like to thank Oscar Hartogensis for providing assistance with the spectra and scintillometer analyses.

Open Access This article is distributed under the terms of the Creative Commons Attribution License which permits any use, distribution, and reproduction in any medium, provided the original author(s) and the source are credited.

Appendix

Path-weighting function

For the virtual LAS measurements, we used the path-weighting function W after [Wang et al. \(1978\)](#) in the formulation of [Hartogensis et al. \(2003\)](#):

$$W(u) = 16\pi k_{\text{LAS}}^2 L_{\text{LAS}} \int_0^\infty k \Phi_n(k) \sin^2 \left[\frac{k^2 L_{\text{LAS}} u(1-u)}{2k_{\text{LAS}}} \right] \left[\frac{2J_1(x_1)2J_1(x_2)}{x_1 x_2} \right]^2 dk, \quad (19)$$

where $u = x/L_{\text{LAS}}$ is the dimensionless position along the path of length L_{LAS} , $k_{\text{LAS}} = 2\pi/\lambda$ is the optical wavenumber of the emitted signal ($\lambda = 940$ nm for the LAS at Cabauw), and $\Phi_n(k) = 0.033k^{-11/3}$ is the three-dimensional spectrum of the refractive index in the inertial subrange. J_1 is the Bessel function of the first kind, $x_1 = kDu/2$ and $x_2 = [kD(1-u)]/2$, where D is the aperture diameter of the scintillometer ($D = 0.31$ m for the LAS at Cabauw). [Hartogensis et al. \(2003\)](#) showed that the path-averaged structure parameter C_T^2 can be derived from the local C_T^2 by

$$\langle \widetilde{C}_T^2 \rangle_p = \int_0^1 C_T^2(u) G(u) du, \quad (20)$$

where

$$G(u) = \frac{W(u)}{\int_0^1 W(u) du}. \quad (21)$$

References

- Andreas EL (1988) Estimating C_n^2 over snow and sea ice from meteorological data. *J Opt Soc Am* 5:481–495
- Beyrich F, de Bruin H et al (2002) Results from one-year continuous operation of a large aperture scintillometer over a heterogeneous land surface. *Boundary-Layer Meteorol* 105:85–97
- Beyrich F, Kouznetsov RD, Leps JP, Lüdi A, Meijninger WML, Weisensee U (2006a) Structure parameters of temperature and humidity from simultaneous eddy-covariance and scintillometer measurements. *Meteorol Z* 14:641–649
- Beyrich F, Leps JP et al (2006b) Area-averaged surface fluxes over the LITFASS region based on eddy-covariance measurements. *Boundary-Layer Meteorol* 121:33–65
- Beyrich F, Bange J et al (2012) Towards a validation of scintillometer measurements: the LITFASS-2009 experiment. *Boundary-Layer Meteorol* 144:83–112
- Braam M, Bosveld FC, Moene AF (2012) On Monin–Obukhov scaling in and above the atmospheric surface layer: the complexities of elevated scintillometer measurements. *Boundary-Layer Meteorol* 144:157–177. doi:10.1007/s10546-012-9716-7
- Burk SD (1981) Comparison of structure parameter scaling expressions with turbulence closure models predictions. *J Atmos Sci* 38:751–761
- Cheinet S, Cumin P (2011) Local structure parameters of temperature and humidity in the entrainment-drying convective boundary layer: a large-eddy simulation analysis. *J Appl Meteorol* 50:472–481
- Cheinet S, Siebesma AP (2007) The impact of boundary layer turbulence on optical propagation. In: Proc. SPIE 6747, Optics in atmospheric propagation and adaptive systems X, Florence, Italy, p 67470A. doi:10.1117/12.741433
- Cheinet S, Siebesma AP (2009) Variability of local structure parameters in the convective boundary layer. *J Atmos Sci* 66:1002–1017
- Corrsin S (1951) On the spectrum of isotropic temperature fluctuations in an isotropic turbulence. *J Appl Phys* 22:469–473
- de Arellano J, Gioli B et al (2004) Entrainment process of carbon dioxide in the atmospheric boundary layer. *J Geophys Res* 109:D18110. doi:10.1029/2004JD004725
- Deardorff JW (1974) Three-dimensional numerical study of the height and mean structure of a heated planetary boundary layer. *Boundary-Layer Meteorol* 7:81–106
- Deardorff JW (1980) Stratocumulus-capped mixed layers derived from a three-dimensional model. *Boundary-Layer Meteorol* 18:495–527
- Fairall CW (1987) A top-down and bottom-up diffusion model of C_T^2 and C_Q^2 in the entraining convective boundary layer. *J Atmos Sci* 44:1009–1017
- Gioli B, Miglietta F, Vaccari FP, Zaldei A, De Martino B (2006) The Sky Arrow ERA, an innovative airborne platform to monitor mass, momentum and energy exchange of ecosystems. *Ann Geophys Italy* 49:109–116
- Glendening JW, Haack T (2001) Influence of advection differencing error upon large-eddy simulation accuracy. *Boundary-Layer Meteorol* 98:127–153
- Grinsted A, Moor JC, Jewrejava S (2004) Application of the cross wavelet transform and wavelet coherence to geophysical time series. *Nonlinear Process Geophys* 11:566–581
- Hartogensis OK, De Bruin HAR (2005) Monin–Obukhov similarity functions of the structure parameter of temperature and the dissipation rate in the stable boundary layer. *Boundary-Layer Meteorol* 116:253–276
- Hartogensis OK, Watts CJ, Rodriguez JC, De Bruin HAR (2003) Derivation of an effective height for scintillometers: La poza experiment in northwest Mexico. *J Hydrol* 4:915–928
- Heus T, van Heerwaarden C, Jonker HJJ, Siebesma AP, Axelsen S et al (2010) Formulation of the Dutch atmospheric large-eddy simulation (DALES) and overview of its applications. *Geosci Model Dev* 3:415–444
- Hill RJ (1978) Spectra of fluctuations in refractivity, humidity, and the temperature-humidity cospectrum in the inertial and dissipation range. *Radio Sci* 13:953–961

- Hill RJ, Clifford SF, Lawrence RS (1980) Refractive-index and absorption fluctuations in the infrared caused by temperature, humidity and pressure fluctuations. *J Opt Soc Am* 70:1192–1205
- Kaimal JC, Wyngaard JC, Haugen DA, Coté OR, Izumi Y (1976) Turbulence structure in the convective boundary layer. *J Atmos Sci* 33:2152–2169
- Kimmel SJ, Wyngaard JC, Otte MJ (2002) “Log-Chipper” turbulence in the convective boundary layer. *J Atmos Sci* 59:1124–1134
- Kohsiek W (1982) Measuring C_T^2 , C_Q^2 , and C_{TQ} in the unstable surface layer, and relations to the vertical fluxes of heat and moisture. *Boundary-Layer Meteorol* 24:89–107
- Kohsiek W (1988) Observation of the structure parameters C_T^2 , C_{TQ} , and C_Q in the mixed layer over land. *Appl Opt* 27:2236–2240
- Kohsiek W, Meijninger WML et al (2002) An extra large aperture scintillometer for long range applications. *Boundary-Layer Meteorol* 105:119–127
- Maronga B, Raasch S (2013) Large-eddy simulations of surface heterogeneity effects on the convective boundary layer during the LITFASS-2003 experiment. *Boundary-Layer Meteorol* 146:17–44. doi:[10.1007/s10546-012-9748-z](https://doi.org/10.1007/s10546-012-9748-z)
- Martin S, Bange J, Beyrich F (2010) Profiling the lower troposphere using the research UAV ‘M²AV’. *Atmos Meas Tech Discuss* 3:1–31
- Meijninger WML, Green AE et al (2002a) Determination of area-averaged water vapour fluxes with large aperture and radio wave scintillometers over a heterogeneous surface - Flevoland field experiment. *Boundary-Layer Meteorol* 105:63–83
- Meijninger WML, Hartogensis OK et al (2002b) Determination of area-averaged sensible heat fluxes with a large aperture scintillometer over a heterogeneous surface—Flevoland field experiment. *Boundary-Layer Meteorol* 105:37–62
- Meijninger WML, Beyrich F, Lüdi A, Kohsiek W, De Bruin HAR (2006) Scintillometer-based turbulent fluxes of sensible and latent heat over a heterogeneous land surface—a contribution to LITFASS-2003. *Boundary-Layer Meteorol* 121:89–110
- Moene AF (2003) Effects of water vapour on the structure parameter of the refractive index for near-infrared radiation. *Boundary-Layer Meteorol* 107:635–653
- Moene AF, Gioli B (2008) Understanding the scintillometer signal: spatial variability of structure parameters using wavelet analysis. In: 18th symposium on boundary layers and turbulence. American Meteorological Society, Stockholm, Sweden, paper 8B.3
- Moeng CH, Wyngaard JC (1988) Spectral analysis of large-eddy simulation of the convective boundary layer. *J Atmos Sci* 45:3573–3597
- Moene AF, Michels BI, Holtslag AAM (2006) Scaling variances of scalars in a convective boundary layer under different entrainment regimes. *Boundary-Layer Meteorol* 120:257–274
- Muschinski A (2004) Local and global statistics of clear-air doppler radar signals. *Radio Sci* 39:RS1008. doi:[10.1020/2003RS002908](https://doi.org/10.1020/2003RS002908)
- Muschinski A, Frehlich R, Balsley BB (2004) Small-scale and large-scale intermittency in the nocturnal boundary layer and the residual layer. *J Fluid Mech* 515:319–351
- Ochs GR, Wang T (1978) Finite aperture scintillometer for profiling wind and C_n^2 . *Appl Opt* 17:3774–3778
- Peltier LJ, Wyngaard JC (1995) Structure-function parameters in the convective boundary layer from large-eddy simulations. *J Atmos Sci* 52:3641–3660
- Petenko IV, Shurygin EA (1999) A two-regime model for the probability density function of the temperature structure parameter in the convective boundary layer. *Boundary-Layer Meteorol* 93:381–394
- Piacsek SA, Williams GP (1970) Conservation properties of convection difference schemes. *J Comput Phys* 198:580–616
- Raasch S, Franke T (2011) Structure and formation of dust-devil-like vortices in the atmospheric boundary layer—a high resolution numerical study. *J Geophys Res* 116:D16120. doi:[10.1029/2011JD016010](https://doi.org/10.1029/2011JD016010)
- Raasch S, Schröter M (2001) PALM—a large-eddy simulation model performing on massively parallel computers. *Meteorol Z* 10:363–372
- Sorbjan Z (1988) Local similarity on the convective boundary layer (CBL). *Boundary-Layer Meteorol* 45:237–250
- Sreenivasan KR (1996) The passive scalar spectrum and the Obukhov–Corrsin constant. *Phys Fluids* 8:189–196
- Stull RB (1988) An introduction to boundary layer meteorology. Kluwer, Dordrecht, 666 pp
- Tatarskii VI (1971) The effects of the turbulent atmosphere on wave propagation. Kefer Press, Jerusalem, 472 pp
- Tennekes H, Lumley JL (1973) A first course in turbulence. MIT, Cambridge, USA, 300 pp
- Torrence C, Compo GP (1998) A practical guide to wavelet analysis. *Bull Am Meteorol Soc* 79:61–78

-
- van den Kroonenberg AC, Martin S, Beyrich F, Bange J (2012) Spatially-averaged temperature structure parameter over a heterogeneous surface measured by an unmanned aerial vehicle. *Boundary-Layer Meteorol* 142:55–77
- Wang T, Ochs GR, Clifford SF (1978) A saturation-resistant optical scintillometer to measure C_n^2 . *J Opt Soc Am* 68:334–338
- Wicker LJ, Skamarock WC (2002) Time-splitting methods for elastic models using forward time schemes. *Mon Weather Rev* 130:2088–2097
- Wilson C, Fedorovich E (2012) Direct evaluation of refractive-index structure functions from large-eddy simulation output for atmospheric convective boundary layers. *Acta Geophys* 60:1474–1492
- Wyngaard JC, LeMone MA (1980) Behavior of the refractive index structure parameter in the entraining convective boundary layer. *J Atmos Sci* 37:1573–1585
- Wyngaard JC, Coté OR, Izumi Y (1971a) Local free convection, similarity, and the budgets of shear stress and heat flux. *J Atmos Sci* 28:1171–1182
- Wyngaard JC, Izumi Y, Collins SAJ (1971b) Behavior of the refractive-index-structure parameter near the ground. *J Opt Soc Am* 61:1646–1650

3.2 Research article B: Monin-Obukhov Similarity relationships for structure parameters of temperature and humidity in the unstable surface layer: results from high-resolution large-eddy simulations

3.2.1 Declaration of my contribution

The article was written by myself and improved by comments on the initial manuscript by Prof. Dr. Siegfried Raasch, Dr. Frank Beyrich (DWD), Dr. Arnold Moene and Miranda Braam (Wageningen/DWD). Additionally the manuscript was improved by comments and suggestions from three anonymous reviewers.

3.2.2 Accepted manuscript

This article has been accepted for publication in the Journal of the Atmospheric Sciences. Submitted: 7 May 2013. Accepted: 17 September 2013. Early online release: 25 September 2013.

Maronga, B.: Monin-Obukhov similarity functions for the structure parameters of temperature and humidity in the unstable surface layer: results from high-resolution large-eddy simulations *J. Atmos. Sci.*, doi:10.1175/JAS-D-13-0135.1, in press. (c)American Meteorological Society. Used with permission.



AMERICAN METEOROLOGICAL SOCIETY

Journal of the Atmospheric Sciences

EARLY ONLINE RELEASE

This is a preliminary PDF of the author-produced manuscript that has been peer-reviewed and accepted for publication. Since it is being posted so soon after acceptance, it has not yet been copyedited, formatted, or processed by AMS Publications. This preliminary version of the manuscript may be downloaded, distributed, and cited, but please be aware that there will be visual differences and possibly some content differences between this version and the final published version.

The DOI for this manuscript is doi: 10.1175/JAS-D-13-0135.1

The final published version of this manuscript will replace the preliminary version at the above DOI once it is available.

If you would like to cite this EOR in a separate work, please use the following full citation:

Maronga, B., 2013: Monin-Obukhov similarity functions for the structure parameters of temperature and humidity in the unstable surface layer: results from high-resolution large-eddy simulations. *J. Atmos. Sci.* doi:10.1175/JAS-D-13-0135.1, in press.

© 2013 American Meteorological Society

LaTeX File (.tex, .sty, .cls, .bst, .bib)

[Click here to download LaTeX File \(.tex, .sty, .cls, .bst, .bib\): JAS_2013_similarity.tex](#)

Generated using version 3.2 of the official L^AT_EX template



1 **Monin-Obukhov similarity functions for the structure parameters**
2 **of temperature and humidity in the unstable surface layer: results**
3 **from high-resolution large-eddy simulations**

4 BJÖRN MARONGA *

Institut für Meteorologie und Klimatologie, Leibniz Universität Hannover, Hannover, Germany

PRELIMINARY ACCEPTED VERSION

* *Corresponding author address:* Björn Maronga, Institut für Meteorologie und Klimatologie, Herrenhäuser Str. 2, 30419 Hannover, Germany
E-mail: maronga@muk.uni-hannover.de

ABSTRACT

5

6 Large-eddy simulations (LES) of free convective to near-neutral boundary layers are used to
7 investigate the surface layer turbulence. The article focuses on the Monin-Obukhov similarity
8 theory (MOST) relationships that relate the structure parameters of temperature C_T^2 and
9 humidity C_q^2 to the surface fluxes of sensible and latent heat, respectively. Moreover, the
10 applicability of local free convection similarity (LFC) scaling is studied. The LES data
11 suggest that the MOST function for C_T^2 is universal. It is shown to be within the range of
12 the functions proposed from measurement data. C_q^2 follows MOST if entrainment of dry air
13 from the free atmosphere is sufficiently small. In this case the similarity functions for C_T^2 and
14 C_q^2 are identical. If entrainment is significant, dissimilarity between the transport of sensible
15 heat and moisture is observed and C_q^2 no longer follows MOST. In the free convection limit
16 the LFC similarity functions should collapse to universal constants. The LES data suggest
17 values around 2.7, in agreement with the value proposed in literature. Like for MOST, the
18 LFC similarity constant for C_q^2 becomes non-universal if entrainment of dry air is significant.
19 It is shown that LFC scaling is applicable even if shear-production of turbulence is moderately
20 high.

21 1. Introduction

22 The measurement of area-averaged surface fluxes of sensible and latent heat at regional
23 scale is necessary for a better understanding of the regional (and global) energy and water
24 cycles. It is also important in order to improve models for meteorological and hydrological
25 processes (De Bruin et al. 1993; Li et al. 2012). Such models, in turn, play an important role
26 in terms of parameterizations in numerical weather prediction models. Traditionally, point
27 measurements using eddy covariance technique are used to measure surface fluxes, but they
28 are only representative if the surface is homogeneous (Andreas 1991). Natural landscapes
29 rarely provide such conditions and single point measurements then cannot be considered to
30 be representative for larger areas.

31 Scintillometers have been increasingly employed in the atmospheric surface layer to mea-
32 sure the refractive index structure parameter C_n^2 as a spatial average over horizontal distances
33 of up to 10 km (Kohsiek et al. 2002; Meijninger et al. 2002, 2006; Evans et al. 2012, among
34 many others). Such a spatial average of C_n^2 can in turn be related to the structure param-
35 eters of temperature C_T^2 and specific humidity C_q^2 (e.g. Hill 1978). Monin-Obukhov similarity
36 theory (MOST) provides a framework that relates the estimates of C_T^2 and C_q^2 to the surface
37 fluxes of sensible and latent heat, respectively. In this way, scintillometers offer a technique
38 for estimating the surface fluxes at spatial scales that might be representative for an area of
39 several square km. Nevertheless, a validation of such scintillometer-based fluxes is challeng-
40 ing, particularly over heterogeneous terrain. A first attempt was made by using independent
41 low-level aircraft flights along a scintillometer path during the LITFASS-2009 experiment
42 (Beyrich et al. 2012). Also, a first large-eddy simulation (LES) - large-aperture scintillometer
43 comparison has been presented by Maronga et al. (2013).

44 In order to estimate the surface fluxes from measurements of C_T^2 and C_q^2 , universal MOST
45 functions are needed that are not given by theory and must be determined experimentally
46 (see Section 2b). Several similarity functions have been proposed in the literature (Wesely
47 1976; Wyngaard et al. 1971b; Andreas 1988; Hill et al. 1992; Thiermann and Grassl 1992;

48 De Bruin et al. 1993; Li et al. 2012), but there is no consensus on a precise form so far.
 49 One reason might be that there are differences in the calculation of the relevant scaling
 50 parameters, namely the Obukhov length L (Obukhov 1946):

$$L = -\frac{\overline{\theta}_v u_*^3}{\kappa g w' \theta'_{v0}}. \quad (1)$$

51 Here, u, v, w are the wind components in x, y and z direction on a Cartesian coordinate
 52 system, respectively. The prime indicates a turbulent fluctuation. $\theta_v, u_* = (\overline{w'u_0^2} + \overline{w'v_0^2})^{1/4}$
 53 and $\overline{w'\theta'_{v0}}$ are virtual potential temperature, friction velocity (with $\overline{w'u_0}$ and $\overline{w'v_0}$ being
 54 the components of the vertical surface momentum flux) and near-surface buoyancy flux,
 55 respectively. g is the gravitational acceleration and κ is the Von Kármán constant with
 56 a commonly accepted value of 0.4. The overbar denotes an average (temporal or spatial).
 57 While some studies take into account the effect of moisture on the buoyancy flux and thus
 58 L , other rather use the Obukhov length for dry air (e.g. Wyngaard et al. 1971b; Wesely
 59 1976; Thiermann and Grassl 1992). It is also usually assumed that the similarity function
 60 functions are identical for temperature and humidity. Li et al. (2012) discussed possible
 61 reasons for dissimilarity between the turbulent transport of heat and moisture that can lead
 62 to differences in the similarity relationships of C_T^2 and C_q^2 . They found such dissimilarity
 63 in their data under weakly unstable conditions and ascribed this to non-local effects like
 64 non-stationarity of the flow, advection and entrainment.

65 In the free convection limit, the similarity relationships should become universal con-
 66 stants, but theory does not yield these constants itself. There is consensus on the constant
 67 for C_T^2 , but it is still an open question whether the constant for C_q^2 is equal to that for C_T^2
 68 (see Section 2c). Theoretically, local free convection (LFC) can be only considered near the
 69 surface when no mean wind is present, but in practice it is often applied also in case of weak
 70 winds (De Bruin et al. 1995; Kohsiek 1982; Kohsiek et al. 2002).

71 Several studies have revealed that the mean vertical profiles of C_T^2 and C_q^2 in the CBL
 72 strongly depend on the entrainment of dry warm air at the top of the mixed layer (e.g.
 73 Wyngaard and LeMone 1980; Druilhet et al. 1983; Fairall 1984, 1987, 1991). In particular,

74 it is found that C_q^2 is often dominated by entrained air from the free atmosphere. Wyngaard
75 and LeMone (1980) showed that deviations from the mixing-layer scaling laws are caused by
76 entrainment effects that lead to a peak of the structure parameters near the capping inversion
77 in free convection. Fairall (1984) studied the effect of wind shear on this peak and found that
78 the wind shear enhancement of entrainment leads to an increase of the peak values. The
79 data of Druilhet et al. (1983) showed two peaks for C_T^2 , one near the surface and a secondary
80 peak in the entrainment layer. For C_q^2 the entrainment peak was dominant, whereas the
81 near-surface peak was only weak. They concluded that if the entrainment characterizes
82 the changes in humidity in the CBL, a new mixing-layer humidity scale should be defined
83 that incorporates the entrainment humidity flux instead of the surface flux. Based on these
84 findings, Fairall (1987) and Fairall (1991) used LES data and the top-down (entrainment)
85 and bottom-up (surface fluxes) approach in order to derive semi-empirical profiles of C_T^2 and
86 C_q^2 for the entire CBL. These profiles take into account the entrainment flux ratio and the
87 boundary layer depth z_i and include also an extension for the surface layer, as proposed by
88 Wyngaard et al. (1971b). However, these semi-empirical profiles all assume that the surface
89 fluxes are dominantly determining the surface layer part of the structure parameter profiles.
90 Moreover, these profiles can be only used when information about the inversion layer is
91 available. This is often challenging and hence MOST/LFC scaling is usually applied instead
92 to relate scintillometer observations to the surface fluxes.

93 While most previous studies in the field of MOST used experimental data, there are
94 few studies that investigated the surface layer similarity by means of idealized numeri-
95 cal experiments using turbulence-resolving LES. Mason and Thomson (2002) showed that
96 Smagorinski-style subgrid-scale (SGS) closures that are commonly used in LES models fail
97 to predict MOST relationships in the near-surface layer correctly. They found a system-
98 atic peak (“overshoot”) in the dimensionless wind shear. Khanna and Brasseur (1997) used
99 LES to study the effect of grid resolution and the used SGS model on the MOST functions
100 for mean fields, variances, budgets of temperature and turbulent kinetic energy under near-

101 neutral to moderately convective conditions. In order to resolve the surface layer they nested
102 a high-resolution mesh in the lower part of their model domain. They stated that the lowest
103 few grid levels are always affected by the SGS model in such a way that the turbulent flow
104 cannot be resolved. Furthermore they found an overshoot in the normalized vertical profiles
105 for mean shear and mean temperature gradient. With increasing grid resolution this over-
106 shoot was moved to lower levels, but it did not vanish. Khanna and Brasseur (1997) showed
107 that this overshoot can be ascribed to the SGS model. Recently, Brasseur and Wei (2010)
108 focused on the mentioned overshoot in the mean gradient of the dimensionless horizontal
109 velocity and developed criteria to design LES that reduce this overshoot. However, they also
110 stated that MOST scaling was not reached in the first couple of grid levels. Khanna and
111 Brasseur (1997) also found that temperature variance satisfied LFC scaling even for condi-
112 tions with considerable wind shear. Moreover, they suggested that not only z/L (where z is
113 the height above ground), but also z_i/L might be a proper scaling parameter in the surface
114 layer. The latter was supported by field measurement data by Johansson et al. (2001), who
115 stated that the normalized temperature variance might have a slight dependence on z_i/L
116 (see also discussion in Johansson et al. 2002).

117 Peltier and Wyngaard (1995) derived C_T^2 and C_q^2 from LES data of a convective boundary
118 layer and derived LFC scaling constants. They particularly found that increased entrainment
119 decrease C_T^2 and increase C_q^2 in the lower mixed-layer. This led to a higher LFC constant
120 for humidity than for temperature. Generally, the derived constants from the LES were
121 smaller than the suggestions from measurement data. Cheinet and Siebesma (2009) and
122 Cheinet and Cumin (2011) used LES to investigate the spatial variability of C_T^2 and C_q^2 ,
123 respectively. Cheinet and Siebesma (2009) found a relation of the spatial variability of C_T^2 to
124 the hexagonal cellular pattern of the convective plumes in the CBL. Moreover, Cheinet and
125 Cumin (2011) could show that the spatial distribution of C_q^2 in the mixed layer is dominated
126 by air that is entrained at the top of the mixed layer, in agreement with previous studies (e.g.
127 Druilhet et al. 1983; Fairall 1987, see above). Implications for surface layer similarity were

128 not discussed, as their numerical grid was too coarse to resolve the surface layer turbulence.
129 Recently, Wilson and Fedorovich (2012) used LES in order to further explore the structure
130 parameters. Particularly they evaluated C_n^2 by calculating the refractive index structure
131 functions. They also derived C_T^2 , C_q^2 and C_{Tq} (joint structure parameter of temperature and
132 humidity) and found that, for visible radiation, temperature contributes dominantly to C_n^2
133 in the lower half of the CBL and that C_{Tq} becomes important near the entrainment layer at
134 top of the CBL.

135 To the author's knowledge, the MOST and LFC relationships for structure parameters
136 have not been studied by means of LES so far. First LFC predictions have been made by
137 Peltier and Wyngaard (1995), but they could not resolve the surface layer sufficiently. In
138 the present article C_T^2 and C_q^2 will be determined from a set of LES that explicitly resolve
139 the bulk part of the surface layer. In a precursor study Maronga et al. (2013) have shown
140 that the structure parameters can be derived from such an LES. They evaluated different
141 methods to obtain the structure parameters and compared these methods to semi-empirical
142 profiles after Kaimal et al. (1976) and Fairall (1987). Maronga et al. (2013) showed that
143 all methods reproduce the proposed shape of the vertical profiles of C_T^2 and C_q^2 very well.
144 Furthermore, it was found that the most reliable method (so called *spectral method*) gave
145 values that were comparable to those proposed by the semi-empirical profiles. Moreover,
146 they compared the LES data with in situ large-aperture scintillometer and aircraft data
147 and found good agreement of the measurement data with the LES predictions within the
148 surface layer. They also showed that changes in the entrainment flux of dry warm air can
149 increase C_q^2 in the mixed layer, while C_T^2 was not modified, in agreement with previous
150 numerical and experimental studies (e.g. Druilhet et al. 1983; Fairall 1987, 1991). Owing to
151 the idealized conditions in the model, such as horizontal homogeneity and prescribed surface
152 fluxes, the LES provides a unique instrument for studying the similarity relationships for
153 structure parameters. By using a very high grid resolution throughout the model domain
154 the turbulence in the surface layer can be sufficiently resolved and no "nested mesh" as used

155 by Khanna and Brasseur (1997) is required.

156 I will focus on the questions that are most relevant for estimating the surface fluxes from
157 scintillometer observations: (i) can the similarity relationships be considered universal and
158 are they the same for C_T^2 and C_q^2 ? (ii) is similarity between the turbulent transport of heat
159 and moisture a general feature of the unstable surface layer? (iii) under which conditions
160 does LFC scaling apply? Moreover I want to put forward the question whether neglecting
161 the effect of moisture on buoyancy (and hence L) is appropriate for estimating the surface
162 fluxes of sensible and latent heat.

163 The paper is organized as follows: Section 2 deals with the theoretical background of
164 MOST and LFC scaling and the current state of the art. Section 3 gives a short overview
165 on the used LES model, case description and data processing. Results are presented in
166 Section 4. A summary is given in Section 5.

167 2. Theory

168 a. *Structure parameters of temperature and humidity*

169 There is vast literature on the definition and deduction of the structure parameters of
170 temperature and humidity from standard meteorological data (e.g. Tatarskii 1971; Wyngaard
171 et al. 1971b; Andreas 1988, among many others). Traditionally C_T^2 and C_q^2 are derived either
172 directly from the structure functions or from the one-dimensional Fourier spectra. Both
173 formulations are mathematically equivalent and require the existence of an inertial subrange.
174 Because the spectral approach requires less computation time we will focus on this approach
175 (see also Maronga et al. 2013). Following Wyngaard et al. (1971b) the structure parameters
176 C_T^2 and C_q^2 are directly proportional to the spectra of temperature and humidity in the
177 inertial subrange, respectively. They can be related to the power spectral density Φ at a

178 given height z by

$$C_T^2(z) = \frac{1}{0.2489} \Phi_\theta(k, z) k^{5/3}, \quad C_q^2(z) = \frac{1}{0.2489} \Phi_q(k, z) k^{5/3}, \quad (2)$$

179 where θ is potential temperature, q is specific humidity, k is a wave number in the inertial
180 subrange, and $0.2489 = 2/3\Gamma(1/3)$ after Muschinski et al. (2004). Note that for convenience
181 the notation C_T^2 with index T (actual temperature) is used.

182 *b. Monin-Obukhov similarity theory*

183 In order to derive the surface fluxes of sensible and latent heat from observations of C_T^2
184 and C_q^2 , MOST is used. Following MOST, the vertical turbulent fluxes over a horizontal
185 homogeneous surface in steady-state conditions are to a first order approximation constant
186 with height within the lowest decameters of the atmosphere (e.g Andreas 1988; Hill 1989;
187 Foken 2006, among others). A common definition of the surface layer is thus the lower part
188 of the boundary layer where the fluxes vary by less than 10 % of their magnitude (Stull 1988).
189 The relevant scaling parameters are the measurement height z , L , the near-surface kinematic
190 flux of heat $\overline{w'\theta'_0}$ (and of moisture $\overline{w'q'_0}$, if humidity is considered), and u_* . Additionally, a
191 temperature scale θ_* and a humidity scale q_* can be defined as:

$$\theta_* = -\frac{\overline{w'\theta'_0}}{u_*}, \quad (3)$$

$$q_* = -\frac{\overline{w'q'_0}}{u_*}. \quad (4)$$

193 According to MOST, any mean turbulence quantity in the surface layer should be a universal
194 function of z/L (or $-z/L$, which is commonly referred to as stability parameter) if properly
195 scaled with θ_* , q_* , u_* , L and z (Andreas 1988). The structure parameters of temperature and
196 humidity should thus satisfy

$$\frac{C_T^2 z^{2/3}}{\theta_*^2} = f_T(z/L), \quad (5)$$

$$\frac{C_q^2 z^{2/3}}{q_*^2} = f_q(z/L), \quad (6)$$

198 with f_T and f_q being universal functions that only depend on z/L . The precise form of f
 199 is not given by MOST and must be determined experimentally. In the present article only
 200 unstable conditions are considered where $\overline{w'\theta'_0}$ is positive. Several empirical functions f have
 201 been proposed for such conditions from measurement data (Wyngaard et al. 1971b; Wesely
 202 1976; Andreas 1988; Thiermann and Grassl 1992; Hill et al. 1992; De Bruin et al. 1993; Li
 203 et al. 2012). A very common form is

$$f_T(z/L) = c_{TT1} [1 - c_{TT2}(z/L)]^{-2/3}, \quad (7)$$

$$f_q(z/L) = c_{qq1} [1 - c_{qq2}(z/L)]^{-2/3}, \quad (8)$$

205 with dimensionless constants c_{TT1} , c_{TT2} , c_{qq1} and c_{qq2} for which different values are proposed
 206 in the literature. The Eqs. (7) and (8) are linear interpolations and the four parameters
 207 provide the blending between neutral and free convective conditions. Li et al. (2012) pointed
 208 out that it is often assumed that $f = f_T = f_q$, but they showed that dissimilarity between
 209 the transport of heat and moisture (and hence in f) occurred in their data for weakly
 210 unstable conditions ($0.01 < -z/L < 0.1$). They refer to Hill (1989), who stated that
 211 if the structure parameters all follow MOST, then their similarity functions must be the
 212 same, and temperature and humidity must be perfectly correlated (correlation coefficient of
 213 $R_{Tq} = 1$). However, often $R_{Tq} \neq 1$ as also shown by Beyrich et al. (2005). Hill (1989) stated
 214 that dissimilarity can be expected due to the fact that MOST is an over-idealization of the
 215 surface layer flow dynamics.

216 Knowing f , the surface fluxes can be determined by rearranging Eqs. (5)-(6) using
 217 Eqs. (3)-(1):

$$\overline{w'\theta'_0} = u_* z^{1/3} (C_T^2)^{1/2} [f_T(z/L)]^{-1/2}, \quad (9)$$

$$\overline{w'q'_0} = u_* z^{1/3} (C_q^2)^{1/2} [f_q(z/L)]^{-1/2}. \quad (10)$$

219 Eqs. (9) and (10) reveal that it requires not only the estimate of the structure parameter, but
 220 also additional measurements of the friction velocity to determine the surface fluxes. Also,
 221 L is required. In practice u_* and L are iteratively solved using wind speed data (Panofsky

222 and Dutton 1984; De Bruin et al. 1993). Local free convection scaling is often applied as it
 223 provides a more simple relation between structure parameters and surface fluxes.

224 *c. Local free convection scaling*

225 The Obukhov length is roughly the height where mechanical and buoyant production of
 226 turbulence are equal. It is commonly expected that free convection occurs when $-z/L \geq 1$
 227 (Andreas 1991). When mechanical production is much less important than buoyant gener-
 228 ation of turbulence (e.g. when winds are calm and $u_* \rightarrow 0$) the Obukhov length is close
 229 to zero and no longer a proper scaling parameter. Under such conditions buoyancy is the
 230 driving force and the surface layer should behave as in free convection. This is termed *local*
 231 *free convection* (LFC) (e.g. Wyngaard et al. 1971a). The list of LFC scaling parameters
 232 becomes:

$$233 \quad w_{\text{LF}} = \left(\frac{g}{\theta_v} \overline{w'\theta'_v} z \right)^{1/3}, \quad (11)$$

$$234 \quad \theta_{\text{LF}} = \frac{\overline{w'\theta'_0}}{w_{\text{LF}}} \quad (12)$$

235 and

$$q_{\text{LF}} = \frac{\overline{w'q'_0}}{w_{\text{LF}}}. \quad (13)$$

236 Due to the limited scales available in LFC (number of relevant variables equals the num-
 237 ber of dimensions), there is only one dimensionless group and the dimensionless structure
 238 parameters must follow

$$239 \quad \frac{C_T^2 z^{2/3}}{\theta_{\text{LF}}^2} = A_T, \quad (14)$$

$$\frac{C_q^2 z^{2/3}}{q_{\text{LF}}^2} = A_q, \quad (15)$$

240 with A_T and A_q being universal constants (see Andreas 1991). There is consensus on the
 241 value of 2.7 for A_T from C_T^2 measurements (Wyngaard et al. 1971b; Kaimal et al. 1976;
 242 Wyngaard and LeMone 1980; Kunkel et al. 1981; Andreas 1991). Wyngaard and LeMone

(1980) found A_q to be around 1.5, while Andreas (1991) suggested that $A_T = A_q$ (when $R_{Tq} = 1$), referring to the study of Hill (1989). Peltier and Wyngaard (1995) found values for the constants between 2.0 and 2.7 in their LES. They also showed that the constant was larger for humidity than for temperature due to entrainment effects. This contradicts the result of Wyngaard and LeMone (1980).

Using Eqs. (11) - (13) in Eqs. (14) - (15) and rearranging yields equations for determining the surface fluxes:

$$\overline{w'\theta'_0} = \frac{C_T^2}{A_T} z^{2/3} \left(\frac{g}{\theta_v} \overline{w'\theta'_{v0}} \right)^{1/3}, \quad (16)$$

$$\overline{w'q'_0} = \frac{C_q^2}{A_q} z^{2/3} \left(\frac{g}{\theta_v} \overline{w'\theta'_{v0}} \right)^{1/3}. \quad (17)$$

Using the proposed formulation for MOST (see Eqs. (7) - (8)) in Eqs. (9) - (10) and looking at the free convection limit (i.e. $-z/L \rightarrow \infty$) yields (see also De Bruin et al. 1995):

$$A_T = \kappa^{-2/3} c_{TT1} c_{TT2}^{-2/3}, \quad (18)$$

$$A_q = \kappa^{-2/3} c_{qq1} c_{qq2}^{-2/3}, \quad (19)$$

showing that LFC scaling can be traced back to MOST in the free convection limit. Note that no independent measurement of the wind speed is required in Eqs. (16) and (17), but the buoyancy flux is needed (cf. Eqs. (9)-(10)). It can be approximated without much error as (see Stull 1988; Andreas 1991):

$$\begin{aligned} \overline{w'\theta'_{v0}} &\approx \overline{w'\theta'_0} \left(1 + 0.61 \overline{q_0} + 0.61 \overline{\theta_0} \frac{\xi}{\beta_0} \right) \\ &\approx \overline{w'\theta'_0} h(\overline{q_0}, \overline{\theta_0}, \beta_0), \end{aligned} \quad (20)$$

with the surface Bowen ratio $\beta_0 = \xi \overline{w'\theta'_0} / \overline{w'q'_0}$ and $\xi = c_p / L_v$. c_p is the specific heat at constant pressure and L_v is the latent heat of vaporization. It follows that

$$\overline{w'\theta'_0} = \left(\frac{C_T^2}{A_T} \right)^{3/4} z \left(\frac{g}{\theta_v} \right)^{1/2} h(\overline{q_0}, \overline{\theta_0}, \beta_0)^{1/2}, \quad (21)$$

$$\overline{w'q'_0} = \left(\frac{C_q^2}{A_q} \right)^{1/2} \left(\frac{C_T^2}{A_T} \right)^{1/4} z \left(\frac{g}{\theta_v} \right)^{1/2} h(\overline{q_0}, \overline{\theta_0}, \beta_0)^{1/2}. \quad (22)$$

261 For the dry boundary layer it holds that $\beta_0 \rightarrow \infty$, $\overline{q_0} \rightarrow 0$ and hence $h \rightarrow 1$. Eq. (21) then
 262 reduces to (see also Wyngaard et al. 1971b)

$$\overline{w'\theta'_0} = \left(\frac{C_T^2}{A_T} \right)^{3/4} z \left(\frac{g}{\overline{\theta}} \right)^{1/2}. \quad (23)$$

263 It is tempting to use Eq. (23) directly to derive $\overline{w'\theta'_0}$ from large-aperture scintillometer
 264 measurements (which give estimates of C_T^2), as neither the friction velocity, nor information
 265 about humidity is required (e.g. De Bruin et al. 1995; Kohsiek 1982; Kohsiek et al. 2002).
 266 A direct consequence of this approximation is, however, that $\overline{w'\theta'_0}$ is usually systematically
 267 underestimated because $h(\overline{q_0}, \overline{\theta_0}) \geq 1$ when $\beta_0 > 0$. This is generally the case under unstable
 268 conditions.

269 Note that in free convection one might also consider mixing-layer similarity throughout
 270 the CBL (e.g. Wyngaard and LeMone 1980; Fairall 1987), but then an additional estimate
 271 of z_i must be provided. This usually requires additional vertically scanning devices, which
 272 are rarely available in combination with scintillometers. Mixing-layer similarity will thus not
 273 be further studied in the present study.

274 3. LES model and case description

275 a. LES model

276 The LES model PALM (revision 893) (Raasch and Schröter 2001; Riechelmann et al.
 277 2012) was used for the present study. It has been widely applied to study different flow
 278 regimes in the convective and neutral boundary layer (e.g. Raasch and Franke 2011; Letzel
 279 et al. 2008). All simulations were carried out using cyclic lateral boundary conditions. The
 280 grid was stretched in the vertical direction well above the top of the boundary-layer to save
 281 computational time in the free atmosphere. MOST was applied as surface boundary con-
 282 dition locally between the surface and the first computational grid level (“local similarity
 283 model”, see also Peltier and Wyngaard 1995), including the calculation of the local friction

284 velocity u_* from the roughness length and the local wind profiles (see also Panofsky and
285 Dutton 1984, Chapter 6.5). A 1.5-order flux-gradient subgrid closure scheme after Deardorff
286 (1980) was applied, which requires the solution of an additional prognostic equation for the
287 subgrid-scale (SGS) turbulent kinetic energy. A 5th-order advection scheme of Wicker and
288 Skamarock (2002) and a 3rd-order Runge–Kutta time step scheme were used (Williamson
289 1980). θ_v is calculated from the prognostic variables θ and q as a three-dimensional quantity
290 in the model so that the buoyancy flux profile could be directly calculated in the model. In
291 case of a prescribed geostrophic wind, a one-dimensional version of the model with fully-
292 parametrized turbulence, using a mixing-length approach after Blackadar (1997) and sta-
293 tionary temperature and humidity profiles, was used for precursor simulations to generate
294 steady-state wind profiles as initialization for the LES.

295 *b. Case description*

296 The set of LES for this study is based on a simulation of the free convective boundary
297 layer which is described in detail in Maronga et al. (2013). The results from the simulation
298 were evaluated by in situ aircraft observations of temperature and humidity at Cabauw
299 (The Netherlands). Maronga et al. (2013) derived the structure parameters of temperature
300 and humidity from the LES data and compared them against aircraft observations of C_T^2
301 and C_q^2 at different heights in the boundary layer as well as with semi-empirical profiles.
302 Furthermore, they showed that C_T^2 , derived from the LES, was in good agreement with
303 measurements of a large-aperture scintillometer that was operated at a height of 41 m. Hence,
304 this simulation suits as a good reference case for the present study.

305 The model was discretized in space with 1024 grid points in each horizontal direction (in
306 the present study 2048 grid points are used). The grid resolution was 4 m in the horizontal
307 directions ($\Delta_x = \Delta_y = 4$ m) and 832 grid points with a resolution of 2 m were used in the
308 vertical direction ($\Delta_z = 2$ m). The simulation was driven by constant kinematic surface
309 fluxes of heat and moisture with a Bowen ratio around 0.27. A roughness length of 0.1 m

310 was used. Neutrally-stratified initial profiles of temperature and humidity with a capping
311 inversion and the free atmosphere above were prescribed (see Fig. 1 and Tab. 1). For a
312 detailed description of the initial parameters, see simulation case A in the study of Maronga
313 et al. (2013, Sect. 3 and Tab. 1).

314 For the present study a set of LES was generated based on the simulation described
315 above. The geostrophic wind speed as well as the prescribed surface fluxes were systemat-
316 ically varied for each simulation. This was done in order to generate a set of simulations
317 (hereafter also referred to as reference simulations) that cover the relevant range of $-z/L$ for
318 near-neutral to free convective conditions. First, the geostrophic wind was increased from 0
319 to 10 m s^{-1} . Second, in order to cover those cases that are dominated by shear-production
320 ($-z/L < 0.1$) the surface fluxes were reduced to 50 % and 10 % of their initial values, based
321 on the simulation with a background wind of 10 m s^{-1} . For sensitivity studies, β_0 was var-
322 ied to values of 0.05 and 0.4 as well as ∞ (dry simulation). Furthermore the lapse rate of
323 temperature in the capping inversion γ was reduced for one case in order to study whether
324 entrainment of warm dry air affects the surface layer dynamics and hence the structure pa-
325 rameters and their similarity relationships. Due to the high computational costs of the study
326 (one simulation took about 2 days of real time on 4096 Intel Xeon Gainestown processors
327 (2.93 GHz) on an SGI Altix ICE 8200 Plus cluster), these sensitivity cases were simulated
328 for two selected background wind speeds only: 0 m s^{-1} (free convection) and 8 m s^{-1} . The
329 full list of simulations with the relevant parameters is given in Table 1.

330 *c. Database and processing*

331 A quasi-stationary state was reached for all cases after 1 h of simulation time. The
332 total simulation time was 2 h and instantaneous data was output every 120s during the
333 second hour of the simulation. As the buoyancy flux is a direct model output in PALM no
334 approximation as introduced in Eq. (20) was needed.

335 The structure parameters of temperature and humidity were derived from the power

336 spectral density of potential temperature and specific humidity by means of Eq. (2) (spec-
 337 tral method). First, all one-dimensional spatial spectra along x - and y -direction in each
 338 horizontal plane were determined, and subsequently averaged. Second, a quality check was
 339 performed to identify an inertial subrange. Third, the structure parameters were then cal-
 340 culated for all k in the inertial subrange and subsequently spectrally averaged. In this way
 341 instantaneous (horizontal averaged) vertical profiles of the structure parameters could be
 342 derived. For a more detailed description of this method see Maronga et al. (2013). They
 343 particularly found that this method gave reliable estimates of the structure parameters.
 344 These instantaneous profiles were derived every 120 s over the analysis period. All figures
 345 in the following showing data points thence contain data for every 120 s of time. Due to
 346 the high computing time required to compute the profiles, the calculation was limited in the
 347 vertical direction to the lowest 150 m of the boundary layer. This was sufficient to cover the
 348 entire surface layer.

349 The boundary-layer depth was in most cases in the order of 1 km (see Section 4a and
 350 Table 1). The profiles of $\overline{w'\theta'}$ displayed a linear decrease with height (not shown). The
 351 top of the surface layer z_{SL} was first defined as the height where $\overline{w'\theta'}$ had decreased by 10 %
 352 of its surface value. This, however, turned out to be approximately $0.1 z_i$. For convenience
 353 and without introducing much error, the height of the surface layer was thus defined as
 354 $z_{\text{SL}} = 0.1 z_i$. This decision is supported by Brasseur and Wei (2010) who stated that MOST
 355 can be valid up to height levels of $0.15 - 0.2 z_i$.

356 4. Results

357 a. Mean profiles

358 Since the focus of this paper is on structure parameters in the surface layer, the mean
 359 characteristics of the boundary-layers simulated shall be discussed only briefly at this point.
 360 The temperature and humidity after 1 h of simulation time all show classical boundary layer

361 profiles with unstable stratification near the surface, a well-mixed layer and a strong capping
 362 inversion above the mixed-layer (see Fig. 1, exemplarily shown for W00). A boundary-layer
 363 depth of about 1.1 km is observed (see Tab. 1). Note that the mixed layer does not tear
 364 down the capping inversion and hence the lapse rate of the capping inversion is a relevant
 365 parameter, while the stability of the free atmosphere is unimportant for the results. During
 366 the analysis period (1-2 h of simulation time) the mixed-layer temperature and humidity both
 367 slightly increase, whereas z_i remains rather constant due to the strong capping inversion.
 368 The entrainment flux ratio r for all reference cases is about -0.25 for sensible heat, 0.3 for
 369 moisture and around -0.15 for the buoyancy flux. Entrainment of dry warm air is thus
 370 small compared to the input of sensible and latent heat at the surface. Therefore, one can
 371 expect that the influence of entrainment processes can be neglected in the surface layer. The
 372 increase in the geostrophic from W00 to W10 does neither affect r nor z_i and thus indicates
 373 that shear does not increase the entrainment significantly, in contrast to the finding of Fairall
 374 (1984). This might be ascribed to the strong capping inversion in the present study that
 375 suppresses entrainment to a considerable degree. In cases W10_F50 and W10_F10 z_i is lower
 376 (1.04 km and 1.0 km, respectively) due to the reduced surface fluxes. The sensitivity cases
 377 W00_γ07 and W08_γ07 (weak capping inversion) show a significantly increased z_i of up to
 378 1.29 km. Due to more entrainment of dry warm air, a drying out of the boundary-layer is
 379 forced that is balanced by the moisture input at the surface. The mean humidity in the
 380 mixed-layer for cases W00_γ07 and W08_γ07 hence is constant in time and the entrainment
 381 flux ratio is about -0.3 for temperature and 1.0 for moisture. A complete list of z_i and the
 382 entrainment flux ratios for each case is given in Table 1.

383 *b. MOST relationships for C_T^2 and C_q^2*

384 It is important to recognize that the LES models reality, but it gives no perfect image of
 385 nature. The observed values for the similarity relationships that are derived in the following
 386 should thus be regarded as “model truth”, but they can be different from what can be

387 expected in nature. On the one hand, modeling errors, e.g. induced by the SGS model or
388 numerical errors can be present. On the other hand, horizontal homogeneity is an idealization
389 that is made for the LES, but can be rarely considered in realistic landscapes. The advantage
390 of the LES here is the full control of all model parameters and boundary conditions. Hence
391 the LES allows for separating effects by varying single parameters, whereas in nature many
392 effects superimpose each other.

393 1) MOST SIMILARITY FUNCTIONS FROM LES

394 The non-dimensional structure parameters (horizontal average) were calculated for the
395 reference simulations for all available time steps and height levels in the surface layer ac-
396 cording to Eqs. (5)-(6). The results are shown as data points against $-z/L$ in Fig. 2. It
397 is obvious that all data points collapse to a single curve, except for the lowest values of
398 $-z/L$ for each simulation. Here, a significant decrease in the non-dimensional structure
399 parameters is visible. These data points relate to the lowest height levels above the surface
400 where turbulent eddies are relatively small and cannot be sufficiently resolved. The nominal
401 resolution of the LES is defined by the truncation size $\Delta = \sqrt[3]{\Delta_x \Delta_y \Delta_z} \approx 3.2$ m. Smaller
402 eddies than this size are parametrized within the SGS model, while larger eddies should be
403 fully resolved. However, in practice the SGS model affects also larger scales, and the actual
404 resolution is found to be typically around $6\Delta \approx 20$ m. Eddies smaller than 20 m still suffer
405 from contributions of the SGS model. This is a known feature of the LES, see e.g. Khanna
406 and Brasseur (1997), Brasseur and Wei (2010). This effect can in turn also artificially mod-
407 ify the turbulence spectra at the lowest levels for high wave numbers as shown by Maronga
408 et al. (2013). It is hence plausible to exclude at least the lowest levels from the analysis.
409 Consequently, taking into account the results shown in Fig. 2, the analysis was restricted to
410 height levels of 14 m and higher (excluding the lowest 7 grid points).

411 Excluding these lowest levels, the decrease in the non-dimensional structure parameters
412 vanishes (not shown) and the remaining data points all follow a single function with only

413 little scatter. This also legitimates the chosen definition of the surface-layer height (see
 414 Section 3c). The data points also show no dependence on time. Moreover, it is evident from
 415 Fig. 2 that $-z/L$ is an appropriate scaling parameter. As each simulation covers a different
 416 range of $-L$, it is evident from Fig. 2 that an increase (decrease) in z has the same effect on
 417 the dimensionless structure parameters as a decrease (increase) in $-L$ (this statement will
 418 be confined later on).

419 Fitting functions f_T and f_q are determined from this (reduced) data set for the first time
 420 from LES data and they are also shown in Fig. 2. The method of least squares using the
 421 formulation in Eqs. (7)-(8) and logarithmized values was employed to find the best fit. The
 422 data follows the proposed shape. However, it appears that the data follows a slope that
 423 is slightly steeper than the proposed $-2/3$ slope. This leads to an overestimation of the
 424 structure parameters by the fit in the free convection limit (for $-z/L > 10$). The LES data
 425 suggest

$$f_T(z/L) = 6.1 [1 - 7.6(z/L)]^{-2/3} \quad (24)$$

426 and

$$f_q(z/L) = 6.3 [1 - 7.4(z/L)]^{-2/3}. \quad (25)$$

427 Figure 3 shows that $f_T \approx f_q$ generally holds, which is expected when MOST is valid for
 428 both, temperature and humidity (Hill 1989; Andreas 1991). The difference between the
 429 coefficients in Eq. (24) and Eq. (25) is thus rather insignificant. Nevertheless, for weakly
 430 unstable conditions ($-z/L < 0.1$) it can be observed that f_T and f_q differ slightly. In the
 431 neutral limit ($-z/L \rightarrow 0$), the similarity functions become

$$f_T = c_{TT1} = 6.1, f_q = c_{qq1} = 6.3, \quad (26)$$

432 which makes a difference of 3% between f_T and f_q . Assuming perfect similarity ($f_T = f_q$)
 433 would give a systematic error in the flux of at most 1.5% (due to the exponent of $-1/2$ in
 434 Eq. (16)) and can thus be neglected. Nevertheless, this difference will be discussed later in
 435 Section 4b3ii. Li et al. (2012), who reported distinct dissimilarity of the turbulent transport

436 of sensible heat and moisture, found values of $c_{TT1} = 6.7 \pm 0.6$ and $c_{qq1} = 3.5 \pm 0.6$, differences
 437 between f_T and f_q that are one order of magnitude larger than what is found in the present
 438 LES fitting functions. As suggested by Li et al. (2012), their finding that the dimensionless
 439 C_T^2 was larger than the dimensionless C_q^2 in the near-neutral region might be explained by
 440 non-local effects, such as unsteadiness or advection, that are not considered in the LES.

441 Figure 4 shows a selection of MOST similarity functions that have been previously derived
 442 from measurement data, together with the fitted similarity functions, derived from the LES
 443 data (red solid lines). The LES results follow the same shape as the proposed functions from
 444 literature. For C_T^2 many authors suggested $c_{TT1} = 4.9$ (Wyngaard et al. 1971b; Andreas
 445 1988; De Bruin et al. 1993), while the LES suggests a higher value of 6.7. However, the
 446 suggested functions of Thiermann and Grassl (1992), Hill et al. (1992) and Li et al. (2012)
 447 suggest even higher values of up to 8.1. The LES data thus seem to be well within the range
 448 of the functions proposed in literature. For C_q^2 we find a significant difference between the
 449 LES ($c_{qq1} = 6.3$) and the study of Li et al. (2012) ($c_{qq1} = 3.5$) which might be ascribed to
 450 the fact that they observed dissimilarity between the transport of heat and moisture.

451 In strongly unstable conditions ($-z/L > 5$), all proposed functions f_T , including the LES
 452 fit, converge. As was stated in Section 2c, in the free convection limit, $A_T = \kappa^{-2/3} c_{TT1} c_{TT2}^{-2/3}$
 453 (analogous for humidity) is the relevant parameter and usually found to be around 2.7 (e.g.
 454 Wyngaard et al. 1971b; Wyngaard and LeMone 1980; Andreas 1991). The LES data yield
 455 values of $A_T = 2.9$ and $A_q = 3.0$, which is close to 2.7. We will have a detailed look at the
 456 free convection limit later in Section 4c.

457 2) DISSIMILARITY OF THE TURBULENT TRANSPORT OF TEMPERATURE AND HUMIDITY

458 A good measure for dissimilarity between the turbulent transport of heat and moisture
 459 is the cross-correlation between temperature and humidity R_{Tq} (Li et al. 2012). Figure 5a
 460 shows R_{Tq} , calculated from the two-dimensional (horizontal) cross-correlation coefficient of
 461 the LES data fields of temperature and humidity. It is visible that $R_{Tq} \geq 0.9$ for all data

462 points. This indicates a nearly perfect correlation between temperature and humidity. For
463 strongly unstable conditions ($-z/L > 1$), the data shows some scatter, but the correlation
464 does not drop below 0.9. A closer look into the data reveals that R_{Tq} generally decreases
465 with height. In the higher levels, the influence of entrained air from the free atmosphere is
466 more prominent, which can decrease the correlation between temperature and humidity.

467 For weakly unstable conditions ($-z/L < 0.1$), the data do not show much scatter, indi-
468 cating a perfect correlation and thus similarity of the turbulent transport of sensible heat and
469 moisture under near-neutral conditions. This is in contrast to Li et al. (2012) who observed
470 large scatter in R_{Tq} for small $-z/L$, leading to dissimilarity between structure parameter
471 relationships. They concluded that this decorrelation can be traced back to non-local effects
472 like non-stationarity of the flow, advection or entrainment effects. Since neither advection
473 nor non-stationarity are present in the LES, no dissimilarity has to be expected. However,
474 we will show in Section 4b3ii that entrainment effects can lead to dissimilarity, which clearly
475 supports the conclusion of Li et al. (2012).

476 3) SENSITIVITY ANALYSIS

477 (i) Definition of the Obukhov length

478 In the definition of the Obukhov length virtual potential temperature and the buoyancy
479 flux are used (see Eq. (1)). In practice, however, L is sometimes calculated using actual tem-
480 perature and sometimes the kinematic surface heat flux (e.g. Wyngaard et al. 1971b; Wesely
481 1976; Thiermann and Grassl 1992). While it is reasonable to use actual temperature without
482 introducing much error, neglecting the contribution of humidity to the buoyancy flux is a
483 rather questionable approximation and requires a sufficiently dry surface and boundary layer
484 (see also Andreas 1991). The present LES data suggest typical deviations of 10 % between
485 surface buoyancy flux and kinematic surface flux of heat (reference cases, not shown). In
486 order to quantify the effect of neglecting all humidity contributions, the MOST similarity

487 functions were additionally calculated using the Obukhov length for dry air L_{dry} (hereafter
488 also referred to as *dry approximation*), which is defined as

$$L_{\text{dry}} = -\frac{\bar{\theta}u_*^3}{\kappa g w' \theta'_0}. \quad (27)$$

489 Figure 3 shows the resulting fitting functions for both L and L_{dry} . Differences between the
490 correct and the dry approximation in the weakly unstable region ($-z/L < 0.1$) are obvious.
491 The dry approximation leads to a shift of f_T and f_q to lower values of $-z/L$ and suggests
492 fitting functions of

$$f_{T,\text{dry}}(z/L_{\text{dry}}) = 5.6 [1 - 7.5 (z/L_{\text{dry}})]^{-2/3} \quad (28)$$

493 and

$$f_{q,\text{dry}}(z/L_{\text{dry}}) = 6.0 [1 - 7.8 (z/L_{\text{dry}})]^{-2/3}. \quad (29)$$

494 In the free convection limit, this formulation yields $A_{T,\text{dry}} = 2.7$ and $A_{q,\text{dry}} = 2.8$ and thus
495 $A_{T,\text{dry}} \approx A_{q,\text{dry}}$. The dry approximation results are also plotted in Fig. 4, showing that
496 they all are within the proposed range of values. Based on this result we can infer neither
497 that one formulation is superior to the other, nor that the found formulations are universal.
498 Nevertheless, we can conclude that the definition of the Obukhov length can be at least one
499 reason for the difference in the proposed functions from literature.

500 (ii) *Effects of humidity*

501 The results from the reference simulations so far suggest that $f_T \approx f_q$. The reference
502 cases, however, consider only conditions with specific values of the kinematic surface fluxes
503 of heat and moisture, and one special state of the capping inversion. In order to get an idea
504 whether the derived functions are actually universal those parameters were varied that can
505 be considered to have an effect on the previous results (see Tab. 1). By using different surface
506 fluxes additional sensitivity simulations were generated with two different values for β_0 of
507 0.05 (case W08_β05) and 0.4 (case W08_β40). Additionally, a simulation without humidity
508 was carried out (case W08_dry, $\beta_0 = \infty$). Due to limited computational resources it was not

feasible to simulate the full $-z/L$ range (see also Section 3b). Hence a specific wind speed of 8 m s^{-1} was chosen. In this way a stability range of approximately $0.1 \leq -z/L \leq 2$ was covered. The reference cases displayed similar absolute entrainment fluxes that were around $0.2 - 0.3$ for temperature and humidity, see Table 1). Any effect of entrainment would thus affect both similarity functions in a similar way. In order to simulate at least one case with a different entrainment regime, a smaller lapse rate in the capping inversion of $\gamma = 7 \text{ K km}^{-1}$ was used (case W08- γ 07). Consequently the boundary layer in case W08- γ 07 was about 20 % higher than for the reference cases. Table 1 shows the entrainment flux ratios for all simulated cases. On the one hand, r_θ (ratio for temperature) was found to be increased in for W08-dry (-0.15) and decreased for W08- β 05 (-0.6), compared to the reference cases. This can be ascribed to the missing/additional contribution of moisture on the buoyancy flux (see also Eq. (20)). In contrast, cases W08- β 40 and W08- γ 07 did not show a significant modification compared to the reference case W08. The entrainment flux ratio for moisture r_q , on the other hand, showed only a response to the different setup for case W08- γ 07 with a value of about 1.

The normalized structure parameters for these sensitivity cases in comparison with the previously derived fitting functions are shown in Fig. 6 a,b. On the one hand, Fig. 6a shows that all data points strictly follow the fitting function proposed for f_T . Neither differences in β_0 nor in the lapse rate affect f_T and therefore we can argue that C_T^2 follows MOST and f_T is universal. Also, modifications due to differences in z_1 cannot be observed. On the other hand, Fig. 6b reveals a different behavior for C_q^2 . First of all, a change in the prescribed surface fluxes does not affect the similarity relationship and the data points follow the proposed function f_q , but case W08- γ 07 suggests higher values of the dimensionless C_q^2 . Moreover, the data points do not follow the proposed decrease for $-z/L > 1$ (equivalent to high values of z). Since no effect of the different lapse rate on C_T^2 was found we infer dissimilarity between the transport of heat and moisture that is caused by entrainment of dry air at the top of the mixed layer (cf. Fig. 6a). This is supported by R_{Tq} , which decreases rapidly with height from values

536 of 0.9 to 0.55 for this simulation (see Fig. 5b). A consequence of this dissimilarity is that
 537 turbulent humidity fluctuations in the surface layer are affected by entrainment and C_q^2 does
 538 no longer follow MOST. This is also in agreement with the findings of Lanotte and Mazzitelli
 539 (2013), who studied the effect of entrainment on the correlation between temperature and a
 540 passive scalar. They found that the correlation coefficient decreased, particularly in the lower
 541 boundary layer, when entrainment was significant. This result supports the assumption of
 542 Li et al. (2012) that entrainment might be a possible reason for dissimilarity between the
 543 transport of heat and moisture. The finding that $f_T \approx f_q$ in the reference simulations can
 544 be traced back to the fact that the entrainment flux ratio in the sensitivity simulations was
 545 ≤ 0.6 (absolute value) for both kinematic heat and moisture and thus sufficiently small to
 546 inhibit entrainment effects on the surface layer structure. In contrast, entrainment of dry
 547 air with an entrainment flux ratio of 1, as found in case W08_γ07, is apparently sufficient
 548 to affect the surface layer structure. The results suggest that the preceding statement that
 549 an increase in z would have the same effect on the dimensionless structure parameters as a
 550 decrease in $-L$ is limited to conditions where entrainment is sufficiently small. If entrainment
 551 is high, data from lower height levels are less affected by entrainment and will be determined
 552 by the surface fluxes and MOST might be considered. As no entrainment flux ratio > 0.6
 553 (absolute value, case W00_β05) was found for temperature, it is possible that there is also a
 554 critical value and that there might be conditions under which C_T^2 no longer follows MOST.
 555 In order to find such a critical value more sensitivity studies with increased entrainment of
 556 warm air (entrainment flux ratio ≥ 1.0) would be required.

557 Figure 6 c,d show the data from the sensitivity simulations with dry approximation of L .
 558 A significant gap is present between the data from case W08_β05 and the proposed fitting
 559 functions, whereas the proposed slope remains. Case W08_dry suggests higher dimensionless
 560 C_T^2 than the reference simulations (see Fig. 6c). This already proves that $f_{T,dry}$ cannot be
 561 considered universal. For case W08_β40 an effect is hardly visible, possibly due to the fact
 562 that the Bowen ratio was similar than in the reference simulation (0.27 and 0.4 for W08 and

563 W08 β 40, respectively). We must conclude that the dry approximation is not valid and no
 564 universal functions can be derived using L_{dry} .

565 *c. Local free convection scaling*

566 The LFC similarity constants A_T and A_q have been calculated from case W00 using
 567 the formulation in Eqs. (14) - (15). The lowest 7 grid points have been excluded from the
 568 analysis according to the results discussed in Section 4b1. Averaging of the remaining data
 569 points yields $A_T \approx 2.7$ and $A_q \approx 2.8$ (specification is given below). Figure 7 shows the
 570 dimensionless C_T^2 and C_q^2 according to Eqs. (14) - (15) derived from the LES data, including
 571 the lowest grid points. The data is complemented by the LFC predictions using A_T and A_q
 572 as given above. It is visible that the lowest 7 grid points deviate significantly from the LFC
 573 prediction, whereas there is very good agreement between LES and LFC prediction at height
 574 levels above 14 m. There the data shows only minor scatter due to variation in time and
 575 height. On closer inspection (hardly visible in Fig. 7), however, it can be observed that A_T
 576 and A_q both show a slight height-dependency up to height levels around 60 m with a peak
 577 value at a height of 40 m. Khanna and Brasseur (1997) and Brasseur and Wei (2010) found
 578 similar peaks for the dimensionless wind shear and temperature gradient and ascribed these
 579 to the SGS model. However, one would expect that this overshoot moves to higher (lower)
 580 levels if coarser (finer) grid resolutions are used in the LES (Sullivan et al. 1994; Brasseur
 581 and Wei 2010). Test simulations with grid resolutions between 5 – 20 m did not show such
 582 an effect for the present data set. We can thus conclude that this peak is not an effect of the
 583 SGS model. Possible other explanations are local shear-induced turbulence generation that
 584 is not considered in LFC scaling (Businger 1973) and the fact that similarity theory itself
 585 is an over-idealization of the surface layer dynamics (Hill 1989). However, as it is visible
 586 from Fig. 7, this height-dependency is not significant and we observe scatter in the data
 587 with deviations of not more than 7% from the mean values of A_T and A_q . The variation in
 588 time and height leads to $A_T = 2.7 \pm 0.2$ (95% confidence interval) which is in remarkable

589 agreement with observations in the lower part of the boundary layer (Wyngaard et al. 1971b;
 590 Kaimal et al. 1976; Wyngaard and LeMone 1980; Kunkel et al. 1981; Andreas 1991). The
 591 value is somewhat lower than 2.9, which was derived from the MOST fitting function earlier
 592 in Section 4b1. This can be traced back to an overestimation of f_T for large $-z/L$ by the
 593 fitting (see Fig. 2 b) and also applies to A_q , where the LES data suggest $A_q = 2.8 \pm 0.2$ for
 594 LFC scaling and the MOST fitting function gave 3.0. Peltier and Wyngaard (1995) found
 595 values between 2.0 – 2.7 in their LES data, suggesting a tendency to lower values than in the
 596 present LES. Note that the present LES data suggest that the value of A_T is roughly equal
 597 to that of A_q anyway, with a tendency of A_q to be higher than A_T . This can be ascribed
 598 to effects of entrainment that were already discussed in Section 4b3ii. This will also be
 599 discussed in Section 4c1.

600 As was stated in Section 2c, LFC is often applied for convenience, even under condi-
 601 tions where shear significantly contributes to turbulence production. Moreover, the effect
 602 of humidity is often neglected as independent measurements are not available. In order to
 603 estimate the error of this approximation, the surface fluxes were calculated for all refer-
 604 ence cases (Eqs. (21)-(22)) and additionally for the formulation for dry air (Eq. (23)) using
 605 $A_T = 2.7$ and $A_q = 2.8$ (we will show later that no universal constants exist for the dry
 606 approximation). Figure 8a, b shows that for case W00 (free convection, $-1/L \approx 0.4 \text{ m}^{-1}$)
 607 the uncertainty in the kinematic surface fluxes of heat and moisture due to variation of A_T
 608 in height and time (see Fig. 7) is about 5% (95% confidence interval). The mean value,
 609 however, is exact, because the values for A_T and A_q have been derived from case W00. With
 610 decreasing $-1/L$ ($0.02 \text{ m}^{-1} \leq -1/L \leq 0.2 \text{ m}^{-1}$) it can be observed that the surface fluxes
 611 are overestimated by up to 5%. The scatter in the derived fluxes (due to variation in time
 612 and height) is slightly increasing to 8 – 10%. For $-1/L < 0.017 \text{ m}^{-1}$ shear-production starts
 613 to dominate the surface layer flow and the flux estimates decrease while the scatter of the
 614 estimates increases. For case W00_F10 the estimate of the flux is 40% too small with scatter
 615 of about 20% around this value. From Fig. 8c it becomes evident that the dry approxi-

616 mation leads to an systematic underestimation of the kinematic surface flux of heat. This
 617 was already predicted in Section 2c because $h \geq 1$ under unstable conditions. For case W00
 618 this leads to an underestimation of the flux of about 10%. On the one hand, the shape
 619 of the curve in Fig. 8c coincides with that shown in Fig. 8a, because the Bowen ratio was
 620 equal in all reference simulations. The scatter, on the other hand, is slightly reduced, due
 621 to the fact that fluctuations in humidity do not lead to additional fluctuations in θ_v . The
 622 underestimation of $\overline{w'\theta'_0}$ depends mainly on the Bowen ratio (see Eq. (21) and Eq. (23)) and
 623 is thus obviously sensitive to changes in the surface fluxes.

624 In summary the LES results suggest that LFC scaling can be applied even under moderate
 625 wind conditions (here for wind speeds up to 8 m s^{-1} with $-1/L \geq 0.017 \text{ m}^{-1}$) without
 626 accepting an systematic error of more than 5% and scatter (due to variation in time and
 627 height) of more than 10% around this value. This estimate of the error is of course based
 628 on virtual measurements at different heights that are already representing the horizontal
 629 average. In practice, the error in the flux will increase if sufficient averaging of turbulent
 630 motions (e.g. by spatially or temporally averaging) is not feasible. Moreover it is shown
 631 that the kinematic surface flux of heat is underestimated if humidity is significant in the
 632 boundary layer, but neglected in the buoyancy term (see Eq. (23)). The magnitude of this
 633 underestimation is mainly given by the surface Bowen ratio. By an independent estimate
 634 of β_0 (see e.g. De Bruin et al. 1999) and using the approximation h by Andreas (1991) one
 635 might overcome the underestimation of $\overline{w'\theta'_0}$.

636 1) SENSITIVITY ANALYSIS

637 In analogy to the analysis in Section 4b3, A_T and A_q were derived from the sensitivity
 638 cases W00_dry, W00_β05, W00_β40 and W00_γ07. Additionally, the dry approximations
 639 $A_{T,\text{dry}}$ and $A_{q,\text{dry}}$ (no humidity considered in the calculation of w_{LF}) were calculated. The
 640 results are shown in Table 2 together with the estimates from MOST fitting functions. It
 641 is apparent that A_T is constant for the sensitivity cases with a value around 2.7 and can

642 thus be considered universal. The MOST fitting function gives a slightly higher value of 2.9,
643 which can be ascribed to the overestimation of the dimensionless C_T^2 by the fitting function
644 f_T as already discussed. A_q can be only considered universal with a value around 2.8 if
645 entrainment is sufficiently small. In this case the assumption that $A_T = A_q$ by Andreas
646 (1991) is valid. When entrainment becomes significant (case W00_γ07), A_q is higher (here
647 3.2 ± 0.5) and A_q is thus no longer universal. This is in agreement with Peltier and Wyngaard
648 (1995) who found a larger value for A_q than for A_T due to entrainment effects in their LES
649 data. The fact that the LFC prediction becomes non-universal for humidity can explain why
650 no consensus was reached on the exact value of A_q so far.

651 Despite the fact that both MOST and LFC scaling suggest $A_{T,dry} \approx A_{q,dry}$ (except case
652 W00_γ07), the dry approximation reveals varying values between 1.5 ± 0.1 and 2.8 ± 0.5 .
653 These results clarify that neglecting the effect of humidity to buoyancy is not a valid approach
654 neither for MOST, nor for LFC scaling, and no universal similarity functions can be obtained.

655 5. Summary

656 The present LES study focused on the derivation of similarity relationships for structure
657 parameters in the unstable atmospheric surface layer. Due to a grid resolution of 2 – 4 m
658 and today's computing capacities it was possible to actually resolve the surface layer with
659 an LES model for a whole set of LES, covering convective to near-neutral boundary layers.
660 This was necessary to cover all relevant stability ranges that are commonly expressed in
661 terms of the parameter $-z/L$. The LES results showed that the flow within the lowest grid
662 levels of the LES should be generally interpreted carefully because effects of the SGS model
663 are present and the flow is not well-resolved.

664 The analysis of the MOST relationships showed that the dimensionless structure param-
665 eters of temperature and humidity strictly follow functions (f_T and f_q) that only depend
666 on $-z/L$, as proposed by theory and previous experimental data. Only little scatter in the

667 LES data was found so that MOST fitting functions, linking the structure parameters to the
668 kinematic surface fluxes of heat and moisture, were derived for the first time from LES data.
669 While there is a lack of explicit fitting functions for C_q^2 in literature, the fitting function for
670 C_T^2 was found to be well within the range of the previously suggested similarity functions
671 from measurement data. It could be shown that increasing (decreasing) the measurement
672 height z had the same effect as decreasing (increasing) L . On the one hand, it thus appears
673 to be a logical approach to place measurement instruments (e.g. scintillometers) as high
674 as possible in order to approach the free convection limit. On the other hand, this would
675 increase the size of the footprint of the measurement.

676 The LES results strongly suggest that C_T^2 follows MOST and that f_T is a universal func-
677 tion. However, for C_q^2 it is found that MOST relationships are only valid if entrainment at
678 the top of the mixed layer is sufficiently small (here if the absolute value of the entrainment
679 flux ratio < 0.6). In this case it holds that $f_T \approx f_q$. For an entrainment flux ratio of 1, dry
680 air that is entrained into the mixed-layer can also affect the surface layer structure. Conse-
681 quently, C_q^2 no longer follows MOST and f_q cannot be considered to be a universal function.
682 Furthermore, it could be shown that higher levels are more affected by entrainment than
683 low levels, in agreement with previous experimental and LES results (e.g. Fairall 1987, 1991;
684 Cheinet and Cumin 2011). This was also visible in the correlation coefficient between tem-
685 perature and humidity, which decreased with height, suggesting that dissimilarity between
686 the turbulent transport of heat and moisture can be induced by entrainment. This finding
687 might explain the dissimilarity observed by Li et al. (2012). The preceding conclusion to per-
688 form measurement as high as possible must thus be limited to conditions where entrainment
689 effects can be neglected. However, a more extensive sensitivity study would be required to
690 define critical values of the entrainment flux ratio.

691 In the free convection limit, where LFC scaling is applicable, the dimensionless structure
692 parameters reduce to constants A_T and A_q . The common value of 2.7 for A_T was reproduced
693 by the LES model, with scatter of 5% in the data. If entrainment is sufficiently small, A_q

694 is found to be around 2.8, so that the assumption $A_T = A_q$ is roughly valid, even though
695 A_q appears to be consistently larger than A_T , which is in agreement with the data of Li
696 et al. (2012) for convective conditions. This difference between A_T and A_q is, however,
697 within the 95 % confidence bounds (see Table 2). Otherwise no universal value for A_q can be
698 derived. The scatter was mostly related to a height-dependence of A_T with an overshoot at
699 a height of 40 m. Possible reasons for this overshoot might be the fact that similarity theory
700 is an over-idealization of the surface layer dynamics (Hill 1989) and local shear-production
701 by the turbulence near the surface (Businger 1973). An error analysis showed that LFC
702 scaling can be applied even for moderate wind conditions (with $-1/L \geq 0.017 \text{ m}^{-1}$) without
703 introducing a systematical error of more than 5 % and scatter of more than 10 % (95 %
704 confidence interval).

705 Neglecting the contribution of humidity on the buoyancy flux (and hence on L and w_{LFC})
706 was found to lead to dimensionless structure parameters that can no longer be expressed
707 in terms of universal functions or constants. Using the formulation for dry air is thus a
708 rather questionable approach and limited to sufficiently dry conditions (see also Andreas
709 1988, 1991). It could be shown that the kinematic surface flux of heat is systematically
710 underestimated when humidity is significant. At least an estimate of the surface Bowen
711 ratio is required to account for the effect of humidity on buoyancy when using LFC scaling.

712 In a follow-up study the MOST and LFC relationships for structure parameters will
713 be derived in the CBL over the heterogeneous LITFASS terrain in the south-east of Berlin
714 (Germany) in order to investigate the effect of surface heterogeneity on structure parameters
715 and their similarity relationships.

716 *Acknowledgments.*

717 The author would like to thank Frank Beyrich (German Weather Service, DWD) and
718 Siegfried Raasch (Leibniz Universität Hannover, Germany) for reading a draft of this ar-
719 ticle. Sincere thanks are given to the Meteorology and Air Quality Group at Wageningen

720 University (The Netherlands) for their valuable comments and the discussion during a visit
721 in Wageningen in 2012. Particularly, the author would like to thank Jordi Vilà as well as
722 Arnold Moene and Miranda Braam. The latter two also provided additional valuable com-
723 ments on the manuscript, which is gratefully acknowledged. Finally, the author would like
724 to thank the three anonymous reviewers for their comments and suggestions that helped to
725 improve the manuscript. This study was supported by the German Research Foundation
726 (DFG) under grants RA 617/20-1 and RA 617/20-3. All simulations were performed on the
727 SGI Altix ICE at The North-German Supercomputing Alliance (HLRN), Hannover/Berlin.
728 NCL¹ has been used for data analysis and visualization.

¹The NCAR Command Language (Version 5.2.1) [Software]. (2010). Boulder, Colorado:
UCAR/NCAR/CISL/VETS. <http://dx.doi.org/10.5065/D6WD3XH5>

729

730

REFERENCES

- 731 Andreas, E. L., 1988: Estimating C_n^2 over snow and sea ice from meteorological data. *J. Opt.*
732 *Soc. Amer.*, **5**, 481–495.
- 733 Andreas, E. L., 1991: Using scintillation at two wavelengths to measure path-averaged heat
734 fluxes in free convection. *Boundary-Layer Meteorol.*, **54**, 167–182.
- 735 Beyrich, F., R. D. K. J.-P. Leps, A. Lüdi, W. M. L. Meijninger, and U. Weisensee, 2005:
736 Structure parameters for temperature and humidity from simultaneous eddy-covariance
737 and scintillometer measurements. *Meteorol. Zeitschrift*, **14**, 641–649.
- 738 Beyrich, F., et al., 2012: Towards a validation of scintillometer measurements: The
739 LITFASS-2009 experiment. *Boundary-Layer Meteorol.*, **144**, 83–112.
- 740 Blackadar, A. K., 1997: *Turbulence and Diffusion in the Atmosphere*. Springer, Berlin, Hei-
741 delberg, New York, 185 pp.
- 742 Brasseur, J. G. and T. Wei, 2010: Designing large-eddy simulation of the turbulent boundary
743 layer to capture law-of-the-wall scaling. *Phys. Fluids*, **22**, 021303.
- 744 Businger, J. A., 1973: A note on free convection. *Boundary-Layer Meteorol.*, **4**, 323–326.
- 745 Cheinet, S. and P. Cumin, 2011: Local structure parameters of temperature and humidity
746 in the entrainment-drying convective boundary layer: A large-eddy simulation analysis.
747 *J. Appl. Meteorol.*, **50**, 472–481.
- 748 Cheinet, S. and A. P. Siebesma, 2009: Variability of Local Structure Parameters in the
749 Convective Boundary Layer. *J. Atmos. Sci.*, **66**, 1002–1017.

- 750 Deardorff, J. W., 1980: Stratocumulus-capped mixed layers derived from a three-dimensional
751 model. *Boundary-Layer Meteorol.*, **18**, 495–527.
- 752 De Bruin, H. A. R., W. Kohsiek, and B. J. J. M. van den Hurk, 1993: A verification of
753 some methods to determine the fluxes of momentum, sensible heat and water vapour
754 using standard deviation and structure parameter of scalar meteorological quantities.
755 *Boundary-Layer Meteorol.*, **63**, 231–257.
- 756 De Bruin, H. A. R., B. J. J. M. van den Hurk, and W. Kohsiek, 1995: The scintillation
757 method tested over a dry vineyard area. *Boundary-Layer Meteorol.*, **76**, 25–40.
- 758 De Bruin, H. A. R., B. J. J. M. Van den Hurk, and I. J. M. Kroon, 1999: On the temperature-
759 humidity correlation and similarity. *Boundary-Layer Meteorol.*, **93**, 453–468.
- 760 Druilhet, A., J. P. Frangi, D. Guedalia, and J. Fonton, 1983: Experimental studies of the tur-
761 bulence structure parameters of the convective boundary layer. *J. Clim. Appl. Meteorol.*,
762 **22**, 594–608.
- 763 Evans, J. G., D. D. McNeil, J. W. Finch, T. Murray, R. J. Harding, H. C. Ward, and A. Ver-
764 hoef, 2012: Determination of turbulent heat fluxes using a large aperture scintillometer
765 over undulating mixed agricultural terrain. *Agric. For. Meteorol.*, **166-167**, 221–233, doi:
766 10.1016/j.agrformet.2012.07.010.
- 767 Fairall, C. W., 1984: Wind shear enhancement of entrainment and refractive index structure
768 parameter at the top of a turbulent mixed layer. *J. Atmos. Sci.*, **41**, 3472–3484.
- 769 Fairall, C. W., 1987: A top-down and bottom-up diffusion model of C_T^2 and C_Q^2 in the
770 entraining convective boundary layer. *J. Atmos. Sci.*, **44**, 1009–1017.
- 771 Fairall, C. W., 1991: The humidity and temperature sensitivity of clear-air radars in the
772 convective boundary layer. *J. Appl. Meteorol.*, **41**, 1064–1074.

- 773 Foken, T., 2006: 50 Years of the Monin-Obukhov Similarity Theory. *Boundary-Layer Mete-*
774 *orol.*, **119**, 431–447, doi:10.1007/s10546-006-9048-6.
- 775 Hill, R. J., G. R. Ochs, and J. J. Wilson, 1992: Measuring surface-layer fluxes of heat and
776 momentum using optical scintillation. *Boundary-Layer Meteorol.*, **58**, 391–408.
- 777 Hill, R. J., 1978: Spectra of Fluctuations in Refractivity, Humidity, and the Temperature-
778 Humidity Cospectrum in the Inertial and Dissipation Range. *Radio Sci.*, **13**, 953–961.
- 779 Hill, R. J., 1989: Implications of Monin-Obukhov Similarity Theory for Scalar Quantities.
780 *J. Atmos. Sci.*, **46**, 2236–2244.
- 781 Johansson, C., A.-S. Smedman, U. Högström, J. G. Brasseur, and S. Khanna, 2001: Critical
782 Test of the Validity of Monin-Obukhov Similarity during Convective Conditions. *J. Atmos.*
783 *Sci.*, **58**, 1549–1566.
- 784 Johansson, C., A.-S. Smedman, U. Högström, and J. G. Brasseur, 2002: Reply to comments
785 by E. L. Andreas and B. B. Hicks (2002). *J. Atmos. Sci.*, **59**, 2608–2614.
- 786 Kaimal, J. C., J. C. Wyngaard, D. A. Haugen, O. R. Coté, Y. Izumi, S. J. Caughey, and
787 C. J. Readings, 1976: Turbulence structure in the convective boundary layer. *J. Atmos.*
788 *Sci.*, **33**, 2152–2169.
- 789 Khanna, S. and J. G. Brasseur, 1997: Analysis of Monin-Obukhov similarity from large-eddy
790 simulations. *J Fluid Mech.*, **345**, 251–286.
- 791 Kohsiek, W., W. M. L. Meijninger, A. F. Moene, B. G. Heusinkveld, O. K. Hartogensis,
792 W. C. A. M. Hillen, and H. A. R. De Bruin, 2002: An extra large aperture scintillometer
793 for long range applications. *Boundary-Layer Meteorol.*, **105**, 119–127.
- 794 Kohsiek, W., 1982: Measuring C_T^2 , C_Q^2 , and C_{TQ} in the unstable surface layer, and relations
795 to the vertical fluxes of heat and moisture. *Boundary-Layer Meteorol.*, **24**, 89–107.

- 796 Kunkel, K. E., D. L. Walters, and G. A. Ely, 1981: Behavior of the Temperature Structure
797 Parameter in a Desert Basin. *J. Appl. Meteorol.*, **20**, 130–136.
- 798 Lanotte, A. S. and I. M. Mazzitelli, 2013: Scalar Turbulence in Convective Boundary Layers
799 by Changing the Entrainment Flux. *J. Atmos. Sci.*, **70**, 248–265.
- 800 Letzel, M. O., M. Krane, and S. Raasch, 2008: High resolution urban large-eddy simulation
801 studies from street canyon to neighbourhood scale. *Atmos. Env.*, **42**, 8770–8784.
- 802 Li, D., E. Bou-Zeid, and H. A. R. De Bruin, 2012: Monin-Obukhov Similarity Functions for
803 the Structure Parameters of Temperature and Humidity. *Boundary-Layer Meteorol.*, **145**,
804 45–67, doi:10.1007/s10546-011-9660-y.
- 805 Maronga, B., A. F. Moene, D. van Dinter, S. Raasch, F. C. Bosveld, and B. Gioli, 2013:
806 Derivation of Structure Parameters of Temperature and Humidity in the Convective
807 Boundary Layer from Large-Eddy Simulations and Implications for the Interpretation of
808 Scintillometer Observations. *Boundary-Layer Meteorol.*, doi:10.1007/s10546-013-9801-6.
- 809 Mason, P. J. and D. J. Thomson, 2002: Stochastic backscatter in large-eddy simulations of
810 boundary layers. *J. Fluid Mech.*, **242**, 51–78.
- 811 Meijninger, W. M. L., F. Beyrich, A. Lüdi, W. Kohsiek, and H. A. R. De Bruin, 2006:
812 Scintillometer-based turbulent fluxes of sensible and latent heat over a heterogeneous land
813 surface - A contribution to LITFASS-2003. *Boundary-Layer Meteorol.*, **121**, 89–110.
- 814 Meijninger, W. M. L., A. E. Green, O. K. Hartogensis, W. Kohsiek, J. C. B. Hoedjes, R. M.
815 Zuurbier, and H. A. R. De Bruin, 2002: Determination of area-averaged water vapour
816 fluxes with large aperture and radio wave scintillometers over a heterogeneous surface -
817 Flevoland field experiment. *Boundary-Layer Meteorol.*, **105**, 63–83.
- 818 Muschinski, A., R. Frehlich, and B. B. Balsley, 2004: Small-scale and large-scale inter-

- 819 mittency in the nocturnal boundary layer and the residual layer. *J. Fluid Mech.*, **515**,
820 319–351.
- 821 Obukhov, A. M., 1946: Turbulence in an atmosphere with a non-uniform temperature.
822 *Tr. Inst. Teor. Geofiz. Akad. Nauk. SSSR*, **1**, 95–115, translation in: *Boundary-Layer*
823 *Meteorol.*, 1971, **2**, 7-29.
- 824 Panofsky, H. A. and J. A. Dutton, 1984: *Atmospheric Turbulence, Models and Methods for*
825 *Engineering Applications*. John Wiley & Sons, New York, 397 pp.
- 826 Peltier, L. J. and J. C. Wyngaard, 1995: Structure-Function Parameters in the Convective
827 Boundary Layer from Large-Eddy Simulations. *J. Atmos. Sci.*, **52**, 3641–3660.
- 828 Raasch, S. and T. Franke, 2011: Structure and formation of dust-devil-like vortices in the
829 atmospheric boundary layer - A high resolution numerical study. *J. Geophys. Res.*, **116**,
830 doi:10.1029/2011JD016010, D16120.
- 831 Raasch, S. and M. Schröter, 2001: PALM - A large-eddy simulation model performing on
832 massively parallel computers. *Meteorol. Z.*, **10**, 363–372.
- 833 Riechelmann, T., Y. Noh, and S. Raasch, 2012: A new method for large-eddy simulations of
834 clouds with Lagrangian droplets including the effects of turbulent collision. *New J. Phys.*,
835 **14**, doi:10.1088/1367-2630/14/6/065008, 065008.
- 836 Stull, R. B., 1988: *An Introduction to Boundary Layer Meteorology*. Kluwer Academic Pub-
837 lishers, Dordrecht, 666 pp.
- 838 Sullivan, P. P., J. C. McWilliams, and C.-H. Moeng, 1994: A subgrid-scale model for large-
839 eddy simulation of planetary boundary-layer flows. *Boundary-Layer Meteorol.*, **71**, 247–
840 276.
- 841 Tatarskii, V. I., 1971: *The Effects of the Turbulent Atmosphere on Wave Propagation*. Kefer
842 Press, Jerusalem, 472 pp.

- 843 Thiermann, V. and H. Grassl, 1992: The measurement of turbulent surface-layer fluxes by
844 use of bichromatic scintillation. *Boundary-Layer Meteorol.*, **58**, 367–389.
- 845 Wesely, M. L., 1976: A Comparison of Two Optical Methods for Measuring Line Averages
846 of Thermal Exchanges Above Warm Water Surfaces. *J. Appl. Meteorol.*, **15**, 1177–1188.
- 847 Wicker, L. J. and W. C. Skamarock, 2002: Time-splitting methods for elastic models using
848 forward time schemes. *Mon. Wea. Rev.*, **130**, 2088–2097.
- 849 Williamson, J. H., 1980: Low-storage Runge-Kutta schemes. *J. Comp. Phys.*, **35**, 48–56,
850 doi:10.1016/0021-9991(80)90033-9.
- 851 Wilson, C. and E. Fedorovich, 2012: Direct evaluation of refractive-index structure func-
852 tions from large-eddy simulation output for atmospheric convective boundary layers. *Acta*
853 *Geophys.*, **60**, 1474–1492.
- 854 Wyngaard, J. C., O. R. Coté, and Y. Izumi, 1971a: Local Free Convection, Similarity, and
855 the Budgets of Shear Stress and Heat Flux. *J. Atmos. Sci.*, **28**, 1171–1182.
- 856 Wyngaard, J. C., Y. Izumi, and S. A. J. Collins, 1971b: Behavior of the refractive-index-
857 structure parameter near the ground. *J. Opt. Soc. Am.*, **61**, 1646–1650.
- 858 Wyngaard, J. C. and M. A. LeMone, 1980: Behavior of the Refractive Index Structure
859 Parameter in the Entraining Convective Boundary Layer. *J. Atmos. Sci.*, **37**, 1573–1585.

860 List of Tables

861	1	Overview of the LES setup, complemented by the maximum values of z_i as well	
862		as entrainment flux ratios for temperature (r_θ), moisture (r_q) and buoyancy	
863		(r_{θ_v}) that have been determined from the LES data. β_0 is the surface Bowen	
864		ratio and γ is lapse rate of potential temperature in the capping inversion.	37
865	2	Overview of similarity constants for local free convection scaling and their	
866		double standard deviation (95% confidence interval), and the estimated values	
867		from the derived MOST fitting functions.	38

TABLE 1. Overview of the LES setup, complemented by the maximum values of z_i as well as entrainment flux ratios for temperature (r_θ), moisture (r_q) and buoyancy (r_{θ_v}) that have been determined from the LES data. β_0 is the surface Bowen ratio and γ is lapse rate of potential temperature in the capping inversion.

Case	Wind (m s ⁻¹)	$\overline{w'\theta'_0}$ (K m s ⁻¹)	$\overline{w'q'_0}$ (g kg ⁻¹ m s ⁻¹)	β_0	γ (K km ⁻¹)	r_θ	r_q	r_{θ_v}	$z_{i,\max}$ (km)
W00	0	0.075	0.11	0.27	27	-0.25	0.3	-0.15	1.08
W02	2	0.075	0.11	0.27	27	-0.25	0.35	-0.15	1.08
W04	4	0.075	0.11	0.27	27	-0.25	0.3	-0.15	1.08
W06	6	0.075	0.11	0.27	27	-0.25	0.3	-0.15	1.08
W08	8	0.075	0.11	0.27	27	-0.2	0.3	-0.15	1.08
W10	10	0.075	0.11	0.27	27	-0.2	0.3	-0.15	1.08
W10_F50	10	0.0375	0.055	0.27	27	-0.3	0.3	-0.15	1.04
W10_F10	10	0.0075	0.011	0.27	27	-0.4	0.3	-0.2	1.0
W00_dry	0	0.075	0.0	∞	27	-0.15	-	-0.15	1.06
W00_ β 05	0	0.075	0.6	0.05	27	-0.6	0.2	-0.15	1.14
W00_ β 40	0	0.109	0.11	0.4	27	-0.2	0.4	-0.15	1.11
W00_ γ 07	0	0.075	0.11	0.27	7	-0.3	1.0	-0.15	1.29
W08_dry	8	0.075	0.0	∞	27	-0.15	-	-0.15	1.06
W08_ β 05	8	0.075	0.6	0.05	27	-0.55	0.2	-0.15	1.14
W08_ β 40	8	0.109	0.11	0.4	27	-0.2	0.4	-0.15	1.11
W08_ γ 07	8	0.075	0.11	0.27	7	-0.3	1.0	-0.10	1.28

TABLE 2. Overview of similarity constants for local free convection scaling and their double standard deviation (95% confidence interval), and the estimated values from the derived MOST fitting functions.

Case	β_0	A_T	A_q	$A_{T,dry}$	$A_{q,dry}$
W00	0.27	2.7 ± 0.2	2.8 ± 0.2	2.3 ± 0.2	2.4 ± 0.2
W00_dry	∞	2.7 ± 0.3	-	2.7 ± 0.3	-
W00_β05	0.05	2.8 ± 0.2	2.8 ± 0.2	1.5 ± 0.1	1.5 ± 0.1
W00_β40	0.4	2.7 ± 0.3	2.8 ± 0.2	2.4 ± 0.2	2.5 ± 0.2
W00_γ07	0.27	2.7 ± 0.3	3.2 ± 0.5	2.3 ± 0.2	2.8 ± 0.5
MOST	0.27	2.9	3.0	2.7	2.8

868 List of Figures

869	1	Vertical mean profiles of a potential temperature and b humidity.	40
870	2	Normalized structure parameters of a temperature and b humidity against	
871		stability parameter $-z/L$. The solid black lines indicate the determined	
872		MOST fitting functions f_T, f_q .	41
873	3	LES fitting functions f_T and f_q and results with dry Obukhov length.	42
874	4	Overview of fitting functions a f_T and b f_q that have been proposed in lit-	
875		erature against stability parameter $-z/L$ and compared to the LES fit (red	
876		solid lines) and the LES fit using L_{dry} (solid blue lines , see Eq. (27)).	43
877	5	Correlation coefficient between temperature and humidity R_{Tq} a for the ref-	
878		erence simulations and b for sensitivity cases (right).	44
879	6	Non-dimensional structure parameters from sensitivity simulations and MOST	
880		fitting function a f_T , b f_q , and with dry approximation c $f_{T,\text{dry}}$ and d $f_{q,\text{dry}}$.	45
881	7	Normalized profiles of a C_T^2 and b C_q^2 complemented with the LFC predictions	
882		using $A_T = 2.7$ and $A_q = 2.8$ in the lower unstable boundary layer for every	
883		120 s.	46
884	8	Uncertainty of estimates of the surface fluxes (a sensible heat, b latent heat	
885		and c sensible heat with dry approximation) using LFC similarity against	
886		inverse Obukhov length. The symbols represent averaged data over each	
887		simulation (where L was more or less constant). The error bars indicate the	
888		scatter in height and time of the 95% confidence interval.	47

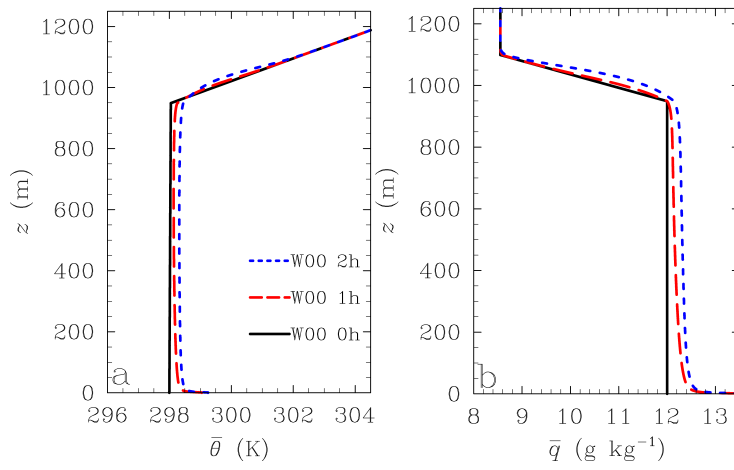


FIG. 1. Vertical mean profiles of **a** potential temperature and **b** humidity.

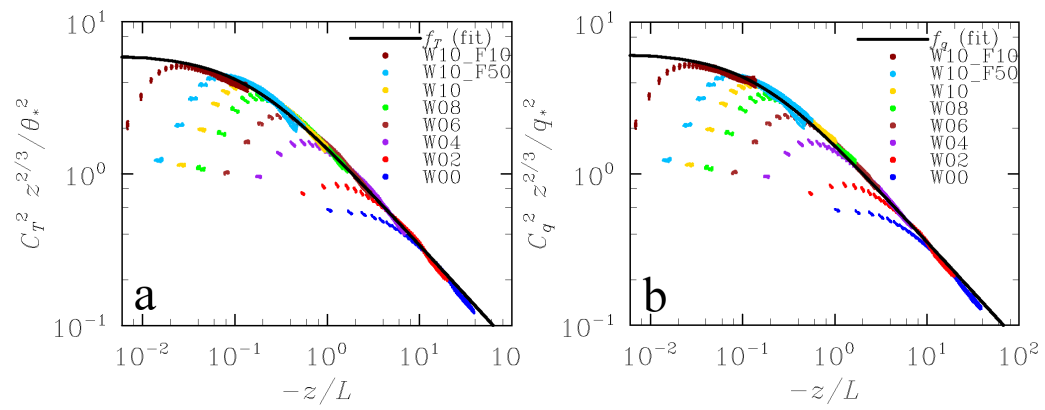


FIG. 2. Normalized structure parameters of **a** temperature and **b** humidity against stability parameter $-z/L$. The **solid black lines** indicate the determined MOST fitting functions f_T , f_q .

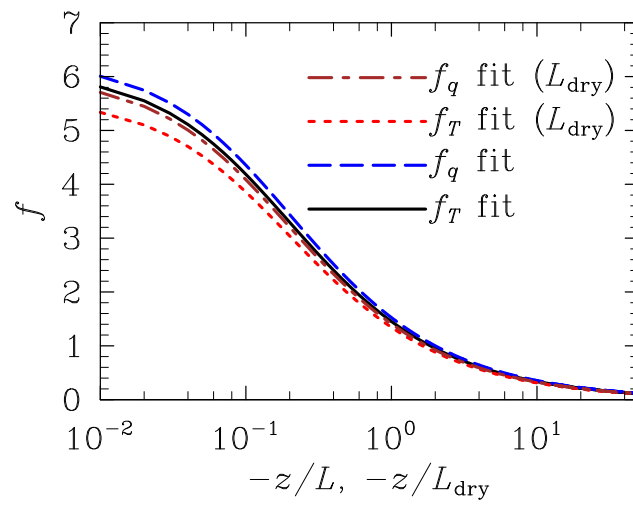


FIG. 3. LES fitting functions f_T and f_q and results with dry Obukhov length.

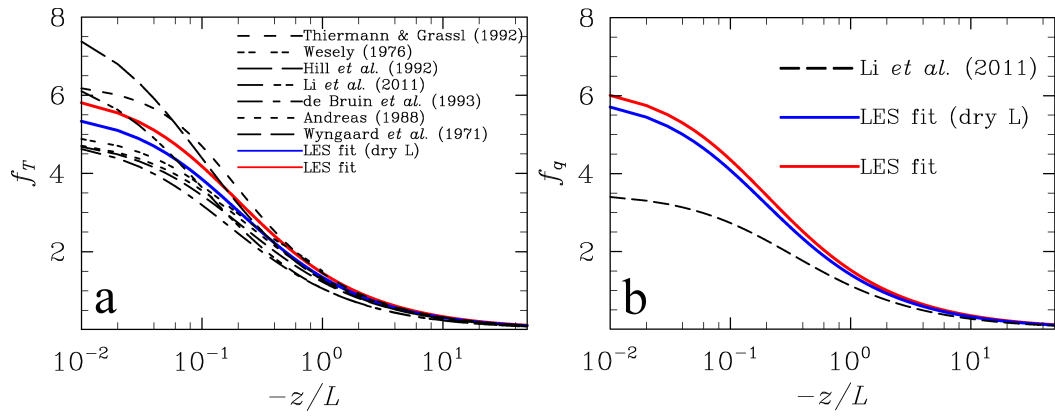


FIG. 4. Overview of fitting functions **a** f_T and **b** f_q that have been proposed in literature against stability parameter $-z/L$ and compared to the LES fit (**red solid lines**) and the LES fit using L_{dry} (**solid blue lines**, see Eq. (27)).

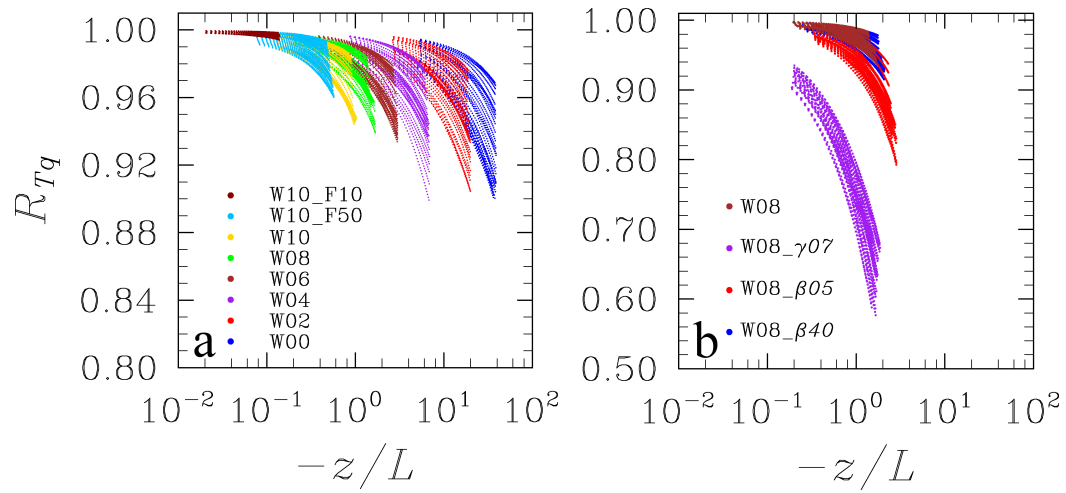


FIG. 5. Correlation coefficient between temperature and humidity R_{Tq} **a** for the reference simulations and **b** for sensitivity cases (right).

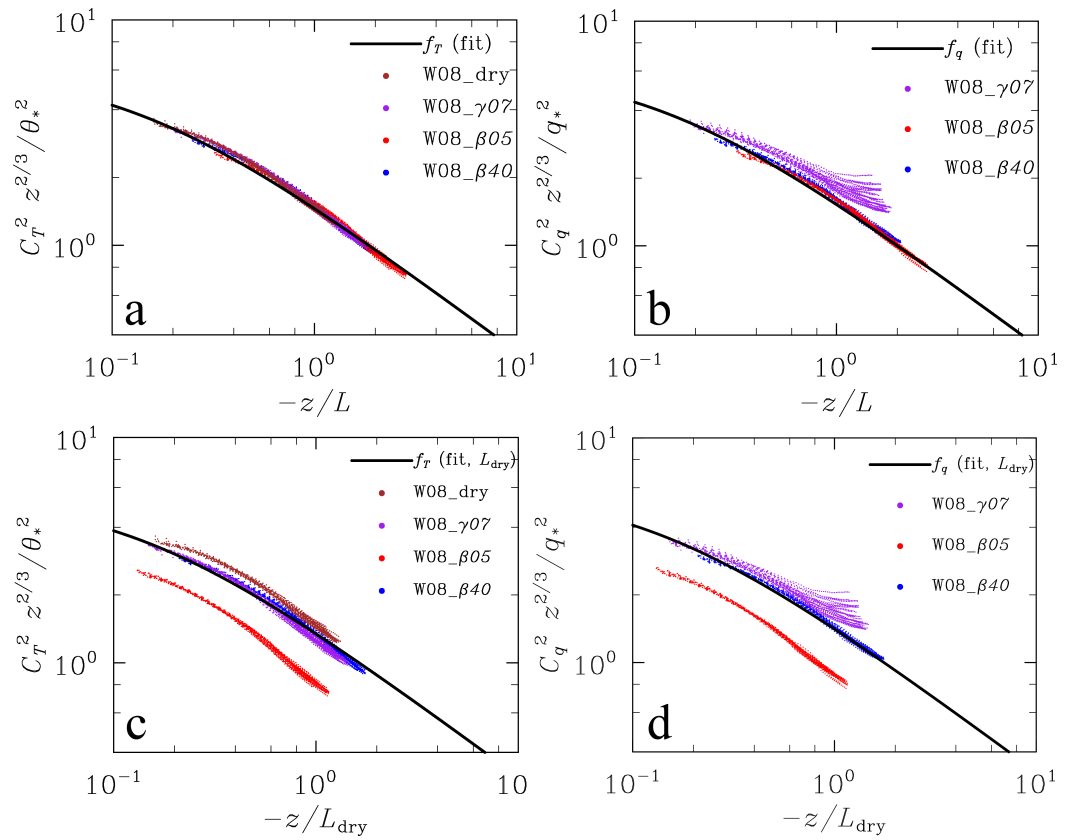


FIG. 6. Non-dimensional structure parameters from sensitivity simulations and MOST fitting function **a** f_T , **b** f_q , and with dry approximation **c** $f_{T,\text{dry}}$ and **d** $f_{q,\text{dry}}$.

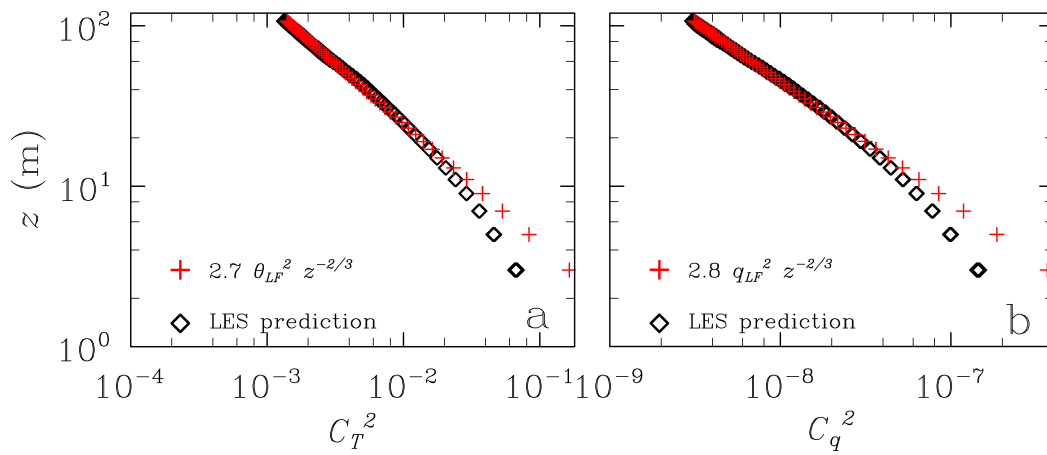


FIG. 7. Normalized profiles of **a** C_T^2 and **b** C_q^2 complemented with the LFC predictions using $A_T = 2.7$ and $A_q = 2.8$ in the lower unstable boundary layer for every 120 s.

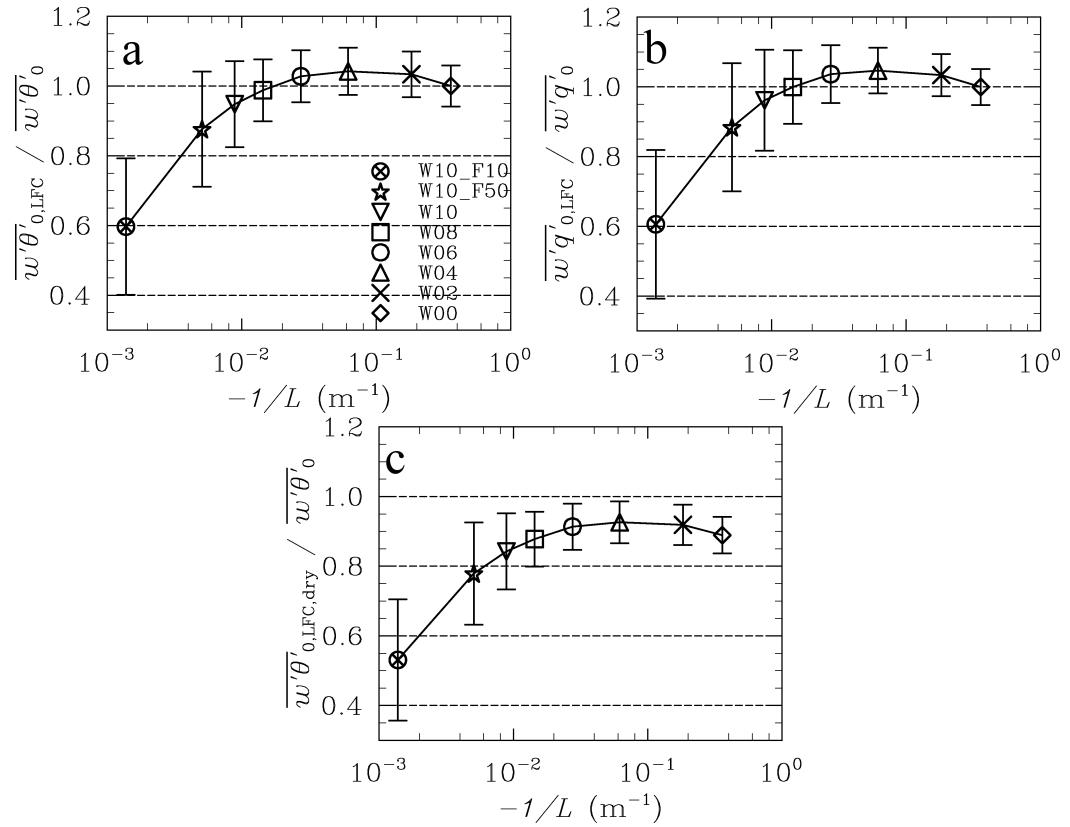


FIG. 8. Uncertainty of estimates of the surface fluxes (**a** sensible heat, **b** latent heat and **c** sensible heat with dry approximation) using LFC similarity against inverse Obukhov length. The **symbols** represent averaged data over each simulation (where L was more or less constant). The **error bars** indicate the scatter in height and time of the 95% confidence interval.

3.3 Research article C: Large-eddy simulations of surface heterogeneity effects on the convective boundary layer during the LITFASS-2003 Experiment

3.3.1 Declaration of my contribution

I carried out all LES and subsequent analyses included in this paper in the scope of my diploma thesis and under supervision of Prof. Dr. Siegfried Raasch. The study itself was inspired by the previous work of Uhlenbrock (2006). The manuscript was written, revised and published during my doctoral studies. The article was improved by comments and suggestions from Prof. Dr. Siegfried Raasch and during the peer review process.

3.3.2 Published article

This article is published with open access in *Boundary-Layer Meteorology*.
Submitted: 15 July 2011. Published online: 12 July 2012, as print: Volume 146, 1 Issue, January 2013.

Maronga, B. and S. Raasch, 2013: Large-Eddy Simulations of Surface Heterogeneity Effects on the Convective Boundary Layer During the LITFASS-2003 Experiment. *Boundary-Layer Meteorol.*, **146**, 17-44, doi: 10.1007/s10546-012-9748-z.

Boundary-Layer Meteorol (2013) 146:17–44
DOI 10.1007/s10546-012-9748-z

ARTICLE

Large-Eddy Simulations of Surface Heterogeneity Effects on the Convective Boundary Layer During the LITFASS-2003 Experiment

Björn Maronga · Siegfried Raasch

Received: 15 July 2011 / Accepted: 14 June 2012 / Published online: 10 July 2012
© The Author(s) 2012. This article is published with open access at Springerlink.com

Abstract We investigate the impact of observed surface heterogeneities during the LITFASS-2003 experiment on the convective boundary layer (CBL). Large-eddy simulations (LES), driven by observed near-surface sensible and latent heat fluxes, were performed for the diurnal cycle and compare well with observations. As in former studies of idealized one- and two-dimensional heterogeneities, secondary circulations developed that are superimposed on the turbulent field and that partly take over the vertical transport of heat and moisture. The secondary circulation patterns vary between local and roll-like structures, depending on the background wind conditions. For higher background wind speeds, the flow feels an effective surface heat-flux pattern that derives from the original pattern by stream-wise averaging. This effective pattern generates a roll-like secondary circulation with roll axes along the mean boundary-layer wind direction. Mainly the upstream surface conditions control the secondary circulation pattern, where the fetch increases with increasing background wind speed. Unlike the entrainment flux that appears to be slightly decreased compared to the homogeneously-heated CBL, the vertical flux of sensible heat appears not to be modified in the mixed layer, while the vertical flux of latent heat shows different responses to secondary circulations. The study illustrates that sufficient time averaging and ensemble averaging is required to separate the heterogeneity-induced signals from the raw LES turbulence data. This might be an important reason why experiments over heterogeneous terrain in the past did not give any clear evidence of heterogeneity-induced effects.

Keywords Convective boundary layer · Large-eddy simulation · LITFASS-2003 · Secondary circulation · Surface heterogeneity

B. Maronga (✉) · S. Raasch
Institut für Meteorologie und Klimatologie, Leibniz Universität Hannover,
Herrenhäuser Str. 2, 30419 Hannover, Germany
e-mail: maronga@muk.uni-hannover.de

1 Introduction

Land-surface heterogeneities can be divided into topographical and land-use heterogeneities that are widely spread over the Earth's surface. Differences in land use represent heterogeneities with a high variability in vegetation, soil texture and wetness. They lead to spatial differences in surface properties such as temperature, humidity and roughness and thus to different surface fluxes of sensible and latent heat as well as momentum. The size of the heterogeneities range from continental scale down to the mesoscale and microscale. In operational weather forecast models, the orography of the land surface is already considered, being a crucial factor for the quality of the forecast. Despite the known effects of large-scale heterogeneities such as land and sea (e.g. the land-sea breeze), it is still uncertain whether heterogeneous land use on the mesoscale and microscale produces significant effects on the atmospheric boundary layer and on the local weather.

In several experimental studies, e.g. LITFASS-98 (Lindenberg Inhomogeneous Terrain Fluxes between Atmosphere and Surface: a long-term Study, [Beyrich et al. 2002a,b](#)), LITFASS-2003 ([Beyrich and Mengelkamp 2006](#)), the International H₂O Project ([Weckwerth et al. 2004](#)) and SMACEX (Soil Moisture-Atmosphere Coupling Experiment, [Kustas et al. 2005](#)), the convective boundary-layer (CBL) characteristics over a heterogeneous land surface have been investigated. However, a heterogeneous effect could hardly be captured.

Over the past two decades, turbulence-resolving large-eddy simulations (LES) have increasingly been used for the investigation of the interaction between surface heterogeneities and the CBL by resolving the bulk of the energy-containing eddies (e.g. [Hechtel et al. 1990](#); [Hadfield et al. 1991, 1992](#); [Shen and Leclerc 1995](#); [Avisar and Schmidt 1998](#); [Gopalakrishnan and Avisar 2000](#); [Raasch and Harbusch 2001](#), hereafter RH01; [Letzel and Raasch 2003](#); [Patton et al. 2005](#), hereafter PSM05; [Courault et al. 2007](#); [Huang and Margulis 2009](#)).

The earlier studies investigated small-scale heterogeneities in the order of a few hundreds of metres with no background flow ([Hechtel et al. 1990](#); [Hadfield et al. 1991](#)) or with background flow ([Hadfield et al. 1992](#)), but found no significant effect on the boundary-layer structure. The later studies of [Shen and Leclerc \(1995\)](#) as well as RH01 used checkerboard-like two-dimensional heterogeneities and reported that the surface heterogeneities in fact must be at least of the size of the boundary-layer height z_i to influence the boundary-layer characteristics. The simulations of sinusoidal stripe-like one-dimensional heterogeneity by [Avisar and Schmidt \(1998\)](#) showed the development of secondary circulations, but that a background wind speed of 5 m s^{-1} suffices to eliminate the effect of the surface heterogeneity. RH01 found the secondary circulations to persist even for background wind speeds up to 7.5 m s^{-1} depending on the mean flow orientation relative to their checkerboard inhomogeneity. [Letzel and Raasch \(2003\)](#) found temporal oscillations in the turbulent kinetic energy (TKE) for larger heterogeneity scales that led to an oscillation of the secondary circulation magnitude. [Kang \(2009\)](#) also investigated these temporal oscillations and suggested that the onset of the oscillations might be the start of a break-up process of fluctuations at the scale of the mesoscale heterogeneity to small-scale fluctuations. [Gopalakrishnan and Avisar \(2000\)](#) found that surface heterogeneities with a characteristic length scale of 5 km decrease the vertical mixing of particles, but increase the horizontal mixing.

PSM05 used one-dimensional soil-moisture heterogeneities in their LES coupled to a soil-vegetation-atmosphere transfer (SVAT) model, which incorporates the feedback between secondary circulations and surface fluxes, while most other studies used prescribed surface fluxes. They reported a dependency of the secondary circulations on the scale of the heterogeneity (wavelength λ), z_i and the initial state of moisture. Particularly, they found that

the strongest CBL response to the heterogeneity occurs for λ/z_i between 4 and 9, owing to the interaction of the secondary circulations and the induced surface fluxes in the SVAT model. Furthermore, PSM05 found the secondary circulations to contribute up to 70 % (height-dependent) to vertical fluxes. The coupled LES-SVAT study of [Courault et al. \(2007\)](#) investigated the feedback of surface heat fluxes to secondary circulations, and suggested that small-scale heterogeneities (here $\lambda = 5$ km) are able to induce secondary circulations that lead to the horizontal transport of moisture from wet to dry areas. [Courault et al. \(2007\)](#) reported a decrease in the surface sensible heat flux over the dry patch, leading to a modification of the area-averaged surface fluxes. [Liu et al. \(2011\)](#) used checkerboard surface heat-flux patterns in their LES and showed that their heterogeneity-induced circulations break-up after a certain time, when λ/z_i is small enough due to the increasing boundary-layer depth. This can be traced back to the results of [Shen and Leclerc \(1995\)](#) and RH01. [Liu et al. \(2011\)](#) also reported no significant impact on the profiles of temperature and the sensible heat flux. [Kang and Davis \(2008\)](#) used a spatial filtering method and showed that the vertical meso-scale transport in the presence of large-scale heterogeneities ($\lambda = 16$ km and $\lambda = 32$ km) is negligible compared to the turbulent transport.

Until now these dependencies of secondary circulations on the background flow as well as on the heterogeneity scale have been investigated by means of idealized one- or two-dimensional periodic heterogeneities only. The question whether the findings mentioned above are also valid over complex terrain, where heterogeneities of a whole range of scales are superimposed upon each other, or whether secondary circulations develop at all, has not been studied to date. Furthermore the question arises, how secondary circulations vary when simulating a full diurnal cycle, in which the surface forcing as well as z_i changes in time.

Some studies reported modifications of the CBL depth in such a way that the mixing layer is deeper over warmer surface patches and thinner over colder patches (e.g. [van Heerwaarden and de Arellano 2008](#), hereafter HA08; [Fesquet et al. 2009](#)). The reason for the spatial variation of z_i in the study of HA08 was associated with rising secondary circulation updrafts that increase the entrainment above the warm patches. Furthermore they reported changes in the entrainment rate, but attributed this finding to differences in their model spin-up or as an effect of horizontal averaging ([Lilly 2002](#)). Moreover, HA08 found the specific humidity variance in the entrainment zone to be larger than under homogeneous conditions and thus suggested that cloud formation might be enhanced over heterogeneous surfaces.

Contrary to most previous studies, [Huang and Margulis \(2009\)](#) recently used observed surface fluxes from SMACEX in their LES to investigate the CBL development over irregular surface heterogeneities. They found increasing entrainment rates for increasing surface heterogeneity scales. Nevertheless their results displayed atypical large entrainment fluxes, whose origin was not discussed. The question of whether area-averaged vertical fluxes are modified due to the effects of observed heterogeneous surfaces has thus not been sufficiently clarified to date.

The present study takes a step forward by explicitly resolving the secondary circulations over a complex non-periodic irregular heterogeneity. Effects of the repetition of the heterogeneity due to cyclic model boundaries are considered. A series of LES was carried out with surface boundary conditions derived from measurements from the LITFASS-2003 experiment ([Beyrich and Mengelkamp 2006](#)). The experimental site (400 km²) was located to the south-east of Berlin (Germany) and exhibited moderately heterogeneous land use as is typically found in Central Europe, including lakes, patches of forest and several agricultural fields. This study attempts to identify secondary circulations and their impact on the CBL over this particular surface heterogeneity. It is found that secondary circulations are much more complex compared to previous studies of regular heterogeneities and that it is difficult

to relate the secondary circulation pattern to the surface heat-flux pattern. The correlation between these patterns is analyzed. Additionally, the impact on the entrainment at the top of the CBL and the effect on area-averaged fluxes are studied. Some preliminary results that have been presented by [Uhlenbrock et al. \(2004\)](#) inspired us in large part to develop the present study. Preliminary results have also been shown in [Beyrich and Mengelkamp \(2006\)](#) and [Foken et al. \(2009\)](#), but are partly revised herein.

The paper is organized as follows: Sect. 2 describes the LES model, the implementation of irregular surface heterogeneities and the driving mechanism for the simulations as well as the determination of secondary circulations over such complex heterogeneities. Simulation results are presented in Sect. 3, while Sect. 4 gives a summary and a brief outlook on further studies.

2 LES Model and Simulations Set-Up

2.1 The Parallelized LES Model PALM

The PARallelized LES Model (PALM) was used for the present study ([Raasch and Etling 1998](#); [Raasch and Schröter 2001](#)). All simulations were carried out using cyclic lateral boundaries, and Monin–Obukhov similarity theory (MOST) was applied between the surface and the first computational grid level. At the beginning of each simulation, a random generator is used to create small perturbations of the velocity field to initiate turbulence.

PALM has been widely applied to study different flow regimes in the homogeneous ([Schröter et al. 2000](#)) and heterogeneous heated CBL (e.g. RH01; [Letzel and Raasch 2003](#); [Steinfeld et al. 2008](#)), in the weakly stable boundary layer ([Beare et al. 2007](#); [Steinfeld et al. 2007](#)) as well as under neutral conditions ([Letzel et al. 2008](#)).

2.2 Determining Secondary Circulations Above Irregular Surface Heterogeneities

In simulations of the flow over real world irregular heterogeneities, cyclic boundary conditions affect the secondary circulations, because the heterogeneity-induced pattern is periodically repeating, which does not occur in reality. Hence, in the vicinity of horizontal boundaries, the flow is exposed to an erroneous surface forcing, especially if the mean flow is directed from the boundaries to the inner model domain. One method to overcome this problem is to restrict data analysis to an inner area of the model domain that is located as far away as possible from the horizontal boundaries. This normally requires enlarging the model domain in order to provide so-called *buffer zones* around the analysis area. Within the buffer zones, observed surface heterogeneities have to be provided as surface boundary conditions. For increasing background wind speed, increasing buffer zones must be defined in order to account for advection from greater distances.

[Prabha et al. \(2007\)](#) investigated secondary circulations over an irregular heterogeneity and attached 1-km wide buffer zones with a homogeneous surface, which we find to be inadequate. [Huang and Margulis \(2009\)](#) simulated irregular surface heterogeneities that were periodically horizontally repeating; this was valid for their purpose, but led to unrealistic secondary circulation patterns. The results of our sensitivity study demonstrate that the choice of a sufficient buffer zone can avoid such systematical shortcomings. The required size of the buffer zone increases for increasing prescribed background wind speed and can easily reach 20 km and more. For a detailed description of the sensitivity study, see Appendix B.

For separating the secondary circulations from the primary circulation, i.e. the random turbulent convection, idealized studies have commonly used combined temporal and spatial averaging (e.g. RH01; PSM05). In the case of one-dimensional heterogeneities (stripes) or two-dimensional heterogeneities (checkerboard pattern), the flow was averaged over repeating surface patches (phase average). For complex observed heterogeneities another approach is necessary. A phase average cannot be applied because patterns have no symmetry axis and do not repeat. In order to simulate the diurnal cycle, as in the present study, time averaging is also limited, because the CBL does not reach a steady state due to the changes in the surface fluxes as well as the increase of z_i in the course of a day. Instead, we thus used a combination of time-averaging and ensemble-averaging methods (1-h time average and eight ensemble runs). The ensemble-averaging method is described in detail in Appendix A.

By means of this ensemble-averaging method, the *heterogeneity-induced* part Φ_{hi} of a quantity Φ for a fixed 1-h averaged time interval, e.g. 1200–1300 UTC, 1300–1400 UTC, etc., can be calculated as follows:

$$\overline{\Phi}_{hi}(x, y, z, t) = \widetilde{\Phi}(x, y, z, t) - \langle \overline{\Phi} \rangle(z, t), \quad (1)$$

where $\widetilde{\Phi}$ and $\overline{\Phi}$ represent the ensemble and the time averages, respectively, and $\langle \Phi \rangle$ denotes the horizontal mean of Φ . For the fixed averaging interval it holds that $\overline{\Phi}_{hi} \approx \Phi_{hi}$ and hence we hereafter simply omit the overbar. The separation of atmospheric variables after PSM05 can be rewritten as:

$$\Phi(x, y, z, t) = \langle \Phi \rangle(z, t) + \Phi_{hi}(x, y, z, t) + \Phi_s(x, y, z, t). \quad (2)$$

The small-scale part Φ_s is also called *background turbulence* (PSM05) or *turbulent* part, which represents the primary circulation of randomly distributed convective plumes.

The described separation of scales in Eq. 2 can also be derived for domain- and time-averaged vertical fluxes:

$$\langle w\overline{\Phi} \rangle(z) = \overline{\langle w \rangle(z) \langle \Phi \rangle(z)} + \langle w_{hi} \Phi_{hi} \rangle(z) + \langle w_s \Phi_s \rangle(z), \quad (3)$$

where $\langle w\overline{\Phi} \rangle$ is the horizontally- and temporally-averaged total flux that can be decomposed into a global part $\overline{\langle w \rangle(z) \langle \Phi \rangle(z)}$, a heterogeneity-induced part $\langle w_{hi} \Phi_{hi} \rangle(z)$ (hereafter $\langle w\overline{\Phi} \rangle_{hi}$) and a turbulent part $\langle w_s \Phi_s \rangle(z)$ (hereafter $\langle w\overline{\Phi} \rangle_s$). Due to cyclic boundaries and the constraint that the equation of continuity for incompressible fluids must be valid, the horizontally-averaged vertical velocity $\langle w \rangle$ in our LES is zero and thus the global part in Eq. 3 vanishes.

In order to determine the effect of surface heterogeneities on z_i , we calculated a local boundary-layer height from the local potential temperature (θ) profile following Sullivan et al. (1998):

$$z_i(x, y) = z, \quad (4)$$

where $\frac{\partial \theta(x, y, z)}{\partial z}$ for given x and y is a maximum. Sullivan et al. (1998) showed that the area-averaged z_i is slightly modified compared to non-local methods. For scaling purposes, we follow this local gradient method instead of calculating $\langle z_i \rangle$ from area-averaged profiles.

2.3 Implementation of the Surface Heterogeneity During LITFASS-2003

The LITFASS area (A_L) can be divided into several land-use classes that have different characteristics. The distribution of these characteristics follows the actual land-surface properties. The map in Fig. 1 (see also Beyrich and Mengelkamp 2006, Figs. 2, 3) shows the land-use

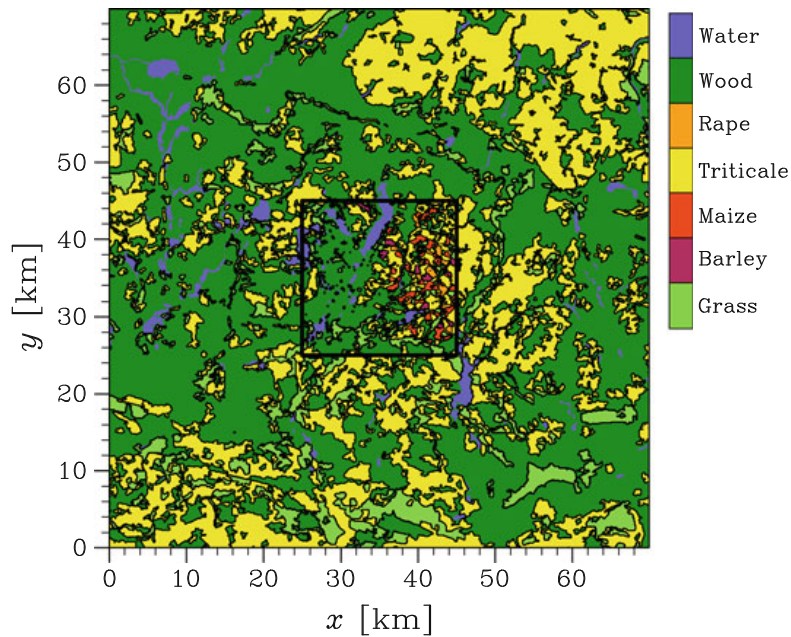


Fig. 1 Distribution of land-use classes in A_L (black box) and surroundings as used in the LES. The classes were derived from the CORINE dataset

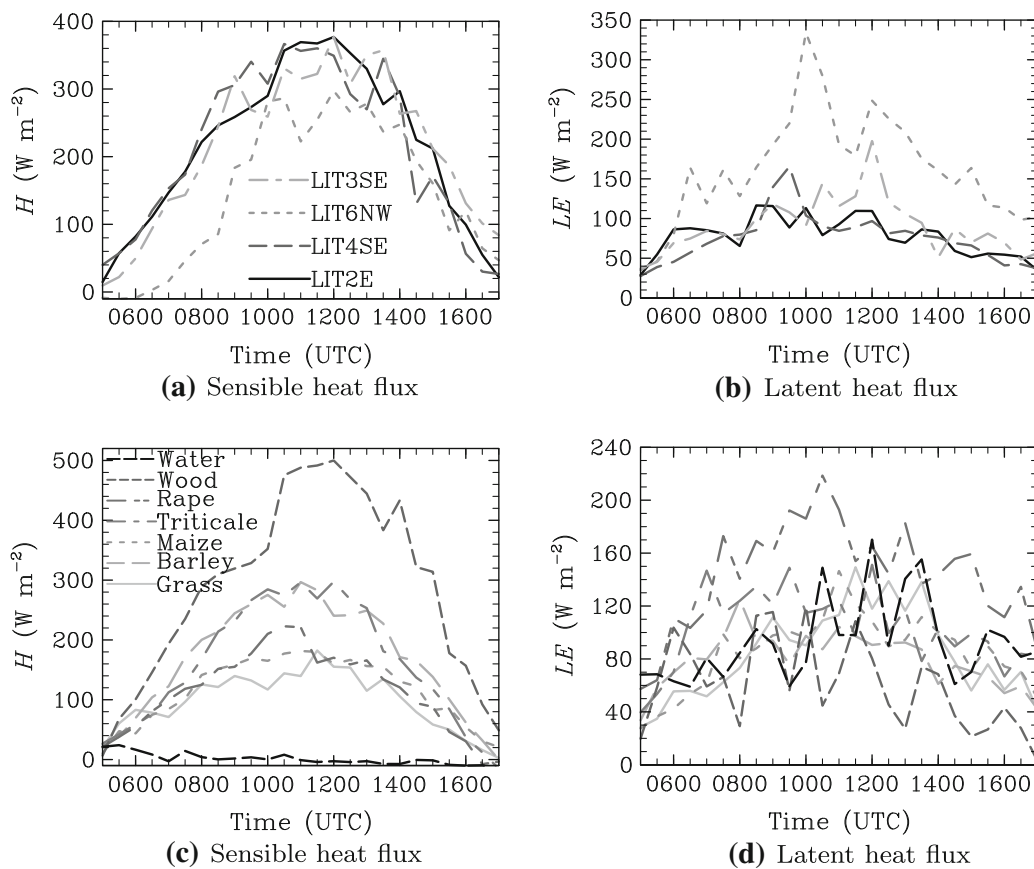


Fig. 2 Time series of the prescribed fluxes of sensible and latent heat at the surface: **a** and **b** are the horizontal mean values as they were used in the homogeneous control runs, while **c** and **d** are the particular fluxes for different land-use classes for case LIT2E

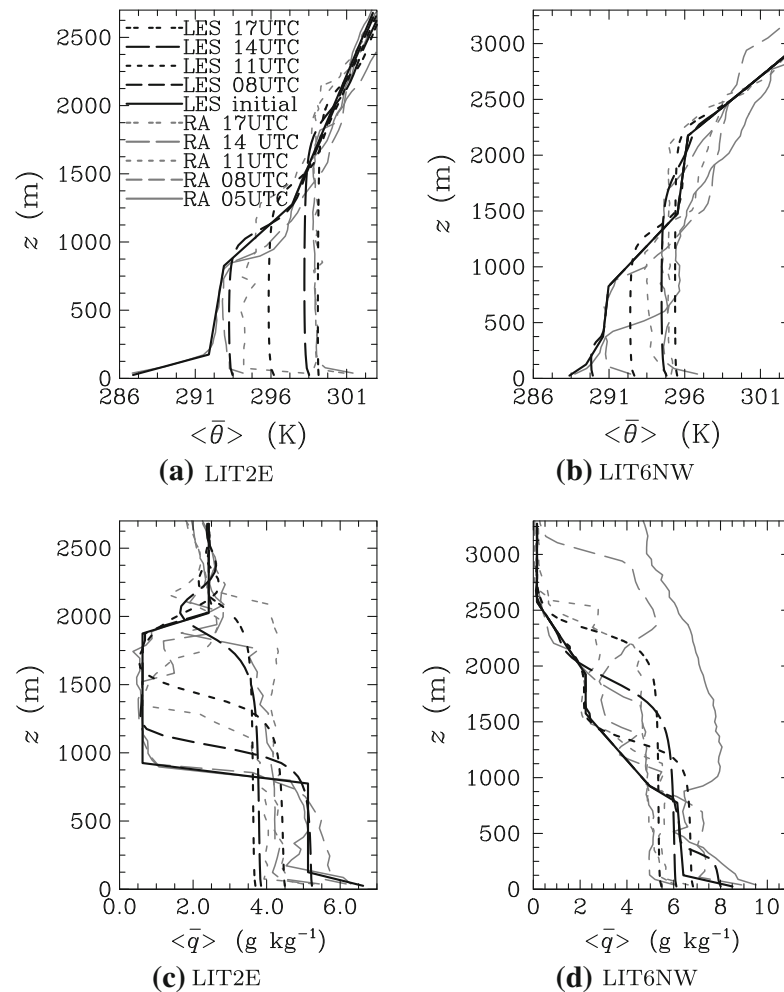


Fig. 3 Profiles of potential temperature (a, b) and specific humidity (c, d) for cases LIT2E (left) and LIT6NW (right) in the course of the day. The LES profiles are domain- and time-averaged (black, 10-min mean), while radiosonde data are shown by grey lines

classes for A_L and the surrounding area, derived from a modified CORINE¹ dataset. We determined the heterogeneity for an area of size 70 km \times 70 km, centred around A_L , which is of size 20 km \times 20 km. The CORINE dataset contains 44 different land-use classes from which 16 were found to be dominant in the greater LITFASS area. For simplification, the classes “pastures” and “natural grasslands” were merged into the class “grass”. The forest patches “mixed forest”, “broad-leaved forest” and “coniferous forest” as well as artificial areas (such as settlements) were merged into the class “forest”. The latter is reasonable since settlements exhibit similar fluxes of sensible and latent heat as well as roughness properties as forest areas. Agricultural fields were treated as triticale/rye, since this was the dominant type in the area. For A_L itself, the tilled fields were observed during the experiment in 2003, subdivided into land-use classes and mapped on the CORINE dataset. The final map is shown in Fig. 1, containing seven different land-use classes: water, wood, rape, triticale, maize, barley and grass.

¹ Abbr. “Coordinated Information on the European Environment”, published by the European Environment Agency (<http://www.eea.europa.eu/publications/COR0-landcover>).

Table 1 Case definition and results of the LITFASS-2003 simulations

Case	Simulation time (UTC)		ff (m s ⁻¹)	dd (°)	Domain (km × km)	$\langle z_i \rangle_{\max}$ (m)
	Start	End				
LIT2E (May 30)	0500	1700	2.0	90	40 × 40	2200
LIT4SE (June 2)	0500	1700	4.0	113	48 × 48	3050
LIT6NW (June 13)	0430	1700	6.0	320	56 × 56	2400
LIT3SE (June 17)	0430	1700	3.2	110	48 × 48	2400

ff and dd are the prescribed geostrophic wind speed and direction, respectively. The domain size refers to the horizontal extent of the model. $\langle z_i \rangle_{\max}$ is the maximum boundary-layer depth during the simulation

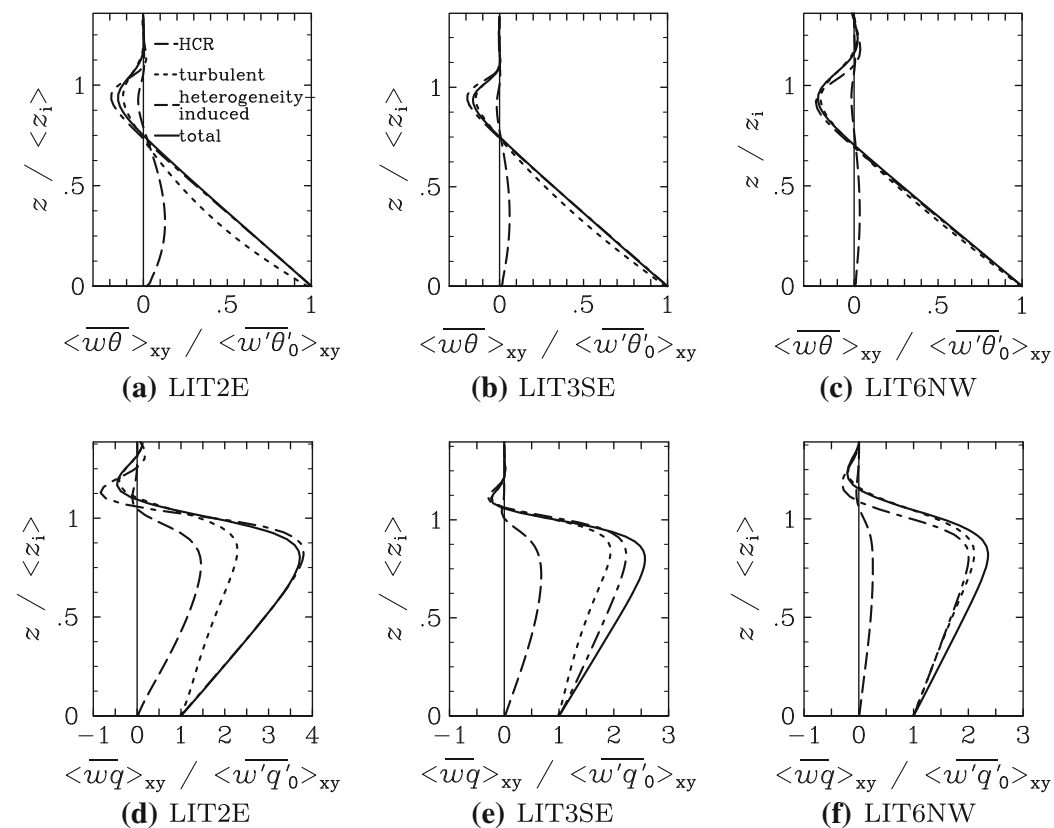


Fig. 4 Normalized profiles of the vertical kinematic heat fluxes (a–c) and moisture fluxes (d–f) for LIT2E, LIT3SE and LIT6NW at 1300 UTC. The total fluxes (solid black lines) are plotted together with their heterogeneity-induced (dashed lines) and turbulent contributions (short dashed lines). Additionally the total flux from the respective homogeneous control runs are plotted (dot-dashed lines). All fluxes have been time-averaged over 1 h and normalized by the prescribed surface fluxes

2.4 Initialization and Forcing of the Simulations

During the LITFASS-2003 experiment, several energy balance stations as well as other measurement systems, including a 99-m tower (see Beyrich and Mengelkamp 2006, Table 1) were located in the fields of different land use (see Beyrich and Mengelkamp 2006, Fig. 4) The quality assurance showed that the eddy-covariance measurements were representative for the respective land-use class (Beyrich et al. 2006; Mauder et al. 2006). Heinemann and

Kerschgens (2006) simulated the full experiment period with a mesoscale model and came to the same conclusion. The surface fluxes from the local measurements were thus used as the driving surface fluxes for all patches of the same type of land use. Local differences of plant characteristics were not considered. The flux data were available half-hourly. To avoid discontinuities in the model forcing, the values were linearly interpolated in time. Since usage of a SVAT model would have required the input of several local vegetation and soil parameters, which were not available, prescribing observed fluxes was found to be the best approach for the simulations.

Besides the surface fluxes, the heterogeneity is characterized by a roughness length z_0 , which was estimated by $z_0 \approx 0.1 \times \text{crop height}$ (after Shuttleworth et al. 1997), where the mean crop height for the respective land-use classes was observed during the measurement period. The canopy layer was not explicitly simulated and the flat orography in A_L was neglected.

Initial values of surface temperature and humidity were taken for each land-use class from the measurements at the energy balance stations. Initial profiles of temperature and humidity were derived from radiosonde data and used for the entire model domain, and the resulting profiles were subsequently recomposed by piecewise linear segments. Since the radiosondes did not provide data for height levels below 112 m, a linear interpolation was carried out between the heterogeneous surface temperature (as well as humidity) and the top of the near-surface temperature inversion in the morning hours. The top of the inversion varied for the simulated days between 75 and 175 m and was obtained from single point measurements, which were assumed to be representative of the entire area.

A one-dimensional version of the PALM code, with fully-parametrized turbulence using a mixing-length approach after Blackadar (1997) and stationary temperature and humidity profiles, was used for precursor simulations to generate steady-state wind profiles as initialization for the LES. The forcing geostrophic winds in the precursor runs (see Table 1) were chosen such that the steady-state wind profiles were in good agreement with measurements from radiosondes, a tropospheric wind profiler as well as with the 99-m tower measurements.

2.5 Domain Sizes

As discussed in Sect. 2.2, it is compulsory to extend the model domain with buffer zones around A_L . Therefore the total horizontal model domain ($x \times y$) varied between $40 \text{ km} \times 40 \text{ km}$ and $56 \text{ km} \times 56 \text{ km}$ (see Table 1). Due to this large domain and the fact that nine simulations (eight ensemble runs, one homogeneous control run, see below) had to be carried out for each case, a grid spacing of 100 m for the horizontal (Δx , Δy) and 50 m for the vertical direction (Δz) was chosen in order to reduce the computational demands. About 80 grid points were used in the vertical direction. The vertical grid was stretched well above the inversion in order to further reduce the computational load. Within the scope of the present study, we also simulated three high-resolution cases (homogeneous surface, heterogeneous surface, heterogeneous surface with topography) with Δx , $\Delta y = 20 \text{ m}$ and $\Delta z = 10 \text{ m}$ to prove that our grid resolution is sufficient to resolve the secondary circulations. In the case of the simulations with topography, the elevation was calculated from the real terrain height plus the height of the trees (at those areas with tall vegetation in A_L). We adjusted the roughness length for these forest areas instead of using a zero-plane displacement. The results of these simulations showed that higher resolution or topography does not have a significant effect on the secondary circulations.

2.6 Case Description

The synoptic conditions have a large effect on the CBL turbulence, and we restricted our study to almost cloud-free days with little large-scale advection. In the presence of clouds, the incoming radiation at the surface can show a high spatial variability that is superimposed upon the surface heterogeneity, while an overcast sky eliminates the influence of the land-use classes to a great extent. The effect of advection by the background flow, on the one hand, “smears” the heterogeneity signal (this will be discussed in detail in Sect. 3.4). On the other hand, it is very difficult to account for temperature and humidity trends due to larger-scale advection within the simulation. A weak background flow is therefore preferred. An overview of the conditions during the LITFASS-2003 measurement period can be found in [Beyrich and Mengelkamp \(2006\)](#). Four days, May 30, June 2, June 13 and June 17, were selected according to the restrictions mentioned above, with synoptic conditions for all days dominated by anticyclonic conditions. The selected days had minimum/maximum temperatures between 13 and 29 °C. We simulated the diurnal cycle from the early morning until the evening transition.

May 30 was characterized by clear skies and a geostrophic wind from the east at 2 m s^{-1} (hereafter also called the weak wind case, LIT2E). Figure 2a, b shows the prescribed area-averaged turbulent surface fluxes of sensible and latent heat (H and LE , respectively) in the course of the day. It is obvious that the Bowen ratio ($B_0 = H/LE$) for case LIT2E was between 3 and 4 during daytime. The sensible heat flux increased in the course of the day up to 380 W m^{-2} , while the latent heat flux was relatively small ($\approx 100 \text{ W m}^{-2}$) and only showed a weakly-developed diurnal cycle. Figure 2c, d shows the measured fluxes for the specific land-use classes for case LIT2E and reveals that the forest was the dominant land-use class regarding the heat input into the atmosphere (up to 500 W m^{-2}). The water patches show no significant contribution to the sensible heat input and rather tended to take up energy in the late afternoon. Areas tilled with triticale and barley exhibited maximum values of $H = 300 \text{ W m}^{-2}$, while for grass, maize and rape, H reached $180\text{--}230 \text{ W m}^{-2}$. The largest sensible heat-flux differences were observed between water and forest, while the tilled areas differed only slightly from each other. In contrast to the sensible heat flux, the latent heat flux was characterized by high fluctuations during the course of day with amplitudes up to 50 % of the total flux (e.g. forest areas), and mainly due to by water vapour release events from the plants. The maximum values were within the range of $100\text{--}220 \text{ W m}^{-2}$. Summed up, the forest patches exhibited the smallest latent heat flux into the atmosphere, due to a low availability of water vapour during a dry period of several weeks ahead of the LITFASS-2003 experiment, while rape was associated with the highest input. An extension of all four lateral boundaries of the model with buffer zones of 10 km was used for case LIT2E, see Appendix B.

June 2 and June 17 (LIT4SE and LIT3SE) displayed higher geostrophic wind speeds of 4 and 3.2 m s^{-1} , respectively, and consequently, a buffer zone of 14 km was used. The wind direction was similar (south-east) in both cases and the surface fluxes were comparable to those in case LIT2E (see Fig. 2a, b). The main difference between the two cases was a greater boundary-layer depth in the simulations ($3,050$ and $2,400 \text{ m}$ for cases LIT4SE and LIT3SE, respectively) compared to LIT2E ($2,200 \text{ m}$). Scattered cumulus and cirrus clouds were observed in the morning.

Due to intense precipitation on the previous days, the Bowen ratio on June 13 (LIT6NW) was approximately one; [Beyrich et al. \(2006\)](#) give a detailed description of the Bowen ratio values during the experiment. For LIT6NW a geostrophic wind speed of 6 m s^{-1} was prescribed from the north-west. Due to the effect of advection, a buffer zone of 18 km was

required. The overcast sky at 0500 UTC rapidly changed to only scattered cumulus and stratocumulus clouds between 0700 and 0900 UTC.

Table 1 sums up model set-up properties, such as the prescribed geostrophic wind and model domain size, as well as the boundary-layer height as found during the simulations. Homogeneous control runs with a spatially-averaged but temporally-varying surface heat flux according to Fig. 2a, b were carried out for comparison.

3 Simulation Results

3.1 Mean Profiles

The temporal development of horizontally-averaged vertical boundary-layer profiles for May 30 (LIT2E) and June 13 (LIT6NW) is shown and compared with radiosonde data in Fig. 3. The solid black lines reflect the initial profiles used in the LES. The initial potential temperature profile on May 30 is characterized by a near-surface inversion with a near-neutral stratified residual layer and a capping inversion above (starting from 1,200 m). June 13 exhibits two residual layers and displays a capping inversion at 2,100 m. This results also in a higher CBL depth during the simulations (see Table 1). During daytime, differences in temperature and humidity between radiosonde and the LES are found, while the height of the capping inversion agrees very well. Differences may generally be attributed to the fact that domain-averaged LES profiles are compared with local observations from the radiosonde. In case LIT2E the mixed-layer temperature is overestimated by the LES by 1.5 K at 1100 UTC, while at 1400 UTC it is slightly underestimated by 0.6 K. At the end of the simulation (1700 UTC) both observations and LES compare very well. The humidity profiles for LIT2E show that the LES slightly underestimated the moisture in the CBL starting from 1400 UTC. However, the radiosonde data show a rather fluctuating humidity in the course of the day and generally they compare well with the LES. In case LIT6NW we had to adjust the initial profiles of temperature and humidity since clouds were observed in the early morning hours that are clearly visible in the humidity profile starting from 900 m and which we could not account for in the LES. The initial LES profiles were thus defined in such a way that they agree with measurements between 0700 and 0800 UTC and at the end of the simulation. Nevertheless it appears that, as in case LIT2E, differences in the temperature up to 1.5 K are present, while the CBL height fits well. The humidity profiles during daytime differ by up to 1.5 g kg^{-1} between LES and the radiosonde measurements.

In spite of the local character of the radiosonde profiles, the temporal development and shapes of the simulated mean vertical profiles of potential temperature and specific humidity (q) as well as $\langle z_i \rangle$ in the course of the day compare well with observations. For LIT3SE and LIT4SE there is an even better agreement (not shown). Hence, using the representative surface-flux measurements for the different land-use classes as the surface boundary condition seems to provide an appropriate forcing for the simulations. This is a prerequisite for any further analysis of the simulation data.

Figure 4 shows vertical profiles of the scalar fluxes at 1300 UTC for the LITFASS simulations and the homogeneous control runs. Both the kinematic heat flux and moisture flux display classical profiles (see e.g. Deardorff 1974; Wyngaard and Coté 1974; Stull 1988). The entrainment flux minimum is about 20 % of the normalized surface flux. The humidity in the boundary layer is rather dominated by the mixing of dry air from the free atmosphere into the boundary layer. Hence, the moisture flux in the entrainment layer is two to three times larger than the respective surface flux. We return to the scalar flux profiles later in Sect. 3.3.

3.2 Secondary Circulations During LITFASS-2003

3.2.1 Spatial Characteristics

The ensemble averaging method (Eq. 1) allows us to determine the secondary circulation patterns over complex surface heterogeneities for the first time. The heterogeneity-induced vertical velocity w_{hi} is an appropriate measure for secondary circulations, since updrafts and downdrafts span the entire boundary layer, reaching maximum values in the middle of the boundary layer. Figure 5 shows isosurfaces of $w_{hi} = \pm 0.3 \text{ m s}^{-1}$ at 1300 UTC for all LITFASS simulations. Please note that cases LIT4SE and LIT3SE were found to exhibit similar characteristics owing to the minor differences in the geostrophic wind speed and direction. Hence, we hereafter often discuss results for case LIT3SE only. It is obvious from Fig. 5b, d that the general pattern for both cases is similar. However, the specific locations of updrafts and downdrafts change significantly even for small changes in the geostrophic wind. For case LIT2E, the shown structures are stationary for the period 1000–1600 UTC, while the other cases display a higher variability in time that is discussed for case LIT6NW in Sect. 3.2.2. Most of the secondary circulation structures in case LIT2E are obviously associated with the underlying thermal heterogeneity (see Figs. 1, 5e). Especially the water–forest discontinuities are connected to updraft and downdraft secondary circulation branches, owing to the surface sensible heat-flux gradients discussed in the previous section (see Fig. 2c). This contrast leads to strong secondary circulations that indicate the underlying surface heterogeneity. The weak background flow from the east has only a minor effect on the secondary circulation patterns. Contrary to the forest–water discontinuities, which cause strong circulations, the heterogeneity-induced circulations over the agricultural dominated area are weaker and the influence of agricultural land-use heterogeneity on the CBL can be regarded as small. One reason for this relates to the length scale of the agricultural heterogeneities, which is often less than the boundary-layer depth and thus does not affect the boundary-layer structure (Shen and Leclerc 1995). Overall, the vertical velocities w_{hi} exhibit typical maximum values of about 15 % of the mixed-layer convective velocity scale w_* (after Deardorff 1974) and hence are one order of magnitude smaller than the randomly distributed convective updraft and downdrafts. The secondary circulations are just a small superposition on the primary circulation.

The background flow has a stronger influence on the other three cases in such a way that direct correlations between the secondary circulations and the surface heterogeneity are not obvious from Fig. 5b–d, but we show in Sect. 3.4 that correlations also persist for these cases with higher background wind speeds of 4–6 m s^{-1} . Cases LIT4SE and LIT3SE show roll-like structures. Case LIT6NW shows a distinct development of such long-ranged rolls all day long, oriented parallel to the mean wind direction (Fig. 5c). The secondary circulation in case LIT6NW appears as a more slender roll-like pattern. Only few structures develop, indicating that the circulation strength is significantly decreased compared to the weaker wind cases (to be discussed below). This is in agreement with the studies of Avissar and Schmidt (1998) and RH01 who noted a damping effect of the background flow on the surface heterogeneity signal. Both studies identified the formation of rolls over idealized heterogeneities. Moreover, RH01 showed that, for two-dimensional heterogeneities, the formation of rolls depends on the flow direction relative to the orientation of the heterogeneity. The present study shows for the first time that roll-like patterns also develop over irregular heterogeneities and that they seem to be a frequent feature for situations with higher background wind speeds.

The vertical profiles of the variance of the heterogeneity-induced velocity components $\sigma_{u_{hi}}^2$, $\sigma_{v_{hi}}^2$ and $\sigma_{w_{hi}}^2$ as well as of heterogeneity-induced temperature and humidity variations

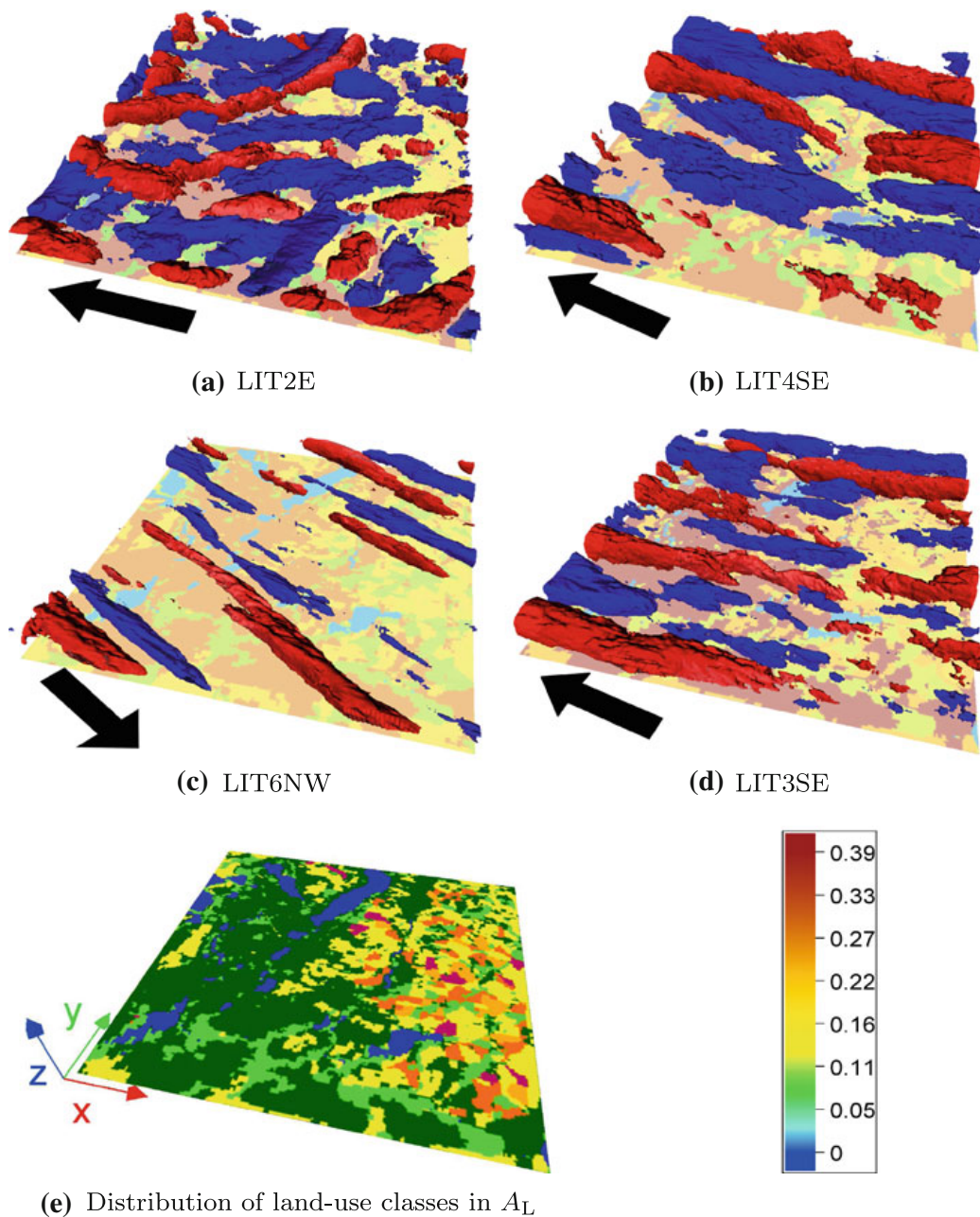


Fig. 5 Secondary circulations over A_L (the area shown is $20 \text{ km} \times 20 \text{ km}$), determined from the LITFASS simulations at 1300 UTC (**a–d**). The figure shows isosurfaces of the heterogeneity-induced vertical velocity. The red isosurface refers to $w_{hi} = 0.3 \text{ m s}^{-1}$ (*updrafts*), the blue one to $w_{hi} = -0.3 \text{ m s}^{-1}$ (*downdrafts*). The *bottom surface* displays the prescribed kinematic heat flux according to the legend (in K m s^{-1}). **e** Land-use classes as in Fig. 1 and the orientation to the numerical grid. The prescribed geostrophic wind direction is indicated by the *arrows* (eye-fitted, see Table 1)

($\sigma_{\theta_{hi}}^2$ and $\sigma_{q_{hi}}^2$, respectively) for the four cases are shown in Fig. 6. The variance profiles of the heterogeneity-induced temperature and humidity variations (Fig. 6c–e) show the same characteristics as for the primary circulation in a CBL (see e.g. Stull 1988). The variance $\sigma_{w_{hi}}^2$ increases with height to peak values in the middle of the CBL, while the peak magnitude of $\sigma_{w_{hi}}^2$ decreases from case LIT2E ($0.26 \text{ m}^2 \text{ s}^{-2}$) to LIT6NW ($0.06 \text{ m}^2 \text{ s}^{-2}$), reflecting the

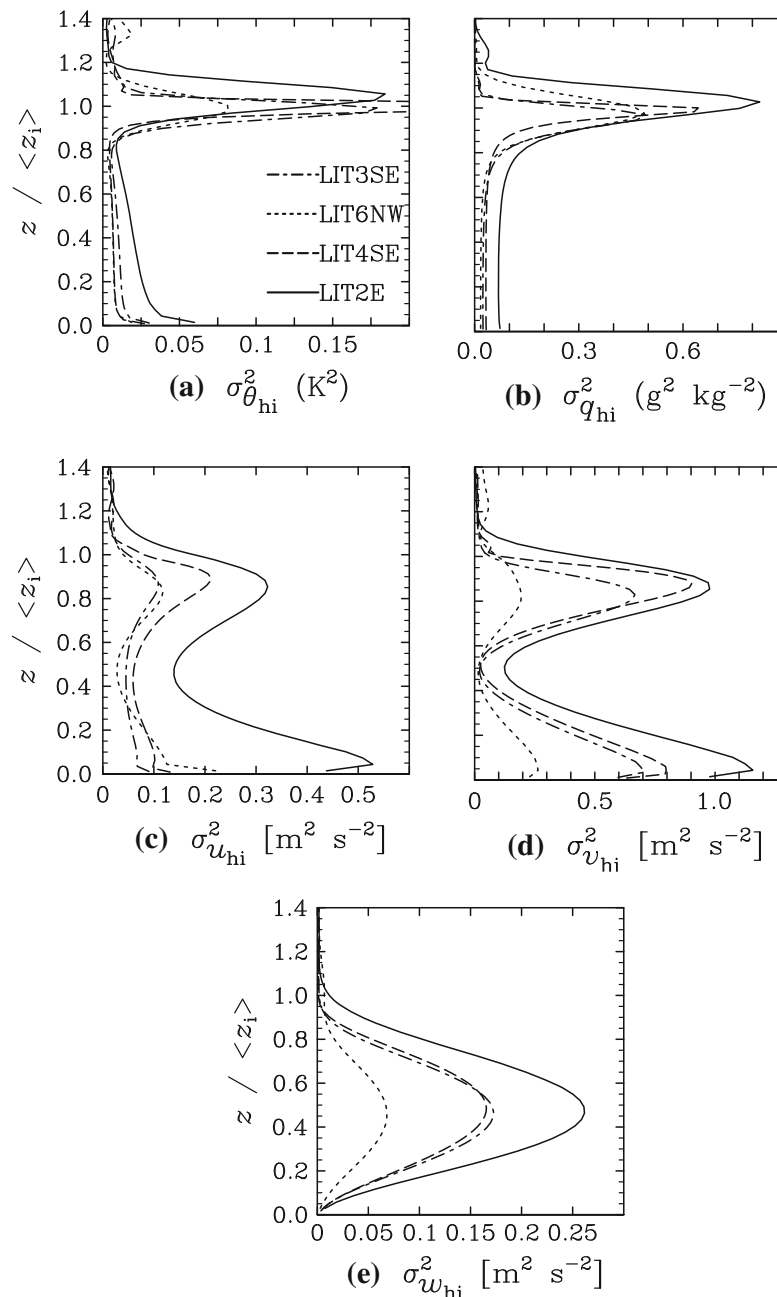


Fig. 6 Profiles of the variances of the heterogeneity-induced potential temperature and specific humidity variations (a, b) as well as velocity components (c–e) at 1300 UTC. The height is normalized with $\langle z_i \rangle$

relative strength of secondary circulations very well. The profiles of $\sigma_{u_{hi}}^2$ and $\sigma_{v_{hi}}^2$ (u_{hi} and v_{hi} refer to the velocity in the x - and y -directions, respectively) both exhibit double peaks, a lower one close to the surface and an upper one near the top of the CBL. These peaks are connected to the horizontal secondary circulation branches, which typically occur near the top and the bottom of the CBL, showing that the secondary circulations span the entire boundary layer. Similar-shaped profiles have been shown by PSM05. The variances of the horizontal velocity components $\sigma_{u_{hi}}^2$ and $\sigma_{v_{hi}}^2$ also clearly show that secondary circulations

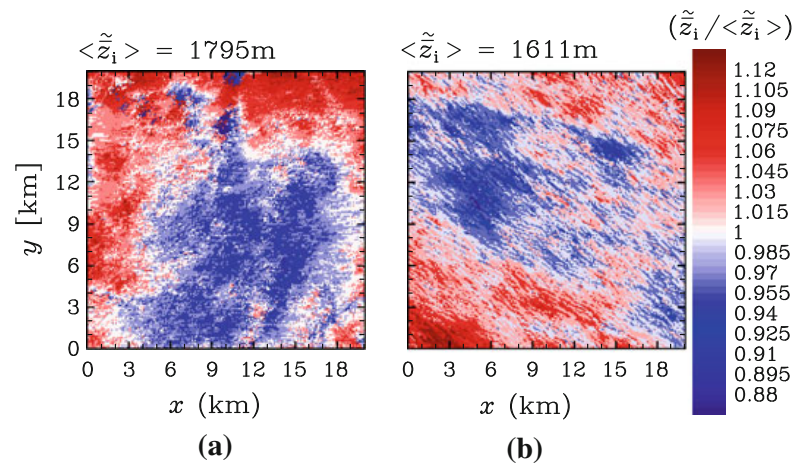


Fig. 7 Horizontal cross-sections of the ensemble- and time-averaged z_i at 1300 UTC over A_L for cases LIT2E (a) and LIT6NW (b). The values are normalized by the horizontal mean (\bar{z}_i) (noted down just above the plots)

become weaker with increasing background wind speed. Our study shows that this effect of the background wind speed on the secondary circulation strength, which was found in several idealized studies before (e.g. Hadfield et al. 1992; Avissar and Schmidt 1998), also holds for complex surface heterogeneities.

In contrast to $\sigma_{w_{hi}}^2$, $\sigma_{\theta_{hi}}^2$ and $\sigma_{q_{hi}}^2$ exhibit high maxima at the top of the CBL (see Fig. 6a, b), caused by a folding of the interface between the boundary layer and free atmosphere. The high variances of the heterogeneity-induced temperature and humidity variations are a result of the variations in the local boundary-layer height. The time- and ensemble-averaged z_i is shown in Fig. 7. In case LIT2E (see Fig. 7a) the large forest patches to the west and the north of A_L (high surface sensible heat flux), lead to an increase in the boundary-layer depth of up to 13 %, while agricultural fields and lakes generally exhibit a lower \bar{z}_i . This folding of the inversion layer was also shown by HA08, and it is probably caused by the higher input of sensible heat over warmer surface patches, particularly forest areas, that increases the local boundary-layer temperature and hence \bar{z}_i (encroachment effect, Stull 1988, Chap. 11.2). The patterns of \bar{z}_i are not related to the secondary circulations (see Fig. 7a, b; cf. Fig. 5a, c). Case LIT2E shows that secondary circulations at the sharp edges of the heterogeneities (Fig. 5a, e) correlate with the regions of sharp gradients in \bar{z}_i , but they do not extend over the centre of larger patches. This finding that secondary circulations develop only at sharp edges of heterogeneities is in agreement with RH01, who have shown this effect for a discontinuous heat-flux amplitude (cf. RH01, Fig. 4). In case LIT6NW (see Fig. 7b) the CBL is deeper in the south-west as well as in the north-east, while lower \bar{z}_i is found at the centre of A_L . In this case it is difficult to relate the pattern to the surface heterogeneity and the encroachment effect because the mean flow “smears” the surface signal significantly.

Near the surface, the variance of the heterogeneity-induced temperature variations (Fig. 6a) shows a lower secondary maximum that is generated by the heterogeneous surface sensible heat flux, while $\sigma_{q_{hi}}^2$ does not show this secondary peak. This proves that the variation in the surface latent heat flux is only of minor importance to the heterogeneity-induced structures.

3.2.2 Temporal Development

The secondary circulation patterns broaden in the course of the day; (Fig. 8) e.g. shows this broadening for case LIT6NW during the period from 1000 to 1500 UTC. This can be

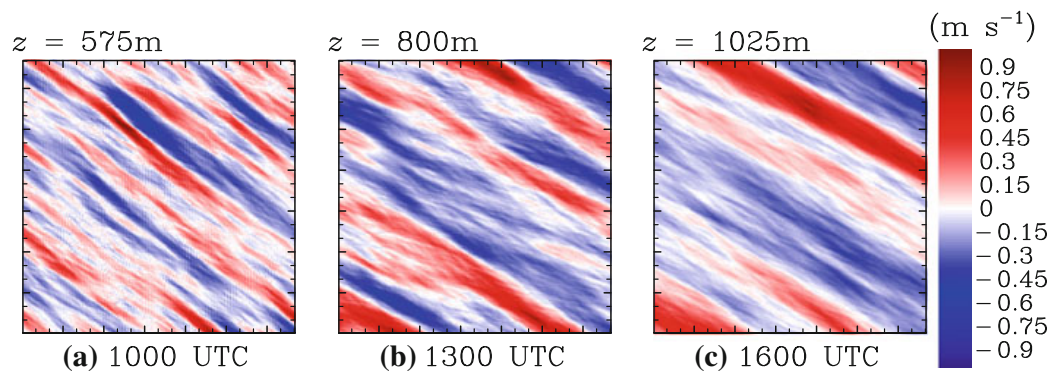


Fig. 8 Horizontal cross-sections of the vertical velocity w_{hi} over A_L (the area shown is $20 \text{ km} \times 20 \text{ km}$, axes are oriented as in Fig. 7) at $z/\langle z_i \rangle = 0.5$ for different times during LIT6NW. The height level is noted above the plots

explained by the findings of Shen and Leclerc (1995) and RH01 that only those heterogeneities with $\lambda/\langle z_i \rangle \geq 1$ are able to extend throughout the entire CBL. Since the prescribed heterogeneities range over different scales and the boundary-layer height increases in the course of the day (see Fig. 3), the scales that are dominantly affecting the boundary layer also change in time. In this way, smaller scales become less and larger scales more important, resulting in broader secondary circulation patterns. Our results clearly show that the dependency of secondary circulations on $\lambda/\langle z_i \rangle$ is also valid for irregularly distributed heterogeneities that cover a large range of scales. Hence the results of Liu et al. (2011), who simulated the flow over two-dimensional heterogeneities with a constant wavelength λ over several hours, can be generalized. They showed that the secondary circulations break down after a few hours, since the boundary-layer depth increased such that $\lambda/\langle z_i \rangle$ becomes too small. Due to the different scales of the LITFASS heterogeneity, such a break-down does not occur, and instead the circulation scale increases in time (broadening, see Fig. 8).

3.3 The Impact of Secondary Circulations on the Area-Averaged Vertical Transport

In order to determine the area-averaged flux $\langle w\Phi \rangle$, we decomposed the total flux into heterogeneity-induced and small-scale turbulent parts according to Eq. 3. In the homogeneously-heated CBL the heterogeneity-induced part is zero and the total flux equals the turbulent flux.

Results are provided for 1300 UTC. Figure 4 shows the mean profiles of the total fluxes $\langle w\theta \rangle$ and $\langle wq \rangle$, which were discussed in Sect. 3.1. It also includes the heterogeneity-induced and turbulent contributions to the mean flux as well as the flux from the respective homogeneous control runs. The heterogeneity-induced part $\langle w\theta \rangle_{hi}$ has its maximum at $z/\langle z_i \rangle = 0.3$ and an entrainment minimum at $z/\langle z_i \rangle = 0.9$. The maximum value depends on the secondary circulation strength (strongest for case LIT2E, weakest for case LIT6NW) and varies between 20 % (LIT2E) and 8 % (LIT6NW) of the total flux at the corresponding height. In general, the turbulent part $\langle w\theta \rangle_s$ makes up the bulk of the total flux. These qualitative results are in agreement with the LES studies of PSM05 and HA08. Compared to the homogeneous control runs, the absolute total fluxes in the entrainment zone are smaller in the presence of surface heterogeneities. Figure 4 shows that the entrainment rate depends on the secondary circulation strength in such a way that stronger secondary circulations decrease the entrainment fluxes. Because Lilly (2002) has shown that the horizontal averaging process for the turbulent flux profiles may cause misleading results in the case of heterogeneously driven boundary

layers, we also analyzed the time series of $\langle z_i \rangle$, derived from the local temperature profiles (Eq. 4). This method confirms a slower growth of $\langle z_i \rangle$ in the heterogeneous cases with $\langle z_i \rangle$ about 50–100 m lower compared to the homogeneous control runs (not shown). This result is in contrast with results from HA08, who did not find any effect of one-dimensional idealized heterogeneities on the entrainment rate. We suppose that at the top of the mixed layer the secondary circulations re-direct a part of the total vertical transport to horizontal transport that decreases the entrainment rate. We are currently analyzing the entrainment modification in detail and will address it in a follow-up paper.

Our main result is that, under the same mean surface fluxes, the total vertical transport above homogeneous and heterogeneous surfaces differs slightly in the entrainment zone. Compared with the homogeneous case, the turbulent transport in the heterogeneous case is smaller in the mixed layer, but secondary circulations compensate for the difference.

As with $\langle w\theta \rangle_{hi}$, $\langle wq \rangle_{hi}$ depends on the secondary circulation strength, with its maximum varying between 39 % (LIT2E) and 11 % (LIT6NW) of the total flux. The findings of the present study suggest a smaller heterogeneity-induced part compared to PSM05, who found the heterogeneity-induced part contributes the bulk of the total flux under certain conditions. Unlike $\overline{\langle w\theta \rangle}$, $\overline{\langle wq \rangle}$ can deviate significantly from the homogeneous control runs (Fig. 4e, f). The maximum is located at $z/\langle z_i \rangle = 0.8$. It is decreased by 2 % in case LIT2E, compared to the homogeneous control run, while in case LIT6NW, $\overline{\langle wq \rangle}$ is increased up to 18 %. The latter is surprising, since the total flux profile is rather expected to approach the homogeneous control run profile, if the secondary circulation weakens. As the synoptic conditions differ from case to case, the behaviour of the moisture flux is probably caused by different inversion strengths and humidity levels in the free atmosphere (see e.g. Fig. 3). However, we could not clearly identify the reasons for the behaviour of $\overline{\langle wq \rangle}$. The quite large differences between homogeneous and heterogeneous simulations of up to 18 % point out that the effect of surface heterogeneities might be relevant for the parametrization of turbulence in numerical weather prediction models that cannot resolve secondary circulations in the range of a few kilometres.

In contrast to former idealized studies (e.g. Chen and Avissar 1994; Lynn et al. 1995; PSM05), who found that the secondary circulations can contribute up to 50–80 %, our investigations of the LITFASS area show a contribution up to 20 % (kinematic heat) and 39 % (moisture).

3.4 Correlations Between the Secondary Circulations and the Surface Heterogeneity

From Fig. 5 it is evident that for all cases with higher wind speed (LIT4SE, LIT3SE, LIT6NW) the secondary circulation structure cannot be easily related to the surface heat-flux pattern, i.e. there seems to be no simple correlation between them. It is also evident that for these cases the secondary circulation patterns switch to more simple roll-like patterns, compared with the pattern of case LIT2E (Fig. 5a). In order to explain the location and strength of the roll-like circulations, our starting hypothesis was that in cases with higher mean wind speed the air advected over the heterogeneities “feels” only a mean surface heat flux that is the surface heat flux averaged along its path. By this “smearing” process, the two-dimensional reduces to a one-dimensional surface heterogeneity that varies only along the crosswind direction. The resulting stripe-like heat-flux pattern should generate roll-like circulations with axes aligned to the mean flow. This would be in agreement with the LES study of RH01, where the development of roll-like secondary circulations was shown under a background wind speed of 7.5 m s^{-1} . They showed that, for an appropriate inflow direction with respect to the heterogeneity, rolls can develop owing to a stretching effect of their near-surface checkerboard temperature pattern.

Table 2 List of sensitivity study cases

Case	Background wind speed (m s ⁻¹)	Buffer zone (km)
BUF202	2	2
BUF206	2	6
BUF210	2	10
BUF214	2	14
BUF218	2	18
BUF402	4	2
BUF406	4	6
BUF410	4	10
BUF414	4	14
BUF418	4	18
BUF606	6	6
BUF610	6	10
BUF614	6	14
BUF618	6	18
BUF622	6	22

For proving this hypothesis, we used a correlation analysis, where we calculated the linear correlation between the surface kinematic heat flux and the vertical velocity, both averaged along the direction of the roll-axis. Case LIT6NW was chosen due to the distinct roll-like secondary circulation pattern (see Fig. 5c) under a high background wind speed of 6 m s⁻¹. The surface kinematic heat flux and w_{hi} at a height $z/\langle z_i \rangle = 0.5$ were averaged along the entire model domain. However, path-averaging of the surface heat flux in the LITFASS cases is problematic since the flux varies in time because of the diurnal cycle. Therefore we decided in the first instance to use data from the buffer sensitivity simulations where the surface forcing was constant in time (BUF606–BUF622, see Table 2). The cases differ in the buffer zone sizes and thus the domain size varied between 28 km × 32 km and 44 km × 64 km. In contrast to case LIT6NW, easterly winds were prescribed. Because of their different domain sizes these cases provided different heterogeneity patterns and hence were a suitable set of simulations with different surface properties to test our hypothesis under more idealized conditions.

We decided to perform the streamwise average over a distance of 129.6 km, which is the distance a parcel of air travels on average during the simulation time of 6 h while it is affected by the underlying heterogeneity. A rotation of the data fields towards the mean wind direction was required and carried out, where the mean wind vector was calculated as the spatial average of the horizontal velocity components at $0.5\langle z_i \rangle$ (height of the maximum of $\sigma_{w_{hi}}$). The data of the original domain were extended by cyclic repetition along the horizontal directions to allow for averaging over a distance of 129.6 km. The heterogeneity-induced vertical velocity w_{hi} after 6 h (60-min average) of simulation time was used for the analysis. Figure 9 shows an example (here case BUF614) of the rotated and extended surface heat flux and the associated vertical velocity at $z/\langle z_i \rangle = 0.5$. The rotated axes are denoted by x' (alongwind) and y' (crosswind), while the sections are oriented along the mean flow, which enters from the right side. Due to the cyclic repetition, the surface heat flux shows repeating structures like lakes, where the lowest values (blue) can be found, or larger forest patches, represented by higher values (red). Consequently, the secondary circulation pattern (Fig. 9a)

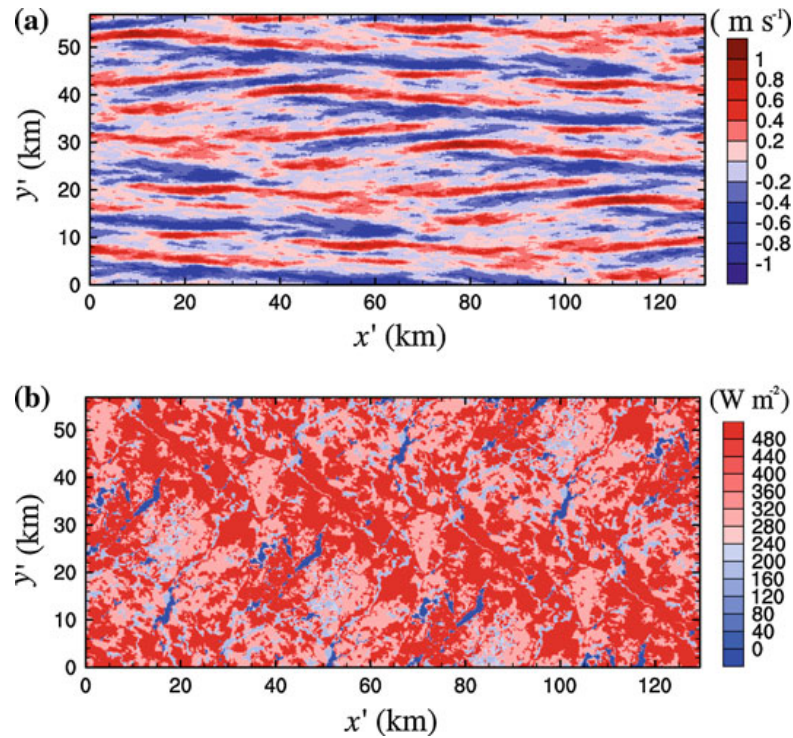


Fig. 9 Horizontal cross-sections of the rotated and extended fields of w_{hi} at $z/\langle z_i \rangle = 0.5$ **(a)** and surface sensible heat flux **(b)** for case BUF614

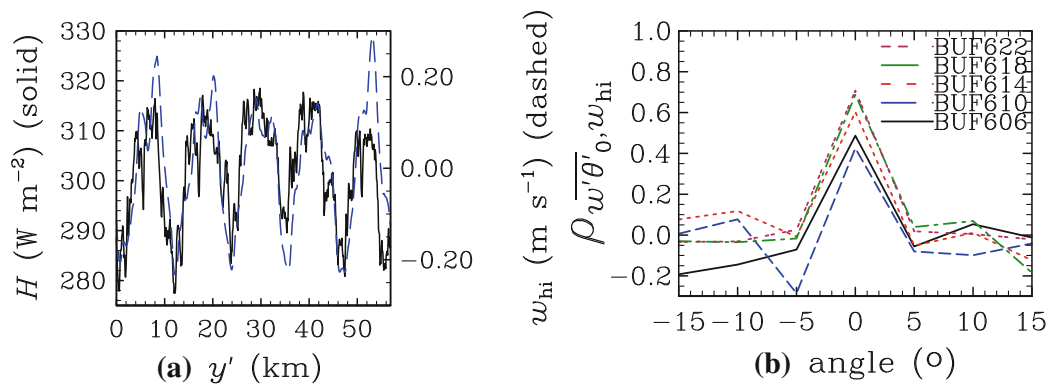


Fig. 10 **a** Streamwise averages of vertical velocity w_{hi} at $z/\langle z_i \rangle = 0.5$ (blue dashed line) and the surface sensible heat flux H (black solid line) for case BUF614 against crosswind axis y' , **b** correlation coefficient between $\overline{w'\theta'_0}$ and w_{hi} against rotation angle of $\overline{w'\theta'_0}$ in relation to the mean wind

shows repeating structures as well. Anyhow, this wallpaper effect does not affect the general result of the correlation analysis that is valid for any kind of heterogeneity pattern.

3.4.1 Streamwise-Averaged Correlations

In order to determine the relation between the secondary circulation structure and the surface heat-flux pattern, we first computed the streamwise average of w_{hi} at $z/\langle z_i \rangle = 0.5$ and $\overline{w'\theta'_0}$. The crosswind variation of both quantities is given in Fig. 10a (case BUF614) and already displays a good correlation between them. From these one-dimensional series we

then calculated the correlation coefficient $\rho_{w'\theta'_0, w_{hi}}$. Additionally we varied the rotation angle of the surface heat-flux field in order to ensure that marginal changes in the rotation angle give totally different streamwise averages that are not correlated to the secondary circulation pattern. Figure 10b shows the correlation coefficient against different angles relative to the mean wind direction. A well-defined peak can be found if the heat flux is streamwise averaged (zero angle) with values of at least 0.4. A variation of the rotation angle of only 5° in any direction decreases the correlation to values close to zero and indicates a clear statistical relation between the secondary circulation and the streamwise-averaged surface heat flux.

The correlation coefficient at zero degree rotation increases with increasing area size and reaches a value of 0.7 (Fig. 10b). The same correlation analysis applied to the buffer zone cases with $v_g = 4 \text{ m s}^{-1}$ (BUF402–BUF418) led to correlations between 0.4 and 0.6. Our hypothesis thus seems to be valid for idealized cases with stationary heat-flux pattern.

Despite the high correlation, systematic shortcomings should be considered that arise from the streamwise average and which are visible e.g. in Fig. 9a. Signals of rolls can be weakened if they do not exactly align with the mean flow or if they do not range over the entire data fields. It is obvious that the secondary circulation at a specific location can only be influenced by the surface heat-flux distribution of a limited upstream region, or in other words, every location has its own footprint (a common issue for turbulence measurements). It is obvious that the size of this footprint will strongly depend on the magnitude of the background wind speed. In Sect. 3.4.2 we will therefore determine the fetch, i.e. the length of this secondary circulation footprint, for different background wind speeds.

We further applied the correlation analysis to case LIT6NW, where the surface heat flux varied with time. To avoid errors in the surface heat flux and the secondary circulation pattern by the diurnal cycle of secondary circulations and surface fluxes, we restricted the averaging distance to the size of the model domain and used the averaged surface heat flux from 1200 to 1300 UTC as well as the secondary circulation at 1300 UTC, which implies a time average of 1 h. The correlation calculated for LIT6NW is also large (0.48), which reveals that our starting hypothesis provides a conclusive explanation for the observed rolls in Fig. 5.

3.4.2 Fetch Study

In this section we will extend the correlation analysis by a method to determine the fetch of the secondary circulations. In order to study if and how the fetch depends on the background wind speed, we used the simulated cases from the sensitivity study (listed in Table 2 in Appendix B) with background wind speeds between 2 and 6 m s^{-1} .

Instead of using streamwise averages ranging over the entire data fields, we now calculated the correlation between the local vertical velocity $w_{hi}(y')$ at $z/\langle z_i \rangle = 0.5$ at a specific alongwind location x'_i , where y' is the crosswind direction, and the surface kinematic heat flux, streamwise averaged in the upwind direction between x'_i and $x'_i + \Delta_f x'$. Here, $\Delta_f x'$ is a length that varied between 1 and 100 km (see also Fig. 11). The correlation coefficient $\rho_{w'\theta'_0, w_{hi}}(x'_i, \Delta_f x')$ thus depends on both the alongwind location x'_i and $\Delta_f x'$, but not on y' . An horizontal average over all x'_i (denoted by $\langle \rangle_{x'}$) is calculated in order to achieve representative statistics for the entire domain. The averaged correlation reads:

$$\left\langle \rho_{w'\theta'_0, w_{hi}} \right\rangle_{x'}(\Delta_f x') = \frac{1}{N_{x'}} \sum_{i=0}^{N_{x'}} \rho_{w'\theta'_0, w_{hi}}(x'_i, \Delta_f x'), \quad \forall \Delta_f x' = 1 \text{ km}, 2 \text{ km}, \dots, x'_{\max}, \quad (5)$$

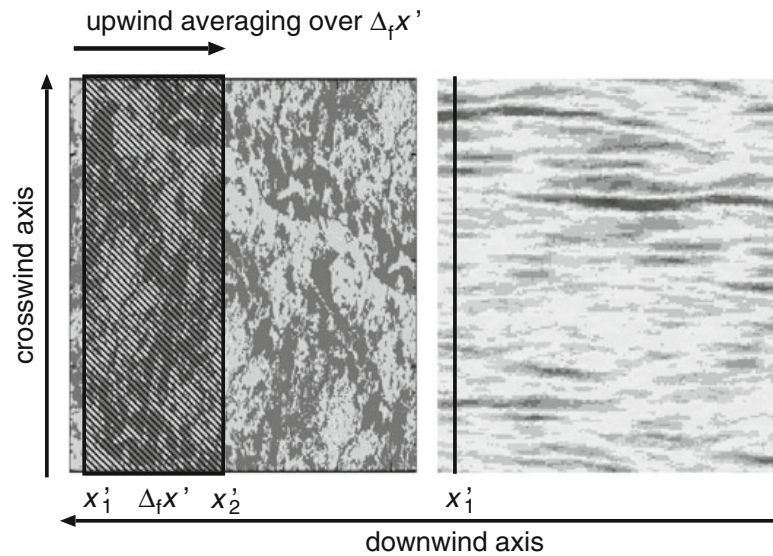


Fig. 11 Schematic figure of the averaging method for the determination of the fetch. The horizontal cross-sections of the surface kinematic heat flux (*left*) and the vertical velocity at $z/(z_i) = 0.5$ are used. The surface heat flux is streamwise averaged over $\Delta_f x' = x'_2 - x'_1$. The correlation coefficient is calculated from this averaged crosswind surface heat-flux series and the crosswind series of the vertical velocity along the path at x'_1

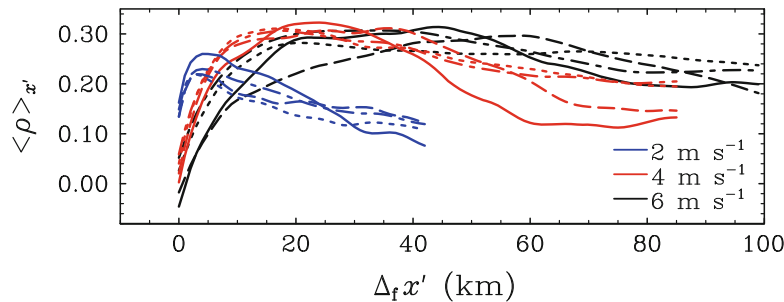


Fig. 12 Spatially-averaged correlation $\langle \overline{\rho_{w'\theta'_0, w_{hi}}} \rangle_{x'}$ against averaging length $\Delta_f x'$ of the surface heterogeneity. The *solid*, *dot-dashed*, *short-dashed* and *dashed* lines represent cases with a buffer zone of 6, 10, 14 and 18 km, respectively. The *colours* mark the wind speed

where x'_{\max} varied between 42 and 100 km depending on the background wind and $N_{x'}$ is the number of grid points along the downwind direction.

Figure 12 shows how this correlation depends on $\Delta_f x'$. A global maximum of the correlation is found for all cases and it appears that the location of the maximum correlation is similar for equal background wind speeds. For $v_g = 2 \text{ m s}^{-1}$, the maximum is located at $(\Delta_f x')_{\max} \approx 5 \text{ km}$, while for higher background winds of $v_g = 4 \text{ m s}^{-1}$ and $v_g = 6 \text{ m s}^{-1}$, the maximum shifts to $(\Delta_f x')_{\max} \approx 19 \text{ km}$ and $(\Delta_f x')_{\max} \approx 35 \text{ km}$, respectively. Since the correlation more or less monotonically decreases beyond the maximum, we define the position of these maxima as the fetch Δ_f . As expected, it is larger for higher wind speeds. The analysis points towards a linear increase of the fetch with wind speed. It is quite evident that the buffer zone size should ideally cover the fetch in the upstream model boundaries in order to simulate realistic secondary circulation patterns. For our simulations we used buffer

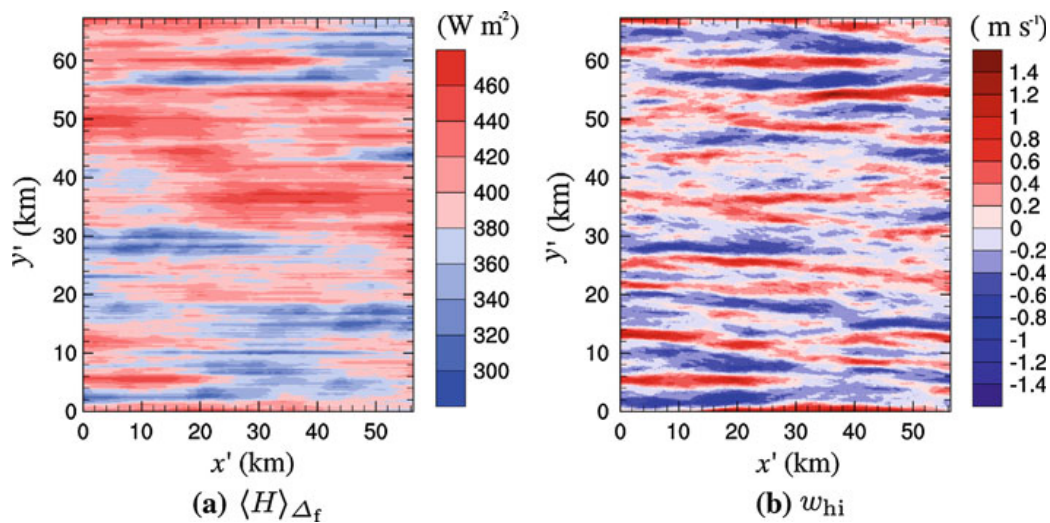


Fig. 13 Horizontal cross-sections of, **a** the effective surface sensible heat flux, **b** the heterogeneity-induced vertical velocity at $z/z_i = 0.5$ for case BUF618

zones between 10 and 18 km, which should suffice for $v_g = 2 \text{ m s}^{-1}$ and $v_g = 4 \text{ m s}^{-1}$. For $v_g = 6 \text{ m s}^{-1}$, however, buffer zones up to 35 km might be necessary.

By knowing the fetch, an *effective surface sensible heat flux* $\langle H \rangle_{\Delta_f}$ can be calculated for each horizontal location in the domain by upstream-averaging of H over the fetch (denoted by $\langle \rangle_{\Delta_f}$). These streamwise-averaged surface heat-flux patterns reflect the upstream moving average of the original surface heat-flux pattern. Figure 13 shows $\langle H \rangle_{\Delta_f}$ and w_{hi} for BUF618. The typical length scale of the $\langle H \rangle_{\Delta_f}$ patches in alongwind direction is in agreement with the respective length of the rolls. Furthermore the crosswind gradients in $\langle H \rangle_{\Delta_f}$ allow us to estimate the development of circulation structures to a high degree (see e.g. the striking rolls in the upper part and the lower left edge of the figure). It thus should be possible to predict the secondary circulation pattern to a considerable extent from a given surface heterogeneity distribution and respective background flow.

4 Summary and Outlook

In the present study the CBL over a complex surface heterogeneity, observed during LITFASS-2003, was investigated with the focus on secondary circulations and their impact on the development of the CBL during the daytime. Four cases with varying background wind speeds were simulated from the early morning until the evening transition. The simulations were initialized and driven by surface fluxes and profiles of temperature and humidity observed during LITFASS-2003. The cases were characterized by geostrophic wind speeds between 2 and 6 m s^{-1} and maximum boundary-layer heights between 2,200 and 3,050 m. The mean profiles of temperature and humidity in the course of the simulations showed that the LES model was able to simulate the observed CBL development.

Particular attention was given to the development and three-dimensional structure of the heterogeneity-induced secondary circulations. A new method was introduced in analogy to former studies, based on a combined extensive time- and ensemble-averaging, to separate the heterogeneity-induced secondary circulations from the randomly distributed thermal convection. Furthermore, a sensitivity study showed that, in the case of irregularly distributed

surface heterogeneities, sufficiently large buffer zones need to be defined around the analysis domain in order to capture effects on secondary circulations from regions further upstream.

The simulated secondary circulations during the four LITFASS simulations spanned the entire CBL and were superimposed on the randomly distributed convection. The circulation strength was found to be typically one order of magnitude smaller than turbulence of the primary circulation. Increasing background wind speeds tended to weaken the secondary circulations as was previously found in idealized studies (e.g. [Avisar and Schmidt 1998](#); RH01). For low wind speeds of 2 m s^{-1} the complex secondary circulation patterns could be directly linked to the underlying sensible heat-flux pattern. For higher wind speeds of $3\text{--}6 \text{ m s}^{-1}$ roll-like structures were observed. For the latter cases, a correlation analysis proved that the flow “feels” only the mean surface heat-flux patterns that derive from the original patterns by averaging them in the streamwise direction. Because these effective patterns are basically aligned to the direction of the mean flow, they generate roll-like secondary circulation patterns. The patterns are found to be mainly controlled by the upstream surface conditions. The upwind fetch of the surface heterogeneity pattern that controls the secondary circulation was found to depend strongly on the background wind speed. Our results point towards a linear increasing fetch with increasing wind speed. A larger fetch and thus longer effective stripe-like surface heat-flux patches explain the elongated rolls in the simulation with a background wind of 6 m s^{-1} . It is shown that the secondary circulation patterns in the simulations can be estimated by calculating the moving average of the surface heat flux in the upstream direction.

The temporal development of the secondary circulations showed that the heterogeneity scales, which affect the CBL, changed in time and smaller scales became less important with increasing z_i . This resulted in a broadening of the secondary circulations in the course of the day and was associated with the dependency of secondary circulations on the ratio of the heterogeneity scale λ to z_i , which was stated for idealized heterogeneities of a single scale in several studies (e.g. [Shen and Leclerc 1995](#)). The present study was able to show that the known dependencies on both λ/z_i and the background wind speed are also valid over irregular surface heterogeneities, where a whole range of scales are superimposed on each other.

The area-averaged vertical flux of sensible heat suggested that the entrainment of warm air in the case of strong secondary circulations over irregular heterogeneous terrain is slightly reduced compared to the homogeneous control runs. In the mixing layer, the vertical transport was partly taken over by the secondary circulations and the turbulent transport was thus found to be decreased, while the sum of both was not modified. The humidity transport was dominated by drying-out due to high entrainment of dry air from the free atmosphere. The latent heat flux showed different responses to secondary circulations, resulting in either a higher or smaller total flux compared to the homogeneous simulations. The reasons for the behaviour of the latent heat flux remain unclear, and might be the result of different conditions in the free atmosphere, and changes in the entrainment of dry air, or an effect of horizontal averaging.

Our simulations illustrated that the surface heterogeneity affects the boundary layer up to the capping inversion that is also reflected in a horizontally varying boundary-layer depth. The often discussed concept of a blending height, above which the influence of the surface heterogeneity vanishes, thus cannot hold, at least under convective conditions and heterogeneity scales larger than z_i . The present study already demonstrated that extensive averaging is required to filter out the random noise of the thermal convection. Probably, turbulence measurements from field campaigns do not provide enough data to allow for sufficient averaging. This may be an important reason that experiments over heterogeneous terrain in the

past did not give any clear evidence of heterogeneity-induced effects. We will address this topic in a follow-up study.

Acknowledgments This research was supported by the German Research Foundation (DFG) under grant RA 617/21-1. All simulations were performed on the SGI Altix ICE at The North-German Supercomputing Alliance (HLRN), Hannover/Berlin. We appreciate the two anonymous reviewers for their constructive and valuable comments that helped to improve the manuscript.

Open Access This article is distributed under the terms of the Creative Commons Attribution License which permits any use, distribution, and reproduction in any medium, provided the original author(s) and the source are credited.

Appendices

Appendix A: Determination of Heterogeneity-Induced Secondary Circulations over Irregular Surface Heterogeneity

In order to isolate the effect of surface heterogeneities, our starting point is the decomposition procedure described by PSM05. Adapted for irregular heterogeneities this decomposition reads

$$\Phi(x, y, z, t) = \langle \Phi \rangle(z, t) + \Phi_{\text{hi}}(x, y, z, t) + \Phi_{\text{s}}(x, y, z, t), \quad (6)$$

where $\langle \Phi \rangle$ is the horizontal mean (global part) of Φ , and Φ_{hi} the heterogeneity-induced part. Φ_{s} is the so-called *background turbulence* that includes the smaller-scale resolved and subgrid-scale contributions due to the randomly distributed thermally driven primary circulations. The only way to eliminate the background turbulence from Eq. 6 is to apply an ensemble average (denoted by a tilde). This requires performing an ensemble of LESs, where each simulation uses different initial random perturbations to trigger convection. In this way, the spatial and temporal distributions of background turbulence are completely different in each ensemble run, while the heterogeneity-induced motion remains the same. If the number of ensembles N is large enough, $\tilde{\Phi}_{\text{s}}$ will tend to zero. Then, Φ_{hi} can be calculated from the ensemble-averaged Eq. 6, viz.

$$\Phi_{\text{hi}}(x, y, z, t) = \tilde{\Phi}(x, y, z, t) - \widetilde{\langle \Phi \rangle}(z, t). \quad (7)$$

However, the number of ensemble runs, which is required to keep the background turbulence signal sufficiently small, was found to be much larger than our computational resources allowed. Therefore, we decided to carry out an additional time average with fixed, non-overlapping time intervals (denoted by the overbar) for each ensemble run, before applying the ensemble average. Time and ensemble averaging of Eq. 6 yields

$$\overline{\Phi}_{\text{hi}}(x, y, z, t) = \overline{\tilde{\Phi}}(x, y, z, t) - \overline{\widetilde{\langle \Phi \rangle}}(z, t). \quad (8)$$

In order to reduce the background turbulence signal sufficiently, the averaging interval should be at least in the order of a few convective turnaround times $t_* = \langle z_i \rangle / w_*$ (after [Deardorff 1974](#)). On the other hand, the interval should not be too large, because the time average will also affect the heterogeneity induced signal that varies in time. As a compromise we used an interval of 1 h and calculated averaged quantities for time periods of e.g. 1200–1300 UTC, 1300–1400 UTC, and so forth. For large horizontal domains as used in our simulations, the horizontally- and temporally-averaged quantities do not vary much among the different ensemble runs, i.e.

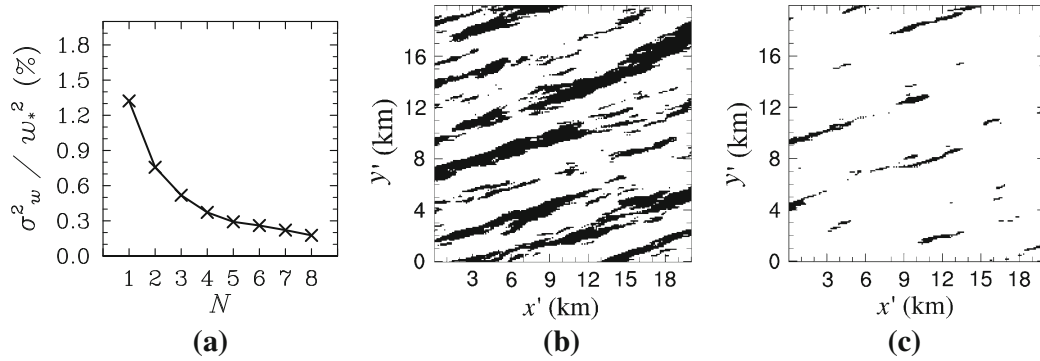


Fig. 14 Height-, time- and ensemble-averaged and normalized variance of the vertical velocity as a function of the number of ensemble runs N for a homogeneously-heated CBL (a), horizontal cross-sections of the vertical velocity at $z/\langle z_i \rangle = 0.5$ for $N = 1$ (b) and $N = 8$ (c), time averaged over 1 h. Dark shaded regions show areas where $w > 0.08 w_*$

$$\widetilde{\langle \Phi \rangle} \simeq \langle \Phi \rangle. \tag{9}$$

This holds for the first, but also higher order moments, because the mean statistical properties of the flow are the same for all ensemble runs. The 1 h-averaged heterogeneity-induced part $\overline{\Phi}_{hi}$ can thus be calculated as

$$\overline{\Phi}_{hi}(x, y, z, t) = \widetilde{\Phi}(x, y, z, t) - \langle \Phi \rangle(z, t). \tag{10}$$

Horizontal averaging of Eq. 10 using Eq. 9 yields

$$\langle \overline{\Phi}_{hi} \rangle = 0, \tag{11}$$

and hence, $\overline{\Phi}_{hi}$ can be regarded as a heterogeneity-induced variation from the mean state.

As the number of ensemble runs is practically limited, we carried out a set of sensitivity simulations in order to determine the required amount of ensemble runs to ensure that the random turbulent part $\widetilde{\Phi}_s$ is sufficiently small. We used the horizontal variance $\sigma_{\overline{w}_{hi}}^2$, height-averaged over the entire boundary layer (denoted by $(\sigma_{\overline{w}_{hi}}^2)_{BL}$). The sensitivity simulations were carried out for a homogeneously-heated stationary CBL (with $v_g = 6 \text{ m s}^{-1}$), because under such conditions \overline{w}_{hi} and its variance should tend to zero when sufficiently averaged. As a criterion we defined a limit of $(\sigma_{\overline{w}_{hi}}^2)_{BL}$, normalized by the convective velocity scale w_*^2 , of 0.2 %. Figure 14a shows how the ratio $(\sigma_{\overline{w}_{hi}}^2)_{BL} / w_*^2$ asymptotically decreases with the number of ensemble runs and the limit is reached for eight ensemble runs. A further reduction of the background turbulence signal would require much more ensemble runs. Figure 14b, c show horizontal cross-sections at $z/\langle z_i \rangle = 0.5$ of the 1-h time-averaged vertical velocity for one of the ensemble runs (Fig. 14b) and the ensemble average over eight runs (Fig. 14c). It is evident that most of the signal from background turbulence, which is still visible in the time-averaged field, has been successfully eliminated for an additional ensemble average over eight runs.

By means of the decomposition of the quantities in Eq. 6, the vertical flux $w\Phi$ can be decomposed as (see also [Chen and Avissar 1994](#)):

$$\begin{aligned} w\Phi &= \langle w \rangle \langle \Phi \rangle + w_{hi} \Phi_{hi} + w_s \Phi_s + \langle w \rangle \Phi_{hi} + w_{hi} \langle \Phi \rangle \\ &+ \langle w \rangle \Phi_s + w_s \langle \Phi \rangle + w_{hi} \Phi_s + w_s \Phi_{hi}. \end{aligned} \tag{12}$$

The heterogeneity-induced signal should not vary much within the averaging period of 1 h. We can thus assume that $\widetilde{\Phi}_{\text{hi}} \approx \Phi_{\text{hi}}$. Since Φ_{hi} is also invariant to ensemble-averaging, we can use the relation $\overline{\widetilde{\Phi}_{\text{hi}}} \approx \Phi_{\text{hi}}$. For time and ensemble averaging, the background turbulent part tends to zero, and Eq. 12 then reduces to

$$\overline{\widetilde{w\Phi}} = \overline{\langle w \rangle \langle \Phi \rangle} + w_{\text{hi}} \Phi_{\text{hi}} + \overline{w_s \Phi_s} + \overline{\langle w \rangle \Phi_s} + \overline{w_s \langle \Phi \rangle} + \overline{\langle w \rangle \Phi_{\text{hi}}} + w_{\text{hi}} \overline{\langle \Phi \rangle}. \quad (13)$$

Applying the horizontal average to Eq. 13 yields

$$\overline{\langle \widetilde{w\Phi} \rangle} = \overline{\langle w \rangle \langle \Phi \rangle} + \langle w_{\text{hi}} \Phi_{\text{hi}} \rangle + \overline{\langle w_s \Phi_s \rangle} + \overline{\langle \langle w \rangle \Phi_s \rangle} + \overline{\langle w_s \langle \Phi \rangle \rangle}, \quad (14)$$

noting that the last two terms of Eq. 13 cancel (follows from Eq. 11). As stated above, Eq. 9 holds also for higher order moments. Eq. 14 thus simplifies to

$$\overline{\langle w\Phi \rangle} = \overline{\langle w \rangle \langle \Phi \rangle} + \langle w_{\text{hi}} \Phi_{\text{hi}} \rangle + \overline{\langle w_s \Phi_s \rangle} + \overline{\langle \langle w \rangle \Phi_s \rangle} + \overline{\langle w_s \langle \Phi \rangle \rangle}, \quad (15)$$

The inter-scale terms on the right side cancel when substituting the small-scale part according to Eq. 6 and applying common averaging rules. Hence, Eq. 15 reduces to

$$\overline{\langle w\Phi \rangle}(z) = \overline{\langle w \rangle \langle \Phi \rangle}(z) + \langle w_{\text{hi}} \Phi_{\text{hi}} \rangle(z) + \overline{\langle w_s \Phi_s \rangle}(z). \quad (16)$$

Appendix B: Determination of a Sufficient Buffer Zone Size

In Sect. 2.2 we explained that irregular surface heterogeneities and cyclic horizontal model boundaries require so-called buffer zones around the analysis area (i.e. the LITFASS domain of $20 \text{ km} \times 20 \text{ km}$, see Fig. 1). If the buffer zones are large enough, secondary circulations in the analysis area should not feel the effects of the cyclic boundaries anymore. We determined the required size of the buffer zones by performing a set of simulations where the buffer size was successively enlarged from 2 to 22 km. Since a strong dependency on the background flow was expected, we also varied the background wind speed between 2 and 6 m s^{-1} , flow from the east. We used constant (in time) surface fluxes from the LITFASS experiment on May 30 (1230–1300 UTC) instead of diurnal cycles for two reasons. One reason is that constant fluxes generate steady-state secondary circulation structures within a short time (compared with the time needed for runs where the diurnal cycle was simulated). For the same reason, the initial profile of potential temperature was set with a slightly stable gradient and capping inversion above 1,200 m. The second reason is that the secondary circulation patterns exhibit a diurnal cycle themselves, if the flow is driven by non-stationary surface fluxes. To derive the pure effects of the buffer zone on the secondary circulations would be more difficult under such conditions. An overview of the set of simulations is given in Table 2. The buffer zones for a given background wind speed were considered to be sufficient when the secondary circulation pattern in the analysis area did not change significantly with increasing buffer zone anymore. We explicitly compared the secondary circulation patterns after 6-h simulation time, but we also calculated the change in the vertical velocity between two simulations with different buffer zone size (not shown). Based on this analysis we decided to use a buffer zone of 10 km for case LIT2E, 14 km for cases LIT3SE and LIT4SE, and 18 km for case LIT6NW. Unfortunately we did not find a suitable measure or limiting value for a sufficient buffer zone size, but as discussed in Sect. 3.4.2, the fetch study supports our decision.

References

- Avissar R, Schmidt T (1998) An evaluation of the scale at which ground-surface heat flux patchiness affects the convective boundary layer using large-eddy simulations. *J Atmos Sci* 55:2666–2689
- Beare RJ, Cortes MAJ et al (2007) An intercomparison of large-eddy simulations of the stable boundary-layer. *Boundary-Layer Meteorol* 118:247–272
- Beyrich F, Mengelkamp HT (2006) Evaporation over a heterogeneous land surface: EVA_GRIPS and the LITFASS-2003 experiment: an overview. *Boundary-Layer Meteorol* 121:5–32
- Beyrich F, Herzog HJ, Neisser J (2002a) The LITFASS project of the DWD and the LITFASS-98 experiment: the project strategy and the experimental setup. *Theor Appl Climatol* 73:3–18
- Beyrich F, Richter SH et al (2002b) Experimental determination of turbulent fluxes over heterogeneous LITFASS area: selected results from the LITFASS-98 experiment. *Theor Appl Climatol* 73:19–34
- Beyrich F, Leps JP et al (2006) Area-averaged surface fluxes over the LITFASS region based on eddy-covariance measurements. *Boundary-Layer Meteorol* 121:33–65
- Blackadar AK (1997) *Turbulence and diffusion in the atmosphere*. Springer, Berlin, 185 pp
- Chen F, Avissar R (1994) The impact of land-surface wetness heterogeneity on mesoscale heat fluxes. *J Appl Meteorol* 33:1323–1340
- Courault D, Drobinski P, Brunet Y, Lacarrere P, Talbot C (2007) Impact of surface heterogeneity on a buoyancy-driven convective boundary layer in light winds. *Boundary-Layer Meteorol* 124:383–403
- Deardorff JW (1974) Three-dimensional numerical study of the height and mean structure of a heated planetary boundary layer. *Boundary-Layer Meteorol* 7:81–106
- Fesquet C, Dupont S, Drobinski P, Dubos T, Barthlott C (2009) Impact of terrain heterogeneity on coherent structure properties: numerical approach. *Boundary-Layer Meteorol* 133:71–92
- Foken T, Mauder M et al (2009) Energy balance closure for the LITFASS-2003 experiment. *Theor Appl Climatol*. doi:10.1007/s00704-009-0216-8
- Gopalakrishnan SG, Avissar R (2000) An LES study of the impacts of land surface heterogeneity on dispersion in the convective boundary layer. *J Atmos Sci* 57:352–371
- Hadfield MG, Cotton WR, Pielke RA (1991) Large-eddy simulations of thermally forced circulations in the convective boundary layer. Part I: A small-scale circulation with zero wind. *Boundary-Layer Meteorol* 57:79–114
- Hadfield MG, Cotton WR, Pielke RA (1992) Large-eddy simulations of thermally forced circulations in the convective boundary layer. Part II: The effect of change in wavelength and wind speed. *Boundary-Layer Meteorol* 58:307–327
- Hechtel LM, Moeng CH, Stull RB (1990) The effects of nonhomogeneous surface fluxes on the convective boundary layer: a case study using large-eddy simulation. *J Atmos Sci* 47:1721–1741
- Heinemann G, Kerschgens M (2006) Simulation of surface energy fluxes using high-resolution non-hydrostatic simulations and comparisons with measurements for the LITFASS-2003 experiment. *Boundary-Layer Meteorol* 121:195–220
- Huang HY, Margulis SA (2009) On the impact of surface heterogeneity on a realistic convective boundary layer. *Water Resour Res* 45:w04425. doi:10.1029/2008WR007175
- Kang SL (2009) Temporal oscillations in the convective boundary layer forced by mesoscale surface heat-flux variations. *Boundary-Layer Meteorol* 132:59–81
- Kang SL, Davis KJ (2008) The effects of mesoscale surface heterogeneity on the fair-weather convective atmospheric boundary layer. *J Atmos Sci* 65:3197–3213
- Kustas WP, Hatfield JL, Prueger JH (2005) The soil moisture-atmosphere coupling experiment (SMACEX): background, hydrometeorological conditions and preliminary findings. *J Hydrometeorol* 6:791–804
- Letzel MO, Raasch S (2003) Large eddy simulation of thermally induced oscillations in the convective boundary layer. *J Atmos Sci* 60:2328–2341
- Letzel MO, Krane M, Raasch S (2008) High resolution urban large-eddy simulation studies from street canyon to neighbourhood scale. *Atmos Environ* 42:8770–8784
- Lilly DK (2002) Entrainment into mixed layers. Part I: Sharp-edged and smoothed tops. *J Appl Meteorol* 59:3340–3352
- Liu G, Sun J, Yin L (2011) Turbulence characteristics of the shear-free convective boundary layer driven by heterogeneous surface heating. *Boundary-Layer Meteorol* 140:57–71. doi:10.1007/s10546-011-9591-7
- Lynn BH, Rind D, Avissar R (1995) The importance of mesoscale circulations generated by subgrid-scale landscape heterogeneities in general circulation models. *J Clim* 8:191–205
- Mauder M, Göckede CLM, Leps JP, Beyrich F, Foken T (2006) Processing and quality control of flux data during LITFASS-2003. *Boundary-Layer Meteorol* 121:67–88
- Patton EG, Sullivan PP, Moeng CH (2005) The influence of idealized heterogeneity on wet and dry planetary boundary layers coupled to the land surface. *J Atmos Sci* 62:2078–2097

- Prabha TV, Karipot A, Binford MW (2007) Characteristics of secondary circulations over an inhomogeneous surface simulated with large-eddy simulation. *Boundary-Layer Meteorol* 123:239–261
- Raasch S, Etling D (1998) Modeling deep ocean convection: large eddy simulation in comparison with laboratory experiments. *J Phys Oceanogr* 28:1786–1802
- Raasch S, Harbusch G (2001) An analysis of secondary circulations and their effects caused by small-scale surface inhomogeneities using large-eddy simulation. *Boundary-Layer Meteorol* 101:31–59
- Raasch S, Schröter M (2001) PALM—a large-eddy simulation model performing on massively parallel computers. *Meteorol Z* 10:363–372
- Schröter M, Bange J, Raasch S (2000) Simulated airborne flux measurements in a LES generated convective boundary layer. *Boundary-Layer Meteorol* 95:437–456
- Shen S, Leclerc MY (1995) How large must surface inhomogeneities be before they influence the convective boundary layer structure? A case study. *Q J R Meteorol Soc* 121:1209–1228
- Shuttleworth W, Yang ZL, Arain MA (1997) Aggregation rules for surface parameters in global models. *Hydrol Earth Syst Sci* 1:217–226
- Steinfeld G, Letzel MO, Raasch S, Kanda M, Inagaki A (2007) Spatial representativeness of single tower measurements and the imbalance problem with eddy-covariance fluxes: results of a large-eddy simulation study. *Boundary-Layer Meteorol* 123:78–98
- Steinfeld G, Raasch S, Markkanen T (2008) Footprints in homogeneously and heterogeneously driven boundary layers derived from a Lagrangian stochastic particle model embedded into large-eddy simulation. *Boundary-Layer Meteorol* 129:225–248
- Stull RB (1988) An introduction to boundary layer meteorology. Kluwer, Dordrecht, 666 pp
- Sullivan PP, Moeng CH, Stevens B, Lenschow DH, Mayor SD (1998) Structure of the entrainment zone capping the convective atmospheric boundary layer. *J Atmos Sci* 55:3042–3064
- Uhlenbrock J, Raasch S, Hennemuth B, Zittel P, Meijninger WML (2004) Effects of land surface heterogeneities on the boundary layer structure and turbulence during LITFASS-2003: large-eddy simulations in comparison with turbulence measurements. In: 6th Symposium on boundary layers and turbulence. American Meteorological Society, Portland (Maine), paper 9,3
- van Heerwaarden CC, de Arellano JVG (2008) Relative humidity as an indicator for cloud formation over heterogeneous land surfaces. *J Atmos Sci* 65:3263–3277
- Weckwerth TM, Parsons DB et al (2004) An overview of the international H₂O project (IHOP_2002) and some preliminary highlights. *Bull Am Meteorol Soc* 85:253–277
- Wyngaard JC, Coté OR (1974) The evolution of a convective planetary boundary layer—a higher-order-closure model study. *Boundary-Layer Meteorol* 7:289–308

3.4 Research article D: The effect of surface heterogeneity on the structure parameters of temperature and humidity - An LES case study for the LITFASS-2003 experiment

3.4.1 Declaration of my contribution

I carried out all simulations and analyses included in this paper. The footprint analysis for the LITFASS-2003 experiment was carried out and provided by Oscar K. Hartogensis from Wageningen University. I wrote the manuscript of the article. The manuscript benefits from discussions with Dr. Frank Beyrich and Dr. Bram van Kesteren (DWD), Dr. Arnold Moene, Miranda Braam and Prof. Dr. Siegfried Raasch. The latter also provided helpful comments on the manuscript.

3.4.2 Draft manuscript

This article will be submitted to *Boundary-Layer Meteorology*.

Maronga, B., O. K. Hartogensis and S. Raasch, 2013: The effect of surface heterogeneity on the structure parameters of temperature and humidity - An LES case study for the LITFASS-2003 experiment. *Boundary-Layer Meteorol.*, to be submitted.

Boundary-Layer Meteorology manuscript No. (will be inserted by the editor)
--

The effect of surface heterogeneity on the structure parameters of temperature and humidity - An LES case study for the LITFASS-2003 experiment

Björn Maronga · Oscar K Hartogensis · Siegfried Raasch ·

Received: date / Accepted: date

Abstract We conduct a high-resolution large-eddy simulation (LES) case study in order to investigate the effect of surface heterogeneity on the structure parameters of potential temperature C_T^2 and specific humidity C_q^2 in the convective boundary layer (CBL). A surface heterogeneity as observed during the LITFASS-2003 experiment is prescribed at the surface of the LES model in order to simulate a realistic CBL development from the early morning until the early afternoon. The surface patches are irregularly distributed and provide different land use types that exhibit different roughness conditions as well as near-surface fluxes of sensible and latent heat that were obtained from eddy-covariance measurements during the LITFASS-2003 experiment. Particular attention is given to the Monin-Obukhov similarity theory (MOST) relationships and local free convection (LFC) scaling in the surface layer for structure parameters, relating C_T^2 and C_q^2 to the surface fluxes of sensible and latent heat, respectively. Moreover we study possible effects of surface heterogeneity on scintillometer measurements that are usually performed in the surface layer. The LES data show that signals of the surface heterogeneity are still present in the structure parameters up to height levels of 100 – 200 m. The assumption of horizontal homogeneity of turbulence that is required by MOST at typical height levels of scintillometer measurements is thus not valid for the studied case and no blending height for structure parameters exists well below the scintillometer path. Moreover, it is found that C_q^2 does not follow MOST which is ascribed to entrainment of dry air at the top of the boundary layer. Nevertheless, it is found that the application of MOST and LFC for C_T^2 still give reliable estimates of the surface flux of sensible heat. It is argued, however, that this flux, derived from scintillometer data, will be rather representative for the local footprint area of the scintillometer than for an area of several square kilometers and thus of size of current numerical weather prediction models.

Keywords Convective boundary layer · Large-eddy simulation · Turbulent structure parameter · Surface heterogeneity

B. Maronga · S. Raasch
Institut für Meteorologie und Klimatologie, Leibniz Universität Hannover,
Herrenhäuser Str. 2, 30419 Hannover, Germany
E-mail: maronga@muk.uni-hannover.de

Oscar K Hartogensis
Meteorology and Air Quality Section, Wageningen University,
Wageningen, The Netherlands

1 Introduction

The turbulent surface fluxes of sensible and latent heat play an important role for the turbulent exchange in the atmospheric boundary layer. The measurement of the area-averaged fluxes at a regional scale is necessary for both a better understanding of the meteorological and hydrological processes as well as for the validation of parameterizations in numerical weather prediction (NWP) models (De Bruin et al., 1993; Li et al., 2012; Beyrich et al., 2012; Braam et al., 2012). The grid resolution in NWP models is usually of size of several kilometers. It is thus essential to measure surface fluxes that are representative for an area of size in the order of square kilometers. Over homogeneous terrain, point measurements using eddy covariance technique are the traditional and most common way to measure the surface fluxes (Andreas, 1991; Lee et al., 2004; Braam et al., 2012). Natural landscapes rarely provide such horizontally homogeneous conditions so that the grid boxes in NWP models often contain different surface patches of farmland, settlements, water, forest etc. The local surface fluxes of the different surface types, however, might differ significantly (e.g. Bange et al., 2006; Beyrich et al., 2006a) and point measurements can no longer be considered to give reliable estimates of the surface fluxes that are representative for areas of several square kilometer.

Scintillometry offers a technique that allows for estimating the surface fluxes of sensible and latent heat by measuring turbulent density fluctuations in the surface layer in terms of the refractive index structure parameter C_n^2 as a spatial average over horizontal distances of up to 10 km (Kohsiek et al., 2002; Meijninger et al., 2002b,a, 2006; Evans et al., 2012, among many others). Hill (1978), among others, showed that C_n^2 might be related to C_T^2 and C_q^2 as the density fluctuations are dominantly caused by fluctuations of temperature and humidity. In order to determine the surface fluxes of sensible and latent heat from the estimates of C_T^2 and C_q^2 , respectively, Monin-Obukhov similarity theory (MOST) is applied. Theoretically, the application of MOST requires a horizontal homogeneous surface (Andreas, 1991; Beyrich et al., 2012). It is thus required that the height of the measurement is above a blending height for structure parameters, above which any signal from a present surface heterogeneity is no longer visible (Wieringa, 1976; Mahrt, 2000; Meijninger et al., 2002b). So far the blending height concept is discussed controversially in literature and it has not been possible to show even its existence (Bange et al., 2006; Beyrich et al., 2012). Surface heterogeneity hence might affect large-aperture scintillometer (LAS) and microwave scintillometer (MWS) measurements, which has not been justified so far. Whereas LAS are used to determine C_T^2 as they are mainly sensitive to temperature fluctuations, MWS are more sensitive to humidity fluctuations and are hence employed in combination with LAS systems for determining C_q^2 (e.g. Kohsiek and Herben, 1983; Meijninger et al., 2002a, 2006; Lüdi et al., 2005). Sührling and Raasch (2013) studied the convective boundary layer (CBL) over the moderately heterogeneous LITFASS area in the south-east of Berlin (Germany) by means of large-eddy simulations (LES) and showed a clear dependence of the turbulent fluxes on the underlying surface up to the top of the CBL. Recently, van den Kroonenberg et al. (2012) employed small unmanned aircraft to study the variability of C_T^2 along an LAS path during the LITFASS-2009 experiment. They found a notable variability of C_T^2 along the path and ascribed this to both temporal variations as well as the underlying surface heterogeneity. However, Sührling and Raasch (2013) pointed out that sufficient independent flight measurements are required to obtain a significant estimate of a heterogeneity-induced effect in terms of turbulent fluxes. The question if there is a heterogeneity-induced effect on C_T^2 and C_q^2 and if it can be measured by aircraft (and scintillometers) is still open.

LES offers a promising technique for studying the effect of surface heterogeneity on the structure parameters and their MOST relationships. Unlike in situ measurements, where the (heterogeneous) surface fluxes are more or less unknown, they can be explicitly prescribed in the LES model. Previous LES studies have shown that C_T^2 and C_q^2 can be reliably derived from LES data of the homogeneously-heated CBL (Peltier and Wyngaard, 1995; Cheinet and Siebesma, 2009; Cheinet and Cumin, 2011; Maronga et al., 2013; Wilson and Fedorovich, 2012). Cheinet and Siebesma (2009) studied the spatial variability of C_T^2 and found a bimodal log-normal distribution near the surface, which was previously found in the SODAR measurements of Petenko and Shurygin (1999). Cheinet and Cumin (2011) studied the behavior of C_T^2 and

C_q^2 in the entrainment-drying CBL and found that the distribution of C_q^2 was determined by entrained air parcels from the free atmosphere, whereas C_T^2 was dominated by the near-surface convective plumes. Cheinet and Siebesma (2007) used a wave propagation modeling framework to derive the scintillation rate and coherence length from virtual path measurements in their LES. They found that the variability of their virtual measurements of C_n^2 increased with height, while the path mean decreased. However, the coarse spatial resolution of their LES did not allow to study the wave propagation at realistic scintillometer heights. A first comparison with in situ aircraft and LAS data was performed by Maronga et al. (2013). They also employed virtual LAS (VLAS) measurements in their LES at realistic height levels above ground to investigate the temporal and spatial variability of C_T^2 measurements by an LAS and could confirm the results of Cheinet and Siebesma (2007). Maronga (2013) calculated the MOST relationships for structure parameters from a set of LES for near-neutral to free convective boundary layers above homogeneous surface and found that universal MOST functions exist for C_T^2 that were well within the range of the proposed functions in literature. Maronga (2013) could also show that dissimilarity between the turbulent transport of heat and moisture can be induced and explained by entrainment of dry air at top of the mixed layer, leading to non-universal similarity functions for C_q^2 . Up to now, all LES studies have been performed for idealized conditions with homogeneous surfaces and under quasi-stationary conditions. The question, whether MOST is also valid over heterogeneous terrain with different surface patches that provide different characteristics concerning surface fluxes and roughness, has not been studied so far.

Maronga and Raasch (2013) simulated the convective boundary layer over heterogeneous LITFASS-2003 terrain (see Fig. 1a), based on the early LES of Uhlenbrock et al. (2004), for four selected days during the LITFASS-2003 experiment (see Beyrich and Mengelkamp, 2006). They found that secondary circulations developed that were superimposed on the randomly distributed convection, partly taking over the vertical transport of heat and moisture. However, they showed that the scale of the surface heterogeneity must be at least of size of the boundary-layer depth z_i to induce such circulations that then span the entire CBL. This agrees with earlier findings from Shen and Leclerc (1995) and Raasch and Harbusch (2001) for idealized two-dimensional surface heterogeneities. Sühling and Raasch (2013) have shown that LES is an appropriate tool for investigating the blending height concept.

In the present case study the CBL over the eastern part of the LITFASS-2003 area (see Fig. 1 a, b, dominated by farmland) is simulated using high-resolution LES that resolve the surface layer turbulence. The structure parameters are derived from LES for the first time over such an irregular surface heterogeneity and are compared with in situ LAS observations observed during the LITFASS-2003 experiment. The concept of a blending height for structure parameters is studied using a lagged two-dimensional correlation analysis method introduced by Sühling and Raasch (2013). Moreover, it will be discussed if MOST can be applied over such heterogeneous landscapes. Furthermore, we will explore possible implications of surface heterogeneity on LAS observations.

The paper is organized as follows: Section 2 outlines the derivation of structure parameters from LES data. Moreover, a brief introduction of the MOST relationships for structure parameters is given. Section 3 describes the LES model PALM, model setup as well as data processing. Simulation results are presented in Section 4. Section 5 gives a summary.

2 Theory and methods

Traditionally, the structure parameters of temperature and humidity are defined and deduced either directly using the structure functions, or using the one-dimensional spectra of temperature and humidity (e.g. Tatarskii, 1971; Wyngaard et al., 1971b; Andreas, 1988). As both formulations should be mathematically equivalent, we focus on the latter approach. Following Wyngaard et al. (1971b) the structure parameters C_T^2 and C_q^2 are directly proportional to the spectra of temperature and humidity in the inertial subrange,

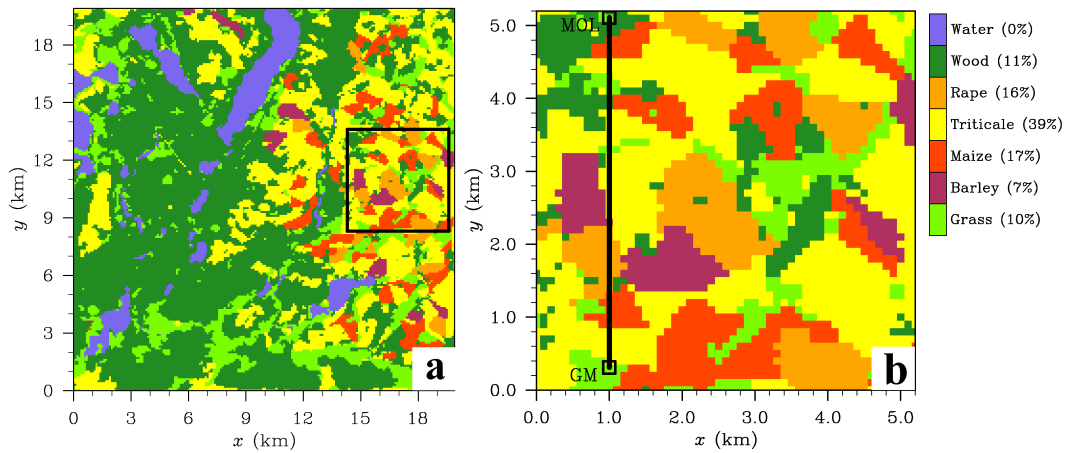


Fig. 1: Distribution of land-use classes: **a** shows the entire LITFASS-area where the *black box* marks the LES model domain. **b** shows a close-up view of the model domain, including the VLAS path (*black line*) from Lindenberg (*MOL*) to Falkenberg (*GM*). The legend indicates the percentage coverage of the particular land-use class in the model domain

respectively. They can be related to the power spectral density Φ (*spectral method*) at a given height by

$$C_S^2 = \frac{1}{0.2489} \Phi_S(k) k^{5/3}, \quad (1)$$

where the given scalar S can be either potential temperature θ or specific humidity q . k is a wave number in the inertial subrange and $0.2489 = 2/3\Gamma(1/3)$ after Muschinski et al. (2004). Note that for potential temperature the notation C_T^2 with index T (actual temperature) is used for convenience.

The recent LES studies of Cheinet and Siebesma (2009) and Maronga et al. (2013) showed that it is also possible to relate C_T^2 and C_q^2 to the (local) dissipation rates of turbulent kinetic energy ε_{TKE} and scalar fluctuations ε_S :

$$C_S^2 = \frac{\beta}{0.2489} \varepsilon_{\text{TKE}}^{-1/3} \varepsilon_S \quad (2)$$

with $\beta \approx 0.4$ being the Obukhov-Corrsin constant (Sreenivasan, 1996). These dissipation rates, in turn, can be modeled using the parametrization of subgrid-scale (SGS) turbulence. A 1.5-order flux-gradient subgrid closure scheme after Deardorff (1980) is used in PALM. According to this scheme, the local structure parameters for a given grid volume (in the inertial subrange) can be calculated by the so-called *dissipation method* and Eq. 2 then yields

$$C_S^2 = \frac{0.2 \beta}{0.2489} l^{4/3} \left(1 + \frac{2l}{\Delta}\right) \left(0.19 + 0.74 \frac{l}{\Delta}\right)^{-1/3} \left(\frac{\partial S}{\partial x_i}\right)^2, \quad (3)$$

where $\Delta = \sqrt[3]{\Delta_x \Delta_y \Delta_z}$ with Δ_x, Δ_y and Δ_z being the grid resolutions of the Cartesian coordinate system ($x_1 = x, x_2 = y, x_3 = z$). The subgrid-scale mixing length l depends on height and stratification. In unstable stratification l usually equals Δ , whereas l becomes smaller in stably stratified regions (Deardorff, 1980). For a detailed derivation and validation of both methods please see Cheinet and Siebesma (2009) and Maronga et al. (2013).

The derivation of the surface fluxes of sensible and latent heat from scintillometer measurements is based on the application of MOST for the structure parameters of temperature and humidity (e.g. Andreas, 1988; Beyrich et al., 2012). Following MOST, a given non-dimensional group of a (turbulent) variable should be only a function of the stability parameter z/L with z being measurement height and L being Obukhov length that is defined as $L = -(\overline{\theta_v u_*^3}) / (\kappa g \overline{w' \theta'_{v0}})$ (Obukhov, 1946). Here, u_* is the friction velocity, θ_v is virtual potential temperature, $\kappa = 0.4$ is the Von Kármán constant, g is gravitational acceleration and $\overline{w' \theta'_{v0}}$ is the near-surface buoyancy flux. C_T^2 and C_q^2 should thus satisfy

$$\frac{C_T^2 z^{2/3}}{\theta_*^2} = f_T(z/L), \quad (4)$$

$$\frac{C_q^2 z^{2/3}}{q_*^2} = f_q(z/L), \quad (5)$$

with $\theta_* = -\overline{w' \theta'_{v0}}/u_*$ and $q_* = -\overline{w' q'_{v0}}/u_*$. Here, $\overline{w' \theta'_{v0}}$ and $\overline{w' q'_{v0}}$ are the kinematic surface fluxes of heat and moisture, respectively. If both C_T^2 and C_q^2 follow MOST, then f_T and f_q should be universal functions of z/L . So far it has not been possible to derive a precise form of f_T and f_q , but several empirical formulations have been proposed for unstable conditions from measurement data (Wyngaard et al., 1971b; Wesely, 1976; Andreas, 1988; Thiermann and Grassl, 1992; Hill et al., 1992; De Bruin et al., 1993; Li et al., 2012). Most suggest the following form

$$f_T(z/L) = c_{TT1} [1 - c_{TT2}(z/L)]^{-2/3}, \quad (6)$$

$$f_q(z/L) = c_{qq1} [1 - c_{qq2}(z/L)]^{-2/3}, \quad (7)$$

with dimensionless constants c_{TT1} , c_{TT2} , c_{qq1} and c_{qq2} that are determined empirically and characterize the transition from near-neutral to free-convective conditions. Hill (1989) pointed out that, if the structure parameters all follow MOST, then their similarity functions must be the same ($f_T = f_q$), and temperature and humidity must be perfectly correlated (correlation coefficient of $R_{Tq} = 1$). However, often it is found that $R_{Tq} \neq 1$ (Beyrich et al., 2005) and it could be shown by Li et al. (2012) and Maronga (2013) that then often it can be observed that $f_T \neq f_q$. Maronga (2013) showed that C_T^2 can be considered to follow MOST, whereas C_q^2 in the surface layer is often affected by entrainment of dry air at the top of the mixed layer and thus does not follow MOST.

When mechanical production is much less important than buoyant generation of turbulence (e.g. when winds are calm and $u_* \rightarrow 0$) the Obukhov length is close to zero and no longer a proper scaling parameter. MOST will thus fail under such conditions. As buoyancy is the driving force the surface layer should behave as in free convection. This is commonly referred to as *local free convection* (LFC) (e.g. Wyngaard et al., 1971a) and the dimensionless structure parameters should follow:

$$\frac{C_T^2 z^{2/3}}{\theta_{LF}^2} = A_T, \quad (8)$$

$$\frac{C_q^2 z^{2/3}}{q_{LF}^2} = A_q, \quad (9)$$

with $\theta_{LF} = \overline{w' \theta'_{v0}}/w_{LF}$, $\theta_{LF} = \overline{w' \theta'_{v0}}/w_{LF}$ and $w_{LF} = \left((g/\overline{\theta_v}) \overline{w' \theta'_{v0}} z \right)^{1/3}$. Due to the limited scales in LFC scaling there is only one dimensionless group and A_T and A_q should be universal constants (see Andreas, 1991). Measurements suggest that $A_T = 2.7$ (Wyngaard et al., 1971b; Kaimal et al., 1976; Wyngaard and LeMone, 1980; Kunkel et al., 1981; Andreas, 1991). While Wyngaard and LeMone (1980) suggests $A_q \approx 1.5$, Andreas (1991) suggested that $A_T = A_q = 2.7$ (when $R_{Tq} = 1$), referring to the study of Hill (1989). The previous LES study of Peltier and Wyngaard (1995) suggested $A_q = 2.0 - 2.7$. However, they also showed

that A_q can be higher than A_T due to entrainment effects. Maronga (2013) found that $A_T = 2.7$ and explicitly showed that the value of A_q is not universal if entrainment of dry air is significant (C_q^2 does not follow MOST/LFC scaling), which can be often the case and could explain the different suggestions in literature. Otherwise it was found that $A_T \approx A_q$.

It can also be shown that LFC scaling can be traced back to MOST using Eqs. 4 - 7 and looking at the free convection limit, i.e. $-z/L \rightarrow \infty$ (De Bruin et al., 1995). It follows that

$$A_T = \kappa^{-2/3} c_{TT1} c_{TT2}^{-2/3}, \quad (10)$$

$$A_q = \kappa^{-2/3} c_{qq1} c_{qq2}^{-2/3}, \quad (11)$$

which gives a direct link between the universal parameters in MOST and LFC scaling.

3 LES model and case description

3.1 LES model

The LES model PALM (revision 1105) (see e.g. Raasch and Schröter, 2001; Riechelmann et al., 2012) was used for the present study. It has been recently applied to study different flow regimes in the convective boundary layer over homogeneous (e.g. Raasch and Franke, 2011; Maronga et al., 2013) and heterogeneous terrain (e.g. Maronga and Raasch, 2013; Sühling and Raasch, 2013). All simulations were carried out using cyclic lateral boundary conditions. The grid was stretched in the vertical direction well above the top of the boundary-layer to save computational time in the free atmosphere. MOST was applied as surface boundary condition locally between the surface and the first computational grid level (“local similarity model”, see also Peltier and Wyngaard, 1995), including the calculation of the local friction velocity u_* . A 1.5-order flux-gradient subgrid closure scheme after Deardorff (1980) was applied, which requires the solution of an additional prognostic equation for the SGS turbulent kinetic energy. A 5th-order advection scheme of Wicker and Skamarock (2002) and a 3rd-order Runge–Kutta time step scheme were used (Williamson, 1980). A one-dimensional version of the model with fully-parametrized turbulence, using a mixing-length approach after Blackadar (1997) and stationary temperature and humidity profiles, was used for precursor simulations to generate steady-state wind profiles as initialization for the LES.

3.2 Case description

This case study is based on the LES setup for the heterogeneous LITFASS area on 30 May 2003 (hereafter referred to as case LIT2E) as it is described in Maronga and Raasch (2013). Topography in the LITFASS area is rather flat and thus neglected in the LES. Case LIT2E was characterized by clear skies and a weak geostrophic wind of 2 m s^{-1} , blowing from the east. Maronga and Raasch (2013) showed that their LES results were in good agreement with the radiosonde data from the LITFASS-2003 experiment. Figure 1a shows the land-use types in the LITFASS area derived from the CORINE¹ data set with a resolution of 100 m. The size of the area was about $20 \text{ km} \times 20 \text{ km}$, containing different surface patches of forest, lakes and farmland, as it was previously used in the LES studies of Maronga and Raasch (2013) and Sühling and Raasch (2013). These studies, however, had relatively coarse grid resolutions of 40 – 100 m in all spatial directions. In order to resolve the turbulence in the surface layer, a much higher grid resolution was required in the present study. Due to limited computing resources it was necessary to limit the model domain to an

¹ Abbr. “Coordinated Information on the European Environment”, published by the European Environment Agency (<http://www.eea.europa.eu/publications/CORO-landcover>)

area of $5.3 \text{ km} \times 5.3 \text{ km}$ with 1600×1600 grid points in the horizontal directions (Fig. 1a, black box and Fig. 1b). Maronga and Raasch (2013) found that the mean boundary-layer depth z_1 reached about 1.8 km at 1400 UTC. We hence used a constant grid resolution up to a height level of 2 km. The grid resolution was 2 m (1000 grid points), in agreement with the previous LES of Maronga and Raasch (2013). Above, the grid was vertically stretched by factor of 1.02 for each plane. Moreover, the simulation time was reduced to a part of the diurnal cycle from 0500 UTC to 1300 UTC. In this way one simulation still required about 120 h of real time on 4096 Intel Xeon Gainestown processors (2.93 GHz) on an SGI Altix ICE 8200 Plus cluster. Due to this high computational demands it was neither possible to simulate more than one case, nor was it possible to repeat a simulation with improved setup in order to overcome weaknesses of the study that will be discussed in Section 4.

In the course of the LITFASS-2003 experiment, LAS observations were made along a 4.8 km long path at a height of 43 m above ground (following topography), ranging from the Lindenberg Meteorological Observatory (MOL) of the German Weather Service (DWD) to the boundary layer measurement site (GM) near Falkenberg (see Beyrich and Mengelkamp, 2006). We located the model domain around the LAS path as shown in Fig. 1b with start and end of the virtual LAS (hereafter VLAS) measurement path in the LES being located on grassland. The LAS path was nearly aligned in north-south direction. For simplification we decided to align the VLAS path exactly along the y -direction in the model, which should not introduce a significant error as the heterogeneity was still prescribed on a 100 m raster. A footprint analysis was carried out afterwards for May 30, 2003 to retrospectively ensure that the chosen model domain was large enough to cover the footprint of the VLAS. The results of this footprint analysis will be discussed in Section 3.3. Figure 1b shows that the surface in the model domain mainly consists of different agricultural fields, where triticale makes up 39% of the total area. The remaining area is covered by maize (17%), rape (16%), forest (11%, including settlements, see Maronga and Raasch 2013), grassland (10%) and barley (7%). No water and only few forest patches are situated in the chosen area. Therewith, the distribution of surface types is significantly different as in the previous LES for the LITFASS area (see Maronga and Raasch, 2013; Sühling and Raasch, 2013) and therewith also the area-averaged surface fluxes.

Initial profiles of θ and q were derived from radiosonde data during the LITFASS-2003 experiment. A heterogeneous roughness length z_0 for the different surface types was estimated as previously done after Shuttleworth et al. (1997) as $z_0 \approx 0.1 \cdot \text{crop height}$. Surface fluxes of sensible and latent heat ($H = \rho c_p \overline{w'\theta'}_0$ and $LE = \rho L_v \overline{w'q'}_0$, respectively, with c_p being the heat capacity of dry air at constant pressure and L_v being latent heat of vaporization) were measured during LITFASS-2003 at energy balance stations located on the different land-use types. Figure 2 shows these measured fluxes in the diurnal cycle until 1300 UTC, showing that forest patches displayed the largest surface sensible heat flux with values of up to 500 W m^{-2} , followed by barley and triticale (up to 300 W m^{-2}) and grass, maize as well as rape (up to 220 W m^{-2}). The surface latent heat flux only displayed a weakly developed diurnal cycle with maximum fluxes of 220 W m^{-2} (rape). These measured fluxes were used as surface fluxes in the LES for all patches of the respective surface type in the model domain. The flux data were available half-hourly and were thus linearly interpolated in time for each time step. For a more detailed discussion of the implementation of the heterogeneity please see Maronga and Raasch (2013) and Sühling and Raasch (2013).

Maronga and Raasch (2013) showed that secondary circulations developed over the LITFASS area, depending on the geostrophic wind, and that a sufficiently large upwind buffer zone is required in order to resolve them. The limited model domain of $5.3 \text{ km} \times 5.3 \text{ km}$ does not allow for resolving the secondary circulations observed by Maronga and Raasch (2013) as large patches of forest and water are missing (see Fig. 1 b, cf. Fig. 1 a). However, they found that these secondary circulations only develop if the heterogeneity scales are at least of size of z_1 and that heterogeneity scales over the eastern part of the LITFASS area (dominated by farmland patches with size in the order of 1 km) are usually too small and the amplitude too low to trigger secondary circulations. Moreover, they stated that secondary circulations are generally weak close to the surface. Effects of such circulations, such as a modification of the turbulent vertical fluxes of heat and moisture, are thus expected to be irrelevant for the present study. Nevertheless, local effects

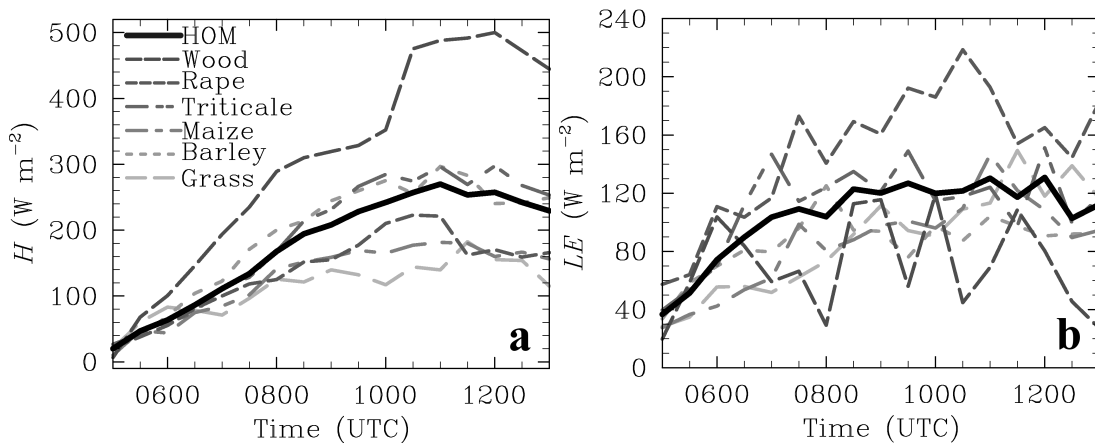


Fig. 2: Time series of the prescribed surface fluxes of **a** sensible and **b** latent heat for the different land-use classes as well as the horizontal average (*solid black line*) as used in the homogeneous control run.

of the surface heterogeneity might remain and are will be most prominent in the lower boundary layer. In order to quantify such effects of the surface heterogeneity, the study is complemented by a run with spatially-averaged but temporally-varying surface heat fluxes (hereafter case HOM, see Fig. 2, solid black line).

3.3 Footprint analysis

A footprint analysis for the VLAS path in the LITFASS area on May 30, 2003 was conducted using the analytical footprint model of Kormann and Meixner (2001) and measurement data from energy balance stations and tower observations close to the LAS installed during the experiment. As easterly winds were observed and prescribed in the model, the footprint of the VLAS was located in the upstream direction. Since cyclic lateral boundary conditions were used, the prescribed surface heterogeneity was periodically repeating, which does not occur in reality. In the vicinity of horizontal boundaries the flow is hence exposed to an erroneous surface forcing (Maronga and Raasch, 2013). It is thus essential that a sufficiently large buffer zone is prescribed so that the VLAS signal is not affected by the cyclic boundary conditions. The surface area was thus chosen in such a way that the VLAS path was located close to the western boundary of the model. Footprints for selected times are shown in Fig. 3. As expected the footprint was located in the area east to the path, with 90 % of the footprint lying within a distance of 500 m from the scintillometer path (see Fig. 1b). The used fetch of 4 km was thus much larger than the required upstream domain according to the footprint analysis. Therefore, it will be possible to compare VLAS measurements with the in situ LAS data observed during LITFASS-2003. A typical contribution of the land use classes to the footprint was (e.g. 11 UTC): 62% triticale, 12% rape, 10% maize, 9% barley, 5% forest and 4% grassland. This composition suggests that the VLAS might see mostly signals from triticale if no blending height exists somewhere below the VLAS.

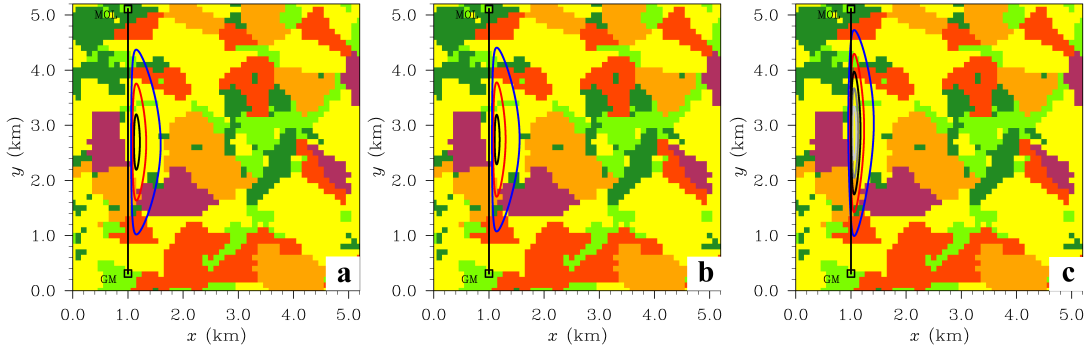


Fig. 3: Selection of the footprints for the LAS during the LITFASS-2003 experiment, derived from the analytical footprint model of Kormann and Meixner (2001), mapped on land-use classes at **a** 0800 UTC, **b** 1000 UTC and **c** 1200 UTC. The contour lines indicate the cumulative footprint areas of 90% (*blue line*), 70% (*red line*), 50% (*black line*), 30% (*gray line*) and 10% (*light gray line*).

3.4 Data processing

3.4.1 LES data

The structure parameters of potential temperature and specific humidity were derived from both the spectral method and the dissipation method (see Eqs. 1 and 3) as described by Maronga et al. (2013). Cheinet and Siebesma (2009) and Maronga et al. (2013) found that the dissipation method yields structure parameters that are too small in their magnitude (compared to semi-empirical profiles), whereas the spectral method gave reliable estimates of C_T^2 and C_q^2 in the study of Maronga et al. (2013). The simulation data in the latter study as well as the data in the present study suggests a constant correction factor for the dissipation method of 1.7 – 1.9 and was determined for the data in the present study to be 1.85 (evaluated at height of the VLAS). We decided to use the dissipation method for this study because it gives local estimates of the structure parameters, which allows for investigating possible local effects of surface heterogeneity on the structure parameters and VLAS measurements. We hence applied the empirical correction factor of 1.85 to the data that was available at 0.1 Hz.

In the present study we use these VLAS measurements along the path from MOL (transmitter) to GM (receiver) (see Fig. 1b) using the method of Maronga et al. (2013) for comparison with in situ LAS data. They employed the dissipation method and calculated the path-weighted average of the structure parameters along horizontal paths in the LES model (see their Fig. 6 and Appendix). They also discussed that, on the one hand, the scintillations seen by an LAS are mainly determined by fluctuations at the scale of the beam diameter (here 0.15 m), whereas smaller scales are averaged out. Larger scales result in variability of the scintillations. On the other hand, the nominal truncation size in the LES is $\Delta \approx 2.7$ m (the actual truncation happens at even larger scales up to 6Δ) so that a part of the variability in the structure parameters is missed by the LES.

The boundary-layer depth increased in the course of the simulation up to 1.5 km. The top of the surface layer z_{SL} was defined as $z_{SL} = 0.1z_i$, in agreement with the study of Maronga (2013) and Brasseur and Wei (2010). z_{SL} indicates the height up to which MOST roughly should be valid. In order to study the MOST relationships for C_T^2 and C_q^2 we thus only used data from height levels $\leq z_{SL}$. Moreover, as pointed out by Khanna and Brasseur (1997), the lowest height levels are always affected by the SGS model and thus cannot resemble the surface layer dynamics correctly. We hence excluded the lowest 7 grid points from the

analysis of the MOST relationships. Due to the very high spatial resolution used in our simulations, the entire surface layer is represented by more than 40 grid points (except the early morning hours before the morning inversion is eroded, see below), so that omitting the lowest levels does not restrict the database for our analysis very much.

4 Results

4.1 Mean profiles

The horizontally-averaged (denoted by angular brackets) profiles of θ and q are shown in Fig. 4 a and b for both cases LIT2E and HOM, respectively. In the early morning (0500 UTC) the temperature and humidity profiles show a near-surface inversion up to a height of 150 m, a residual layer with slightly stable stratification above and a capping inversion starting at 850 m. At 0700 UTC the near-surface inversion is eroding and the residual layer is incorporated into the developing mixed layer. During this so called morning transition z_i rapidly increases from 200 m to 1000 m. At 1300 UTC z_i has increased to 1500 m. Maronga and Raasch (2013) found a mean z_i of 1795 m for the entire LITFASS area. However, they showed that z_i was up to 15% smaller over the farmland area due to less heat input into the atmosphere over agricultural dominated patches (see their Fig. 7 a). This explains the lower z_i in the present study.

The temperature profiles show a warming of the boundary layer with a maximum mixed-layer temperature close to 297 K at 1300 UTC. Humidity is dominated by entrainment of dry air in the course of the day in such a way that the mean humidity in the mixed layer is continuously decreasing after 0700 UTC, reaching 4 g kg^{-1} at 1300 UTC. Both the profiles of $\langle\theta\rangle$ and $\langle q\rangle$ are comparable with the previous LES for the LITFASS area (see Maronga and Raasch, 2013). It is also visible from Fig. 4 a and b that the mean profiles and in particular the height of the temperature inversion (and thus z_i) are not modified significantly by the surface heterogeneity. While Maronga and Raasch (2013) showed that secondary circulations developed that spanned the entire boundary and affected the horizontally-averaged z_i , the surface heterogeneity in the present study does not show such effects, most likely due to the fact that the heterogeneity scales and amplitudes are rather small (compared to the amplitude between forest and water patches that led to strong secondary circulations in the study of Maronga and Raasch (2013)). The surface heterogeneity can thus not trigger secondary circulations and is supposed to retain a more local character that might affect the lowest decameters of the atmosphere, but that does not show any effect in the upper mixed or entrainment layer.

Fig. 4 c and d show the mean profiles of C_T^2 and C_q^2 , respectively. $\langle C_T^2\rangle$ and $\langle C_q^2\rangle$ both display a maximum near the surface, caused by generation of small-scale turbulence by rising thermals and wind shear. $\langle C_T^2\rangle$ is decreasing in the mixed layer up to height levels where entrainment processes become important, leading to temperature fluctuations at the interface between mixed layer and free atmosphere and thus a peak in $\langle C_T^2\rangle$. The shape of $\langle C_T^2\rangle$ is in agreement with the results from the previous LES studies (Peltier and Wyngaard, 1995; Cheinet and Siebesma, 2009; Maronga et al., 2013). $\langle C_q^2\rangle$ is increasing throughout the mixed layer, suggesting that fluctuations of humidity in the CBL are controlled by entrainment of dry air at the top of the mixed layer. This is in agreement with observations (e.g. Druilhet et al., 1983). Secondary peaks of $\langle C_T^2\rangle$ and $\langle C_q^2\rangle$ that can be observed at 800 m (at 0700 UTC) can be ascribed to turbulent fluctuations at top of the residual layer during the morning transition. Peaks for $\langle C_q^2\rangle$ around 2000 m are caused by the humidity jump from 1900 – 2000 m. For both $\langle C_T^2\rangle$ and $\langle C_q^2\rangle$ some differences between cases LIT2E and HOM can be observed, even though they appear to be marginal, particularly for $\langle C_T^2\rangle$. We will investigate whether these differences might affect the structure parameters at height of an LAS system and their similarity relationships in the following Section 4.2.

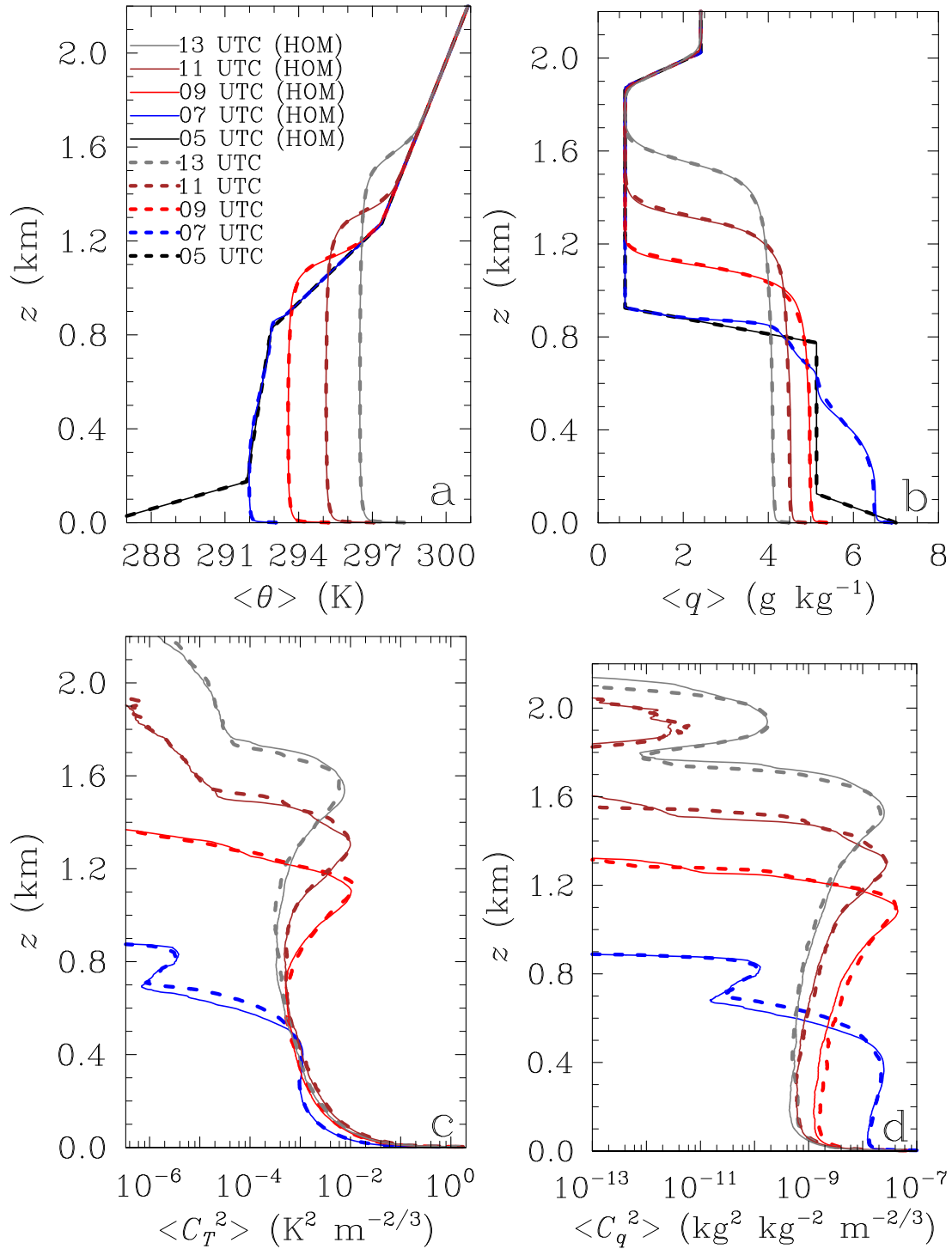


Fig. 4: Mean profiles of **a** potential temperature, **b** specific humidity, **c** C_T^2 and **d** C_q^2 for cases LIT2E and HOM.

4.2 Monin-Obukhov similarity relationships

The mean profiles of C_T^2 in the lowest 150 m are shown in Fig. 5. They reveal that $\langle C_T^2 \rangle$ in case LIT2E is higher than in case HOM (also valid for $\langle C_q^2 \rangle$, not shown). On average the difference is 4.2% and 12.0% for C_T^2 and C_q^2 , respectively (not shown). If the MOST/LFC scaling parameters are the same, this difference might affect the MOST and LFC relationships for C_T^2 and C_q^2 . Due to the non-linear relationships between structure parameters and surface fluxes (Eq. 4-5,8-9, see also Maronga, 2013), the induced percentage error will be, however, smaller. We can thus assume that the MOST relationships can be only slightly modified. The dimensionless structure parameters have been calculated for every 10s according to Eqs. 4 and 5. The results are shown in Fig. 6. It is visible that the data points of the dimensionless $\langle C_T^2 \rangle$ differ slightly between cases LIT2E and HOM, which can be related to the difference in $\langle C_T^2 \rangle$ that was discussed above (see Fig. 5). Since the range of the stability parameter $-z/L$ covers only values from about 10 – 200, that is close to free convective conditions, it is not possible to derive representative fitting functions f_T (and hence values for c_{TT1} and c_{TT2}). Much more data points for conditions with higher geostrophic winds and lower surface fluxes would be required in order to cover the whole stability range from free-convective down to near-neutral conditions with $-z/L \approx 0.01$ (see e.g. Li et al., 2012). Nevertheless, as we have many data points close to free convective conditions it makes sense to derive c_{TT1} and c_{TT2} from this data set as one can deduce the LFC parameter A_T from them using Eq. 10. The LES data suggest

$$f_{T,\text{LIT2E}}(z/L) = 4.2 [1 - 4.2(z/L)]^{-2/3} \quad (12)$$

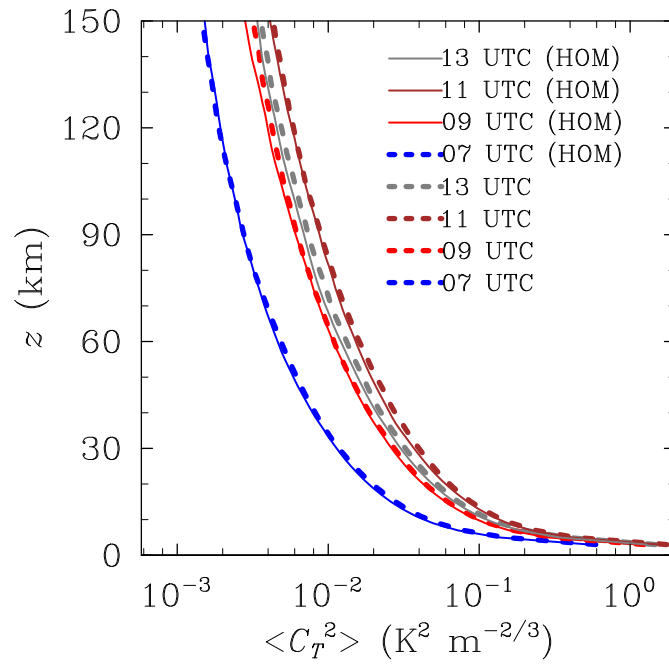
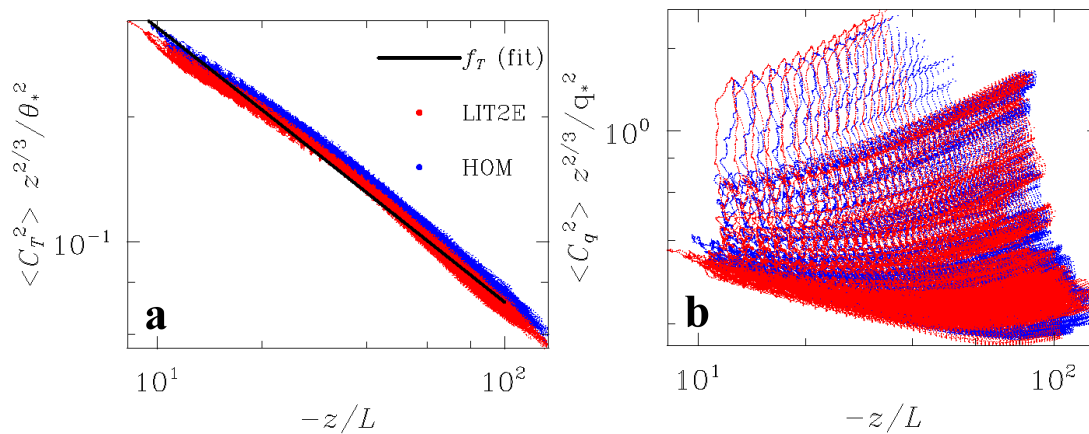
and

$$f_{T,\text{HOM}}(z/L) = 4.4 [1 - 4.8(z/L)]^{-2/3}. \quad (13)$$

which is significantly different from the values of $c_{TT1} = 6.1$ and $c_{TT2} = 7.6$ that were derived over homogeneous terrain in the study of Maronga (2013). As stated above, these values can not be compared to the obtained values in the present study because only conditions close to free convection were considered. This is particularly true for c_{TT1} , which describes the behavior in the neutral limit. From the values of c_{TT1} and c_{TT2} in the present study it follows that $A_{T,\text{LIT2E}} = 3.0$ and $A_{T,\text{HOM}} = 2.8$. This difference between $A_{T,\text{LIT2E}}$ and $A_{T,\text{HOM}}$, though relatively small, indicates that the MOST functions over heterogeneous terrain might indeed differ from those over homogeneous terrain. However, we can assume that heterogeneity effects will be less prominent for near-neutral conditions as surface heterogeneity signals are known to be weakened for increasing wind speed or weak surface fluxes (e.g. Avissar and Schmidt, 1998). The largest effect of surface heterogeneity on the MOST relationships will be present in the free convection limit. This finding is only based on one single case study with a certain surface heterogeneity and amplitude. Moreover, the difference in A_T appears to be rather small (0.2) so that we cannot infer whether such a deviation exists for any kind of given heterogeneous terrain. We will come back to this question later.

Fig. 6 b shows that the dimensionless $\langle C_q^2 \rangle$ does not collapse on a single curve and it is evident that no fitting function f_q exists for the structure parameter of humidity. We must conclude that C_q^2 does not follow MOST at all. This finding can be attributed to the fact that the entrainment flux ratio for case LIT2E was around three (see Maronga and Raasch, 2013). As was shown by Maronga (2013), C_q^2 no longer follows MOST if the entrainment flux ratio is at least one. The entrainment of dry air is then the dominant process that generates humidity fluctuations that are also affecting C_q^2 in the surface layer, in agreement with the assumption of Li et al. (2012). The present study supports this finding so that it is impossible to derive a value for A_q . As a direct consequence, MWS measurements should not be used to derive the surface flux of latent heat when entrainment of dry air becomes too large.

Because the values for $-z/L$ indicated that LFC scaling can be applied (see above), we calculated A_T using LFC scaling (see Eqs. 8 - 9). The results are shown in Fig. 7 and reveal scattered values between 2.6 and 3.25. Generally, we observe more scatter in the data than found in the idealized LES study of Maronga (2013), who used free convective conditions (no geostrophic wind) to obtain A_T^2 . This might be ascribed to

Fig. 5: Vertical profiles of $\langle C_T^2 \rangle$ in the lower boundary layer.Fig. 6: Dimensionless structure parameters (MOST scaling) against stability parameter $-z/L$. **a** shows temperature, complemented by the LES fitting function f_T , and **b** humidity.

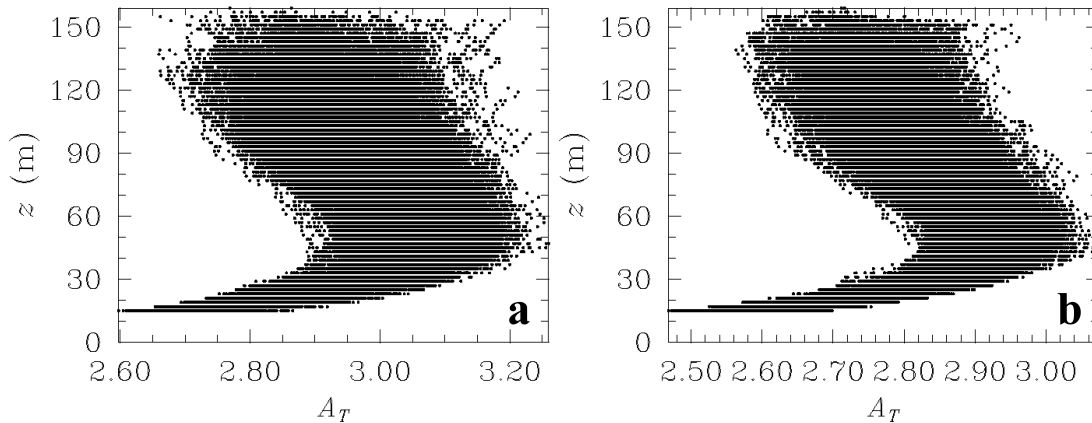


Fig. 7: Dimensionless structure parameter of temperature (LFC scaling) **a** for case LIT2E and **b** for case HOM.

the non-stationarity of the flow due to the diurnal cycle and particularly to the fact that a geostrophic wind is present, which is violating the assumption for LFC scaling that $u_* \rightarrow 0$. Averaging over all data points of the dimensionless $\langle C_T^2 \rangle$ yields $A_{T,\text{LIT2E}} = 3.0 \pm 0.2$ and $A_{T,\text{HOM}} = 2.8 \pm 0.2$ (95% confidence interval) which is in agreement with the predictions by MOST scaling in the free convection limit shown above. These values are slightly higher than the value of 2.7 that is reported from measurements (e.g. Wyngaard et al., 1971b; Wyngaard and LeMone, 1980; Andreas, 1991) and also from the recent LES (Maronga, 2013). For case HOM the difference is only small (0.1) and within the confidence interval (± 0.2). This difference might be related to the fact that perfect free convective conditions are not reached (see above). The difference between cases LIT2E and HOM, even though also small (0.2), are most likely be related to surface heterogeneity effects. We will discuss possible errors that might be induced by this difference and implications for LAS observations over heterogeneous terrain in Section 4.4.

4.3 Blending height

As stated by Beyrich et al. (2012), MOST theoretically should be only applied if a blending height for structure parameters lies somewhere below the scintillometer path. Otherwise, the scintillometer will “see” the fluxes from different surface patches and a footprint analysis must be employed to relate the LAS signal to the surface fluxes of the different surface types (Meijninger et al., 2002b, 2006; Beyrich et al., 2012). Furthermore, in the latter case, MOST is violated which might introduce additional errors. Then, the derived surface fluxes can at best only be regarded as representative for the footprint area of the LAS. The spatial distribution of surface types and thus surface fluxes within this footprint area, however, might be completely different from the area-averaged fluxes.

Sühling and Raasch (2013) introduced a method to explore the blending height in case of a heterogeneous surface heating for two days of the LITFASS-2003 experiment, including May 30 that is object of the present study. They particularly found that high correlations between the surface fluxes and the turbulent fluxes can be still seen even in the entrainment zone. We used their method and calculated the two-dimensional cross-correlation ρ between the spatial surface heat flux distribution and the horizontal cross-sections of

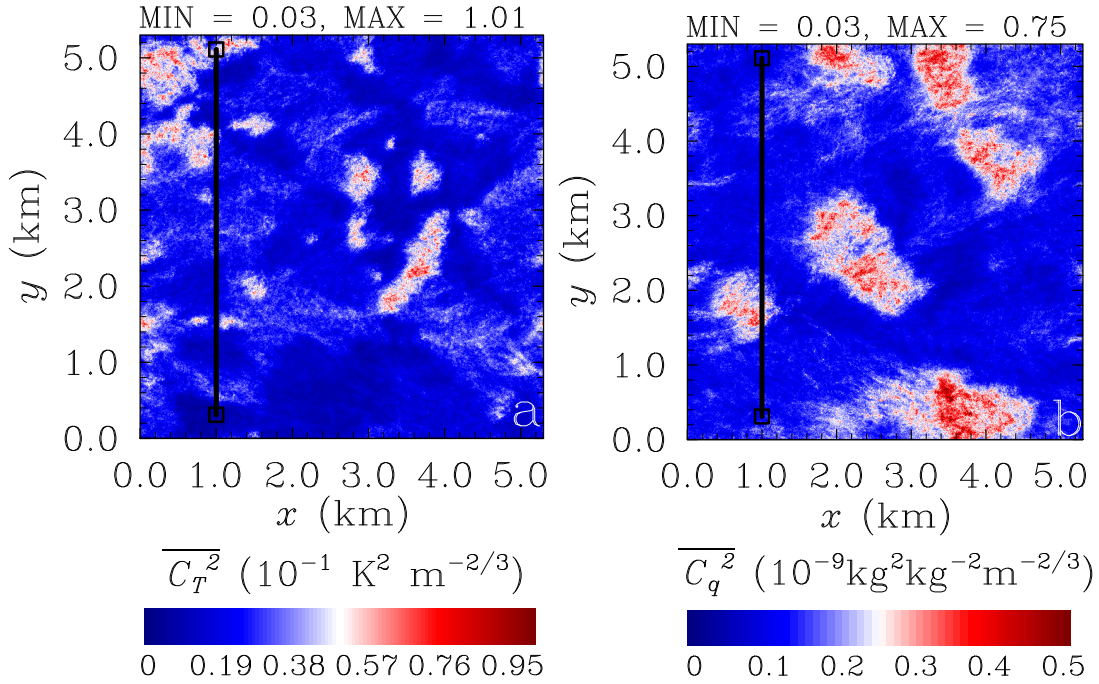


Fig. 8: Horizontal cross-sections of time-averaged (30 min) **a** C_T^2 , **b** C_q^2 at a height level of 43 m at 1100 UTC.

the structure parameters against different spatial lags in x - and y -direction at different height levels. For a detailed description of this method we refer to Sühring and Raasch (2013).

Exemplarily, Fig. 8 shows the horizontal cross-sections of $\overline{C_T^2}$ and $\overline{C_q^2}$ at VLAS height (43 m) at 1100 UTC. The data has been temporally-averaged (indicated by the overbar) over an interval of 30 min so that noise from the randomly-distributed turbulence is significantly reduced. It is obvious that a heterogeneity-induced signal is still visible in both $\overline{C_T^2}$ and $\overline{C_q^2}$ at height of the VLAS, particularly from the patches with the highest surface fluxes of sensible and latent heat, respectively. This was mainly forest with a surface flux of sensible heat of $\approx 470 \text{ W m}^{-2}$ (see Fig. 2 a) and rape with a surface flux of latent heat of $\approx 170 \text{ W m}^{-2}$ (see Fig. 2 b). Comparing Fig. 8 with the land-use map (see Fig. 1 b) reveals that very patches can be easily identified in the horizontal cross-sections of the structure parameters. Horizontal isotropy of turbulence can thus not be assumed, at least at the VLAS height at 1100 UTC. This is supported by the correlation coefficients between $\overline{w'\theta'_0}$ and $\overline{C_T^2}$ (denoted as $\rho_{\overline{w'\theta'_0}, \overline{C_T^2}}$) as well as between $\overline{w'q'_0}$ and $\overline{C_q^2}$ (denoted as $\rho_{\overline{w'q'_0}, \overline{C_q^2}}$). $\rho_{\overline{w'\theta'_0}, \overline{C_T^2}}$ is shown against spatial lag in x - and y - direction in Fig. 9 for three different height levels. Close to the surface the maximum correlation is high with values close to 1 and a spatial lag of 0 m (Fig. 9 a). At a height of 43 m (VLAS) the maximum correlation has decreased to values of 0.65, shifted downstream (in x -direction) to $x = -25$ m. At 200 m height, the maximum decreased to 0.3 and moved further downstream to $x = -150$ m. This vertical skewing of the maximum correlation can be ascribed to the boundary layer wind, that is advecting the heterogeneity signal along the mean wind direction.

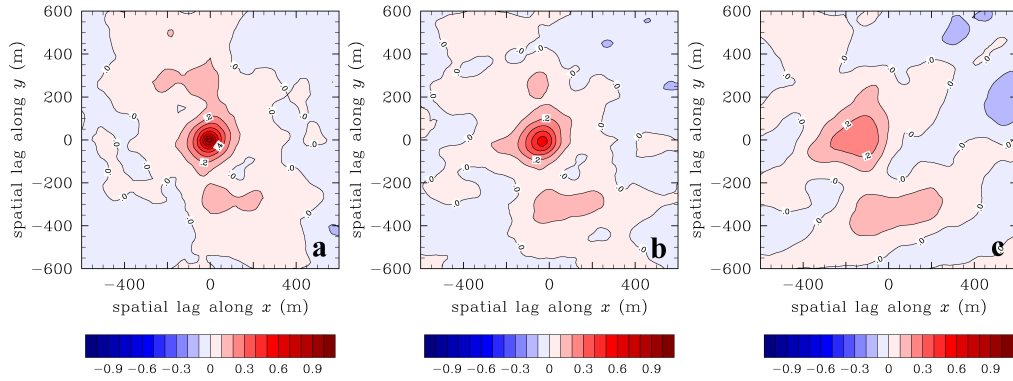


Fig. 9: Correlation coefficients at 11 UTC (30 min average) between $\overline{w'\theta'_0}$ and $\overline{C_T^2}$ at height levels of **a** 5 m, **b** 43 m (height of the VLAS) and **c** 200 m.

Based on this finding we calculated the vertical profiles of the maximum correlation in each horizontal plane (denoted as $(\rho)_{\max}$) for each hour of simulation time. The results are shown in Fig. 10. $(\rho_{\overline{w'\theta'_0}, \overline{C_T^2}})_{\max}$ shows that the $\overline{C_T^2}$ signal is highly correlated to $\overline{w'\theta'_0}$ close to the surface, but that the correlation is decreasing with height down to values between 0.2–0.3 at height levels roughly between 200–600 m (valid for the whole simulated time period). $(\rho_{\overline{w'q'_0}, \overline{C_q^2}})_{\max}$ is rapidly decreasing in the lowest 100 m, presumably due to the dominant entrainment of dry air that is not affected by the surface heterogeneity, but influencing the humidity fluctuations in the surface layer. Both $(\rho_{\overline{w'\theta'_0}, \overline{C_T^2}})_{\max}$ and $(\rho_{\overline{w'q'_0}, \overline{C_q^2}})_{\max}$ show no secondary peak near the entrainment zone, which suggests that heterogeneity signals of the structure parameters do not expand into the upper mixed layer. Sühling and Raasch (2013) found that, even though the correlation between the surface flux of sensible heat and the flux in the mixed layer was low, a high anti-correlation could be observed in the entrainment zone. From the low correlation in the mixed layer found in the present study we can thus not say anything about the existence of a blending height. However, the high correlation in the lowest 100–200 m suggests that the blending height must be considerably higher than the LAS system installed at 43 m during the LITFASS-2003 experiment (Beyrich and Mengelkamp, 2006). If the observed high correlation in the present study is not case-specific, our results can be valid for all common LAS systems that are usually installed at heights < 70 m and usually over moderately heterogeneous terrain (e.g. Kobsiek et al., 2002; Meijninger et al., 2002b; Beyrich et al., 2012). In order to prove that heterogeneity signals have to be considered in LAS observations, $(\rho)_{\max}$ is shown in Fig. 11 at height of the VLAS in the course of the day. It is obvious that the correlation between $\overline{w'\theta'_0}$ and $\overline{C_T^2}$ is around 0.7. Signals from the surface heterogeneity will hence be visible in the VLAS signal all day long. For $\overline{C_q^2}$ the correlation is smaller and fluctuating between 0.2 and 0.6. This might be ascribed to the fact that the surface signal does reach the VLAS height when entrainment events, such as the eroding residual layer during the morning transition (see Section 4.1), penetrate deep into the surface layer and reduce the correlation between $\overline{C_q^2}$ and $\overline{w'q'_0}$ (see decrease in $(\rho_{\overline{w'q'_0}, \overline{C_q^2}})_{\max}$ at 0700 UTC). Under such conditions the $\overline{C_q^2}$ signal is no longer determined by the surface flux of latent heat so that MOST cannot be applied at all, even though the turbulence at measurement height might be regarded as horizontally homogeneous. That explains why it was not possible to determine f_q and A_q (see Section 4.2). This analysis is of course based on a part of the diurnal cycle of a specific day with a specific surface heterogeneity, but we can already say that a blending

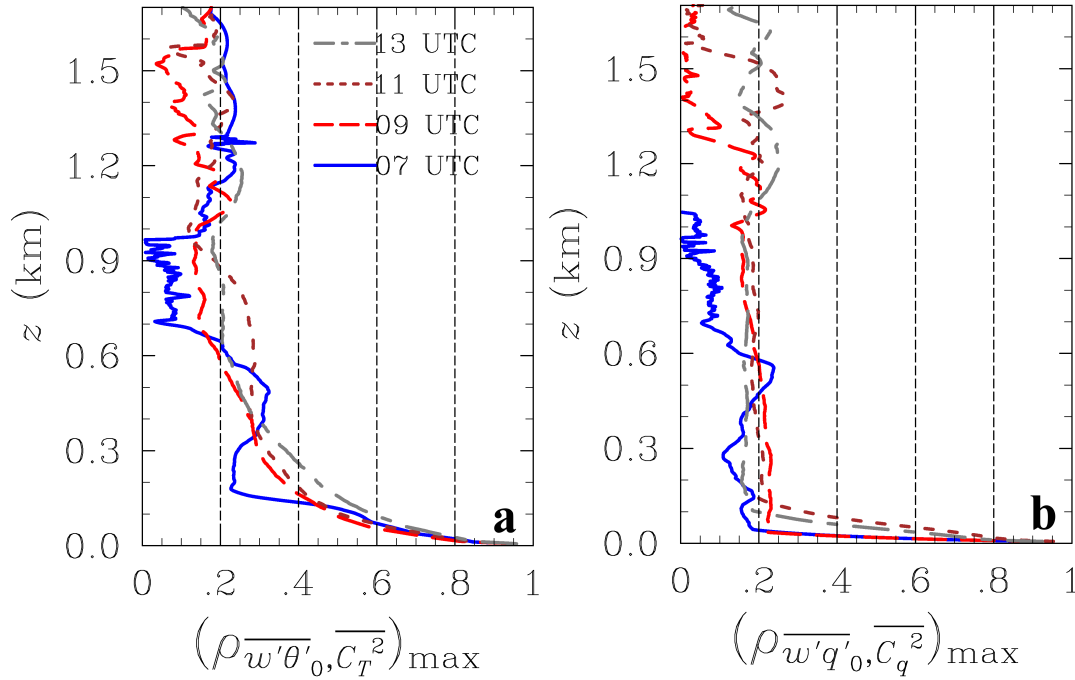


Fig. 10: Vertical profiles of the maximum values of the correlation coefficient in each horizontal cross-section between **a** $\overline{w'\theta'_0}$ and C_T^2 and **b** $\overline{w'q'_0}$ and C_q^2 . The data was averaged in time over an interval of 30 min.

height - if existing at all - will be often located much higher than usual surface layer measurements and that heterogeneity signals thus will affect scintillometer measurements and thus have to be considered in the interpretation of the data.

4.4 Spatial and temporal variability of structure parameters and VLAS measurements

In Sections 4.1 and 4.3 we showed that surface heterogeneity can affect the structure parameters and their similarity relationships. In this section we will discuss the impact for LAS measurements. Fig. 12 shows the time series of $\langle C_T^2 \rangle$ and $\langle C_q^2 \rangle$ at a height of 43 m and thus at height of the VLAS. It appears that $\langle C_T^2 \rangle$ reflects the evolution of $\langle \overline{w'\theta'_0} \rangle$ very well (cf. Fig. 2a). It is thus plausible that MOST might be an appropriate framework for deriving the surface flux of sensible heat from measurements of C_T^2 . Moreover, it is also visible that the value of $\langle C_T^2 \rangle$ is higher for case LIT2E than for case HOM, which is in agreement with the mean profiles shown in Fig. 5. This result suggests that the surface heterogeneity generates additional temperature fluctuations that lead to a higher $\langle C_T^2 \rangle$.

In contrast, $\langle C_q^2 \rangle$ does not back up the temporal development of $\langle \overline{w'q'_0} \rangle$ in the course of the day (cf. Fig. 2b). A strong peak is visible at 0700 UTC that cannot be related to any release event of latent heat at the surface. From a comparison with the temporal development of the CBL height (see also Fig. 4 a) it becomes evident that this peak is related to the erosion of the morning inversion and the subsequent encroachment of the residual layer into the mixed layer. The second peak around 0800 UTC is also related

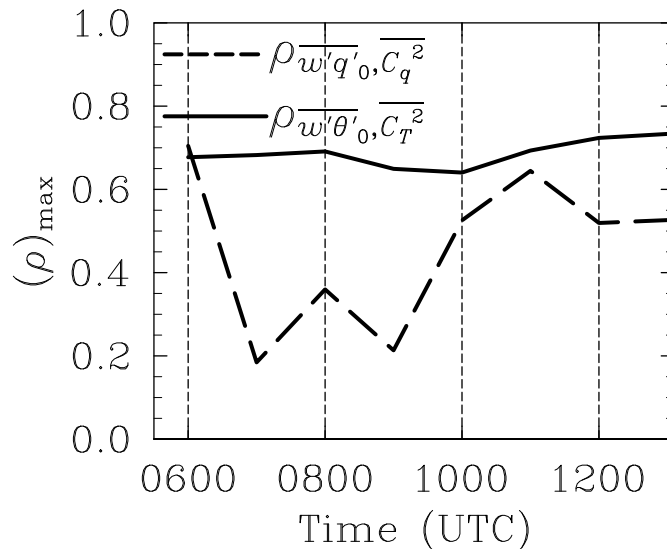


Fig. 11: Time series of the maximum values of the correlation coefficient in the horizontal cross-section at a height of 43 m between **a** $\overline{w'\theta'_0}$ and $\overline{C_T^2}$ and **b** $\overline{w'q'_0}$ and $\overline{C_q^2}$. The data was averaged in time over an interval of 30 min.

to an entrainment event (cf. Fig. 11). This is consistent with the findings in Section 4.2 that $\langle C_q^2 \rangle$ does not follow MOST and that MWS measurements cannot be used for deriving $\langle w'q'_0 \rangle$ when entrainment of dry air is sufficiently high. Effects of surface heterogeneity on $\langle C_q^2 \rangle$ are not prominent, because the dominant entrainment appears to be rather homogeneous and not affected by the heterogeneity (see discussion in Section 4.3).

In order to quantify how surface heterogeneity affects LAS observations, we will now investigate the temporal variability of VLAS observations (denoted by $[C_T^2]$) and the variability of C_T^2 along the VLAS path. As was shown in Fig. 8, surface heterogeneity effects are visible in the temporally-averaged data at height of the VLAS. Fig. 13 a shows the time series of the instantaneous $[C_T^2]$, together with the temporally-averaged VLAS measurements $\overline{[C_T^2]}$, the horizontally and temporally-averaged data $\overline{\langle C_T^2 \rangle}$ and the in situ LAS observations during the LITFASS-2003 experiment (denoted by $\overline{[C_T^2]}_{\text{LAS}}$). The instantaneous $[C_T^2]$ is rapidly varying in time due to the turbulence along the measurement path. In the morning these fluctuations are rather small because turbulence is low. In the course of the day, the turbulence intensifies and hence also the fluctuations in the VLAS signal increase. Case HOM shows a very similar behavior of the instantaneous VLAS signal (Fig. 13 b). Now we applied a temporal average of an interval of 30 min to the VLAS observations, which was the same averaging interval as incorporated in the LAS data. The choice of this interval is also confirmed by the study of Maronga et al. (2013). They showed that (in free convection) the required temporal average to sufficiently remove turbulent fluctuations from the scintillometer signal, is a function of the ratio of the path length to the path height above ground. In the present study this ratio is 112, for which Maronga et al. (2013) suggest an averaging interval of at least 30 min (see their Fig. 11). The averaged data reveals that $\overline{[C_T^2]}$ is converging to the horizontal average $\overline{\langle C_T^2 \rangle}$ fairly well. This seems to be a promising result regarding the determination of the area-averaged fluxes from the VLAS observations. However, differences between $\overline{[C_T^2]}$ and $\overline{\langle C_T^2 \rangle}$ of on average 5% persist. Fig. 13 b gives evidence that this

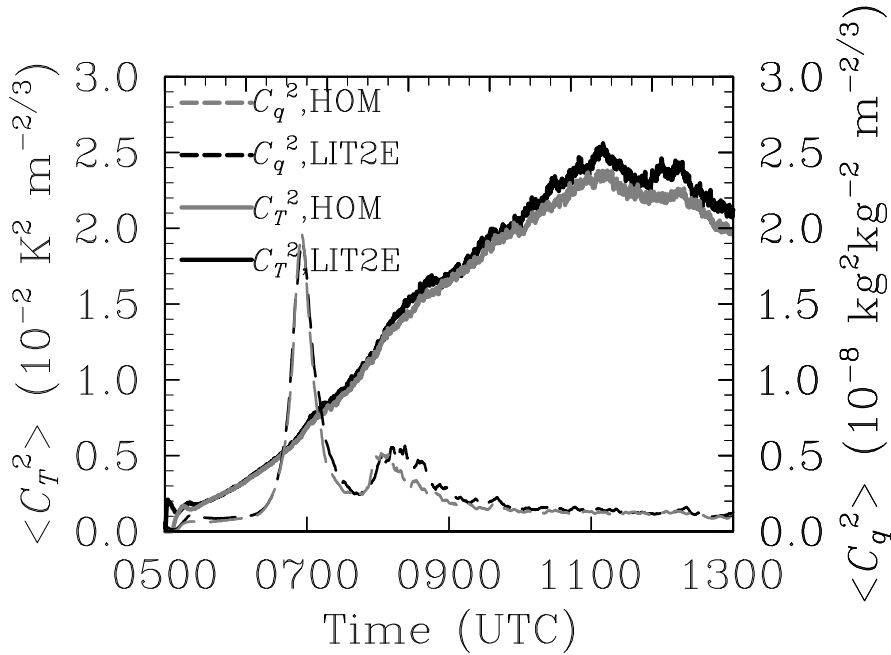


Fig. 12: Time series of **a** $\langle C_T^2 \rangle$ and $\langle C_q^2 \rangle$ at a height level of 43 m.

difference is caused by the surface heterogeneity as no such difference can be observed in case HOM. Here, the time-averaged VLAS measurement is in very good agreement with the time- and area-averaged C_T^2 .

The comparison of $[C_T^2]$ with the LAS data observed during the LITFASS-2003 experiment shows that the diurnal cycle of C_T^2 is captured very well by the LES (see Fig.13 a). Nevertheless it is also visible that the LAS data surprisingly measured a C_T^2 that is about a factor of two lower than the C_T^2 derived from the LES. The surface flux measured by the LAS (using MOST, not shown) was consequently around 200 W m^{-2} around noon, whereas the area-averaged flux in the LES was around 250 W m^{-2} (see Fig. 2a). Meijninger et al. (2006) showed that the LAS data compares well to the aggregated eddy-covariance fluxes. A careful look into the eddy-covariance data unfortunately revealed, that the prescribed surface fluxes in the LES were higher than the measured eddy-covariance fluxes. These wrong forcing data have been used for several years (Uhlenbrock et al., 2004; Maronga and Raasch, 2013; Sühling and Raasch, 2013) and the inconsistency in the data had not been discovered before - mainly because the simulated boundary layers still compared well to observations. As a consequence, the used fluxes in the present study are about 50 W m^{-2} too high, which explains the discrepancy between VLAS and LAS observation. Unfortunately, as stated in Section 3.2, it was not possible to repeat the simulations with corrected surface fluxes. Nevertheless, the other analyses included in this and the former studies should not be significantly affected by these inaccurate fluxes. In the present study this issue restricts only the direct validation of the VLAS measurements with the in situ LAS data.

In order to explore whether time-averaging is an appropriate procedure to quantify surface heterogeneity signal along the VLAS and possibly to relate the local structure parameters to the local surface fluxes, different time-averaging intervals have been applied to the LES data. Fig. 14 shows the variability of C_T^2

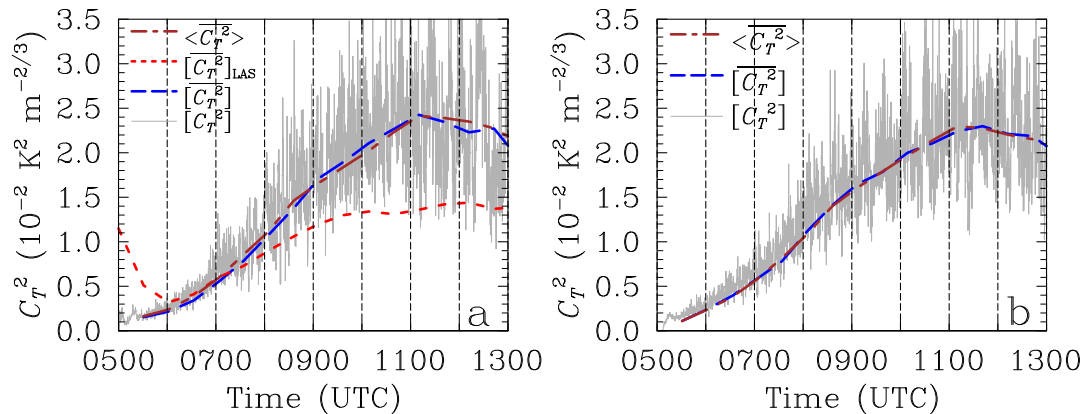


Fig. 13: Time series of C_T^2 derived from VLAS measurements. **a** shows the instantaneous VLAS signal (**gray solid line**) in comparison with the 30 min average (dashed blue line) and the horizontal average of C_T^2 (**brown dot-dashed line**) as well as the in situ LAS observations (**red short dashed line**), **b** is as **a**, but for case HOM.

along the VLAS path exemplarily at 1100 UTC for the instantaneous data as well as for the time-averaged data for averaging intervals of 30 min, 60 min and 120 min. The plots are complemented by the underlying prescribed surface fluxes and the local fluxes that have been derived using MOST and the parameters $c_{TT1} = 6.1$ and $c_{TT2} = 7.6$ as proposed by Maronga (2013). It is visible that the instantaneous signal cannot be related to the surface fluxes and that sufficient averaging is essential (Fig. 14 a). The averaging interval, however, is limited due to changing surface fluxes and state of turbulence in the diurnal cycle. Fig. 14 b shows that the surface heterogeneity is indeed visible in the time-averaged C_T^2 (30 min average). The local surface fluxes derived from MOST give reasonable values, particularly in the vicinity of strongly-heated patches such as forest at the beginning of the path and around 1.5 km (cf. Fig. 8 and Fig. 1b). The comparison of the standard deviation of C_T^2 along the VLAS path between cases LIT2E and HOM ($0.0135 \text{ K m}^{-2/3}$ and $0.0068 \text{ K m}^{-2/3}$, respectively) indicates that half of the variability along the path in case LIT2E is still caused by random noise from turbulence. It will thus be difficult for in situ measurements (such as low-level aircraft flights) to identify the surface heterogeneity that is a priori unknown. Fig. 14 c and d point out that a longer time-averaging interval (60 min and 120 min, respectively) does not improve the statistics. Quite the contrary, the signal from the surface heterogeneity weakens as the surface fluxes change in the diurnal cycle, but half of the variability is still caused by random noise. The assumption by van den Kroonenberg et al. (2012) that they were able to detect a surface heterogeneity signal by means of a very limited ensemble of aircraft flights at different times and different days should be judged with caution.

Our results demonstrate not only that the VLAS measurements are well below the blending height (if existent at all), but also that signals from the local surface fluxes can be seen in the VLAS signal, if an adequate time average (here 30 min) is applied. The local fluxes that have been derived by MOST are then in fairly good agreement with the prescribed surface value. Hence we can assume that MOST might also be a useful framework for deriving local surface fluxes.

A direct comparison between the time-averaged surface fluxes (averaging interval of 30 min) derived from the VLAS observations using MOST and LFC (denoted by $\overline{H}_{\text{MOST}}$ and $\overline{H}_{\text{LFC}}$, respectively) and the respective prescribed fluxes at the surface is given in Fig. 15. For c_{TT1} and c_{TT2} we again used the

The effect of surface heterogeneity on C_T^2 and C_q^2

21

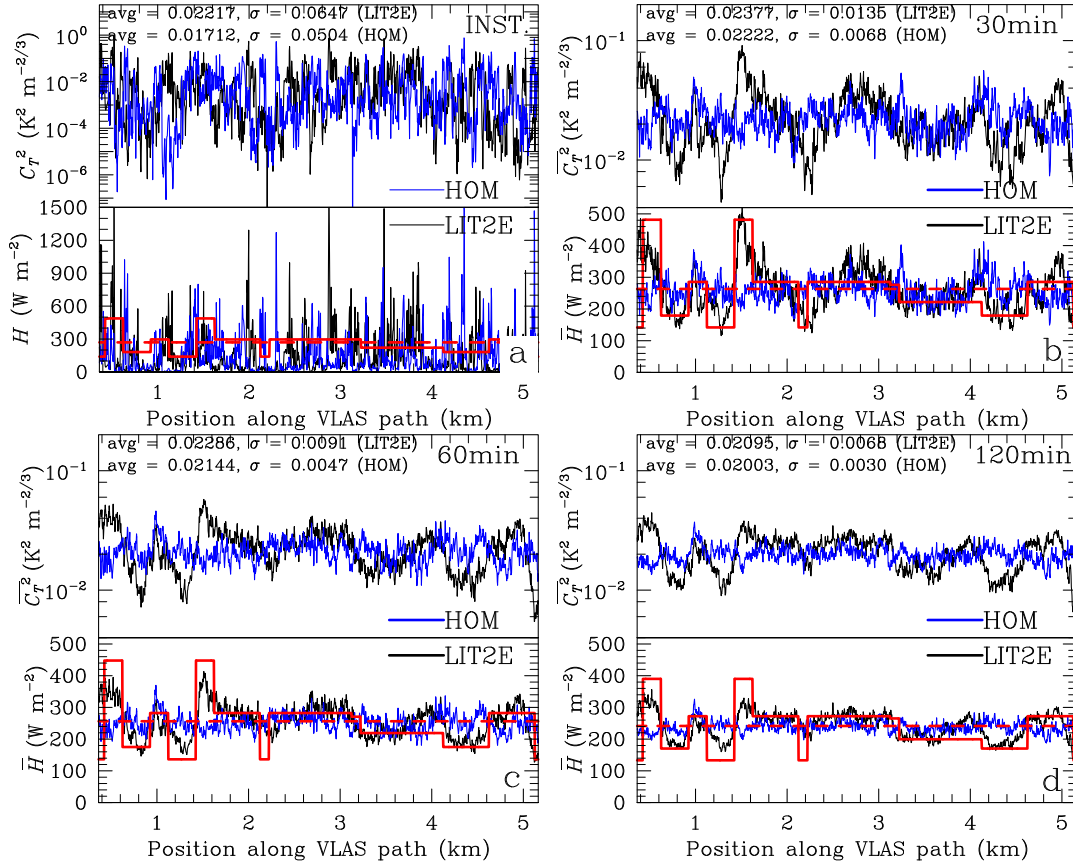


Fig. 14: C_T^2 along the VLAS path at 1100 UTC from case LIT2E (black solid lines, top graphs of each plot) and in comparison with case HOM (blue solid lines). **a** shows the instantaneous signal, whereas **b**, **c** and **d** show time-averaged data with averaging intervals of 30 min, 60 min and 120 min, respectively. The underlying surface fluxes of sensible heat for case LIT2E and case HOM (red solid line and red dashed line, respectively) as well as MOST predictions using the C_T^2 data shown in the top graphs (black solid lines and blue solid lines for cases LIT2E and HOM, respectively) are given in the bottom graphs of each plot. Path averaged values (“avg”) and the standard deviation (σ) along the path are listed in the graphs.

values of 6.1 and 7.6, respectively, as proposed by Maronga (2013). For A_T we used the very common value of 2.7 (e.g. Andreas, 1991; Maronga, 2013). It is visible from Fig. 15 b that for case HOM, $\overline{[H]}_{\text{MOST}}$ is in remarkable agreement with the prescribed values at the surface with a relative error of only 1.2%. This result shows that the derived MOST function for C_T^2 that was proposed by Maronga (2013) does not only apply for quasi-stationary conditions, but also for a diurnal cycle. For $\overline{[H]}_{\text{LFC}}$ a slight overestimation for surface fluxes $> 120 \text{ W m}^{-2}$ is visible so that the relative error is 4.0% (Fig. 15 d). This can be ascribed to the fact that the local free convection is not perfectly reached (due to the geostrophic wind of 2 m s^{-1}) and the fact that LFC is an over-idealization of the surface layer structure (Hill, 1989). Fig. 15 a and c suggest

that the VLAS observations compare well to the area-averaged surface fluxes. However, higher deviations of 2.7 % and 5.5 % for MOST and LFC scaling have to be considered, respectively. This is 1.5 % higher for both MOST and LFC scaling compared to case HOM and must be caused by the surface heterogeneity. Moreover, it is evident that the VLAS-derived fluxes for case LIT2E tend to overestimate the prescribed surface fluxes, particularly when $\overline{\langle H \rangle} > 150 \text{ W m}^{-2}$. This is in agreement with Lagouarde et al. (2002), Meijninger et al. (2002b) and Meijninger et al. (2006) who showed that the non-linearity between structure parameters and surface fluxes (see Section 4.2) lead to a systematic overestimation of the LAS-derived fluxes over heterogeneous terrain.

It should be noted that this good agreement between the VLAS-derived fluxes with the surface fluxes over heterogeneous terrain might be not universal, because it is based on one single case study, and we suppose that this good agreement between VLAS fluxes and area-averaged fluxes in case LIT2E is mainly due to the fact that the footprint of the VLAS is coincidentally representative for the entire area, i.e. the heterogeneity is rather homogeneously distributed in the simulated area. If one would also take into account the western part of the LITFASS area in the simulation that was dominated by forest area, large patches with high surface fluxes of sensible heat would increase the area-averaged flux (see Fig. 1 a, cf. Maronga and Raasch, 2013, , Fig. 2 a). As the footprint for the VLAS would not change and still be located over the farmland area, the area-averaged surface fluxes are then supposed to be highly underestimated by the VLAS. Unfortunately, as argued in Section 3.2, we could not simulate a second case in order approve this hypothesis.

5 Summary

A case study for May 30 of the LITFASS-2003 experiment was conducted using high-resolution LES that actually resolve the surface layer turbulence. The CBL over the heterogeneous LITFASS terrain was simulated from the early morning until early afternoon, using prescribed surface fluxes of sensible and latent heat. The model domain used in this study was much smaller in comparison to previous LES of the LITFASS-2003 area and of size of $5.3 \text{ km} \times 5.3 \text{ km}$, mainly covering by agricultural fields. The data was compared with a homogeneous control run using spatially-averaged surface fluxes. The turbulent structure parameters of temperature and humidity were derived from the simulation data over heterogeneous terrain and compared to data from the homogeneous simulation as well as with in situ LAS data observed during the LITFASS-2003 experiment. Particular attention was given to the spatial distribution of C_T^2 and C_q^2 in the surface layer and their MOST/LFC relationships.

It was found for the heterogeneous simulation that, compared to the homogeneous simulation, the mean C_T^2 and C_q^2 in the surface layer are about 4 % and 12 % higher, respectively. It could be shown that this difference slightly modifies the MOST/LFC relationships for C_T^2 . However, it turned out that the induced error did not exceed 1.5 % for both MOST and LFC scaling and is thus very small. It was also discussed that the VLAS-derived fluxes tend to overestimate the prescribed surface fluxes due to non-linear relationship between structure parameters and fluxes, in agreement with previous scintillometer studies (Lagouarde et al., 2002; Meijninger et al., 2002b, 2006). As in the previous LES study of Maronga (2013) it was found that no MOST/LFC relationships can be obtained for C_q^2 from the LES data as entrainment of dry air at top of the mixed layer was the dominant process generating humidity fluctuations. These fluctuations, in turn, affect the surface layer dynamics in such a way that the surface flux of latent heat is to great extent decoupled from the distribution of C_q^2 in both the heterogeneous and homogeneous simulation.

A correlation analysis using the method introduced by Sührling and Raasch (2013) was used in order to investigate the blending height concept for structure parameters. We could show that the structure parameters in the surface layer exhibit significant signals of the prescribed surface heterogeneity all day long. This finding was more pronounced for C_T^2 as entrainment of dry air was affecting the humidity fluctuations in the surface layer and thus decreased the correlation between the surface flux of latent heat

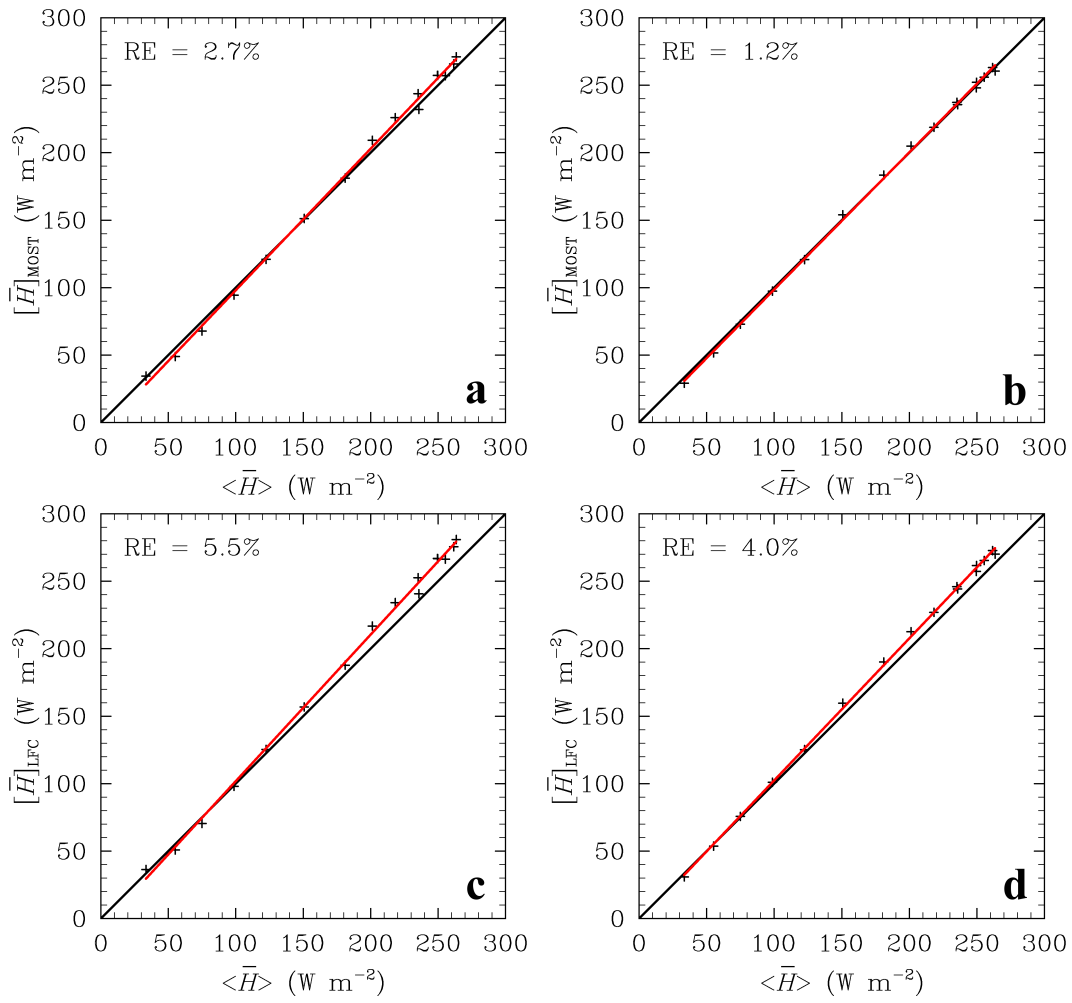


Fig. 15: Surface flux of sensible heat derived from the time-averaged (30 min) VLAS measurements (denoted as $[\overline{H}]$) against the prescribed values at the surface (horizontal average). **a** shows the results using MOST scaling for case LIT2E, **b** using MOST scaling for case HOM, **c** using LFC scaling for case LIT2E and **d** using LFC scaling for case HOM. The relative error of the VLAS measurement in relation to $\langle \overline{H} \rangle$ is listed in the graphs.

and C_T^2 . Consequently, horizontal homogeneity of turbulence as required by MOST cannot generally be expected, at least under synoptic conditions of weak geostrophic winds and high surface fluxes. As a result we conclude that, under such conditions, LAS observations will not be representative for an area of several square kilometers (in the order of NWP grid boxes, e.g. 100 km²), but rather for their local footprint area of very limited size (here in the order of 5 km²). As this footprint might be composed of different surface patches with differing surface properties, including fluxes of sensible and latent heat, the obtained surface flux from an LAS system does not necessarily have to be representative for a larger area. Our findings are of course based on a single case where the LAS footprint was much smaller than under synoptic conditions with higher geostrophic winds and lower buoyant forcing at the surface.

VLAS measurements in the LES were used along a 4.8 km long path, in agreement with the LAS setup during LITFASS-2003. A direct comparison showed, however, that the VLAS measurements did overestimate the path-weighted C_T^2 as observed by the LAS. A revision of the prescribed surface flux data revealed that the data that have been used for several LES studies for the LITFASS-2003 experiment (Uhlenbrock et al., 2004; Maronga and Raasch, 2013; Sühling and Raasch, 2013) were too high in comparison with the measured eddy covariance data. Unfortunately this inconsistency had not been noticed before. However, it was also stated that this fact merely affected the direct evaluation of the VLAS with the LAS and that the conducted simulations were so computational expensive that they could not be repeated with corrected surface flux data.

Moreover, we employed the VLAS measurements in order to investigate the effect of surface heterogeneity on LAS observations. It was found that sufficient time-averaging is required (here 30 min, as suggested by Maronga et al. (2013)) to obtain representative fluxes and that signals of the underlying surface heterogeneity affect the VLAS observations. Whereas the VLAS measurement converged to the area-averaged value over homogeneous terrain, the VLAS observation in the heterogeneous simulation were found to retain rather local character and showed a mean deviation of 5 % from the area-average. Due to the fact that the surface fluxes changed in the course of the day so that no stationary conditions were reached in the simulation, the averaging interval was limited. Therefore, noise from the turbulence along the path made up 50 % of the variability of C_T^2 along the VLAS path. This shows that it will be quite difficult for in situ measurements, such as low level aircraft flights, to capture and quantify effects of the surface heterogeneity in the C_T^2 signal.

Even though the blending height analysis clearly suggested that the VLAS measurement cannot be considered to yield representative estimates of the area-averaged surface flux of sensible heat, it would be necessary to perform a more sophisticated footprint analysis for the LES to approve that the VLAS “sees” only the surface fluxes in its footprint area. Moreover, it would be worthwhile to include the western part of the LITFASS area that was dominated by forest patches so that the area-averaged surface flux deviates significantly from the average flux over the farmland area simulated in the present study. Both will be part of our future research. In a follow up study we will employ a Lagrangian footprint model, embedded into the LES (see Steinfeld et al., 2008), over the heterogeneous LITFASS-2003 terrain in order to determine more elaborated footprints that take into account the surface heterogeneity. Moreover, more idealized simulations with different synoptic conditions (higher geostrophic wind and lower surface fluxes) or a different spatial distribution of the surface heterogeneity could evaluate whether the violation of MOST has a generally minor effect on LAS-derived surface fluxes like it was observed in the present case study.

Acknowledgements This study was supported by the German Research Foundation (DFG) under grants RA 617/20-1 and RA 617/20-3. All simulations were performed on the SGI Altix ICE at The North-German Supercomputing Alliance (HLRN), Hannover/Berlin. NCL² has been used for data analysis and visualization.

² The NCAR Command Language (Version 5.2.1) [Software]. (2010). Boulder, Colorado: UCAR/NCAR/CISL/VETS. <http://dx.doi.org/10.5065/D6WD3XH5>

References

- Andreas EL (1988) Estimating C_n^2 over snow and sea ice from meteorological data. *J Opt Soc Amer* 5:481–495
- Andreas EL (1991) Using scintillation at two wavelengths to measure path-averaged heat fluxes in free convection. *Boundary-Layer Meteorol* 54:167–182
- Avissar R, Schmidt T (1998) An evaluation of the scale at which ground-surface heat flux patchiness affects the convective boundary layer using large-eddy simulations. *J Atmos Sci* 55:2666–2689
- Bange J, Spieß T, et al (2006) Turbulent fluxes from helipod flights above quasi-homogeneous patches within the litfass area. *Boundary-Layer Meteorol* 121:127–151
- Beyrich F, Mengelkamp HT (2006) Evaporation over a heterogeneous land surface: EVA_GRIPS and the LITFASS-2003 experiment: An overview. *Boundary-Layer Meteorol* 121:5–32
- Beyrich F, Leps RDKJP, Lüdi A, Meijninger WML, Weisensee U (2005) Structure parameters for temperature and humidity from simultaneous eddy-covariance and scintillometer measurements. *Meteorol Zeitschrift* 14:641–649
- Beyrich F, Leps JP, et al (2006a) Area-averaged surface fluxes over the LITFASS region based on eddy-covariance measurements. *Boundary-Layer Meteorol* 121:33–65
- Beyrich F, Bange J, Hartogensis OK, Raasch S, Braam M, van Dinther D, Gräf D, van Kesteren B, van den Kroonenberg AC, Maronga B, Martin S, Moene AF (2012) Towards a validation of scintillometer measurements: The LITFASS-2009 experiment. *Boundary-Layer Meteorol* 144:83–112
- Blackadar AK (1997) *Turbulence and Diffusion in the Atmosphere*. Springer, Berlin, Heidelberg, New York
- Braam M, Bosveld FC, Moene AF (2012) On the monin-obukhov scaling in and above the atmospheric surface layer: The complexities of elevated scintillometer measurements. *Boundary-Layer Meteorol* 144:157–177, DOI 10.1007/s10546-012-9716-7
- Brasseur JG, Wei T (2010) Designing large-eddy simulation of the turbulent boundary layer to capture law-of-the-wall scaling. *Phys Fluids* 22, 021303
- Cheinet S, Cumin P (2011) Local structure parameters of temperature and humidity in the entrainment-drying convective boundary layer: A large-eddy simulation analysis. *J Appl Meteorol* 50:472–481
- Cheinet S, Siebesma AP (2007) The impact of boundary layer turbulence on optical propagation. In: *Proc. SPIE 6747, Optics in Atmospheric Propagation and Adaptive Systems X*, Florence, Italy, p 67470A, DOI 10.1117/12.741433
- Cheinet S, Siebesma AP (2009) Variability of Local Structure Parameters in the Convective Boundary Layer. *J Atmos Sci* 66:1002–1017
- De Bruin HAR, Kohsiek W, VanDenHurk BJJM (1993) A verification of some methods to determine the fluxes of momentum, sensible heat and water vapour using standard deviation and structure parameter of scalar meteorological quantities. *Boundary-Layer Meteorol* 63:231–257
- De Bruin HAR, Van den Hurk BJJM, Kohsiek W (1995) The scintillation method tested over a dry vineyard area. *Boundary-Layer Meteorol* 76:25–40
- Deardorff JW (1980) Stratocumulus-capped mixed layers derived from a three-dimensional model. *Boundary-Layer Meteorol* 18:495–527
- Druilhet A, Frangi JP, Guedalia D, Fonton J (1983) Experimental studies of the turbulence structure parameters of the convective boundary layer. *J Clim Appl Meteorol* 22:594–608
- Evans JG, McNeil DD, Finch JW, Murray T, Harding RJ, Ward HC, Verhoef A (2012) Determination of turbulent heat fluxes using a large aperture scintillometer over undulating mixed agricultural terrain. *Agric For Meteorol* 166-167:221–233, DOI 10.1016/j.agrformet.2012.07.010
- Hill RJ (1978) Spectra of Fluctuations in Refractivity, Humidity, and the Temperature-Humidity Cospectrum in the Inertial and Dissipation Range. *Radio Sci* 13:953–961
- Hill RJ (1989) Implications of Monin-Obukhov Similarity Theory for Scalar Quantities. *J Atmos Sci* 46:2236–2244
- Hill RJ, Ochs GR, Wilson JJ (1992) Measuring surface-layer fluxes of heat and momentum using optical scintillation. *Boundary-Layer Meteorol* 58:391–408
- Kaimal JC, Wyngaard JC, Haugen DA, Coté OR, Izumi Y, Caughey SJ, Readings CJ (1976) Turbulence structure in the convective boundary layer. *J Atmos Sci* 33:2152–2169
- Khanna S, Brasseur JG (1997) Analysis of Monin-Obukhov similarity from large-eddy simulations. *J Fluid Mech* 345:251–286
- Kohsiek W, Herben M (1983) Evaporation derived from optical and radiowave scintillation. *Appl Opt* 22:2566–2570
- Kohsiek W, Meijninger WML, Moene AF, Heusinkveld BG, Hartogensis OK, Hillen WCAM, De Bruin HAR (2002) An extra large aperture scintillometer for long range applications. *Boundary-Layer Meteorol* 105:119–127
- Kormann R, Meixner FX (2001) An analytical footprint model for non-neutral stratification. *Boundary-Layer Meteorol* 99:207–224
- Kunkel KE, Walters DL, Ely GA (1981) Behavior of the Temperature Structure Parameter in a Desert Basin. *J Appl Meteorol* 20:130–136
- Lagouarde JP, Bonnefond JM, Kerr YH, McAnaney KJ, Irvine M (2002) Integrated sensible heat flux measurements of a two-surface composite landscape using scintillometry. *Boundary-Layer Meteorol* 105:5–35

- Lee X, Massman W, Law B (2004) Handbook of micrometeorology. Kluwer Academic Publishers, Dordrecht
- Li D, Bou-Zeid E, De Bruin HAR (2012) Monin-Obukhov Similarity Functions for the Structure Parameters of Temperature and Humidity. *Boundary-Layer Meteorol* 145:45–67, DOI 10.1007/s10546-011-9660-y
- Lüdi A, Beyrich F, Matzler C (2005) Determination of the turbulent temperature-humidity correlation from scintillometric measurements. *Boundary-Layer Meteorol* 117:525–550
- Mahrt L (2000) Surface heterogeneity and vertical structure of the boundary layer. *Boundary-Layer Meteorol* 96:33–62
- Maronga B (2013) Monin-Obukhov similarity functions for the structure parameters of temperature and humidity in the unstable surface layer: results from high-resolution large-eddy simulations. *J Atmos Sci* DOI 10.1175/JAS-D-13-0135.1
- Maronga B, Raasch S (2013) Large-Eddy Simulations of Surface Heterogeneity Effects on the Convective Boundary Layer During the LITFASS-2003 Experiment. *Boundary-Layer Meteorol* 146:17–44, DOI 10.1007/s10546-012-9748-z
- Maronga B, Moene AF, van Dinter D, Raasch S, Bosveld FC, Gioli B (2013) Derivation of Structure Parameters of Temperature and Humidity in the Convective Boundary Layer from Large-Eddy Simulations and Implications for the Interpretation of Scintillometer Observations. *Boundary-Layer Meteorol* DOI 10.1007/s10546-013-9801-6
- Meijninger WML, Green AE, Hartogensis OK, Kohsiek W, Hoedjes JCB, Zuurbier RM, De Bruin HAR (2002a) Determination of area-averaged water vapour fluxes with large aperture and radio wave scintillometers over a heterogeneous surface - Flevoland field experiment. *Boundary-Layer Meteorol* 105:63–83
- Meijninger WML, Hartogensis OK, Kohsiek W, Hoedjes JCB, Zuurbier RM, De Bruin HAR (2002b) Determination of area-averaged sensible heat fluxes with a large aperture scintillometer over a heterogeneous surface - Flevoland field experiment. *Boundary-Layer Meteorol* 105:37–62
- Meijninger WML, Beyrich F, Lüdi A, Kohsiek W, De Bruin HAR (2006) Scintillometer-based turbulent fluxes of sensible and latent heat over a heterogeneous land surface - A contribution to LITFASS-2003. *Boundary-Layer Meteorol* 121:89–110
- Muschinski A, Frehlich R, Balsley BB (2004) Small-scale and large-scale intermittency in the nocturnal boundary layer and the residual layer. *J Fluid Mech* 515:319–351
- Obukhov AM (1946) Turbulence in an atmosphere with a non-uniform temperature. *Tr Inst Teor Geofiz Akad Nauk SSSR* 1:95–115, translation in: *Boundary-Layer Meteorol.*, 1971, 2, 7–29
- Peltier LJ, Wyngaard JC (1995) Structure-Function Parameters in the Convective Boundary Layer from Large-Eddy Simulations. *J Atmos Sci* 52:3641–3660
- Petenko IV, Shurygin EA (1999) A two-regime model for the probability density function of the temperature structure parameter in the convective boundary layer. *Boundary-Layer Meteorol* 93:381–394
- Raasch S, Franke T (2011) Structure and formation of dust-devil-like vortices in the atmospheric boundary layer - A high resolution numerical study. *J Geophys Res* 116, DOI 10.1029/2011JD016010, D16120
- Raasch S, Harbusch G (2001) An analysis of secondary circulations and their effects caused by small-scale surface inhomogeneities using large-eddy simulation. *Boundary-Layer Meteorol* 101:31–59
- Raasch S, Schröter M (2001) Palm - a large-eddy simulation model performing on massively parallel computers. *Meteorol Z* 10:363–372
- Riechermann T, Noh Y, Raasch S (2012) A new method for large-eddy simulations of clouds with Lagrangian droplets including the effects of turbulent collision. *New J Phys* 14, DOI 10.1088/1367-2630/14/6/065008, 065008
- Shen S, Leclerc MY (1995) How large must surface inhomogeneities be before they influence the convective boundary layer structure? A case study. *QJR Meteorol Soc* 121:1209–1228
- Shuttleworth W, Yang ZL, Arain MA (1997) Aggregation rules for surface parameters in global models. *Hydrol Earth Syst Sci* 1:217–226
- Sreenivasan KR (1996) The passive scalar spectrum and the Obukhov-Corrsin constant. *Phys Fluids* 8:189–196
- Steinfeld G, Raasch S, Markkanen T (2008) Footprints in homogeneously and heterogeneously driven boundary layers derived from a Lagrangian stochastic particle model embedded into large-eddy simulation. *Boundary-Layer Meteorol* 129:225–248
- Sühring M, Raasch S (2013) Heterogeneity-induced heat flux patterns in the convective boundary layer: Can they be detected from observations and is there a blending height? - A large-eddy simulation study for the LITFASS-2003 experiment. *Boundary-Layer Meteorol* DOI 10.1007/s10546-013-9822-1
- Tatarskii VI (1971) The Effects of the Turbulent Atmosphere on Wave Propagation. Kefer Press, Jerusalem
- Thiermann V, Grassl H (1992) The measurement of turbulent surface-layer fluxes by use of bichromatic scintillation. *Boundary-Layer Meteorol* 58:367–389
- Uhlenbrock J, Raasch S, Hennemuth B, Zittel P, Meijninger WML (2004) Effects of land surface heterogeneities on the boundary layer structure and turbulence during LITFASS-2003: Large-eddy simulations in comparison with turbulence measurements. In: 6th Symposium on Boundary Layers and Turbulence, Am Meteorol Soc, Portland (Maine), paper 9.3
- van den Kroonenberg AC, Martin S, Beyrich F, Bange J (2012) Spatially-Averaged Temperature Structure Parameter Over a Heterogeneous Surface Measured by an Unmanned Aerial Vehicle. *Boundary-Layer Meteorol* 142:55–77
- Wesely ML (1976) A Comparison of Two Optical Methods for Measuring Line Averages of Thermal Exchanges Above Warm Water Surfaces. *J Appl Meteorol* 15:1177–1188

- Wicker LJ, Skamarock WC (2002) Time-splitting methods for elastic models using forward time schemes. *Mon Wea Rev* 130:2088–2097
- Wieringa J (1976) An Objective Exposure Correction Method for Average Wind Speeds Measured at a Sheltered Location. *Quart J Roy Meteorol Soc* 102:241–253
- Williamson JH (1980) Low-storage Runge-Kutta schemes. *J Comp Phys* 35:48–56, DOI 10.1016/0021-9991(80)90033-9
- Wilson C, Fedorovich E (2012) Direct evaluation of refractive-index structure functions from large-eddy simulation output for atmospheric convective boundary layers. *Acta Geophys* 60:1474–1492
- Wyngaard JC, LeMone MA (1980) Behavior of the Refractive Index Structure Parameter in the Entraining Convective Boundary Layer. *J Atmos Sci* 37:1573–1585
- Wyngaard JC, Coté OR, Izumi Y (1971a) Local Free Convection, Similarity, and the Budgets of Shear Stress and Heat Flux. *J Atmos Sci* 28:1171–1182
- Wyngaard JC, Izumi Y, Collins SAJ (1971b) Behavior of the refractive-index-structure parameter near the ground. *J Opt Soc Am* 61:1646–1650

4 Summary and outlook

Large-eddy simulations have been conducted in order to study the turbulence in the atmospheric boundary layer. The main focus of this study was to quantify the effect of surface heterogeneity on the convective boundary layer and the structure parameters of temperature and humidity in general, and particularly to study possible implications for scintillometer observations. However, first of all simulations using a horizontal homogeneous surface have been performed. This was done in order to validate different methods to derive the structure parameters from LES data and to study general features of these structure parameters.

First of all, the turbulent structure parameters of temperature and humidity were investigated by means of LES of the homogeneously-heated CBL. Two high-resolution simulations of the morning and afternoon CBL, driven by airborne and surface measurements at Cabauw (The Netherlands), were performed. Three different methods, based on the Fourier spectrum of turbulence, a method based on local dissipation rates and a new method based on the local estimate of the Fourier spectrum using wavelet analysis were used to obtain vertical profiles of the structure parameters from LES data. It was found that the methods based on the power spectral density in the inertial subrange from Fourier spectra and wavelet analysis compare very well with the proposed semi-empirical profiles after Kaimal et al. (1976) and Fairall (1987). The derivation of local estimates of the structure parameters by means of the method based on wavelets, however, turned out to be rather problematic as it required enormous computing time. Moreover, C_T^2 and C_q^2 from aircraft observations and LAS measurements at Cabauw were derived. The LES estimates of C_T^2 were in very good agreement with the LAS observations. The LES data compared well for C_q^2 with the aircraft observations, but C_T^2 from the aircraft data did not show the proposed decrease with height, for which no satisfying explanation could be found. It can possibly be ascribed to wind shear or temperature variance production by a mesoscale gradient in advected scalar fields (Kimmel et al., 2002), which was not considered in the LES. However, to the author's present knowledge this is the first study that evaluated structure parameters from LES directly with scintillometer and aircraft observations.

Local structure parameters were derived by means of a method based on local dissipation from the LES data. The characteristics of these local structure parameters were in agreement with recent LES of Cheinet and Siebesma (2009) and Cheinet and Cumin (2011) and reflect the structure of turbulence well. This was shown by means of probability density functions that supported the two-regime model, developed by Petenko and Shurygin (1999) based on SODAR measurements. Moreover, both dissipation and wavelet method displayed the same cellular pattern of high and low turbulence in the surface layer. However, a gap in the magnitude between the structure parameters from spectral and dissipation method was observed. It can be ascribed to a combined effect of the approximation of the local gradients of temperature and humidity by means of central difference and additional numerical dissipation of the 5th-order scheme after Wicker and Skamarock (2002). Central differencing in space implies an underestimation of local scalar gradients that makes up 50 % of the observed gap in the structure parameters. A comparison of the vertical profiles from simulations with the 5th-order advection scheme and the 2nd-order scheme of Piacsek and Williams (1970), which does not suffer from numerical dissipation, showed that the remaining underestimation of the structure parameter vanished in the absence of numerical

dissipation.

Horizontal virtual path measurements of C_T^2 at different heights were used in order to explore the spatial and temporal variability along an aircraft flight leg or LAS path. The representativeness of path measurements for a horizontal area was studied using the statistical uncertainty due to the randomly distributed convection. It was found that fluctuations of C_T^2 in time and space along a given path lead to a high variability of the path-averaged virtual measurements, which can affect LAS and aircraft observations. This estimated uncertainty increased with height up to the middle of the mixed layer.

The statistical uncertainty which resulted from this variability depended on the path length, the height above ground as well as the temporal averaging interval. The required spatial averaging in the surface layer was hence found to depend on the ratio of path length to height above ground. For LAS this ratio is a constant and the time-averaging must thus be chosen in an appropriate way. For the LAS which is installed at Cabauw at a height of 41 m above ground (Kohsiek et al., 2002), it is found that the path length of 9.8 km is sufficient to obtain representative measurements for the fairly homogeneous area with a statistical uncertainty $\leq 10\%$. For other LAS, which cover a shorter path (e.g. at Lindenberg, Germany, see Meijninger et al., 2006), a longer time-averaging interval is required to reduce the statistical uncertainty below 10%. This study points out that for a daytime CBL an averaging-interval of up to 1 h might be necessary for LAS measurements, depending on LAS beam height and path length. Such long averaging-intervals are strictly limited by changes in the surface fluxes in the diurnal cycle. Consequently, a higher statistical uncertainty has to be considered, if sufficient averaging is not possible. For aircraft measurements, where a temporal averaging is not feasible, it is found that the statistical uncertainty is higher than for LAS and can reach the order of 25% for a path length of 10 km, depending on the height above ground. In order to derive the surface sensible heat flux from C_T^2 by means of MOST (see the study described in Section 3.2), the height of the LAS must be within the surface layer. It is evident that for shallow CBLs (e.g. in the morning hours), the LAS might not be well within the surface layer so that the scintillation method might fail to give reliable estimates of the surface fluxes.

Based on these results the MOST relationships for structure parameters in the unstable atmospheric surface layer have been investigated using a set of idealized LES. Due to a grid resolution of 2–4 m and today's computing capacities it was possible to actually resolve the surface layer for this set of LES, covering convective to near-neutral boundary layers. This was necessary to cover all relevant stability ranges that are commonly expressed in terms of the parameter $-z/L$. The LES results showed that the flow within the lowest grid levels of the LES should be generally interpreted carefully, because effects of the SGS model are present and the turbulent flow is not well-resolved. The analysis of the MOST relationships showed that the dimensionless structure parameters of temperature and humidity strictly follow functions (f_T and f_q) that only depend on $-z/L$, as proposed by theory and previous experimental data. Only little scatter in the LES data was found so that MOST fitting functions, linking the structure parameters to the kinematic surface fluxes of heat and moisture, were derived for the first time from LES data. While there is lack of explicit fitting functions for C_q^2 in literature, the fitting function for C_T^2 was found to be well within the range of the previously suggested similarity functions from measurement data. It could be shown that increasing (decreasing) the measurement height z had the same effect as decreasing (increasing) L . The LES results strongly suggest that C_T^2 follows MOST and that f_T is a universal function. However, for C_q^2 it is found that MOST relationships are only valid if entrainment at the top of the mixed layer is sufficiently small (here if the absolute value of the entrainment flux ratio < 0.6). In this case it holds that $f_T \approx f_q$. For an entrainment flux ratio of 1, dry air that is entrained into the mixed-layer can also affect the surface layer structure. Consequently, C_q^2 no longer follows MOST and f_q cannot be considered to be a universal function. However, a more extensive sensitivity study would be required to define critical values of the entrainment flux ratio. In the free

convection limit, where LFC scaling is applicable, the dimensionless structure parameters reduce to constants A_T and A_q . The common value of 2.7 for A_T was reproduced by the LES model, with scatter of 5 % in the data. If entrainment is sufficiently small, A_q is found to be around 2.8, so that the assumption $A_T = A_q$ is roughly valid. Otherwise no universal value for A_q can be derived. The scatter was mostly related to a height-dependence of A_T with an overshoot at a height of 40 m. Possible reasons for this overshoot might be the fact that similarity theory is an over-idealization of the surface layer dynamics (Hill, 1989) or local shear-production by the turbulence near the surface so that LFC is not perfectly valid near the surface. On the one hand, it thus appears to be a logical approach to place measurement instruments (e.g. scintillometers) as high as possible in order to approach the free convection limit. On the other hand, this would increase the size of the footprint of the measurement. An error analysis showed that LFC scaling can be applied even for moderate wind conditions (with $-1/L < 0.17$ m) without introducing a systematical error of more than 5 % and scatter of more than 10 % (95 % confidence interval).

Neglecting the contribution of humidity on the buoyancy flux (and hence on L and w_{LF}) was found to result in dimensionless structure parameters that can no longer be expressed in terms of universal functions or constants. Using the formulation for dry air is thus a rather questionable approach and limited to sufficiently dry conditions. It could be shown that the kinematic surface flux of heat is systematically underestimated when humidity is significant. At least an estimate of the surface Bowen ratio is required to account for the effect of humidity on buoyancy when using LFC scaling.

All these analyses have been performed for a horizontally homogeneous surface. In contrast, natural landscapes are rarely homogeneous and surface heterogeneities such as forest and water areas, or different agricultural fields are a frequent feature (e.g. in Central Europe). Previous studies have shown that such surface heterogeneities can affect the CBL significantly, leading to secondary circulations and horizontal anisotropy of turbulence. Under such conditions the application of scintillometers is questionable as MOST requires horizontal homogeneity of turbulence. Moreover, heterogeneity-induced circulations might affect micro-meteorological measurements.

The CBL over a complex irregular surface heterogeneity was thus investigated using LES. The heterogeneity was observed during the LITFASS-2003 experiment. The focus of this study was on secondary circulations and their impact of the CBL development during daytime in the LITFASS area of size of $20 \text{ km} \times 20 \text{ km}$. Four cases with varying background wind speeds between 2 and 6 m s^{-1} were simulated with LES (grid spacing of 50 – 100 m) from the early morning until the evening transition. The simulations were initialized and validated with temperature and humidity profiles observed from radiosonde measurements during LITFASS-2003. Heterogeneous and time-dependent surface fluxes of sensible and latent heat were prescribed at the bottom boundary of the model. The simulated CBL showed boundary-layer depths between 2.2 km and 3.1 km. A method was introduced, in analogy to former studies, to separate the heterogeneity-induced secondary circulations from the randomly distributed thermal convection. In this way it was possible to derive the secondary circulation patterns. These patterns varied between complex local structures in case of a weak background wind speed of 2 m s^{-1} that could be linked to the underlying surface heterogeneity, and more simple roll-like structures that occurred for higher wind speeds. For the latter case, a correlation analysis proved that the flow “feels” only the mean surface heat-flux patterns that derive from the original patterns by averaging them in streamwise direction. Because these patterns are usually aligned to the direction of the mean flow, they generate the roll-like secondary circulation patterns. The observed secondary circulations during the LITFASS simulations spanned the entire CBL and were superimposed on the randomly distributed convection. The circulation strength was found to be typically an order of magnitude smaller than turbulence of the primary circulation. The temporal development of the secondary circulation patterns showed that the heterogeneity scales, which affect the CBL, changed in time and smaller scales became

less important with increasing z_i . This resulted in a broadening of the secondary circulations in the course of the day and was associated with the dependency of secondary circulations on the ratio of the heterogeneity scale λ/z_i , which is well-known from many idealized studies (e.g. Shen and Leclerc, 1995). This study could show that this relationship also holds for irregular surface heterogeneities, where a whole range of scales are superimposed on each other. The eastern part of the LITFASS area was dominated by farmland and displayed small heterogeneity scales and weak heat-flux amplitudes, so that no secondary circulations were observed in this area.

The area-averaged vertical fluxes of sensible and latent heat showed that the secondary circulations partly take over the vertical transport in the mixed layer. The turbulent transport was thus decreased. The total transport of sensible heat was found not to be modified, whereas the total flux of latent heat displayed a heterogeneous response to secondary circulations. This modification led to either increased or decreased total fluxes of latent heat which is possibly ascribed to an effect of the surface heterogeneity on the entrainment at top of the mixed layer. The relative contribution of secondary circulations in the surface layer, however, was small. Micro-meteorological measurements in the surface layer (such as scintillometers) will thus be less affected by secondary circulations. As it was found that the secondary circulation patterns span the entire boundary-layer depth, the often discussed concept of a blending height, above which the influence of the surface heterogeneity vanishes, is thus questionable. This holds at least under convective conditions, heterogeneity scales larger than z_i and sufficiently strong heterogeneity amplitudes. This study demonstrates that extensive averaging is required to filter out the random noise of the thermal convection. Probably, turbulence measurements from field campaigns do not provide enough data to allow for sufficient averaging. This may be an important reason that experiments over heterogeneous terrain in the past did not give any clear evidence of secondary circulations.

Furthermore it could be shown that the surface heterogeneity signals are advected over long distances of several kilometers. A sensitivity study showed that sufficiently large buffer zones need to be defined around the analysis domain in order to capture the secondary circulations further upstream. The size of these buffer zones is a function of the background wind speed and varied between 10 and 18 km for the investigated cases. Micro-meteorological measurements are performed close to the surface. As the secondary circulations are weak in the surface layer, such huge buffer zones are not required to study heterogeneity effects on these measurements. Instead local effects from smaller heterogeneities will be more important.

Finally, a case study for May 30 of the LITFASS-2003 experiment was conducted using high-resolution LES that actually resolve the surface layer turbulence (grid spacing of 2 – 4 m). Due to the high computational costs only this single case could be studied. The CBL over the heterogeneous LITFASS terrain was simulated from the early morning until early afternoon, using prescribed surface fluxes of sensible and latent heat. The model domain used in this study was much smaller in comparison to previous LES of the LITFASS-2003 area and of size of 5.3 km \times 5.3 km, mainly covering by agricultural fields located in the eastern part of the LITFASS area. As in the previous study the data was compared with a homogeneous control run using spatially-averaged surface fluxes. The turbulent structure parameters of temperature and humidity were derived from the simulation data over heterogeneous terrain and compared to data from the homogeneous simulation as well as with in situ LAS data observed during the LITFASS-2003 experiment. Particular attention was given to the distribution of C_T^2 and C_q^2 in the surface layer and their MOST/LFC relationships.

It was found for the heterogeneous simulation that, compared to the homogeneous simulation, the mean C_T^2 and C_q^2 in the surface layer were about 4 % and 12 % higher, respectively. It could be shown that this difference slightly modifies the MOST/LFC relationships for C_T^2 . However, it turned out that the induced error did not exceed 1.5 % for both MOST and LFC scaling and is thus

very small. It was also discussed that the VLAS-derived fluxes tend to overestimate the prescribed surface fluxes due to non-linear relationship between structure parameters and fluxes, in agreement with previous scintillometer studies (Lagouarde et al., 2002; Meijninger et al., 2002a, 2006). As for the homogeneous simulations based on the Cabauw setup, it was found that no MOST/LFC relationships can be obtained for C_q^2 from the LES data as entrainment of dry air at top of the mixed layer was the dominant process generating humidity fluctuations. These fluctuations, in turn, affect the surface layer dynamics in such a way that the surface flux of latent heat is to great extent decoupled from the distribution of C_q^2 in both the heterogeneous and homogeneous simulation.

A correlation analysis using the method introduced by Sührling and Raasch (2013) was used in order to investigate the blending height concept for structure parameters. It could be shown that the structure parameters in the surface layer exhibit significant signals of the prescribed surface heterogeneity all day long. This finding was more pronounced for C_T^2 as entrainment of dry air was affecting the humidity fluctuations in the surface layer and thus decreased the correlation between the surface flux of latent heat and C_q^2 . Consequently, horizontal homogeneity of turbulence as required by MOST cannot generally be expected, at least under synoptic conditions of weak geostrophic winds and high surface fluxes. As a result one can conclude that, under such conditions, LAS observations will not be representative for an area of several square kilometers (in the order of NWP grid boxes, e.g. 100 km²), but rather for their local footprint area of very limited size (here in the order of 5 km²). As this footprint might be composed of different surface patches with differing surface properties, including fluxes of sensible and latent heat, the obtained surface flux from an LAS system does not necessarily have to be representative for a larger area. Our findings are of course based on a single case where the LAS footprint was much smaller than under synoptic conditions with higher geostrophic winds and lower buoyant forcing at the surface.

VLAS measurements in the LES were used along a 4.8 km long path, in agreement with the LAS setup during LITFASS-2003. A direct comparison showed, however, that the VLAS measurements did overestimate the path-weighted C_T^2 as observed by the LAS. A revision of the prescribed surface flux data revealed that the data that have been used for years for several LES studies for the LITFASS-2003 experiment (Uhlenbrock et al., 2004; Sührling and Raasch, 2013) were too high in comparison with the measured eddy covariance data. Unfortunately this inconsistency had not been noticed before. However, it was also argued that this fact merely affected the direct evaluation of the VLAS with the LAS and that the conducted simulations were computational expensive so that they could not be repeated with corrected surface flux data. Moreover, VLAS measurements were employed in order to investigate the effect of surface heterogeneity on LAS observations. It was found that sufficient time-averaging is required (here 30 min, as suggested by the representativeness analysis for the Cabauw simulations) to obtain representative fluxes and that signals of the underlying surface heterogeneity affect the VLAS observations. Whereas the VLAS measurement converged to the area-averaged value over homogeneous terrain, the VLAS observation in the heterogeneous simulation were found to retain rather local character and showed a mean deviation of 5 % from the area-average. Due to the fact that the surface fluxes changed in the course of the day so that no stationary conditions were reached in the simulation, the averaging interval was limited. Therefore, noise from the turbulence along the path made up 50 % of the variability of C_T^2 along the VLAS path. This shows that it will be quite difficult for in situ measurements, such as low level aircraft flights, to capture and quantify effects of the surface heterogeneity in the C_T^2 signal.

Outlook

Several open questions in scintillometry could be discussed in the scope of this study and the results from the present study provide a basis for future research. Wilson and Fedorovich (2012) used

LES and derived the structure parameters from LES data directly using the structure functions of temperature and humidity. Theoretically, their method should give equal results as the spectral method used in the present study. It would be interesting, however, to evaluate this assumption. Moreover, it would be also possible to deduce a new method from the structure functions to derive local structure parameters (not shown). A comparison of the three used methods in the present study with the method of Wilson and Fedorovich (2012) as well as with the new approach would gain a better physical understanding and possible deficiencies of all methods.

Moreover, more idealized simulations with different synoptic conditions (higher geostrophic wind, lower surface fluxes) or a different surface heterogeneity could evaluate whether the violation of MOST has generally a small effect on LAS-derived surface fluxes as found in the present case study. The finding that C_T^2 followed MOST was based on a relatively small database. C_q^2 was found to not follow MOST if the entrainment flux ratio for humidity was at least one. For temperature such a high ratio was never reached and typical values were found to be around 0.2. The conclusion that the MOST function for C_T^2 was “universal” might thus be only the consequence of the entrainment flux ratio for temperature not being sufficiently high. Sensitivity simulations with smaller temperature lapse rates in the free atmosphere could give more insight whether the MOST functions for C_T^2 can really be considered universal.

The surface heterogeneity for the LITFASS area was only available on a 100 m-raster. For the high-resolution LES case study of May 30 this heterogeneity was simply mapped to the finer grid. In this way, more area of heterogeneity boundaries were prescribed than actually observed in nature. More sophisticated upscaling schemes would allow to investigate if the chosen simple mapping has an effect on the LES results.

In order to prove that the VLAS gives reliable estimates of the footprint-averaged surface fluxes it would be necessary to perform a more elaborated footprint analysis for the LES. Moreover, it would be necessary to include the western part of the LITFASS area that was dominated by forest patches so that the area-averaged surface flux deviates significantly from the average flux over the farmland area simulated in the present study. A Lagrangian footprint model embedded into the LES (see Steinfeld et al., 2008) could be used over the heterogeneous LITFASS-2003 terrain in order to determine more elaborated footprints that consider the surface heterogeneity.

Finally, the friction velocity as well as the Obukhov length are required to derive the surface fluxes of sensible and latent heat from LAS/MWS observations. Scintillometers, however, do not provide measurements of the two quantities. Tower data, commonly mounted close the scintillometer, are hence used in combination with scintillometers observations of the structure parameters to determine the surface fluxes. This in turn could induce errors as tower (point measurement) and scintillometers (path-averaged measurements) may have considerably different footprint areas. LES could be an ideal tool to evaluate this possible source of errors in the surface fluxes.

Acknowledgments

First of all I would like to thank my advisor Prof. Dr. Siegfried Raasch for his continuous conceptual guidance and supervising. I also want to thank my colleagues who participated in the international research project “Turbulent Structure Parameters over Heterogeneous Terrain - Implications for the Interpretation of Scintillometer Data” for the discussions at the project meetings. Particular thanks go to Dr. Arnold Moene from Wageningen University (The Netherlands) for inviting me to Wageningen in June 2012, and for sharing his profound knowledge in both scintillometry and LES in many discussions and email correspondence. Additionally, I received substantial scientific support from Dr. Frank Beyrich (DWD) and Dr. Oscar Hartogensis (Wageningen University).

For inviting me to Bergen (Norway) in November 2012, I sincerely thank Prof. Dr. Joachim Reuder (University of Bergen) and Dr. Igor Ezau (NERSC). Moreover, I would like to thank all members of the PALM group at the Institute of Meteorology and Climatology of the Leibniz Universität Hannover for creating a pleasant working atmosphere, particularly my officemates Dr. Christoph Knigge and Theres Riechelmann. On the technical and bureaucratic side, special thanks go to Dr. Notker Fechner for the competent IT support and Christiane Brünig as well as Berit Parbel for their help with any kind of form and application I had to deal with.

Theres Riechelmann and Dr. Rieke Heinze are gratefully acknowledged for proofreading parts of this thesis from a scientific point of view. Moreover, I would like to thank all coauthors of the papers included in this thesis for their contributions to the individual manuscripts.

I sincerely thank Jennifer Petersen, Antigone Reiff and Jeanette Schröter for their friendship and company over the last years. Finally, I would like to thank my family, particularly my parents Annelore and Frank Maronga and my grandmother Dorothea Maronga, for supporting me my whole life. Special thanks go to my girlfriend Dr. Corinna Labusch for identifying structural weaknesses of the first draft of this thesis, for continuous proofreading and for her encouragement during the final phase of my doctoral studies. Thank you so much!

This study was supported by the German Research Foundation (DFG) under grants RA 617/20-1, RA 617/20-3 and RA 617/21-1. All simulations were performed on the SGI Altix ICE at The North-German Supercomputing Alliance (HLRN), Hannover/Berlin. All figures included in this thesis were created using NCL and VAPOR¹.

¹www.vapor.ucar.edu

Appendix

Some basic analysis tools using the languages NCL and FORTRAN have been developed in the scope of this study. In order to allow a reproduction of these results for further studies these fundamental tools can be found in this appendix.

Appendix A: NCL script spectral_method.ncl

spectral_method.ncl

```

1  undef("CX2_spec")
2
3  ; This function calculates the turbulent structure parameter from power spectra
4  function CX2_spec(data2d:float,delta:double,slope_tolerance:float, \
5                    rms_tolerance:float,block_interval:float)
6
7  ;
8  ;-- input values:
9  ;-- data2d: 2d array of the quantity in space (grid points must be equal in both
10 ;--          directions)
11 ;-- delta: grid length (must be equal in both directions)
12 ;-- slope_tolerance: default value of 0.3 should be used
13 ;-- rms_tolerance: default value of 15.0 should be used
14 ;-- block_interval: default vale of 0.15 should be used
15 ;
16 ;-- output attributes:
17 ;-- @spec: spectrum of the quantity
18 ;-- @CX2: structure parameter
19 ;-- @k: wave numbers of the spectrum
20 ;-- @pcnt: portion of the inertial subrange of the total spectrum in percent
21
22 begin
23
24   if ( verbose .eq. False ) then
25     print("+++ Starting CX2_spec... +++")
26   end if
27
28   output      = new((/1,1,1,1/),double)
29   output!0    = "spec"
30   output!1    = "CX2"
31   output!2    = "k"
32   output!3    = "pcnt"
33
34 ;
35 ;-- some precalculations
36   gp_x = dimsizes(data2d(0,:))
37   gp_y = dimsizes(data2d(:,0))
38
39   spectra_x   = new( (/gp_y,(gp_x / 2)/), float)
40   spectra_y   = new( (/gp_x,(gp_y / 2)/), float)
41   var_x       = new( (/gp_y/), float)
42   var_y       = new( (/gp_x/), float)
43   spectra_x_avg = new( (/gp_x / 2)/), float)
44   spectra_y_avg = new( (/gp_y / 2)/), float)
45
46   PI = 3.14159265
47
48 ;
49 ;-- calculate spectra in x direction. specx_anal parameters can be changed
50 ;-- it is assumed, that the total number of grid points is an EVEN number!
51   do p = 0, gp_y-1
52     tmp = specx_anal (data2d(p,:),0,3,0.3)
53     if ( p .eq. 0 ) then
54       k_x = tmp@frq * 2.0 * PI / delta
55     end if
56
57     sumup = 0.0d0
58     do i=0, dimsizes(tmp@spcx)-2
59       dk = tmp@frq(i+1) - tmp@frq(i)
60       sumup = sumup + (tmp@spcx(i) + tmp@spcx(i+1)) / 2.0 * dk
61     end do
62
63 ;
64 ;-- revised scaling: tmp@spcx is the spectral density. it is scaled owing
65 ;-- to the grid resolution. the area under the curve is still the variance!
66   scaling      = doubletofloat(2.0 * PI / delta)
67   spectra_x(p,:) = tmp@spcx / scaling

```

spectral_method.ncl

```

68     end do
69
70 ;
71 ;-- calculate spectra in y direction.
72     do p = 0, gp_x-1
73         tmp = specx_anal (data2d(:,p),0,3,0.3)
74         if ( p .eq. 0 ) then
75             k_y = tmp@frq * 2.0 * PI / delta
76         end if
77
78 ;
79 ;-- revised scaling: tmp@spcx is the spectral density. it is scaled owing
80 ;-- to the grid resolution. the area under the curve is still the variance!
81         scaling = doubletofloat((2.0 * PI / delta))
82         spectra_y(p,:) = tmp@spcx / scaling
83     end do
84
85 ;
86 ;-- averaging along the spatial directions
87     spectra_x_avg = dim_avg_n(spectra_x,0)
88     spectra_y_avg = dim_avg_n(spectra_y,0)
89
90     delete(spectra_x)
91     delete(spectra_y)
92 ;
93 ;-- set up tolerance limits
94     pmax = dimsizes(k_x)-1 ; number of wave numbers k_x
95     int = (log(max(k_x)) - log(min(k_x)) ) * block_interval * 0.5
96
97     upper_limit = (-5.0/3.0) + slope_tolerance * (-5.0/3.0)
98     lower_limit = (-5.0/3.0) - slope_tolerance * (-5.0/3.0)
99
100 ;
101 ;-- calculate mean of x,y: x and y must have the same dimension -> k_x=k_y
102     spectra_xy = new( (/dimsizes(spectra_x_avg)/), float)
103     spectra_xy(:) = 0.5 * (spectra_x_avg(:) + spectra_y_avg(:))
104
105     delete(spectra_x_avg)
106     delete(spectra_y_avg)
107
108 ;
109 ;-- define output fields
110     CX2 = new ( (/1/), double)
111     CX2_pre = new ( (/pmax+1/), double)
112     RMS = new ( (/1/), double)
113     RMS_loc = new ( (/pmax+1/), double)
114
115 ;
116 ;-- perform two checks to separate the inertial subrange
117
118 ;
119 ;-- calculate the slope of the spectra dspdk for all heights in
120 ;-- logarithmic scale
121     dspdk = new( (/dimsizes(spectra_xy)/), double)
122     dsp = new( (/1/), double)
123
124 ;-- this loop: using a block-intervall scheme
125     dspdk(pmax) = (log(spectra_xy(pmax)) - log(spectra_xy(pmax-1))) \
126                 / (log(k_x(pmax)) - log(k_x(pmax-1)))
127
128     dspdk_int = new( (/dimsizes(spectra_xy)/), double)
129
130     do p = 0, pmax-1
131         dsp = log(spectra_xy(p+1)) - log(spectra_xy(p))
132         dk = doubletofloat( log(k_x(p+1)) - log(k_x(p)) )
133         dspdk(p) = dsp / dk
134     end do

```

```

135
136 do p = 0, pmax
137   frq_counter = 0.0
138   dspdk_int(p) = 0.0
139   do q = 0, pmax
140     if ( abs(log(k_x(p)) - log(k_x(q))) .le. int ) then
141       dspdk_int(p) = dspdk_int(p) + dspdk(q)
142       frq_counter = frq_counter + 1.0
143     end if
144   end do
145   if ( frq_counter .eq. 0.0 ) then
146     dspdk_int(p) = dspdk_int(p) / (frq_counter + 1E-20)
147   else
148     dspdk_int(p) = dspdk_int(p) / frq_counter
149   end if
150 end do
151
152 dspdk = dspdk_int
153
154 ;
155 ;-- summing over all CX2 in the inertial subrange: slope = -5/3
156 sum_sp = new ( (/1/), double )
157 sum_sp = 0.0
158
159 ;
160 ;-- calculate full CX2-spectrum
161 k_index = new(/dimsizes(k_x),3/), integer)
162 k_index = -999
163
164 insu_counter = 0.0
165 sum_sp      = 0.0
166
167 CX2_pre(:) = (1.0/0.2489)*spectra_xy(:)*k_x(:)^(5.0/3.0)
168
169 ;
170 ;-- calculate the RMS=stddev in a 15% interval of the total log-k_x-space
171 do p = 0, pmax
172   RMS_loc(p) = 0.0
173   frq_counter = 0.0
174   if (log(k_x(p)) .ge. (min(log(k_x))+int) .and. \
175       log(k_x(p)) .le. (max(log(k_x))-int)) \
176   then
177     do q = 0, pmax
178       if ( abs(log(k_x(p)) - log(k_x(q))) .le. int ) then
179         RMS_loc(p) = RMS_loc(p) + CX2_pre(q)
180         frq_counter = frq_counter + 1.0
181       end if
182     end do
183     if ( frq_counter .gt. 2.0 ) then
184       RMS_mean = RMS_loc(p) / frq_counter
185       RMS_loc(p) = 0.0
186       do q = 0, pmax
187         if ( abs(log(k_x(p)) - log(k_x(q))) .le. int ) then
188           RMS_loc(p) = RMS_loc(p) + (CX2_pre(q) - RMS_mean)^2.0
189         end if
190       end do
191       RMS_loc(p) = sqrt(RMS_loc(p) / frq_counter)
192     ;
193     ;-- calculate the relative standard deviation in %
194     ;-- his method differs slightly from hartogenesis(2006)
195     RMS_loc(p) = RMS_loc(p)*100.0 / (RMS_mean + 1.0e-20)
196   else
197     RMS_loc(p) = -9999
198   end if
199 else
200   RMS_loc(p) = -9999
201 end if

```

```

202
203   end do
204 ;
205 ;-- check if both criteria (RMS < 15 and slope in the inertial sub-
206 ;-- range are valid, then average over those CX2 values
207 ;-- the k_index gives information about the valid range:
208 ;-- 0: valid slope after slope check
209 ;-- 1: valid RMS range after RMS check
210 ;-- 2: valid spectrum/CX2 range after both checks
211   do p = 0, pmax
212     RMS_loc(ind(ismissing(RMS_loc(:)))) = 9999.9
213     if ( dspdk(p) .ge. upper_limit .and. dspdk(p) .le. lower_limit ) then
214       k_index(p,0) = 1
215     else
216       k_index(p,0) = 0
217     end if
218     if ( RMS_loc(p) .le. rms_tolerance ) then
219       k_index(p,1) = 1
220     else
221       k_index(p,1) = 0
222     end if
223     if ( k_index(p,0) .eq. 1 .and. k_index(p,1) .eq. 1 ) then
224       sum_sp = sum_sp + CX2_pre(p)
225       insu_counter = insu_counter + 1.0
226       k_index(p,2) = 1
227     else
228       k_index(p,2) = 0
229     end if
230     RMS_loc(ind(RMS_loc(:) .eq. 9999.9)) = -9999
231   end do
232 ;
233 ;-- no values in the inertial subrange --> missing value
234   valid_percent = insu_counter / (pmax+1) * 100.0
235 ;
236 ;
237 ;-- some informational output, setting of missing values
238   if (valid_percent .le. 10.0) then
239     if ( insu_counter .ne. 0 ) then
240       CX2 = sum_sp / (insu_counter)
241     else
242       CX2 = -9999
243     end if
244     if ( verbose .eq. False ) then
245       print("--- (" + valid_percent + "%), CX2 = " + CX2)
246     end if
247   else
248     CX2 = sum_sp / (insu_counter)
249     if ( verbose .eq. False ) then
250       print("+++ (" + valid_percent + "%), CX2 = " + CX2)
251     end if
252   end if
253 ;
254 ;
255 ;-- define output
256   output@spec = spectra_xy
257   output@CX2 = CX2
258   output@k = k_x
259   output@pcnt = valid_percent
260 ;
261   delete(k_index)
262   delete(dspdk)
263   delete(spectra_xy)
264   delete(RMS_loc)
265   delete(k_x)
266 ;
267   return(output)
268 end

```


Appendix B: NCL script wavelet_method1.ncl

wavelet_method2.ncl

```

1  undef("CX2_wavelet_loc")
2
3  ; This function calculates the local turbulent structure parameter from wavelets
4  function CX2_wavelet_loc(data2d:float,delta:double,slope_tolerance:float, \
5      rms_tolerance:float,block_interval:float,s0_scale:float,\
6      k_low:integer, k_high:integer,restart:logical,tag:string)
7
8  ;
9  ;-- input values:
10 ;-- data2d: 2d array of the quantity in space (grid points must be equal in both
11 ;--          directions)
12 ;-- delta: grid length (must be equal in both directions)
13 ;-- slope_tolerance: default value of 0.3 should be used
14 ;-- rms_tolerance: default value of 15.0 should be used
15 ;-- block_interval: default vale of 0.15 should be used
16 ;-- s0_scale: scale of the smallest wavelet
17 ;-- k_low: lower limit of the wavelet window
18 ;-- k_high: upper limit of the wavelet window
19 ;-- restart: true or false, used for restarts
20 ;-- tag: manual string for output, not for any calculation purpose
21
22 begin
23
24     s0_fixed = s0_scale*delta
25
26 ;
27 ;-- some precalculations
28     gp_x = dimsizes(data2d(0,:))
29     gp_y = dimsizes(data2d(:,0))
30
31     var_x      = new( (/gp_y/), float)
32     var_y      = new( (/gp_x/), float)
33
34     PI = 3.14159265
35
36 ;
37 ;-- calculate spectra in x direction. specx_anal parameters can be changed
38     mother     = 1
39     param      = 4.0
40     s0         = s0_fixed
41     dj         = 0.25
42     jtot      = 1 + doubletoint(((log10(int2dble(gp_x)*delta/s0))/dj)/log10(2.))
43     npad      = gp_x
44     noise     = 1
45     isigtest  = 1
46     siglvl    = 0.05
47     nadof     = 0
48     spectra_x = new( (/gp_y,jtot,gp_x/), float)
49     spectra_y = new( (/gp_x,jtot,gp_y/), float)
50     spectra_xav = new( (/gp_y,jtot/), float)
51     spectra_yav = new( (/gp_x,jtot/), float)
52
53     gp_y1 = gp_y-1
54     gp_x1 = gp_x-1
55     twopi = 2 * PI
56
57     do p = 0, gp_y1
58         tmp = wavelet (data2d(p,:),mother,delta,param,s0,dj,jtot,npad,noise, \
59             isigtest,siglvl,nadof)
60         if ( p .eq. 0 ) then
61             k_x = (twopi) / tmp@period
62         end if
63
64         spectra_x(p,.,:) = onedtond (tmp@power, (/jtot,gp_x/ ) )
65     end do
66
67 ;

```

wavelet_method1.ncl

```

68     end if
69
70     spectra_x(p, :, :) = onedtond (tmp@power, (/jtot, gp_x/) )
71     spectra_xav(p, :) = dim_avg_n(spectra_x(p, :, :), 1)
72
73 ;    spatial averaging
74     sum2 = 0.0d0
75
76     sum1 = spectra_xav(p, :)
77
78 ;    spectral integration
79     sum3 = 0.0d0
80
81     do i = 0, dimsizes(spectra_xav(p, :))-2
82         ds = abs(1.0/tmp@period(i) - 1.0/tmp@period(i+1))
83         sum2 = sum2 + ( sum1(i) + sum1(i+1) ) / 2.0 *ds
84     end do
85
86     delete(sum1)
87
88     scaling = doubletofloat(2.0 * PI)
89
90     spectra_xav(p, :) = spectra_xav(p, :) * doubletofloat(tmp@stdev^2.0 / sum2)\
91         / scaling
92
93     end do
94
95 ;
96 ;-- calculate spectra in y direction.
97     mother = 1
98     param = 4.0
99     s0 = s0_fixed
100    dj = 0.25
101    jtot = 1 + doubletoint(((log10(int2dble(gp_x)*delta/s0))/dj)/log10(2.))
102    npad = gp_y
103    noise = 1
104    isigtest = 1
105    siglvl = 0.05
106    nadof = 0
107
108    do p = 0, gp_x-1
109        tmp = wavelet (data2d(:, p), mother, delta, param, s0, dj, jtot, npad, noise, \
110            isigtest, siglvl, nadof)
111        if ( p .eq. 0 ) then
112            k_y = (2 * PI) / tmp@period
113        end if
114
115        spectra_y(p, :, :) = onedtond (tmp@power, (/jtot, gp_y/) )
116
117        spectra_yav(p, :) = dim_avg_n(spectra_y(p, :, :), 1)
118
119 ;    spatial averaging
120        sum2 = 0.0d0
121
122        sum1 = spectra_yav(p, :)
123 ;    spectral integration
124        sum3 = 0.0d0
125        do i = 0, 35
126            ds = abs(1.0/tmp@period(i) - 1.0/tmp@period(i+1))
127            sum2 = sum2 + ( sum1(i) + sum1(i+1) ) / 2.0 *ds
128        end do
129
130        delete(sum1)
131
132        spectra_yav(p, :) = spectra_yav(p, :) * doubletofloat(tmp@stdev^2.0 / \
133            sum2) / scaling
134

```

wavelet_method1.ncl

```

135     end do
136
137 ;
138 ;-- averaging along the spatial directions of S(x,jtot,y). the result is S(jtot)
139     spectra_x_avg2 = dim_avg_n(spectra_xav,0)
140     spectra_y_avg2 = dim_avg_n(spectra_yav,0)
141     delete(spectra_xav)
142     delete(spectra_yav)
143
144 ;
145 ;-- set up tolerance limits
146     pmax = dimsizes(k_x)-1 ; number of wave numbers k_x
147     int  = (log(max(k_x)) - log(min(k_x)) ) * block_interval * 0.5
148
149     upper_limit = (-5.0/3.0) + slope_tolerance * (-5.0/3.0)
150     lower_limit = (-5.0/3.0) - slope_tolerance * (-5.0/3.0)
151
152 ;
153 ;-- calculate mean of x,y: x and y must have the same dimension -> k_x=k_y
154     spectra_xy = new( (/dimsizes(spectra_x_avg2)/), float)
155     spectra_xy(:) = 0.5 * (spectra_x_avg2(:) + spectra_y_avg2(:))
156
157     delete(spectra_x_avg2)
158     delete(spectra_y_avg2)
159
160 ;
161 ;-- define output fields
162     CX2 = new ( (/1/), double)
163     CX2_pre = new ( (/pmax+1/), double)
164     RMS = new ( (/1/), double)
165     RMS_loc = new ( (/pmax+1/), double)
166
167 ;
168 ;-- perform two checks to separate the inertial subrange
169 ;
170 ;-- calculate the slope of the spectra dspdk for all heights in
171 ;-- logarithmic scale
172     dspdk = new( (/dimsizes(spectra_xy)/), double)
173     dsp = new( (/1/), double)
174
175 ;-- this loop: using a block-intervall scheme
176     dspdk(pmax) = (log(spectra_xy(pmax)) - log(spectra_xy(pmax-1))) \
177                 / (log(k_x(pmax)) - log(k_x(pmax-1)))
178
179     dspdk_int = new( (/dimsizes(spectra_xy)/), double)
180
181     do p = 0, pmax-1
182         dsp = log(spectra_xy(p+1)) - log(spectra_xy(p))
183         dk = ( log(k_x(p+1)) - log(k_x(p)) )
184         dspdk(p) = dsp / dk
185     end do
186
187     do p = 0, pmax
188         frq_counter = 0.0
189         dspdk_int(p) = 0.0
190         do q = 0, pmax
191             if ( abs(log(k_x(p)) - log(k_x(q))) .le. int ) then
192                 dspdk_int(p) = dspdk_int(p) + dspdk(q)
193                 frq_counter = frq_counter + 1.0
194             end if
195         end do
196         dspdk_int(p) = dspdk_int(p) / frq_counter
197     end do
198
199     dspdk = dspdk_int
200
201 ;

```

wavelet_method1.ncl

```

202 ;-- summing over all CX2 in the inertial subrange: slope = -5/3
203 sum_sp = new ( (/1/), double )
204 sum_sp = 0.0
205
206 ;
207 ;-- calculate full CX2-spectrum
208 k_index = new(/dimsizes(k_x),3/), integer)
209 k_index = -999
210
211 insu_counter = 0.0
212 sum_sp      = 0.0
213
214 CX2_pre(:) = (1.0/0.2489)*spectra_xy(:)*k_x(:)^(5.0/3.0)
215
216 ;
217 ;-- calculate the RMS=stddev in a 15% interval of the total log-k_x-space
218 do p = 0, pmax
219   RMS_loc(p) = 0.0
220   frq_counter = 0.0
221   if (log(k_x(p)) .ge. (min(log(k_x))+int) .and. \
222       log(k_x(p)) .le. (max(log(k_x))-int) \
223       then
224     do q = 0, pmax
225       if ( abs(log(k_x(p)) - log(k_x(q))) .le. int) then
226         RMS_loc(p) = RMS_loc(p) + CX2_pre(q)
227         frq_counter = frq_counter + 1.0
228       end if
229     end do
230     if ( frq_counter .gt. 2.0 ) then
231       RMS_mean = RMS_loc(p) / frq_counter
232       RMS_loc(p) = 0.0
233       do q = 0, pmax
234         if ( abs(log(k_x(p)) - log(k_x(q))) .le. int) then
235           RMS_loc(p) = RMS_loc(p) + (CX2_pre(q) - RMS_mean)^2.0
236         end if
237       end do
238       RMS_loc(p) = sqrt(RMS_loc(p) / frq_counter)
239     ;
240     ;-- calculate the relative standard deviation in %
241     ;-- his method differs slightly from hartogenesis(2006)
242     RMS_loc(p) = RMS_loc(p)*100.0 / (RMS_mean + 1E-20)
243   else
244     RMS_loc(p) = -9999
245   end if
246 else
247   RMS_loc(p) = -9999
248 end if
249
250 end do
251 ;
252 ;-- check if both criteria (RMS < 15 and slope in the inertial sub-
253 ;-- range are valid, then average over those CX2 values
254 ;-- the k_index gives information about the valid range:
255 ;-- 0: valid slope after slope check
256 ;-- 1: valid RMS range after RMS check
257 ;-- 2: valid spectrum/CX2 range after both checks
258 do p = 0, pmax
259   RMS_loc(ind(ismissing(RMS_loc(:)))) = 9999.9
260   if ( dspdk(p) .ge. upper_limit .and. dspdk(p) .le. lower_limit ) then
261     k_index(p,0) = 1
262   else
263     k_index(p,0) = 0
264   end if
265   if ( RMS_loc(p) .le. rms_tolerance ) then
266     k_index(p,1) = 1
267   else
268     k_index(p,1) = 0

```

wavelet_method1.ncl

```

269     end if
270     if ( k_index(p,0) .eq. 1 .and. k_index(p,1) .eq. 1) then
271         sum_sp = sum_sp + CX2_pre(p)
272         insu_counter = insu_counter + 1.0
273         k_index(p,2) = 1
274     else
275         k_index(p,2) = 0
276     end if
277     RMS_loc(ind(RMS_loc(:) .eq. 9999.9)) = -9999
278 end do
279 ;
280 ;-- no values in the inertial subrange --> missing value
281 valid_percent = insu_counter / (pmax+1) * 100.0
282 ;
283 ;
284 ;-- some informational output, setting of missing values
285
286 if (valid_percent .le. 10.0) then
287     if ( insu_counter .ne. 0 ) then
288         CX2 = sum_sp / (insu_counter)
289     end if
290     CX2 = -9999
291     if ( verbose .eq. False ) then
292         print("--- (" + valid_percent + "%), CX2 = " + CX2)
293     end if
294 else
295     CX2 = sum_sp / (insu_counter)
296     if ( verbose .eq. False ) then
297         print("+++ (" + valid_percent + "%), CX2 = " + CX2)
298     end if
299 end if
300
301 k_range_index = ind(k_index(:,2) .eq. 1)
302 ;
303 ;
304 ;-- define output
305 output = new(/1,1,1,1,1,1/),double)
306 output!0 = "spec"
307 output@spec = spectra_xy
308 output!1 = "CX2"
309 output@CX2 = CX2
310 output!2 = "k"
311 output@k = k_x
312 output!3 = "pcnt"
313 output@pcnt = valid_percent
314 output!4 = "k_low"
315 output@k_low = min(k_range_index)
316 output!5 = "k_high"
317 output@k_high = max(k_range_index)
318
319 delete(k_index)
320 delete(dspdk)
321 delete(spectra_xy)
322 delete(RMS_loc)
323 delete(k_x)
324
325 return(output)
326 end

```

Appendix C: NCL script wavelet_method2.ncl

```

                                wavelet_method2.ncl
1  undef("CX2_wavelet_loc")
2
3  ; This function calculates the local turbulent structure parameter from wavelets
4  function CX2_wavelet_loc(data2d:float,delta:double,slope_tolerance:float, \
5                          rms_tolerance:float,block_interval:float,s0_scale:float,\
6                          k_low:integer, k_high:integer,restart:logical,tag:string)
7
8  ;
9  ;-- input values:
10 ;-- data2d: 2d array of the quantity in space (grid points must be equal in both
11 ;--          directions)
12 ;-- delta: grid length (must be equal in both directions)
13 ;-- slope_tolerance: default value of 0.3 should be used
14 ;-- rms_tolerance: default value of 15.0 should be used
15 ;-- block_interval: default value of 0.15 should be used
16 ;-- s0_scale: scale of the smallest wavelet
17 ;-- k_low: lower limit of the wavelet window
18 ;-- k_high: upper limit of the wavelet window
19 ;-- restart: true or false, used for restarts
20 ;-- tag: manual string for output, not for any calculation purpose
21
22 begin
23
24     s0_fixed = s0_scale*delta
25
26 ;
27 ;-- some precalculations
28     gp_x = dimsizes(data2d(0,:))
29     gp_y = dimsizes(data2d(:,0))
30
31     var_x      = new( (/gp_y/), float)
32     var_y      = new( (/gp_x/), float)
33
34     PI = 3.14159265
35
36 ;
37 ;-- calculate spectra in x direction. specx_anal parameters can be changed
38     mother     = 1
39     param      = 4.0
40     s0         = s0_fixed
41     dj         = 0.25
42     jtot      = 1 + doubletoint(((log10(int2dble(gp_x)*delta/s0))/dj)/log10(2.))
43     npad      = gp_x
44     noise     = 1
45     isigtest  = 1
46     siglvl    = 0.05
47     nadof     = 0
48     spectra_x = new( (/gp_y,jtot,gp_x/), float)
49     spectra_y = new( (/gp_x,jtot,gp_y/), float)
50     spectra_xav = new( (/gp_y,jtot/), float)
51     spectra_yav = new( (/gp_x,jtot/), float)
52
53     gp_y1 = gp_y-1
54     gp_x1 = gp_x-1
55     twopi = 2 * PI
56
57     do p = 0, gp_y1
58         tmp = wavelet (data2d(p,:),mother,delta,param,s0,dj,jtot,npad,noise, \
59                       isigtest,siglvl,nadof)
60         if ( p .eq. 0 ) then
61             k_x = (twopi) / tmp@period
62         end if
63
64         spectra_x(p,.,:) = onedtond (tmp@power, (/jtot,gp_x/ ) )
65     end do
66
67 ;

```

wavelet_method2.ncl

```

68 ;-- calculate spectra in y direction.
69 mother = 1
70 param = 4.0
71 s0 = s0_fixed
72 dj = 0.25
73 jtot = 1 + doubletoint(((log10(int2dble(gp_x)*delta/s0))/dj)/log10(2.))
74 npad = gp_y
75 noise = 1
76 isigtest = 1
77 siglvl = 0.05
78 nadof = 0
79
80 do p = 0, gp_x1
81   tmp = wavelet (data2d(:,p),mother,delta,param,s0,dj,jtot,npad,noise, \
82     isigtest,siglvl,nadof)
83   if ( p .eq. 0 ) then
84     k_y = (twopi) / tmp@period
85   end if
86
87   spectra_y(p, :, :) = onedtond (tmp@power, (/jtot, gp_y/ ) )
88
89 end do
90
91 spectra_2d = new ( (/gp_x, gp_y, jtot/), double)
92 CX2_xy = new ( (/gp_x, gp_y, jtot/), double)
93 CX2_xy_av = new ( (/gp_x, gp_y/), double)
94
95 if ( restart .eq. False ) then
96   system("/bin/rm -f DATA/xy_wavelet_ME.nc")
97   ncdf = addfile("DATA/xy_wavelet_ME.nc", "c")
98
99   CX2_xy_av!0 = "x"
100  CX2_xy_av!1 = "y"
101  spectra_2d!0 = "x"
102  spectra_2d!1 = "y"
103  spectra_2d!2 = "k"
104  xmax = (gp_x-1) * delta
105  ymax = (gp_y-1) * delta
106  CX2_xy_av&x = fspan(0.0, xmax, gp_x)
107  CX2_xy_av&y = fspan(0.0, ymax, gp_y)
108  spectra_2d&x = fspan(0.0, xmax, gp_x)
109  spectra_2d&y = fspan(0.0, ymax, gp_y)
110  spectra_2d&k = k x
111  ncdf->CX2 = CX2_xy_av
112  ncdf->spectra_2d = spectra_2d
113  istart = 0
114 else
115   ncdf = addfile("DATA/xy_wavelet_ME.nc", "r")
116   CX2_xy_av = ncdf->CX2
117   istart = ncdf->i
118 end if
119 delete(ncdf)
120
121 if ( verbose .eq. False ) then
122   print("+++ start long calculation...")
123 end if
124
125 ;-- averaging of x and y spectra
126 gp_y1 = gp_y-1
127 gp_x1 = gp_x-1
128 temp1 = 1.0/0.2489
129 temp2 = 5.0/3.0
130
131 do i=istart, gp_x1
132   do j=0, gp_y1
133     spectra_2d(i, j, k_low:k_high) = ( spectra_x(j, k_low:k_high, i) + \
134       spectra_y(i, k_low:k_high, j) ) * 0.5

```

wavelet_method2.ncl

```
135         CX2_xy_av(i,j) = avg( temp1 * spectra_2d(i,j,k_low:k_high) * \
136                               k_x(k_low:k_high)^temp2 )
137     end do
138
139
140     ncdf = addfile("DATA/xy_wavelet_" + tag + ".nc" ,"w")
141     ncdf->CX2      = CX2_xy_av
142     ncdf->spectra_2d = spectra_2d
143     ncdf->i        = (i+1)
144     delete(ncdf)
145
146     if ( verbose .eq. False ) then
147         print("+++ next line" + i)
148     end if
149
150 end do
151
152 wks = gsn_open_wks("eps","example")
153 gsn_define_colormap(wks,"rainbow")
154 res = True
155 res@cnFillOn = True
156 res@trYReverse = False
157 res@gsnSpreadColors = True
158 plot = gsn_csm_contour(wks,CX2_xy_av(:,:),res)
159
160 ;
161 ;-- define output
162 output = CX2_xy_av
163
164 return(output)
165 end
```


Appendix D: Extract from FORTRAN source code

user_actions.f90

```

user_actions.f90
1  ! code snippet from user_actions.f90
2
3  SUBROUTINE user_actions( location )
4
5      USE control_parameters
6      USE cpulog
7      USE indices
8      USE interfaces
9      USE pegrid
10     USE user
11     USE arrays_3d
12     USE grid_variables
13     USE constants
14     USE cloud_parameters
15     USE statistics
16
17     IMPLICIT NONE
18
19     CHARACTER (LEN=*) :: location
20
21     INTEGER :: i, j, k
22     REAL    :: coeff1, coeff2, coeff3, coeff_pt, coeff_q, coeff_ptq, pr_dz,&
23             kh_dz
24
25     REAL    :: q_avg, t_avg, p_avg, e_avg, m1, m2, a_t, a_q
26
27
28     CALL cpu_log( log_point(24), 'user_actions', 'start' )
29
30  !
31  !-- Here the user-defined actions follow
32  !-- No calls for single grid points are allowed at locations before and
33  !-- after the timestep, since these calls are not within an i,j-loop
34  SELECT CASE ( location )
35
36      CASE ( 'before_timestep' )
37  !
38  !-- Enter actions to be done before every timestep here
39
40
41      CASE ( 'after_integration' )
42
43          CALL user_diffusivities( pt, pt_reference )
44
45          !$OMP DO
46          DO i = nxl, nxr
47              DO j = nys, nyn
48                  DO k = nzb+2, nzt-1
49  !
50  !-- calculate structure parameters
51  !-- discretization uses central finite differencing
52  !-- the levels nzb, nzb+1 and nzt are not calculated
53          coeff_pt = (( pt(k,j,i+1) - pt(k,j,i-1) ) * 0.5*ddx)**2.0 &
54                    + (( pt(k,j+1,i) - pt(k,j-1,i) ) * 0.5 * ddy)**2.0 &
55                    + (( pt(k+1,j,i) - pt(k-1,j,i) ) / &
56                      (dzu(k-1) + dzu(k)) &
57                      )**2.0
58          coeff_q = (( q(k,j,i+1) - q(k,j,i-1) ) * 0.5 * ddx)**2.0 &
59                    + (( q(k,j+1,i) - q(k,j-1,i) ) * 0.5 * ddy)**2.0 &
60                    + (( q(k+1,j,i) - q(k-1,j,i) ) / &
61                      (dzu(k-1) + dzu(k)) &
62                      )**2.0
63          coeff_ptq = (( pt(k,j,i+1) - pt(k,j,i-1) ) * 0.5 * ddx) &
64                     * (( q(k,j,i+1) - q(k,j,i-1) ) * 0.5 * ddx) &
65                     + (( pt(k,j+1,i) - pt(k,j-1,i) ) * 0.5 * ddy) &
66                     * (( q(k,j+1,i) - q(k,j-1,i) ) * 0.5 * ddy) &
67                     + (( pt(k+1,j,i) - pt(k-1,j,i) ) / &
68                       (dzu(k-1) + dzu(k)) &
69                       )

```

```

user_actions.f90
68          * (( q(k+1,j,i) - q(k-1,j,i) ) /           &
69              (dzu(k-1) + dzu(k)) )
70
71 !
72 !--      calculate dissipation rates
73          kh_dz      = 0.5 * (kh(k+1,j,i) + kh(k,j,i))
74          dsq(k,j,i) = 2.0 * kh_dz * coeff_q
75          dsptq(k,j,i) = 2.0 * kh_dz * coeff_ptq
76          dspt(k,j,i) = 2.0 * kh_dz * coeff_pt
77          dse(k,j,i) = diss(k,j,i)
78 !
79 !--      calculate structure parameters
80          pr_dz      = 0.5 * ( pr_n(k+1,j,i) + pr_n(k,j,i) )
81          coeff1     = (beta_1 * 0.2 / 0.2489) * pr_dz
82          coeff2     = 0.5 * ( diss_p(k+1,j,i) + diss_p(k,j,i) )
83          ct2(k,j,i) = coeff1 * coeff2 * coeff_pt
84          cq2(k,j,i) = coeff1 * coeff2 * coeff_q
85          ctq(k,j,i) = coeff1 * coeff2 * coeff_ptq
86
87          ENDDO
88          ENDDO
89          ENDDO
90
91          CALL exchange_horiz( ct2, nbgp )
92          CALL exchange_horiz( cq2, nbgp )
93          CALL exchange_horiz( ctq, nbgp )
94          CALL exchange_horiz( dse, nbgp )
95          CALL exchange_horiz( dspt, nbgp )
96          CALL exchange_horiz( dsq, nbgp )
97          CALL exchange_horiz( dsptq, nbgp )
98
99
100         CASE DEFAULT
101           message_string = 'unknown location "' // location // "'
102           CALL message( 'user_actions', 'UI0001', 1, 2, 0, 6, 0 )
103
104         END SELECT
105
106         CALL cpu_log( log_point(24), 'user_actions', 'stop' )
107
108     END SUBROUTINE user_actions
109
110 END MODULE user_actions_mod
111

```

Appendix E: FORTRAN source code avg.f90

avg.f90

```

1 ! avg.f90 - FORTRAN program to calculate secondary circulations and other
2 ! ensemble-averaged quantities
3 !
4 ! Compilation:
5 ! ifort avg.f90 -r8 -O3 -openmp -I /sw/dataformats/netcdf/3.6.2/include
6 ! -L /sw/dataformats/netcdf/3.6.2/lib
7 ! -lnetcdf -lnetcdf -o avg
8 !
9 ! Usage:
10 ! provide namelist file 'parin_input_file', where input_file is a variable
11 ! e.g. input_file = "test". The file parin_test could then contain e.g.:
12 ! &inipar file(1) = 'BH3005_r1/OUTPUT/BH3005_r1_3d_av.1.nc',
13 !       file(2) = 'BH3005_r2/OUTPUT/BH3005_r2_3d_av.1.nc',
14 !       file(3) = 'BH3005_r3/OUTPUT/BH3005_r3_3d_av.nc',
15 !       file(4) = 'BH3005_r4/OUTPUT/BH3005_r4_3d_av.nc',
16 !       file(5) = 'BH3005_r5/OUTPUT/BH3005_r5_3d_av.nc',
17 !       file(6) = 'BH3005_r6/OUTPUT/BH3005_r6_3d_av.nc',
18 !       file(7) = 'BH3005_r7/OUTPUT/BH3005_r7_3d_av.nc',
19 !       file(8) = 'BH3005_r8/OUTPUT/BH3005_r8_3d_av.nc',
20 !       path   = '/gfs2/work/nikmaron/palm/current_version/JOBS/',
21 !       num_of_runs = 8,
22 !       variable = 'w',
23 !       mode = 'induced',
24 !       timestep_average = 1,
25 !       output_filename = 'BH3005_N8', /
26 !
27 ! Start avg:
28 ! ./avg parin_test
29 ! or submit a job to a queuing system.
30 !
31 MODULE globals
32
33   IMPLICIT NONE
34   REAL, DIMENSION (:, :, :, :), ALLOCATABLE :: data, data_tmp, tmp4d_array
35   INTEGER :: timestep_average = 1
36   CHARACTER (LEN=3) :: filename_cycle_chr, filename_cycle_chr_2d
37   CHARACTER (LEN=10) :: variable
38   CHARACTER (LEN=100), DIMENSION(:) :: file(1:20)
39   CHARACTER (LEN=100) :: path, file_out, input_file, output_filename, &
40     post_process_type = 'none', mode = 'none'
41   INTEGER :: ncid, varid, num_of_dims, num_of_vars, num_of_atts, uldimid, &
42     ftnum, ncid_out, filename_cycle, ncid2d, ncid2d_out
43   INTEGER, DIMENSION(:), ALLOCATABLE :: dlen, vlen, var_atts, var_dim, xtype, &
44     out_dim_id, out_var_id, out2d_dim_id, &
45     out2d_var_id
46   INTEGER, DIMENSION(:, :), ALLOCATABLE :: var_dim_ids, att_len, att_type, &
47     att_num
48   CHARACTER (LEN=10), DIMENSION(:), ALLOCATABLE :: dname, vname
49   CHARACTER (LEN=10), DIMENSION(:, :), ALLOCATABLE :: att_name
50
51   REAL, DIMENSION (:), ALLOCATABLE :: dim1, dim2, dim3, dim4
52   LOGICAL :: file_exists, split = .FALSE.
53
54   INTEGER :: dim_t, dim_x, dim_y, dim_z, num_of_runs, time_a, time_e, &
55     time_rate, z_offset = 5, t_stride=1, t_start, t_end, &
56     mem_node = 64
57
58   SAVE
59
60 END MODULE
61
62 MODULE indices
63
64   IMPLICIT NONE
65
66   INTEGER :: j, m, n, t, z, y, x
67
68   SAVE
69 END MODULE
70
71 PROGRAM avg
72
73   USE netcdf
74   USE globals
75
76   IMPLICIT NONE

```

avg.f90

```

77
78 EXTERNAL nccall
79
80 INTEGER :: i, omp_get_num_procs, omp_set_num_procs, t
81
82 NAMELIST /inipar/ num_of_runs, variable, file, path, mem_node, mode,      &
83                   output_filename, timestep_average, post_process_type,  &
84                   split
85
86
87 PRINT*, '*****'
88 PRINT*, '* Post-Processing Tool for PALM NetCDF data *'
89 PRINT*, '*****'
90
91 READ (*,*,ERR=13,END=13) input_file
92 13 CONTINUE
93
94 OPEN ( 11, FILE='parin'//TRIM(input_file), FORM='FORMATTED', STATUS='OLD' )
95 READ ( 11, inipar, ERR=10, END=11 )
96 GOTO 12
97
98 10 PRINT*, '+++ Error in \$inipar-namelist found'
99 STOP '+++ Stopping.'
100 11 PRINT*, '+++ No \$inipar-namelist found'
101 STOP '+++ Stopping.'
102
103 12 CONTINUE
104 PRINT*, '*** Loaded:'
105 PRINT*, '   num_of_runs = ', num_of_runs
106 PRINT*, '   path = ', TRIM(path)
107 PRINT*, '   variable = ', TRIM(variable)
108 PRINT*, '   mode = ', TRIM(mode)
109 PRINT*, '   ouput_file = ', TRIM(output_filename)
110 PRINT*, '   p.-process = ', TRIM(post_process_type)
111 PRINT*, '   time avg. = ', timestep_average
112 PRINT*, '   mem split = ', split
113 PRINT*, '   OMP threads = ', omp_get_num_procs()
114
115 PRINT*, '*** Processing...'
116 CALL SYSTEM_CLOCK(count=time_a)
117 CALL SYSTEM_CLOCK(count_rate=time_rate)
118
119 CALL nccall ( 'init', 1 )
120
121 DO t = 1, dim_t-1, t_stride
122   t_start = t
123   t_end = t + t_stride - 1
124   DO i = 1, num_of_runs
125
126     CALL nccall ( 'open', i )
127
128     CALL nccall ( 'read', i )
129
130     CALL user_actions ( 'each_run', i )
131
132     CALL nccall ( 'close', i )
133
134     DEALLOCATE ( data_tmp )
135
136   END DO
137
138   PRINT*, '*** LP: after loop'
139   CALL user_actions ( 'after_loop', i )
140
141 !
142 !-- Calculate elapsed time
143 CALL SYSTEM_CLOCK(count=time_e)
144   PRINT*, '   Time elapsed for calculation: ', &
145         (time_e - time_a) / time_rate, 's'
146   CALL SYSTEM_CLOCK(count=time_a)
147
148   PRINT*, '*** LP: post_processing'
149   CALL user_actions ( 'post_processing', 0 )
150
151 !
152 !-- Calculate elapsed time

```

avg.f90

```

153     CALL SYSTEM_CLOCK(count=time_e)
154     PRINT*, '   Time elapsed for calculation: ', &
155           (time_e - time_a) / time_rate, 's'
156     CALL SYSTEM_CLOCK(count=time_a)
157
158     IF ( TRIM(mode) /= 'none' ) THEN
159         PRINT*, '*** LP: write data'
160         CALL nccall ( 'write', 0 )
161     ELSE
162         PRINT*, '*** LP: write data (skipped)'
163     END IF
164     DEALLOCATE ( data )
165
166 END DO
167
168 CALL nccall ( 'close_out', 0 )
169 !
170 !-- Check only if dim1 is allocated, because in this case, all other
171 !-- variables should be allocated as well.
172 IF ( ALLOCATED( dim1 ) ) THEN
173     DEALLOCATE ( dim1, dim2, dim3, dim4, dlen, vlen, dname, vname, &
174               att_name, var_atts, var_dim, xtype, var_dim_ids, &
175               att_len, att_type, att_num )
176 ENDIF
177 IF ( ALLOCATED( out_dim_id ) ) THEN
178     DEALLOCATE ( out_dim_id, out_var_id )
179 END IF
180 IF ( ALLOCATED( out2d_dim_id ) ) THEN
181     DEALLOCATE ( out2d_dim_id, out2d_var_id )
182 END IF
183
184 !
185 !-- Calculate elapsed time and give some informational output
186 CALL SYSTEM_CLOCK(count=time_e)
187 PRINT*, '   Time elapsed for calculation: ', &
188       (time_e - time_a) / time_rate, 's'
189 PRINT*, '*** Finished.'
190
191 END PROGRAM
192
193
194 !*****
195
196 SUBROUTINE nccall ( action, i )
197
198     USE globals
199     USE indices
200     USE netcdf
201
202     IMPLICIT NONE
203
204     EXTERNAL check, time_averaging, init_2d_file
205
206     CHARACTER (LEN=*) :: action
207     REAL :: local_average, tmp_avg, mem
208     INTEGER :: i, k
209     REAL    :: omp_get_wtime, omp_time_start, omp_time_end
210
211     SELECT CASE ( TRIM( action ) )
212
213     CASE ( 'open' )
214
215         CALL check (nf90_open(TRIM(path)//TRIM(file(i)), NF90_NOWRITE, ncid),&
216                 nf90_noerr )
217
218     CASE ( 'init' )
219
220         CALL check (nf90_open(TRIM(path)//TRIM(file(i)), NF90_NOWRITE, ncid),&
221                 nf90_noerr )
222
223 !
224 !-- Get global information, number of dimensions, number of variables
225 !-- and so on
226 CALL check ( nf90_inquire(ncid, num_of_dims, num_of_vars, &
227             num_of_atts, uldimid, fmtnum), nf90_noerr )
228

```

avg.f90

```

229 !
230 !-- Get information about the dimensions (names and lengths)
231 ALLOCATE ( dname(0:num_of_dims-1), dlen(0:num_of_dims-1) )
232
233 DO m=0,num_of_dims-1
234     CALL check( nf90_inquire_dimension(ncid, m+1, dname(m), dlen(m)),&
235               nf90_noerr )
236
237 END DO
238
239 !
240 !-- Get information about the variables (names, types, dimensions,
241 !-- dimension ids and attributes
242 ALLOCATE ( vname(0:num_of_vars-1), vlen(0:num_of_vars-1),      &
243           var_dim(0:num_of_vars-1),                          &
244           var_dim_ids(0:num_of_vars-1, num_of_dims),          &
245           xtype(0:num_of_vars-1), var_atts(0:num_of_vars-1) )
246
247 DO m=0,num_of_vars-1
248     CALL check ( nf90_inquire_variable(ncid, m+1, vname(m), xtype(m), &
249               var_dim(m), var_dim_ids(m,:), var_atts(m)), nf90_noerr )
250 END DO
251
252 !
253 !-- Get information about the attributes (units, long_name,...)
254 !-- Keep in mind, that num_of_atts (=4 in PALM) has nothing to do with the
255 !-- actual number of attributes for each variable. It might have to been
256 !-- increased for unusual data.
257 ALLOCATE ( att_name(0:num_of_vars-1,0:num_of_atts-1) )
258
259 DO m=0,num_of_vars-1
260     DO n=0,var_atts(m)-1
261         CALL check ( nf90_inq_attname(ncid, m+1, n+1, att_name(m,n)), &
262               nf90_noerr )
263     END DO
264 END DO
265
266 ALLOCATE ( att_type(0:num_of_vars-1,0:num_of_atts-1), &
267           att_len(0:num_of_vars-1,0:num_of_atts-1), &
268           att_num(0:num_of_vars-1,0:num_of_atts-1) )
269
270 DO m=0,num_of_vars-1
271     DO n=0,var_atts(m)-1
272         CALL check ( nf90_inquire_attribute(ncid, m+1, att_name(m,n), &
273               att_type(m,n), att_len(m,n), att_num(m,n)), &
274               nf90_noerr )
275     END DO
276 END DO
277 !
278 !-- Define filename for data output (increasing numbers avoids overwriting
279 !-- of old data)
280 IF ( TRIM(mode) /= 'none' ) THEN
281
282     file_exists = .TRUE.
283     filename_cycle = 0
284
285     DO WHILE ( file_exists == .TRUE. )
286         filename_cycle = filename_cycle + 1
287         WRITE(filename_cycle_chr, FMT='(I3)') filename_cycle
288         filename_cycle_chr = ADJUSTL(filename_cycle_chr)
289         file_out = TRIM(path)//TRIM(output_filename)//'_'//      &
290                 TRIM(mode)//'_'//TRIM(variable)//'_'//      &
291                 TRIM(filename_cycle_chr)//'.nc'
292         INQUIRE(FILE=file_out, EXIST=file_exists)
293         IF ( .NOT. file_exists ) file_exists = .FALSE.
294     END DO
295
296 !
297 !-- Prepare NetCDF output
298 CALL check( nf90_create(TRIM(file_out), NF90_CLOBBER, &
299               ncid_out), nf90_noerr)
300
301 END IF
302
303 DO m=num_of_dims,num_of_vars-1
304     IF ( vname(m) == TRIM( variable ) ) THEN

```

avg.f90

```

305 !--      Read dimension values (x, y, z, t)
306      ALLOCATE ( dim1(1:dlen(var_dim_ids(m, 1))-1) )
307      CALL check ( nf90_get_var(ncid, var_dim_ids(m, 1), dim1), &
308                  nf90_noerr )
309
310      ALLOCATE ( dim2(1:dlen(var_dim_ids(m, 2))-1) )
311      CALL check ( nf90_get_var(ncid, var_dim_ids(m, 2), dim2), &
312                  nf90_noerr )
313
314      ALLOCATE ( dim3(1:dlen(var_dim_ids(m, 3))-1) )
315      CALL check ( nf90_get_var(ncid, var_dim_ids(m, 3), dim3), &
316                  nf90_noerr )
317
318      ALLOCATE ( dim4(1:dlen(var_dim_ids(m, 4))-1) )
319      CALL check ( nf90_get_var(ncid, var_dim_ids(m, 4), dim4), &
320                  nf90_noerr )
321
322      dim_t = dlen(var_dim_ids(m, 4))-1
323      dim_z = dlen(var_dim_ids(m, 3))-1
324      dim_y = dlen(var_dim_ids(m, 2))-1
325      dim_x = dlen(var_dim_ids(m, 1))-1
326
327      mem = REAL(mem_node) * 1000.0 * 1000.0 * 1000.0
328
329      IF ( split == .TRUE. ) THEN
330          t_stride = INT( mem / (16.0*REAL(dim_x)*REAL(dim_y)*
331                              REAL(dim_z)) ) &
332      ELSE
333          t_stride = dim_t
334      END IF
335      IF ( t_stride > dim_t ) t_stride = dim_t
336      PRINT*, '*** Memory of ', mem, ' node, 'GB leads to', t_stride
337      PRINT*, '      timesteps in each loop.'
338
339      IF ( TRIM(mode) /= 'none' ) THEN
340          ALLOCATE ( out_dim_id(1:var_dim(m)), &
341                  out_var_id(1:var_dim(m)+1) )
342
343          DO j=1,var_dim(m)
344              CALL check( nf90_def_dim(ncid_out, &
345                          dname(var_dim_ids(m,j))-1,&
346                          dlen(var_dim_ids(m, j))-1), out_dim_id(j)), &
347                          nf90_noerr )
348              CALL check( nf90_def_var(ncid_out, &
349                          dname(var_dim_ids(m,j))-1,&
350                          xtype(var_dim_ids(m, j))-1), out_dim_id(j), &
351                          out_var_id(var_dim(m)+1) ), nf90_noerr )
352          END DO
353
354      !
355      !--      Write global attributes
356      CALL check( nf90_def_var(ncid_out, TRIM(vname(m)), xtype(m), &
357                  out_dim_id, out_var_id(var_dim(m)+1) ), &
358                  nf90_noerr )
359
360      CALL check( nf90_copy_att(ncid, NF90_GLOBAL, 'title', &
361                  ncid_out, &
362                  NF90_GLOBAL), nf90_noerr )
363
364      CALL check( nf90_copy_att(ncid, NF90_GLOBAL, 'Conventions', &
365                  ncid_out, NF90_GLOBAL), nf90_noerr )
366
367      CALL check( nf90_copy_att(ncid, NF90_GLOBAL, 'time_avg', &
368                  ncid_out, NF90_GLOBAL), nf90_noerr )
369
370      CALL check( nf90_put_att(ncid_out, NF90_GLOBAL, 'VAR_LIST', &
371                  ';//TRIM(vname(m))//;' ), nf90_noerr )
372
373      !
374      !--      Write variable attributes
375      DO j=0,var_atts(m)-1
376          CALL check( nf90_copy_att(ncid, m+1, TRIM(att_name(m,j)), &
377                          ncid_out, out_var_id(var_dim(m)+1) ), &
378                          nf90_noerr )
379      END DO
380

```

avg.f90

```

381      DO k=0,var_dim(m)-1
382      DO j=0,var_atts(k)-1
383      CALL check( nf90_copy_att(ncid, var_dim_ids(m,k+1),      &
384      TRIM(att_name(k,j)), ncid_out,      &
385      out_dim_id(k+1)),&
386      nf90_noerr )
387      END DO
388      END DO
389
390      CALL check( nf90_enddef(ncid_out), nf90_noerr )
391
392      !
393      !--      Write arrays to file
394      CALL check( nf90_put_var(ncid_out, out_dim_id(1), dim1), &
395      nf90_noerr )
396      CALL check( nf90_put_var(ncid_out, out_dim_id(2), dim2), &
397      nf90_noerr )
398      CALL check( nf90_put_var(ncid_out, out_dim_id(3), dim3), &
399      nf90_noerr )
400      CALL check( nf90_put_var(ncid_out, out_dim_id(4), dim4), &
401      nf90_noerr )
402
403      END IF
404
405      EXIT
406
407      END IF
408      END DO
409
410      IF ( post_process_type == 'zi' ) THEN
411      CALL init_2d_file( 'zi', 'meters', 'zi' )
412      END IF
413
414      CASE ( 'read' )
415      DO m=num_of_dims,num_of_vars-1
416      IF ( vname(m) == TRIM( variable ) ) THEN
417      !
418      !--      Loading data field
419      IF ( .NOT. ALLOCATED ( data ) ) THEN
420      ALLOCATE ( data(1:dlen(var_dim_ids(m, 1))-1, &
421      1:dlen(var_dim_ids(m, 2))-1, &
422      1:dlen(var_dim_ids(m, 3))-1), &
423      1:t_stride )
424      data = 0.0D0
425      ENDF
426
427      ALLOCATE ( data_tmp(1:dlen(var_dim_ids(m, 1))-1, &
428      1:dlen(var_dim_ids(m, 2))-1, &
429      1:dlen(var_dim_ids(m, 3))-1), &
430      1:t_stride )
431      data_tmp = 0.0D0
432      CALL check ( nf90_get_var(ncid, m+1, data_tmp,      &
433      start = (/ 1, 1, 1, t_start /),      &
434      count = (/ dim_x, dim_y, dim_z, t_stride/ ) ), nf90_noerr )
435      EXIT
436      END IF
437      END DO
438      PRINT*, '      [, i, ' ] loaded dataset.'
439
440      CASE ( 'write' )
441
442
443      DO m=num_of_dims,num_of_vars-1
444      IF ( vname(m) == TRIM( variable ) ) THEN
445      CALL check( nf90_put_var(ncid_out, out_var_id(var_dim(m)+1), &
446      data, start = (/ 1, 1, 1, t_start/), &
447      count = (/dim_x, dim_y, dim_z, t_stride/)), &
448      nf90_noerr )
449      EXIT
450      END IF
451      END DO
452
453      CASE ( 'close' )
454
455      CALL check( nf90_close(ncid), nf90_noerr )
456

```


avg.f90

```

457     CASE ( 'close_out' )
458
459         IF ( TRIM(mode) /= 'none' ) THEN
460             CALL check( nf90_close(ncid_out), nf90_noerr )
461             PRINT*, '*** Written file: ', TRIM(file_out)
462             PRINT*, '    with cycle number ', TRIM(filename_cycle_chr)
463         END IF
464
465         IF ( TRIM(post_process_type) /= 'none' ) THEN
466             CALL check( nf90_close(ncid2d_out), nf90_noerr )
467             PRINT*, '*** Written file: ', TRIM(file_out)
468             PRINT*, '    with cycle number ', TRIM(filename_cycle_chr_2d)
469         END IF
470
471     CASE DEFAULT
472         PRINT*, 'action = ', action
473         STOP '+++ NetCDF error.'
474
475     END SELECT
476
477 END SUBROUTINE
478
479 SUBROUTINE user_actions ( action, i )
480
481     USE globals
482     USE indices
483     USE netcdf
484
485     CHARACTER (LEN=*) :: action
486     REAL :: local_average, tmp_avg
487     INTEGER :: i, k
488     REAL :: omp_get_wtime, omp_time_start, omp_time_end, dptdz_threshold
489     REAL, DIMENSION(:, :, :), ALLOCATABLE :: dptdz, z_i
490
491     SELECT CASE ( TRIM( action ) )
492
493     CASE ( 'each_run' )
494         !
495         !--      If necessary do a time averaging over some steps
496         IF ( timestep_average > 1 ) THEN
497             CALL time_averaging ( dim_x, dim_y, dim_z, t_stride )
498         END IF
499
500         !$OMP PARALLEL PRIVATE( x, y, z, t )
501         !$OMP DO
502         DO t=1, t_stride
503             DO z=1, dim_z
504                 DO y=1, dim_y
505                     DO x=1, dim_x
506                         data(x,y,z,t) = data(x,y,z,t) + data_tmp(x,y,z,t)
507                     END DO
508                 END DO
509             END DO
510         END DO
511         !$OMP END DO
512         !$OMP END PARALLEL
513
514     CASE ( 'after_loop' )
515
516         IF ( mode == 'ensemble' ) THEN
517
518             !$OMP PARALLEL PRIVATE( x, y, z, t )
519             !$OMP DO
520             DO t=1, t_stride
521                 DO z=1, dim_z
522                     DO y=1, dim_y
523                         DO x=1, dim_x
524                             data(x,y,z,t) = data(x,y,z,t) / REAL( num_of_runs )
525                         END DO
526                     END DO
527                 END DO
528             END DO
529             !$OMP END DO
530             !$OMP END PARALLEL
531
532         ELSEIF ( mode == 'induced' ) THEN

```

avg.f90

```

533      omp_time_start = omp_get_wtime()
534
535      !$OMP PARALLEL PRIVATE( x, y, z, t )
536      !$OMP DO
537      DO t=1, t_stride
538          DO z=1, dim_z
539              DO y=1, dim_y
540                  DO x=1, dim_x
541                      data(x,y,z,t) = data(x,y,z,t) / REAL( num_of_runs )
542                  END DO
543              END DO
544          END DO
545      END DO
546      !$OMP END DO
547      !$OMP END PARALLEL
548
549      PRINT*, "MAXIMUM:", MAXVAL(data)
550      PRINT*, "MINIMUM:", MINVAL(data)
551
552      !$OMP PARALLEL PRIVATE( x, y, z, t, tmp_avg )
553      !$OMP DO
554      DO t=1, t_stride
555          DO z=1, dim_z
556              tmp_avg = local_average( t, z, dim_y, dim_x )
557              DO y=1, dim_y
558                  DO x=1, dim_x
559                      data(x,y,z,t) = data(x,y,z,t) - tmp_avg
560                  END DO
561              END DO
562          END DO
563      END DO
564      !$OMP END DO
565      !$OMP END PARALLEL
566
567      omp_time_end = omp_get_wtime()
568      PRINT*, '+++ OpenMP Loop = ', omp_time_end - omp_time_start
569
570      PRINT*, "MAXIMUM:", MAXVAL(data)
571      PRINT*, "MINIMUM:", MINVAL(data)
572
573      END IF
574
575      IF ( timestep_average > 1 ) THEN
576          data(:,:,1:timestep_average-1) = 0.0
577      END IF
578
579      CASE ( 'post_processing' )
580
581      !
582      !-- Calculate the local boundary layer height with the gradient method
583      !-- according to SULLIVAN(1998), modified by UHLENBROCK(2006). The
584      !-- method still is not able to calculate the boundary layer height
585      !-- above an soil inversion like it's the case over heterogeneous
586      !-- surfaces, e.g. over lakes.
587      IF ( post_process_type == 'zi' ) THEN
588
589          ALLOCATE ( dptdz(1:dim_x, 1:dim_y, 2:dim_z) )
590          ALLOCATE ( z_i(1:dim_x, 1:dim_y, 1:t_stride) )
591
592          z_i = 0.0
593          dptdz_threshold = 0.3 / 100.0
594
595
596          DO t=1, t_stride
597
598              !$OMP PARALLEL PRIVATE( x, y, z )
599              !$OMP DO
600              DO y=1, dim_y
601                  DO x=1, dim_x
602                      DO z=2, dim_z-1
603                          dptdz(x,y,z) = ( data(x,y,z,t) - data(x,y,z-1,t) ) &
604                              / ( dim3(z+1) - dim3(z) )
605                      END DO
606                  END DO
607              ENDDO
608              !$OMP END DO

```

```

609          !$OMP END PARALLEL
610
611          DO y=1, dim_y
612              DO x=1, dim_x
613                  DO z=z_offset, dim_z-4
614
615                      IF ( dptdz(x,y,z) > dptdz_threshold .AND.           &
616                          dptdz(x,y,z) > dptdz(x,y,z+1) .AND.           &
617                          dptdz(x,y,z) > dptdz(x,y,z+2) .AND.           &
618                          dptdz(x,y,z) > dptdz(x,y,z+3) .AND.           &
619                          dptdz(x,y,z) > dptdz(x,y,z+4) )                 &
620                          THEN
621                              z_i(x,y,t) = ( dim3(z+1) + dim3(z) ) * 0.5
622                              EXIT
623                          ENDIF
624                      END DO
625                  END DO
626              END DO
627
628          ENDDO
629          !
630          !-- Write to a pseudo-4d array according palm standard
631          ALLOCATE ( tmp4d_array(1:dim_x,1:dim_y,1:1,t_stride) )
632          tmp4d_array(:, :, 1, :) = z_i(:, :, :)
633
634          CALL check( nf90_put_var(ncid2d_out, out2d_var_id(5),           &
635                      tmp4d_array,                                       &
636                      start = (/ 1, 1, 1, t_start/),                       &
637                      count = (/dim_x, dim_y, 1, t_stride/)),           &
638                      nf90_noerr )
639          DEALLOCATE ( tmp4d_array )
640          DEALLOCATE ( dptdz )
641          DEALLOCATE ( z_i )
642      END IF
643
644      CASE DEFAULT
645          PRINT*, 'action = ', action
646          STOP '+++ Error.'
647
648  END SELECT
649
650  END SUBROUTINE
651
652  FUNCTION local_average(t, z, m, n)
653  !
654  !-- Function for calculating a horizontal average. This is used to calculate the
655  !-- heterogeneity induced quantity
656  !-- USE globals
657  USE globals
658
659  IMPLICIT NONE
660
661  REAL :: local_average, sum
662  INTEGER :: i, j, m, n, t, z
663
664  sum = 0.0D0
665
666  !$OMP PARALLEL PRIVATE( i, j ) REDUCTION(+:sum)
667
668  !$OMP DO
669  DO j = 1, m
670      DO i = 1, n
671          sum = sum + data(i,j,z,t)
672      END DO
673  END DO
674  !$OMP END DO
675
676  !$OMP END PARALLEL
677
678
679  local_average = sum / ( REAL(n) * REAL(m) )
680  RETURN
681
682  END FUNCTION local_average
683
684  SUBROUTINE time_averaging( length )

```

```

685
686 USE globals
687
688 IMPLICIT NONE
689
690 INTEGER, INTENT(IN), DIMENSION(:) :: length(1:4)
691 INTEGER :: t, j, x, y, z
692 REAL, DIMENSION (:,:,,:), ALLOCATABLE :: data_tmp2
693
694 ALLOCATE ( data_tmp2(1:length(1),1:length(2),1:length(3),1:length(4)) )
695 data_tmp2 = 0.0D0
696
697 !$OMP PARALLEL PRIVATE( t, j, x, y, z )
698
699 !$OMP DO
700 DO t=timestep_average, length(4)
701   DO j=0, timestep_average-1
702     DO z=1, length(3)
703       DO y=1, length(2)
704         DO x=1, length(1)
705           data_tmp2(x,y,z,t) = data_tmp2(x,y,z,t) + data_tmp(x,y,z,t-j)
706         END DO
707       END DO
708     END DO
709   END DO
710   DO z=1, length(3)
711     DO y=1, length(2)
712       DO x=1, length(1)
713         data_tmp2(x,y,z,t) = data_tmp2(x,y,z,t) / REAL(timestep_average)
714       END DO
715     END DO
716   END DO
717 END DO
718 !$OMP END DO
719 !$OMP END PARALLEL
720
721 !$OMP PARALLEL PRIVATE( t, x, y, z )
722
723 !$OMP DO
724 DO t=1, length(4)
725   DO z=1, length(3)
726     DO y=1, length(2)
727       DO x=1, length(1)
728         data_tmp(x,y,z,t) = data_tmp2(x,y,z,t)
729       END DO
730     END DO
731   END DO
732 END DO
733 !$OMP END DO
734 !$OMP END PARALLEL
735
736 DEALLOCATE ( data_tmp2 )
737 END SUBROUTINE
738
739 !
740 !-- The subroutine check will stop the program in case of an NetCDF error
741 SUBROUTINE check(status, ierr)
742
743 USE netcdf
744
745 IMPLICIT NONE
746
747 INTEGER, INTENT(IN) :: status, ierr
748
749 IF ( status /= ierr ) THEN
750   PRINT*, TRIM(nf90_strerror(status))
751   STOP '+++ Stopped.'
752 END IF
753
754 END SUBROUTINE check
755
756 SUBROUTINE init_2d_file ( var, units, long_name )
757
758 USE netcdf
759 USE globals
760
```

avg.f90

```

761  IMPLICIT NONE
762
763  CHARACTER(*), INTENT(IN) :: var, units, long_name
764
765  !
766  !-- Define filename for data output (increasing numbers avoids overwriting of
767 !-- old data)
768  file_exists = .TRUE.
769  filename_cycle = 0
770
771  DO WHILE ( file_exists == .TRUE. )
772    filename_cycle = filename_cycle + 1
773    WRITE(filename_cycle chr 2d, FMT='(I3)') filename_cycle
774    filename_cycle_chr_2d = ADJUSTL(filename_cycle chr 2d)
775    file_out = TRIM(path)//TRIM(output_filename)//'_/' &
776              TRIM(post_process_type)//'_/' &
777              TRIM(filename_cycle chr 2d)//'.nc'
778    INQUIRE(FILE=file_out, EXIST=file_exists)
779    IF ( .NOT. file_exists ) file_exists = .FALSE.
780  END DO
781
782  !
783  !-- Prepare NetCDF output
784  CALL check(nf90_create(TRIM(file_out), NF90_CLOBBER, ncid2d_out),nf90_noerr)
785
786  ALLOCATE ( out2d_dim_id(1:4), out2d_var_id(1:5) )
787
788  CALL check( nf90_def_dim(ncid2d_out, 'x', dim_x, out2d_dim_id(1)), &
789             nf90_noerr)
790  CALL check( nf90_def_var(ncid2d_out, 'x', NF90_DOUBLE, out2d_dim_id(1), &
791             out2d_var_id(1)), nf90_noerr )
792  CALL check( nf90_put_att(ncid2d_out, out2d_var_id(1), 'units', 'meters'), &
793             nf90_noerr )
794
795  CALL check( nf90_def_dim(ncid2d_out, 'y', dim_y, out2d_dim_id(2)), &
796             nf90_noerr)
797  CALL check( nf90_def_var(ncid2d_out, 'y', NF90_DOUBLE, out2d_dim_id(2), &
798             out2d_var_id(2)), nf90_noerr)
799  CALL check( nf90_put_att(ncid2d_out, out2d_var_id(2), 'units', 'meters'), &
800             nf90_noerr )
801
802  CALL check( nf90_def_dim(ncid2d_out, 'zu1_xy', 1, out2d_dim_id(3)), &
803             nf90_noerr)
804  CALL check( nf90_def_var(ncid2d_out, 'zu1_xy', NF90_DOUBLE, &
805             out2d_dim_id(3), &
806             out2d_var_id(3)), nf90_noerr)
807  CALL check( nf90_put_att(ncid2d_out, out2d_var_id(3), 'units', 'meters'), &
808             nf90_noerr )
809
810  CALL check( nf90_def_dim(ncid2d_out, 'time', NF90_UNLIMITED, &
811             out2d_dim_id(4)), nf90_noerr )
812  CALL check( nf90_def_var(ncid2d_out, 'time', NF90_DOUBLE, out2d_dim_id(4), &
813             out2d_var_id(4)), nf90_noerr)
814  CALL check( nf90_put_att(ncid2d_out, out2d_var_id(4), 'units', 'seconds'), &
815             nf90_noerr )
816
817  CALL check( nf90_def_var(ncid2d_out, TRIM(var), NF90_DOUBLE, out2d_dim_id, &
818             out2d_var_id(5) ), nf90_noerr )
819  CALL check( nf90_put_att(ncid2d_out, out2d_var_id(5), 'units', &
820             TRIM(units)), &
821             nf90_noerr)
822  CALL check( nf90_put_att(ncid2d_out, out2d_var_id(5), 'long_name', &
823             TRIM(long_name)), nf90_noerr)
824
825  CALL nccall ( 'open', 1 )
826  !
827  !-- Write global attributes
828  CALL check( nf90_copy_att(ncid, NF90_GLOBAL, 'Conventions', ncid2d_out, &
829             NF90_GLOBAL), nf90_noerr )
830
831  CALL nccall ( 'close', 1 )
832
833  CALL check( nf90_put_att(ncid2d_out, NF90_GLOBAL, 'title', &
834             TRIM(post_process_type) ), nf90_noerr )
835
836  CALL check( nf90_put_att(ncid2d_out, NF90_GLOBAL, 'VAR_LIST', &

```

avg.f90

```
837          ';//TRIM(var)//';' ), nf90_noerr )
838
839      CALL check( nf90_undef(ncid2d_out), nf90_noerr )
840
841      !
842      !-- Write arrays to file
843      CALL check( nf90_put_var(ncid2d_out, out2d_dim_id(1), dim1), nf90_noerr )
844      CALL check( nf90_put_var(ncid2d_out, out2d_dim_id(2), dim2), nf90_noerr )
845      CALL check( nf90_put_var(ncid2d_out, out2d_dim_id(3), dim3(1)), nf90_noerr )
846      CALL check( nf90_put_var(ncid2d_out, out2d_dim_id(4), dim4), nf90_noerr )
847
848      END SUBROUTINE
```

Bibliography

- Andreas, E. L. (1988):** Estimating C_n^2 over snow and sea ice from meteorological data. *J. Opt. Soc. Amer.*, 5, p. 481–495.
- Andreas, E. L. (1991):** Using scintillation at two wavelengths to measure path-averaged heat fluxes in free convection. *Boundary-Layer Meteorol.*, 54, p. 167–182.
- Arakawa, A., Lamb, V. R. (1977):** Computational design of the basic dynamical processes of the UCLA general circulation model. In: J. Chang (Ed.), 1977: *General circulation models of the atmosphere*. *Methods in Computational Physics*, Berlin, 17, p. 173-265.
- Avissar, R., Schmidt, T. (1998):** An Evaluation of the Scale at which Ground-Surface Heat Flux Patchiness Affects the Convective Boundary Layer Using Large-Eddy Simulations. *J. Atmos. Sci.*, 55, p. 2666–2689.
- Bange, J., Spieß, T., et. al. (2006):** Turbulent fluxes from Helipod flights above quasi-homogeneous patches within the LITFASS area. *Boundary-Layer Meteorol.*, 121, p. 127–151.
- Beyrich, F., Bange, J., Hartogensis, O. K., Raasch, S., Braam, M., van Dinter, D., Gräf, D., van Kesteren, B., van den Kroonenberg, A. C., Maronga, B., Martin, S., Moene, A. F. (2012):** Towards a validation of scintillometer measurements: The LITFASS-2009 experiment. *Boundary-Layer Meteorol.*, 144, p. 83–112.
- Beyrich, F., de Bruin, H., et al. (2002):** Results from one-year continuous operation of a large aperture scintillometer over a heterogeneous land surface. *Boundary-Layer Meteorol.*, 105, p. 85–97.
- Beyrich, F., Herzog, H.-J., Neisser, J. (2002a):** The LITFASS project of the DWD and the LITFASS-98 experiment: The project strategy and the experimental setup. *Theor. Appl. Climatol.*, 73, p. 3–18.
- Beyrich, F., Leps, J.-P., et. al. (2006a):** Area-averaged surface fluxes over the LITFASS region based on eddy-covariance measurements. *Boundary-Layer Meteorol.*, 121, p. 33–65.
- Beyrich, F., Mengelkamp, H.-T. (2006):** Evaporation over a Heterogeneous Land Surface: EVA_GRIPS and the LITFASS-2003 Experiment: An Overview. *Boundary-Layer Meteorol.*, 121, p. 5–32.
- Beyrich, F., Richter, S. H., et al. (2002b):** Experimental determination of turbulent fluxes over heterogeneous LITFASS area: selected results from the LITFASS-98 experiment. *Theor. Appl. Climatol.*, 73, p. 19–34.
- Blackadar, A. K. (1997):** *Turbulence and Diffusion in the Atmosphere*. Springer, Berlin, Heidelberg, New York.
- Brasseur, J. G., Wei, T. (2010):** Designing large-eddy simulation of the turbulent boundary layer to capture law-of-the-wall scaling. *Phys. Fluids*, 22, 021303.

- Businger, J. A., Wyngaard, J. C., Izumi, Y., Bradley, E. F. (1971):** Flux–profile relationships in the atmospheric surface. *J. Atmos. Sci.*, 28, p. 181–189.
- Cheinet, S., Cumin, P. (2011):** Local Structure Parameters of Temperature and Humidity in the Entrainment-Drying Convective Boundary Layer: A Large-Eddy Simulation Analysis. *J. Appl. Meteorol.*, 50, p. 472–481.
- Cheinet, S., Siebesma, A. P. (2007):** The impact of boundary layer turbulence on optical propagation. *Proc. SPIE 6747, Optics in Atmospheric Propagation and Adaptive Systems X*, p. 67470A. Florence, Italy. doi:10.1117/12.741433.
- Cheinet, S., Siebesma, A. P. (2009):** Variability of Local Structure Parameters in the Convective Boundary Layer. *J. Atmos. Sci.*, 66, p. 1002–1017.
- Courant, R., Friedrichs, K., Lewy, H. (1928):** Über die partiellen Differentialgleichungen der mathematischen Physik. *Math. Ann.*, 100, p. 32–74.
- Courault, D., Drobinski, P., Brunet, Y., Lacarrere, P., Talbot, C. (2007):** Impact of surface heterogeneity on a buoyancy-driven convective boundary layer in light winds. *Boundary-Layer Meteorol.*, 124, p. 383–403.
- De Bruin, H. A. R., Kohsiek, W., VanDenHurk, B. J. J. M. (1993):** A verification of some methods to determine the fluxes of momentum, sensible heat and water vapour using standard deviation and structure parameter of scalar meteorological quantities. *Boundary-Layer Meteorol.*, 63, p. 231–257.
- De Bruin, H. A. R., Van den Hurk, B. J. J. M., Kohsiek, W. (1995):** The scintillation method tested over a dry vineyard area. *Boundary Layer Meteorol.*, 76, p. 25–40.
- Deardorff, J. W. (1970):** A numerical study of three-dimensional turbulent channel flow at large Reynolds numbers. *J Fluid Mech.*, 41, p. 453–480. doi:10.1017/S0022112070000691.
- Deardorff, J. W. (1980):** Stratocumulus-capped mixed layers derived from a three-dimensional model. *Boundary-Layer Meteorol.*, 18, p. 495–527.
- Druilhet, A., Frangi, J. P., Guedalia, D., Fonton, J. (1983):** Experimental Studies of the Turbulence Structure Parameters of the Convective Boundary Layer. *J. Clim. Appl. Meteorol.*, 22, p. 594–608.
- Evans, J. G., McNeil, D. D., Finch, J. W., Murray, T., Harding, R. J., Ward, H. C., Verhoef, A. (2012):** Determination of turbulent heat fluxes using a large aperture scintillometer over undulating mixed agricultural terrain. *Agric. For. Meteorol.*, 166-167, p. 221–233. doi: 10.1016/j.agrformet.2012.07.010.
- Fairall, C. W. (1984):** Wind Shear Enhancement of Entrainment and Refractive Index Structure Parameter at the Top of a Turbulent Mixed Layer. *J. Atmos. Sci.*, 41, p. 3472–3484.
- Fairall, C. W. (1987):** A Top-Down and Bottom-Up Diffusion Model of C_T^2 and C_Q^2 in the Entraining Convective Boundary Layer. *J. Atmos. Sci.*, 44, p. 1009–1017.
- Fairall, C. W. (1991):** The Humidity and Temperature Sensitivity of Clear-Air Radars in the Convective Boundary Layer. *J. Appl. Meteorol.*, 41, p. 1064–1074.
- Fesquet, C., Dupont, S., et. al. (2009):** Impact of Terrain Heterogeneity on Coherent Structure Properties: Numerical Approach. *Boundary-Layer Meteorol.*, 133, p. 71–92.

- Garratt, J. R. (1992):** The atmospheric boundary layer. Cambridge University Press, Cambridge.
- Gopalakrishnan, S. G., Avissar, R. (2000):** An LES study of the impacts of land surface heterogeneity on dispersion in the convective boundary layer. *J. Atmos. Sci.*, 57, p. 352–371.
- Grinsted, A., Moor, J. C., Jewrejava, S. (2004):** Application of the cross wavelet transform and wavelet coherence to geophysical time series.. *Nonlinear Processes in Geophys.*, 11, p. 581–566.
- Hadfield, M. G., Cotton, W. R., Pielke, R. A. (1991):** Large-eddy simulations of thermally forced circulations in the convective boundary layer. Part I: a small-scale circulation with zero wind. *Boundary-Layer Meteorol.*, 57, p. 79–114.
- Hadfield, M. G., Cotton, W. R., Pielke, R. A. (1992):** Large-eddy simulations of thermally forced circulations in the convective boundary layer. Part II: the effect of change in wavelength and wind speed. *Boundary-Layer Meteorol.*, 58, p. 307–327.
- Hartogensis, O. K., De Bruin, H. A. R. (2005):** Monin-Obukhov similarity functions of the structure parameter of temperature and TKE dissipation rate in the Stable Boundary Layer. *Boundary-Layer Meteorol.*, 116, p. 253–276.
- Hechtel, L. M., Moeng, C.-H., Stull, R. B. (1990):** The effects of Nonhomogeneous Surface Fluxes on the Convective Boundary Layer: A Case Study using Large-Eddy Simulation. *J. Atmos. Sci.*, 47, p. 1721–1741.
- Hill, R. J. (1978):** Spectra of Fluctuations in Refractivity, Humidity, and the Temperature-Humidity Cospectrum in the Inertial and Dissipation Range. *Radio Sci.*, 13, p. 953–961.
- Hill, R. J. (1989):** Implications of Monin-Obukhov Similarity Theory for Scalar Quantities. *J. Atmos. Sci.*, 46, p. 2236–2244.
- Hill, R. J., Clifford, S. F., Lawrence, R. S. (1980):** Refractive-index and absorption fluctuations in the infrared caused by temperature, humidity and pressure fluctuations. *J. Opt. Soc. Am.*, 70, p. 1192–1205.
- Hill, R. J., Ochs, G. R., Wilson, J. J. (1992):** Measuring surface-layer fluxes of heat and momentum using optical scintillation. *Boundary-Layer Meteorol.*, 58, p. 391–408.
- Huang, H.-Y., Margulis, S. A. (2009):** On the impact of surface heterogeneity on a realistic convective boundary layer. *Water Resour. Res.*, 45, w04425, doi:10.1029/2008WR007175.
- Johansson, C., Smedman, A.-S., Högström, U., Brasseur, J. G. (2002):** Reply to comments by E. L. Andreas and B. B. Hicks (2002). *J. Atmos. Sci.*, 59, p. 2608–2614.
- Johansson, C., Smedman, A.-S., Högström, U., Brasseur, J. G., Khanna, S. (2001):** Critical Test of the Validity of Monin-Obukhov Similarity during Convective Conditions. *J. Atmos. Sci.*, 58, p. 1549–1566.
- Kaimal, J. C., Wyngaard, J. C., Haugen, D. A., Coté, O. R., Izumi, Y. (1976):** Turbulence Structure in the Convective Boundary Layer. *J. Atmos. Sci.*, 33, p. 2152–2169.
- Kang, S.-L. (2009):** Temporal Oscillations in the Convective Boundary Layer Forced by Mesoscale Surface Heat-Flux Variations. *Boundary-Layer Meteorol.*, 132, p. 59–81.
- Kang, S.-L., Davis, K. J. (2008):** The Effects of Mesoscale Surface Heterogeneity on the Fair-Weather Convective Atmospheric Boundary Layer. *J. Atmos. Sci.*, 65, p. 3197–3213.

- Khanna, S., Brasseur, J. G. (1997):** Analysis of Monin-Obukhov similarity from large-eddy simulations. *J Fluid Mech.* 345, p. 251–286.
- Kimmel, S. J., Wyngaard, J. C., Otte, M. J. (2002):** “Log-Chipper” Turbulence in the Convective Boundary Layer. *J. Atmos. Sci.* 59, p. 1124–1134.
- Kohsiek, W. (1982):** Measuring C_T^2 , C_Q^2 , and C_{TQ} in the Unstable Surface Layer, and Relations to the Vertical Fluxes of Heat and Moisture. *Boundary-Layer Meteorol.* 24, p. 89–107.
- Kohsiek, W., Meijninger, W. M. L., et al. (2002):** An extra large aperture scintillometer for long range applications. *Boundary-Layer Meteorol.* 105, p. 119–127.
- Kustas, W. P., Hatfield, J. L., Prueger, J. H. (2005):** The Soil Moisture–Atmosphere Coupling Experiment (SMACEX): Background, Hydrometeorological Conditions and Preliminary Findings. *J. Hydrometeor.* 6, p. 791–804.
- Lagouarde, J.-P., Bonnefond, J.-M., Kerr, Y. H., McAneney, K. J., Irvine, M. (2002):** Integrated sensible heat flux measurements of a two-surface composite landscape using scintillometry. *Boundary-Layer Meteorol.* 105, p. 5–35.
- Letzel, M. O., Krane, M., Raasch, S. (2008):** High resolution urban large-eddy simulation studies from street canyon to neighbourhood scale. *Atmos. Env.* 42, p. 8770–8784. doi: 10.1016/j.atmosenv.2008.08.001.
- Letzel, M. O., Raasch, S. (2003):** Large Eddy Simulation of Thermally Induced Oscillations in the Convective Boundary Layer. *J. Atmos. Sci.* 60, p. 2328–2341.
- Li, D., Bou-Zeid, E., De Bruin, H. A. R. (2012):** Monin-Obukhov Similarity Functions for the Structure Parameters of Temperature and Humidity. *Boundary-Layer Meteorol.* 145, p. 45–67. doi:10.1007/s10546-011-9660-y.
- Lilly, D. K. (2002):** Entrainment into Mixed Layers. Part I: Sharp-Edged and Smoothed Tops. *J. Appl. Meteorol.* 59, p. 3340–3352.
- Liu, G., Sun, J., Yin, L. (2011):** Turbulence Characteristics of the Shear-Free Convective Boundary Layer Driven by Heterogeneous Surface Heating. *Boundary-Layer Meteorol.* 140, p. 57–71. doi: 10.1007/s10546-011-9591-7.
- Mahrt, L. (2000):** Surface heterogeneity and vertical structure of the boundary layer. *Boundary-Layer Meteorol.* 96, p. 33–62.
- Martin, S., Bange, J., Beyrich, F. (2010):** Profiling the lower troposphere using the research UAV ‘M²AV’. *Atmos. Meas. Tech. Discuss.* 3, p. 1–31.
- Mason, P. J., Thomson, D. J. (2002):** Stochastic backscatter in large-eddy simulations of boundary layers. *J. Fluid Mech.* 242, p. 51–78.
- Meijninger, W. M. L., Beyrich, F., Lüdi, A., Kohsiek, W., De Bruin, H. A. R. (2006):** Scintillometer-based turbulent fluxes of sensible and latent heat over a heterogeneous land surface - A contribution to LITFASS-2003. *Boundary-Layer Meteorol.* 121, p. 89–110.
- Meijninger, W. M. L., Green, A. E., et al. (2002a):** Determination of area-averaged water vapour fluxes with large aperture and radio wave scintillometers over a heterogeneous surface - Flevoland field experiment. *Boundary-Layer Meteorol.* 105, p. 63–83.

- Meijninger, W. M. L., Hartogensis, O. K., et al. (2002b):** Determination of area-averaged sensible heat fluxes with a large aperture scintillometer over a heterogeneous surface - Flevoland field experiment. *Boundary-Layer Meteorol.* 105, p. 37–62.
- Moene, A. F., Gioli, B. (2008):** Understanding the scintillometer signal: spatial variability of structure parameters using wavelet analysis. 18th Symposium on Boundary Layers and Turbulence. Am Meteorol Soc, Stockholm (Sweden). paper 8B.3.
- Muschinski, A. (2004):** Local and global statistics of clear-air Doppler radar signals. *Radio Sci.* 39. doi:10.1020/2003RS002908. RS1008.
- Muschinski, A., Frehlich, R., Balsley, B. B. (2004):** Small-scale and large-scale intermittency in the nocturnal boundary layer and the residual layer. *J. Fluid Mech.* 515, p. 319–351.
- Noh, Y., Goh, G., Raasch, S. (2011):** Examination of the mixed layer deepening process during convection using LES. *J. Phys. Oceanogr.* 40, p. 2189–2195. doi:10.1175/2010JPO4277.1.
- Obukhov, A. M. (1946):** Turbulence in an atmosphere with a non-uniform temperature. *Tr. Inst. Teor. Geofiz. Akad. Nauk. SSSR.* 1, p. 95–115. translation in: *Boundary-Layer Meteorol.*, 1971, 2, p. 7–29.
- Ochs, G. R., Wang, T. (1978):** Finite aperture scintillometer for profiling wind and C_n^2 . *Appl. Opt.* 17, p. 3774–3778.
- Panofsky, H. A., Dutton, J. A. (1984):** *Atmospheric Turbulence, Models and Methods for Engineering Applications.* John Wiley & Sons, New York.
- Patrinos, A. N. A., Kistler, A. L. (1977):** A Numerical Study of the Chicago Lake Breeze. *Boundary-Layer Meteorol.* 12, p. 93–123.
- Patton, E. G., Sullivan, P. P., Moeng, C.-H. (2005):** The Influence of Idealized Heterogeneity on Wet and Dry Planetary Boundary Layers Coupled to the Land Surface. *J. Atmos. Sci.* 62, p. 2078–2097.
- Peltier, L. J., Wyngaard, J. C. (1995):** Structure-Function Parameters in the Convective Boundary Layer from Large-Eddy Simulations. *J. Atmos. Sci.* 52, p. 3641–3660.
- Petenko, I. V., Shurygin, E. A. (1999):** A two-regime model for the probability density function of the remperature structure parameter in the convective boundary layer. *Boundary-Layer Meteorol.* 93, p. 381–394.
- Piacsek, S. A., Williams, G. P. (1970):** Conservation properties of convection difference schemes. *J. Comput. Phys.* 6, p. 392–405.
- Raasch, S., Etling, D. (1991):** Numerical simulation of rotating turbulent thermal convection. *Beitr. Phys. Atmos.* 64, p. 185–199.
- Raasch, S., Etling, D. (1998):** Modeling deep ocean convection: Large eddy simulation in comparison with laboratory experiments. *J. Phys. Oceano.* 28, p. 1786–1802.
- Raasch, S., Harbusch, G. (2001):** An Analysis of Secondary Circulations and their Effects caused by small-scale Surface Inhomogeneities using Large-Eddy Simulation. *Boundary-Layer Meteorol.* 101, p. 31–59.
- Raasch, S., Schröter, M. (2001):** PALM - A large-eddy simulation model performing on massively parallel computers. *Meteorol. Z.* 10, p. 363–372.

- Riechelmann, T., Noh, Y., Raasch, S. (2012):** A new method for large-eddy simulations of clouds with Lagrangian droplets including the effects of turbulent collision. *New J. Phys.* 14. doi:10.1088/1367-2630/14/6/065008. 065008.
- Roache, P. J. (1985):** Computational Fluid Dynamics. Hermosa Publishers, Albuquerque, New Mexiko.
- Schumann, U. (1975):** Subgrid Scale Model for Finite Difference Simulations of Turbulent Flows in Plane Channels and Annuli. *J. Comput. Phys.* 18, p. 376–404.
- Shen, S., Leclerc, M. Y. (1995):** How large must surface inhomogeneities be before they influence the convective boundary layer structure? A case study. *Q.J.R. Meteorol. Soc.* 121, p. 1209–1228.
- Smagorinsky, J. (1963):** General Circulation Experiments with the Primitive Equations. *Mon. Wea. Rev.* 91, p. 99–164. doi:10.1175/1520-0493(1963)091<0099:GCEWTP>2.3.CO;2.
- Sreenivasan, K. R. (1996):** The passive scalar spectrum and the Obukhov–Corrsin constant. *Phys. Fluids*. 8, p. 189–196.
- Steinfeld, G., Raasch, S., Markkanen, T. (2008):** Footprints in homogeneously and heterogeneously driven boundary layers derived from a Lagrangian stochastic particle model embedded into large-eddy simulation. *Boundary-Layer Meteorol.* 129, p. 225–248.
- Stull, R. B. (1988):** An Introduction to Boundary Layer Meteorology. Kluwer Academic Publishers, Dordrecht.
- Sühring, M., Raasch, S. (2013):** Heterogeneity-induced heat flux patterns in the convective boundary layer: Can they be detected from observations and is there a blending height? - A large-eddy simulation study for the LITFASS-2003 experiment. *Boundary-Layer Meteorol.* doi: 10.1007/s10546-013-9822-1.
- Tatarskii, V. I. (1961):** Wave Propagation in a Turbulent Medium. McGraw-Hill, New York, Toronto, London.
- Thiermann, V., Grassl, H. (1992):** The measurement of turbulent surface-layer fluxes by use of bichromatic scintillation. *Boundary-Layer Meteorol.* 58, p. 367–389.
- Torrence, C., Compo, G. P. (1998):** A Practical Guide to Wavelet Analysis. *Bull. Am. Meteorol. Soc.* 79, p. 61–78.
- Uhlenbrock, J. (2006):** Numerische Untersuchung der konvektiven Grenzschicht über realen heterogenen Landoberflächen mit einem Grobstruktursimulationsmodell. PhD Thesis, Leibniz University of Hannover. Hannover.
- Uhlenbrock, J., Raasch, S., Hennemuth, B., Zittel, P., Meijninger, W. M. L. (2004):** Effects of land surface heterogeneities on the boundary layer structure and turbulence during LITFASS-2003: Large-eddy simulations in comparison with turbulence measurements. 6th Symposium on Boundary Layers and Turbulence. Am Meteorol Soc, Portland (Maine). paper 9,3.
- van den Kroonenberg, A. C., Martin, S., Beyrich, F., Bange, J. (2012):** Spatially-Averaged Temperature Structure Parameter Over a Heterogeneous Surface Measured by an Unmanned Aerial Vehicle. *Boundary-Layer Meteorol.* 142, p. 55–77.
- van Heerwaarden, C. C., Vilà-Guerau de Arellano, J. (2008):** Relative Humidity as an Indicator for Cloud Formation over Heterogeneous Land Surfaces. *J. Atmos. Sci.* 65, p. 3263–3277.

- Weckwerth, T. M., Parsons, D. B., et. al. (2004):** An Overview of the International H2O Project (IHOP_2002) and Some Preliminary Highlights. *Bull. Am. Meteorol. Soc.*, 85, p. 253–277.
- Wesely, M. L. (1976):** A Comparison of Two Optical Methods for Measuring Line Averages of Thermal Exchanges Above Warm Water Surfaces. *J. Appl. Meteorol.*, 15, p. 1177–1188.
- Wicker, L. J., Skamarock, W. C. (2002):** Time-splitting methods for elastic models using forward time schemes. *Mon. Wea. Rev.*, 130, p. 2088–2097.
- Wieringa, J. (1976):** An Objective Exposure Correction Method for Average Wind Speeds Measured at a Sheltered Location. *Quart. J. Roy. Meteorol. Soc.*, 102, p. 241–253.
- Williamson, J. H. (1980):** Low-storage Runge-Kutta schemes. *J Comput. Phys.*, 35, p. 48–56.
- Wilson, C., Fedorovich, E. (2012):** Direct Evaluation of Refractive-Index Structure Functions from Large-Eddy Simulation Output for Atmospheric Convective Boundary Layers. *Acta Geophys.*, 60, p. 1474–1492.
- Wyngaard, J. C., Izumi, Y., Collins, S. A. J. (1971):** Behavior of the Refractive-Index-Structure Parameter near the Ground. *J. Opt. Soc. Am.*, 61, p. 1646–1650.
- Wyngaard, J. C., LeMone, M. A. (1980):** Behavior of the Refractive Index Structure Parameter in the Entraining Convective Boundary Layer. *J. Atmos. Sci.*, 37, p. 1573–1585.

Curriculum Vitae

Personal Details

Family Name	Maronga
First Name	Björn
Date of birth	06 March 1984
Place of birth	Bad Segeberg, Germany
Nationality	German

Academic career

Since 01/2012	Research associate at the Institute of Meteorology and Climatology, Leibniz Universität Hannover, Germany; DFG research project on “High-resolution LES studies of the turbulent structure of the lower atmospheric boundary layer over heterogeneous terrain and implications for the interpretation of scintillometer data” (RA 617/20-1, RA 617/20-3).
09/2011 - 12/2011	Assistant lecturer at the Institute of Meteorology and Climatology, Leibniz Universität Hannover, Germany; tutorial development for the LES model PALM and model usability improvements.
07/2010 - 09/2011	Research associate at the Institute of Meteorology and Climatology, Leibniz Universität Hannover, Germany; DFG research project on “High-resolution LES studies of the turbulent structure of the lower atmospheric boundary layer over heterogeneous terrain and implications for the interpretation of scintillometer data” (RA 617/20-1, RA 617/20-3).
02/2009 - 06/2010	Student assistant at the Institute of Meteorology and Climatology, Leibniz Universität Hannover, Germany; DFG research project on “The effect of land surface heterogeneity on the atmospheric boundary-layer structure and measurements” (RA 617/21-1), programming and rendering of scientific animations.
12/2008	Student assistant at the Nansen Environmental and Remote Sensing Centre, Bergen, Norway; development of an atmosphere-ocean coupling for large-eddy simulation models.

**University
Education**

- 04/2008 - 06/2008 **Student assistant** at the Institute of Meteorology and Climatology, Leibniz Universität Hannover, Germany; tutorial supervision for “thermodynamics and statics”.
- 06/2010 **German ”Diplom“ in meteorology.** Final grade: cum laude (1.6). Diploma thesis on ”The Effect of Surface Heterogeneities on the convective Boundary Layer during LITFASS-2003 - An LES Study“. Final grade: magna cum laude (1.0).
- 01/2009 - 06/2010 **Studies in meteorology,** Leibniz Universität Hannover, Germany.
- 08/2008 - 12/2008 **Studies in meteorology,** University of Bergen, Norway.
- 10/2003 - 07/2008 **Studies in meteorology,** Leibniz Universität Hannover, Germany.

**Peer-Reviewed
Publications**

- Maronga B, Hartogensis OK, Raasch S, 2013:** The effect of surface heterogeneity on the structure parameters of temperature and humidity - An LES case study for the LITFASS-2003 experiment. *Boundary-Layer Meteorol.*, under preparation.
- Sühring M., B. Maronga, F. Herbolt and S. Raasch, 2013:** On the effect of surface heat-flux heterogeneities on the mixed-layer top entrainment. *Boundary-Layer Meteorol.*, under revision.
- Maronga B, 2013:** Monin-Obukhov similarity functions for the structure parameters of temperature and humidity in the unstable surface layer: results from high-resolution large-eddy simulations *J. Atmos. Sci.*, doi: 10.1175/JAS-D-13-0135.1, in press.
- Maronga B, Moene AF, van Dinter D, Raasch S, Bosveld F, Gioli B, 2013:** Derivation of structure parameters of temperature and humidity in the convective boundary layer from large-eddy simulations and implications for the interpretation of scintillometer observations. *Boundary-Layer Meteorol.*, **148**, 1-30, doi: 10.1007/s10546-013-9801-6.
- Maronga B, Raasch S, 2013:** Large-Eddy Simulations of Surface Heterogeneity Effects on the Convective Boundary Layer During the LITFASS-2003 Experiment. *Boundary-Layer Meteorol.*, **146**, 17-44, doi: 10.1007/s10546-012-9748-z.

**Conference
Contributions**

Beyrich F, Bange J, Hartogensis OK, Raasch S, Braam M, van Dinter D, Gräf D, van Kesteren B, van den Kroonenberg A, Maronga B, Martin S, Moene AF, 2012: Towards a validation of scintillometer measurements: The LITFASS-2009 experiment. *Boundary-Layer Meteorol.*, **144**, 83-112, doi: 10.1007/s10546-012-9715-8.

Maronga B, Raasch S, 2013: Monin-Obukhov similarity relationships for structure parameters of temperature and humidity under unstable conditions - results from surface-layer resolving LES *13th EMS Annual Meeting & 11th European Conference on Applications of Meteorology (ECAM), Reading, UK.*

Maronga B, Moene AF, van Dinter D, Raasch S, 2012: Investigations of structure parameters and their similarity relationships in the convective boundary layer by means of large-eddy simulations and comparison with measurement data. *20th AMS Symposium on Boundary Layers and Turbulence, Boston (MA), USA.*

Drüke S, Sühling M, Maronga B, Raasch S, 2012: The Effect of cloud shadows on coherent structures and secondary circulations in the convective boundary layer over homogeneous and heterogeneous terrain. *20th AMS Symposium on Boundary Layers and Turbulence, Boston (MA), USA.*

Herbort F, Maronga B, Sühling M, Raasch S, 2012: The effect of surface heat flux heterogeneities on the mixed-layer top entrainment. *20th AMS Symposium on Boundary Layers and Turbulence, Boston (MA), USA.*

Beyrich F, Bange J, Hartogensis OK, Raasch S, Braam M, van Dinter D, Gräf D, Martin S, van den Kroonenberg A, Moene AF, van Kesteren B, Maronga B, 2012: An Attempt to Validate Scintillometer Measurements: The LITFASS-2009 Experiment. *20th AMS Symposium on Boundary Layers and Turbulence, Boston (MA), USA.*

Maronga B, van Dinter D, Moene AF, Raasch S, 2012: Derivation of turbulent structure parameters from large-eddy simulations and comparison with large-aperture scintillometer data and aircraft observations. *EGU General Assembly 2012, Vienna, Austria.*

Beyrich F, Bange J, Hartogensis OK, Raasch S, Braam M, Gräf D, van Kesteren B, Maronga B, Martin S, Moene AF, 2010: LITFASS-2009: Lindenberg-Falkenberg Flugzeug, Szintillometer und LES Studie. *DACH 2010, Bonn, Germany.*

Maronga B, Raasch S, 2010: Correlations between thermal surface heterogeneities and secondary circulations during LITFASS-2003 - An LES study. *19th AMS Symposium on Boundary Layers and Turbulence, Keystone (CO), USA.*